



Editor, **YOGESH JALURIA** (2010)
Assistant to the Editor, **S. PATEL**

Associate Editors

Gautam Biswas, Indian Institute of Technology, Kanpur (2009)
Louis C. Burmeister, University of Kansas (2008)
Minking Chyu, University of Pittsburgh (2009)
Suresh V. Garimella, Purdue University (2007)
A. Haji-Sheikh, University of Texas at Arlington (2008)
Anthony M. Jacobi, University of Illinois (2008)
Yogendra Joshi, Georgia Institute of Technology (2008)
Satish G. Kandlikar, Rochester Institute of Technology (2007)
Jay M. Khodadadi, Auburn University (2007)
Jose L. Lage, Southern Methodist University (2008)
Sai C. Lau, Texas A&M University (2009)
Ben Q. Li, University of Michigan, Dearborn (2009)
Raj M. Manglik, University of Cincinnati (2009)
Chang H. Oh, Idaho National Laboratory (2007)
Ranga Pitchumani, University of Connecticut (2007)
Ramendra P. Roy, Arizona State University (2007)
Jamal Seyed-Yagoobi, Illinois Institute of Technology (2009)
Bengt Sundén, Lund Institute of Technology, Sweden (2008)
Walter W. Yuen, University of California at Santa Barbara (2008)

Past Editors

V. DHIR
J. R. HOWELL
R. VISKANTA
G. M. FAETH
K. T. YANG
E. M. SPARROW

HEAT TRANSFER DIVISION
Chair, **RODNEY DOUGLASS**
Vice Chair, **TIM TONG**
Past Chair, **MICHAEL JENSEN**

PUBLICATIONS COMMITTEE
Chair, **BAHRAM RAVANI**

OFFICERS OF THE ASME
President, **TERRY E. SHOUP**
Executive Director,
VIRGIL R. CARTER
Treasurer,
THOMAS D. PESTORIUS

PUBLISHING STAFF
Managing Director, Publishing
PHILIP DI VIETRO
Manager, Journals
COLIN McATEER
Production Assistant
MARISOL ANDINO

Transactions of the ASME, Journal of Heat Transfer (ISSN 0022-1481) is published monthly by The American Society of Mechanical Engineers, Three Park Avenue, New York, NY 10016. Periodicals postage paid at New York, NY and additional mailing offices.
POSTMASTER: Send address changes to Transactions of the ASME, Journal of Heat Transfer, c/o THE AMERICAN SOCIETY OF MECHANICAL ENGINEERS, 22 Law Drive, Box 2300, Fairfield, NJ 07007-2300.
CHANGES OF ADDRESS must be received at Society headquarters seven weeks before they are to be effective.
Please send old label and new address.

STATEMENT from By-Laws. The Society shall not be responsible for statements or opinions advanced in papers or ... printed in its publications (B7.1, Para. 3).

COPYRIGHT © 2006 by The American Society of Mechanical Engineers. For authorization to photocopy material for internal or personal use under those circumstances not falling within the fair use provisions of the Copyright Act, contact the Copyright Clearance Center (CCC), 222 Rosewood Drive, Danvers, MA 01923, tel: 978-750-8400, www.copyright.com.
Request for special permission or bulk copying should be addressed to Reprints/Permission Department.
Canadian Goods & Services Tax Registration #126148048

Journal of Heat Transfer

Published Monthly by ASME

VOLUME 128 • NUMBER 10 • OCTOBER 2006

RESEARCH PAPERS

Forced Convection

977 Rheological Characteristics and Turbulent Friction Drag and Heat Transfer Reductions of a Very Dilute Cationic Surfactant Solution
Jinjia Wei, Yasuo Kawaguchi, Bo Yu, and Ziping Feng

984 Heat Transfer to Small Horizontal Cylinders Immersed in a Fluidized Bed
J. Friedman, P. Koundakjian, D. Naylor, and D. Rosero

Jets, Wakes, and Impingement Cooling

990 Local Convective Heat Transfer From a Constant Heat Flux Flat Plate Cooled by Synthetic Air Jets
M. B. Gillespie, W. Z. Black, C. Rinehart, and A. Glezer

Natural and Mixed Convection

1001 Self-Preserving Mixing Properties of Steady Round Buoyant Turbulent Plumes in Uniform Crossflows
F. J. Diez, L. P. Bernal, and G. M. Faeth

1012 Effect of Surface Radiation on Multiple Natural Convection Solutions in a Square Cavity Partially Heated from Below
El Hassan Ridouane and Mohammed Hasnaoui

Radiative Heat Transfer

1022 Radiative Properties of Dense Fibrous Medium Containing Fibers in the Geometric Limit
R. Coquard and D. Baillis

1031 Metaheuristic Optimization of a Discrete Array of Radiant Heaters
Jason M. Porter, Marvin E. Larsen, J. Wesley Barnes, and John R. Howell

1041 Photon Monte Carlo Simulation for Radiative Transfer in Gaseous Media Represented by Discrete Particle Fields
Anquan Wang and Michael F. Modest

Micro/Nanoscale Heat Transfer

1050 Measurement and Modeling of Condensation Heat Transfer Coefficients in Circular Microchannels
Todd M. Bandhauer, Akhil Agarwal, and Srinivas Garimella

Conduction

1060 The Effect of Internal Temperature Gradients on Regenerator Matrix Performance
K. L. Engelbrecht, G. F. Nellis, and S. A. Klein

Heat Transfer Enhancement

1070 Thermohydraulics of Laminar Flow Through Rectangular and Square Ducts With Transverse Ribs and Twisted Tapes
Debashis Pramanik and Sujoy K. Saha

1081 Design Optimization of Size and Geometry of Vortex Promoter in a Two-Dimensional Channel
Tunc Icoz and Yogesh Jaluria

(Contents continued on inside back cover)

This journal is printed on acid-free paper, which exceeds the ANSI Z39.48-1992 specification for permanence of paper and library materials. ©™
♻️ 85% recycled content, including 10% post-consumer fibers.

TECHNICAL BRIEFS

- 1093 **A Discussion of Transpiration Cooling Problems through an Analytical Solution of Local Thermal Nonequilibrium Model**
J. H. Wang and H. N. Wang
- 1099 **Similarity Solution of Laminar Axisymmetric Jets With Effect of Viscous Dissipation**
A. M. Kalteh and A. Abbassi
- 1103 **Heat Transfer Correlations for Turbulent Mixed Convection in the Entrance Region of a Uniformly Heated Horizontal Tube**
Walter Grassi and Daniele Testi

The ASME Journal of Heat Transfer is abstracted and indexed in the following:

Applied Science and Technology Index, Chemical Abstracts, Chemical Engineering and Biotechnology Abstracts (Electronic equivalent of Process and Chemical Engineering), Civil Engineering Abstracts, Compendex (The electronic equivalent of Engineering Index), Corrosion Abstracts, Current Contents, E & P Health, Safety, and Environment, Ei EncompassLit, Engineered Materials Abstracts, Engineering Index, Enviroline (The electronic equivalent of Environment Abstracts), Environment Abstracts, Environmental Engineering Abstracts, Environmental Science and Pollution Management, Fluidex, Fuel and Energy Abstracts, Index to Scientific Reviews, INSPEC, International Building Services Abstracts, Mechanical & Transportation Engineering Abstracts, Mechanical Engineering Abstracts, METADEX (The electronic equivalent of Metals Abstracts and Alloys Index), Petroleum Abstracts, Process and Chemical Engineering, Referativnyi Zhurnal, Science Citation Index, SciSearch (The electronic equivalent of Science Citation Index), Theoretical Chemical Engineering

Rheological Characteristics and Turbulent Friction Drag and Heat Transfer Reductions of a Very Dilute Cationic Surfactant Solution

Jinjia Wei

State Key Laboratory of Multiphase Flow
in Power Engineering,
Xi'an Jiaotong University,
Xi'an, Shaanxi 710049, China

Yasuo Kawaguchi¹

Department of Mechanical Engineering,
Faculty of Science and Technology,
Tokyo University of Science,
Noda, Chiba 278-8510, Japan
e-mail: yasuo@rs.noda.tus.ac.jp

Bo Yu

Oil and Gas Storage
and Transportation Engineering,
China University of Petroleum,
Beijing, 102249, People's Republic of China

Ziping Feng

Daikin Air Conditioning
Engineering Laboratory Ltd.,
Sakai, 591-8511, Japan

Turbulent friction drag and heat transfer reductions and rheological characteristics of a very dilute cationic surfactant solution, cetyltrimethyl ammonium chloride (CTAC)/sodium salicylate (NaSal) aqueous solution, were experimentally investigated at various temperatures. It was found that there existed a critical temperature above which drag and heat transfer reductions disappeared and shear viscosities rapidly dropped to that of water. It was surmised that drag and heat transfer reductions had a certain relationship with rheological characteristics and a rheological characterization of CTAC/NaSal surfactant solutions was performed to clarify this relationship. The effects of Reynolds number and fluid temperature and concentration on drag and heat transfer reductions were qualitatively explained by analyzing the measured shear viscosity data at different shear rates and solution temperatures and concentrations. The Giesekus model was found to fit the measured shear viscosities reasonably well for different temperatures and concentrations of the surfactant solution and the model parameter values obtained by fitting were correlated with temperature at certain solution concentrations. From the correlation results, the temperature effect on viscoelasticity of surfactant solutions was analyzed to relate the rheological characteristics with drag and heat transfer reduction phenomena. [DOI: 10.1115/1.2345422]

Keywords: drag reduction, heat transfer reduction, rheological characteristics, Giesekus model

Introduction

Polymer and dilute surfactant solutions have been found to reduce turbulent friction drag greatly [1–4]. In the Reynolds number region of industrial interest, the amount of turbulent friction drag reduction (DR) sometimes approaches 80%. Recently, surfactants have been widely accepted to be the most practical drag-reducing additives in district heating and cooling systems (DHC) for reducing pumping power or increasing flow rate because they are rather stable and quickly recover from the degradation as compared with polymers [5–7]. When surfactants are used in DHC systems, very dilute solutions are preferred in order to reduce the environmental impacts and prevent corrosion in the system [8]. More recently, Li et al. [9,10] reported a 60–80% turbulent drag reduction by use of a very dilute cetyltrimethyl ammonium chloride (CTAC)/sodium salicylate (NaSal) aqueous solution with surfactant mass concentration of only 30 ppm, indicating that this surfactant is a very promising drag-reducing additive. Turbulent drag reduction is good news, but is usually accompanied by the problem of turbulent heat transfer reduction. Li et al. [9,10] also made detailed heat transfer measurements and found that the heat transfer coefficient decreased drastically and the heat transfer reduction (HTR) was somewhat larger than that of drag reduction. This is a serious drawback in DHC systems because in these systems the circulating fluid supplies/removes heat and the heat transfer characteristics in heat exchangers are of great importance. It is expected that

maximum DR occurs in the transport pipes and minimum HTR occurs in the heat exchangers. Unlike the Newtonian fluid flow, drag and heat transfer performance of surfactant solution flow was experimentally found to be affected not only by Reynolds number but also by concentration and temperature of surfactant solution [9,10]. The reason for these effects has not yet been well explained. Some experimental and analytical studies of dilute surfactant solutions have been conducted for revealing the turbulent drag-reducing mechanisms and controlling the DR and HTR for industrial applications [11–14]. In these studies, turbulence quantities in surfactant flow were measured or computed and significant modifications of turbulence structure were found, such as damping fluctuations of wall-normal velocity, enhancing that of streamwise velocity as well as attenuating Reynolds stress. In some other studies, the microstructure and rheological characteristics of surfactant solutions with surfactant concentrations larger than 1000 ppm were investigated [15–17]. A rodlike or threadlike micelle network was found in the surfactant solution and the surfactant solution often showed a strong viscoelasticity or/and a large elongational viscosity. The network structure was believed to give solution viscoelasticity and high elongational viscosity, and thus cause DR and HTR occurrence. Although the rheological characteristics of surfactant solution may well explain the DR and HTR mechanism, the rheology of a very dilute effective drag-reducing surfactant solution, CTAC/NaSal solution (less than 500 ppm), has rarely been reported and most of the characteristics are unknown because the industrial importance of rheological characteristics of this kind of solution has not been widely recognized and the measurements are difficult as compared with thick polymeric and dense surfactant solutions. Macias et al. [18] inves-

¹Corresponding author.

Contributed by the Heat Transfer Division of ASME for publication in the JOURNAL OF HEAT TRANSFER. Manuscript received August 31, 2004; final manuscript received February 24, 2006. Review conducted by Raj M. Manglik.

tigated the shear thickening characteristics of dilute CTAT solutions with surfactant mass concentration ranging from 700 ppm to 2000 ppm using particle image velocimetry (PIV) and rheometry. They found for the lower concentrations the shear stress played an important role in the microstructure formation and the shear induced structure (SIS) often occurred, making the rheological characteristics very complicated. Rheological characteristics are also important in direct numerical simulations (DNS) to reveal the drag-reducing mechanism since a constitutive equation of stress is required in the momentum and energy equations. Due to the currently limited understanding of the complex rheological features of surfactant systems, it is difficult to develop the surfactant constitutive equations from molecular theories as was done for polymer solutions. However, with rheological data available for drag-reducing surfactant solutions, it is not so difficult to test the constitutive equations which have been well established for polymer solutions. Lu [19] tested three models, the linear Maxwell model, the quasilinear Oldroyd's fluid B model, and the nonlinear Giesekus model, by using the rheological data for several kinds of drag-reducing surfactant solutions. The results showed that simple models cannot describe these surfactant solutions well enough and the Giesekus model with nonlinear stress terms can fit rheological data reasonably well for these surfactant solutions.

In this study, in order to understand the DR and HTR behavior and rheological characteristics of the very dilute CTAC/NaSal aqueous solution as well as their relationship, DR and HTR characteristics were experimentally investigated at various temperatures and Reynolds numbers, and the shear and elongational viscosities of CTAC/NaSal aqueous solution were measured at different temperatures and concentrations. The rheological characteristics were analyzed by using the Giesekus model and found to be related to the drag-reducing mechanisms of this kind of surfactant solution.

Experiment

Sample Material. The tested cationic surfactant was cetyltrimethyl ammonium chloride (CTAC) (Toho Chemical Industry Co., Ltd., Japan). Sodium salicylate (NaSal) was used as the counterion for aiding the formation of rodlike micelle, the formation of which is considered to be the reason for drag reduction. The surfactant solution was prepared by adding the same mass concentrations of surfactant and counterion to the desired amount of distilled water and tap water for the rheological and drag and heat transfer measurements, respectively. The molar ratio of CTAC to NaSal was 1:2. The surfactant concentration was marked by the concentration of CTAC, and solutions of five mass concentrations (50, 75, 100, 150, and 200 ppm) were made for the rheological measurements as well as one solution of mass concentration of 30 ppm for the DR and HTR measurements.

Drag and Heat Transfer Reduction Measurements. Turbulent drag and heat transfer reduction experiments were carried out in a closed loop fluid flow facility shown schematically in Fig. 1. The system consisted of a reservoir tank (2.0 m³), a pump, a settling chamber equipped with a nozzle, a two-dimensional channel, a diffuser and an electromagnetic flowmeter with a resolution of 0.01 m³/min. In order to maintain a constant fluid temperature, a control system with 15 kW heater and cooling coil was installed in the reservoir tank. The temperature of the fluid was controlled to within ± 0.1 K around a prescribed value.

The test section was 30 mm high, 500 mm wide, and 6 m long (inside measurements). Most of the test section was made of transparent acrylic resin having thickness of 20 mm. The surfactant aqueous solution was circulated by the pump and supplied to the settling chamber. The chamber was equipped with a perforated pipe, stainless steel mesh, and 1/12.5 contraction nozzle. At the entrance of the test section, a 150 mm long honeycomb having 10 \times 10 mm² rectangular openings was used to remove large eddies. A heater plate was placed at the position 4 m downstream

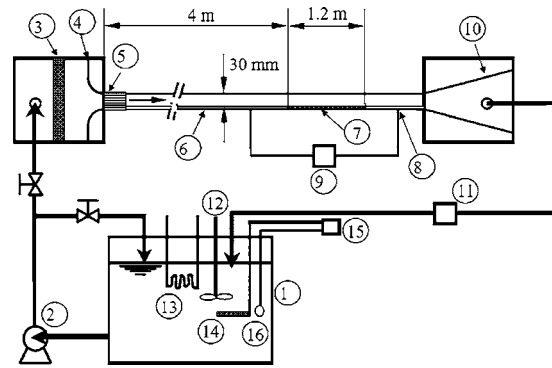


Fig. 1 Schematic diagram of two-dimensional water channel: (1) reservoir tank; (2) pump; (3) filter; (4) contraction; (5) honeycomb; (6) 2D channel; (7) heater plate; (8) pressure tap; (9) pressure transducer; (10) diffuser; (11) flow meter; (12) stirrer; (13) cooling coil; (14) heater; (15) heater regulator; (16) thermocouple

from the inlet of the test section. The heater plate consisted of a polycarbonate resin base plate (10 \times 500 \times 1200 mm³, thickness \times width \times length) and five strips of stainless steel foil heaters (20 μ m thick, 97 mm wide, and 1.2 m long for each). The heaters were glued on the surface of the base plate and were heated uniformly by an ac power supply. The voltage and current were measured to calculate the wall heat flux. A total of 20 thermocouples (200 μ m wires) were located on the backside of the heater foils to measure the surface temperature of the test plate. The local heat transfer coefficient was calculated based on the wall temperature T_w , bulk mean temperature T_b , and heat flux at the heat surface. The wall heat flux q_w was set to a constant of 4.2 kW/m² in the experiments. The friction factor f was calculated from the pressure drop in the channel measured by static pressure taps with a pressure transducer resolution of 0.1 Pa.

Rheological Measurements. Shear viscosity is a fundamental but very important rheological property of surfactant solutions probed by experimental techniques. Shear viscosity measurements were carried out in the stress controlled mode by use of an ARES rheometer (advanced rheometric expansion system), which was equipped with a double wall Couette cell and was manufactured by Rheometrics Scientific F. E. Ltd., Japan. The geometry of the ARES rheometer is shown in Fig. 2(a) and the major dimensions are listed in Table 1. The solution temperature was set from 20 $^{\circ}$ C to 40 $^{\circ}$ C and was controlled by a Julabo F25 Refrigerated Circulator (Julabo Labortechnik GMBH, Germany). A preshear at $\dot{\gamma} = 10$ 1/s was applied for 20 min before the rate sweep test. However, 40 min preshear was applied before the first measurement due to the large gap between the required temperature and the

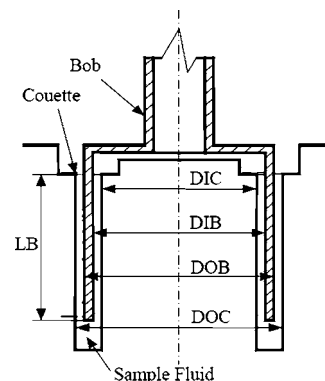


Fig. 2 Schematics of flow geometries of ARES rheometers

Table 1 Major dimensions of flow geometry of ARES rheometers

DIC (mm)	DIB (mm)	DOB (mm)	DOC (mm)	LB (mm)
27.94	29.50	32.00	34.00	31.90

starting temperature. Measurements were performed for shear rates $\dot{\gamma}$ ranging from 10 up to 100 1/s. Both the delay time and measurement time were equal to 5 min.

Uncertainty Analyses. Uncertainty of the calculated results was estimated by using the root-sum-square method of Kline and McClintock [20]. By calibration of measuring instruments, the uncertainties of measured values for temperature, pressure drop, flow rate of surfactant solution, and the voltage and resistance of the electric film heater were determined to be ± 0.1 K, ± 1.0 Pa, $\pm 7.5 \times 10^{-3}$ m³/min, ± 1.4003 V, and ± 0.1 Ω , respectively. The distance of the pressure taps, the length of the heating plate, channel height, and spanwise width have uncertainties of ± 0.7 , ± 0.7 , ± 0.1 , and ± 0.14 mm, respectively. For convenience, the uncertainties of the experimental results that were calculated from measured values were expressed as percentages compared to the values of the results. The bulk velocity and Reynolds number both have uncertainty of $\pm 1.5\%$. Because of the small value of pressure drop of drag-reducing flow, the Fanning friction factor f has uncertainty of $\pm 4.7\%$. The uncertainty of the Colburn factor j_H is affected significantly by uncertainties of temperature and heat flux. With the heat loss taken into account, the uncertainty of j_H is estimated to be less than $\pm 6\%$. The concentration, viscosities, and shear rates of surfactant solution have uncertainties of ± 0.5 , ± 2 , and $\pm 0.1\%$, respectively.

Results and Discussion

Friction Factor and Heat Transfer Coefficient. Figure 3 shows friction factor—Reynolds number relation for CTAC/NaSal surfactant solution in channel flow at temperatures of 30°C and 44°C. Reynolds number was defined using the bulk mean velocity U_b , channel height H , and solvent (water) kinematic viscosity ν . Shown in the same figure are Dean's [21] line which describes a two-dimensional Newtonian turbulent channel flow and the minimum friction drag asymptote given by Zakin et al. [7] for surfactant fluid flow. These two lines are given by the following equations, respectively:

$$f = 0.073 \text{Re}^{-0.25} \quad (1)$$

$$f = 0.32 \text{Re}^{-0.55} \quad (2)$$

The term “drag reduction” (DR) is defined as the deficit of Fanning friction factor from that of solvent (Newtonian) flow at the same Reynolds number. At the temperature of 30°C, it can be

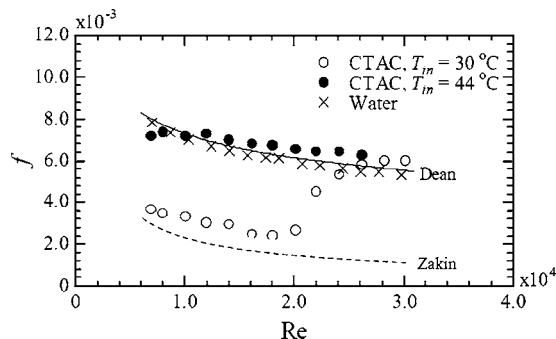


Fig. 3 Friction factors versus Reynolds number in a two-dimensional channel

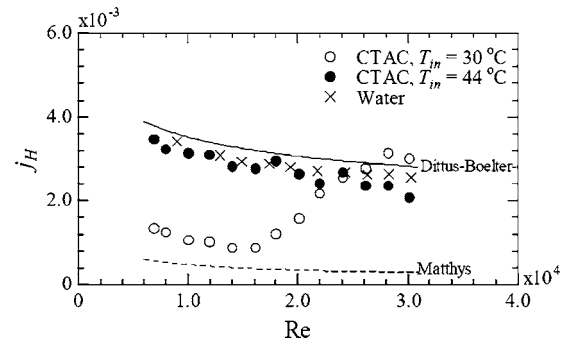


Fig. 4 Colburn j factors versus Reynolds number in a two-dimensional channel

seen that the Fanning friction factors f are close to Zakin's minimum friction factor asymptote [7] before a certain Reynolds number, after which the friction factors increase up to Dean's friction factor line [21]. The maximum DR is about 61% and occurs at a Reynolds number of 1.6×10^4 . The Reynolds number above which the DR begins to disappear rapidly is called the critical Reynolds number Re_c . At the temperature of 44°C, friction factors are very close to that of water and Dean's line, showing no evidence of DR. This change may correspond to the breakdown of the micelle network structure and micellar shape transition from rodlike to globular.

Figure 4 shows the relationship between the Colburn factor j_H and Reynolds number for CTAC/NaSal surfactant solution in channel flow at temperatures of 30°C and 44°C. Shown in the same figure are the Dittus-Boelter [22] line which describes the Newtonian fluid heat transfer of a developed turbulent pipe flow and the minimum heat transfer asymptote of Colburn factor j_H given by Matthy's [23] for polymer solutions. These two lines are given by the following equations, respectively:

$$\text{Nu}_D = 0.023 \text{Re}_D^{0.8} \text{Pr}^{0.4} \quad (3)$$

$$j_H = 0.03 \text{Re}^{-0.45} \quad (4)$$

where D is the hydraulic diameter, $D = 4HW/(H+W)$ for the channel. Re_D is the Reynolds number based on D , and Nu_D is the Nusselt number based on D .

The term “heat transfer reduction” (HTR) is defined as the deficit of Colburn factor from that of solvent (Newtonian) flow at the same Reynolds number. For $T_{in} = 30^\circ\text{C}$, Colburn factors are close to Matthy's minimum Colburn factor asymptote [23] before a critical Reynolds number after which they increase up to the Dittus-Boelter line [22]. This relationship is very similar to that of friction factor with Reynolds number. However, by carefully comparing Fig. 3 with Fig. 4, we can see that the value of HTR is larger than that of DR. The maximum HTR is about 71% and occurs at a Reynolds number of 1.6×10^4 . For $T_{in} = 44^\circ\text{C}$, no evidence of HTR is observed.

Temperature Dependence of DR and HTR. From the above experimental results, we can see that temperature has a large effect on DR and HTR. In order to find the temperature dependence of DR and HTR, the friction drag and heat transfer coefficient were measured at a fixed Reynolds number of 1.2×10^4 at various inlet temperatures T_{in} . Figure 5 shows measured values of Fanning friction factor f and Colburn factor j_H . It can be seen that f and j_H at $T_{in} = 43^\circ\text{C}$ jump up to the values about three times as high as those at a critical temperature, $T_{in} = 40^\circ\text{C}$, showing that the flow and thermal field become fully turbulent. The existence of a critical temperature is a very interesting phenomenon since we can control the fluid temperature actively near the critical temperature region by thermal heating to get different values of DR and HTR for different purposes. In transport pipes, great drag

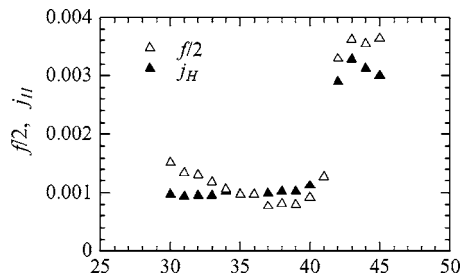


Fig. 5 Inlet fluid temperature dependence of friction factors and Colburn j factors

reduction can be obtained within low temperature ranges, whereas, in heat exchangers, the heat transfer performance can be improved greatly by a temperature only several degrees higher than the critical one.

Shear Viscosity and Giesekus Model. Figures 6(a)–6(d) show the measured shear viscosity η versus surfactant solution temperature T with shear rate $\dot{\gamma}$ as a parameter at surfactant mass concentration $C_m=50, 75, 100,$ and 200 ppm, respectively. For comparison, the shear viscosity of water indicated by a dash line is also shown in Figs. 6(a)–6(d). The solid lines shown in Figs. 6(a)–6(d) represent the correlation lines of the experimental data for different shear rates. From Fig. 6(a), we can see that the shear viscosity η decreases gradually with increasing temperature T . The effect of shear rate $\dot{\gamma}$ on η is very small and the measured shear viscosity is close to that of water. Thus the surfactant solution with a mass concentration of 50 ppm shows Newtonian characteristics of shear viscosity. However, for the higher concentrations shown in Figs. 6(b)–6(d), all the measured shear viscosities are much higher than that of water. It can also be seen from Figs. 6(b)–6(d) that for a certain shear rate there exists a critical temperature above which shear viscosities decrease rapidly to that of water. The effect of temperature on shear viscosities before the critical temperature is not obvious except for the 200 ppm case at lower shear rates where shear viscosities decrease gradually with increasing temperature. Generally speaking, if temperature does not exceed the critical temperature the shear viscosities decrease with increasing shear rate, showing shear thinning characteristics. The much higher viscosities of surfactant solution are probably due to the formation of the micelle network structure and the critical temperature corresponds to the start of destruction of the network. The critical temperature decreases with increasing mass concentration of surfactant solution. Specifically, it is about 38°C at $C_m=75$ irrespective of shear rate, but it is in the range of $31\text{--}36^\circ\text{C}$ and $26\text{--}29^\circ\text{C}$ at $C_m=100$ ppm and 200 ppm, respectively, depending on shear rate. This result is unexpected since it is generally considered that the network strength increases with increasing surfactant concentration, resulting in an increased critical temperature to breakdown the network. But for this very dilute solution with surfactant concentration one or two orders of magnitude smaller than the surfactant concentrations determined by other researchers, this phenomenon is actually found in our measurements. For $C_m=100$ ppm and 200 ppm, we can see that the critical temperature increases with increasing shear rate. Beyond the critical temperature, the solution temperature increases with increasing shear rate at the same shear viscosity. This is different from the Newtonian fluid the temperature of which does not change with shear rate.

In the very dilute surfactant solution, the network structure is weak or incomplete. The role of the shear stress in the formation of micelle structure is more important than that in the dense solution case [18]. We may consider that the shear induced structure probably occurs in the solution and this structure makes the internal energy of the surfactant solution change greatly with the addition of shear energy. Figure 7 shows the change of solution

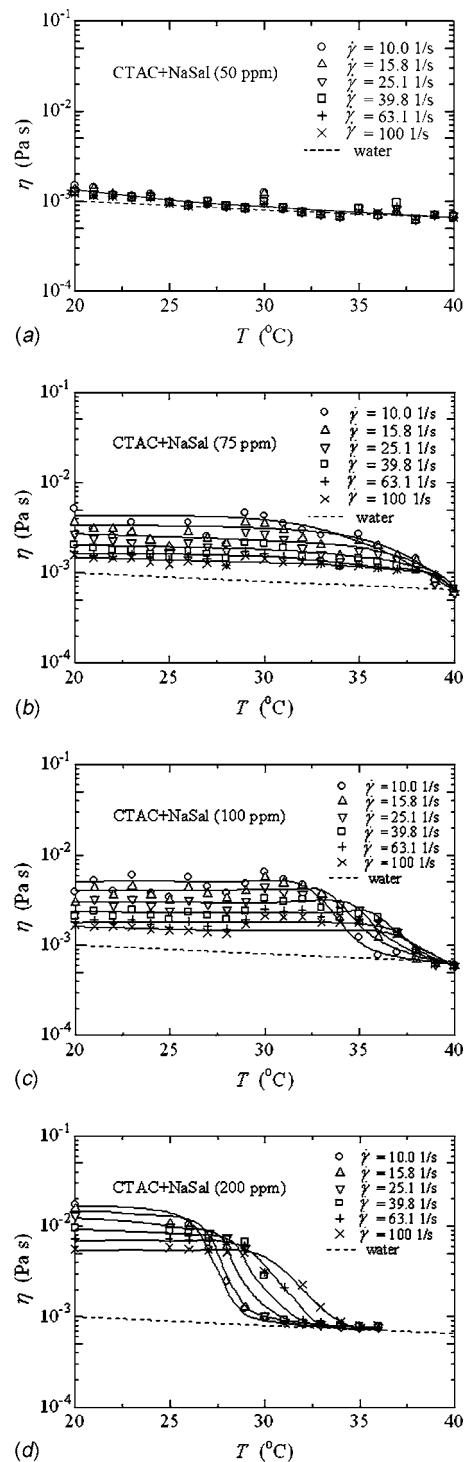


Fig. 6 Shear viscosities versus solution temperature (a) $C_m=50$ ppm, (b) $C_m=75$ ppm, (c) $C_m=100$ ppm, and (d) $C_m=200$ ppm

temperature with the variation of input shear rate at the same shear viscosity for $C_m=75, 100,$ and 200 ppm. Generally speaking, T increases with increasing shear rate up to a critical one and then levels off. The shear stress helps to form the micelle network structure in the solution and the strength of the micelle structure increases with increasing shear stress to some extent. This may be the reason why the drag and heat transfer reductions of surfactant solution increase with increasing Reynolds number up to the critical Reynolds number Re_c as shown in Figs. 3 and 4. The change

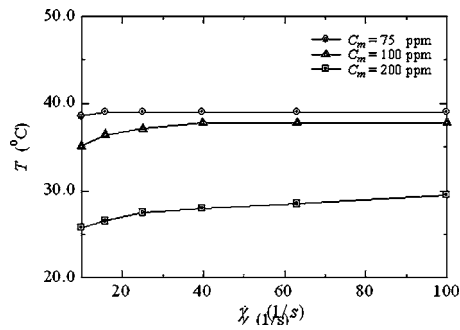


Fig. 7 Solution temperature versus shear rate at the same shear viscosity

of solution temperature with shear rate is larger for lower solution concentration than that for higher solution concentration before the critical shear rate, indicating that the shear rate is more effective for aiding the microstructure formation in the surfactant solutions with lower concentration as compared with the larger concentration solutions, thus at the same shear rate below a critical one, the strength of the micelle network is greater for the lower concentration case than that for the higher concentration case. In the previous experimental study [10], DR was found to increase with decreasing surfactant concentration for Reynolds number less than Re_c . Considering that the DR is related to the strength of the micelle network, these experimental results are broadly in accordance with our above analysis. As is well known, Brownian motion of micelles increases with increasing temperature. The stronger the network structure becomes, the stronger the Brownian motion required to break down the microstructure. Therefore, the critical temperature corresponding to the breakdown of the micelle network structure increases with increasing shear rate and decreasing concentration. This is in accordance with the present experimental findings that the critical temperature in the shear viscosity measurements decreases with solution concentration and increases with shear rate, further indicating that there is some inherent relationship between the DR and rheological properties. Of course, when the shear rate becomes too large, the network structure can play the opposite role of destroying the network structure. That is the reason for the existence of critical Reynolds numbers in DR and HTR measurements as shown in Figs. 3 and 4, and the critical Reynolds number also corresponds to the destruction of the micelle network structure. It can also be seen from Fig. 7 that the critical shear rate above which the solution temperature does not change with the variation of shear rate increases with increasing solution concentration (the critical shear rate is not detected in the present investigated range of shear rate for $C_m = 200$ ppm). This also agrees with the previous experimental finding that the critical Reynolds number increases with increasing solution concentration [10]. Therefore, rheological characteristics of surfactant solutions are very complex, and Newtonian or non-Newtonian characteristics of shear viscosity are dependent on shear rate as well as on solution temperature and concentration.

From the present experiment, a mass concentration less than 50 ppm shows waterlike shear viscosity, indicating that no micelle network structure is formed in the solution. However, in our DR and HTR measurements, we did find large turbulent drag and heat transfer reduction as shown in Figs. 3–5. This was probably due to the nonuniform distribution of surfactant in large channel flow. For the very dilute surfactant solution of 30 ppm, it was impossible to form a uniform large micelle network structure in the whole channel. It is generally believed that the existence of surfactant in the buffer layer of drag-reducing flow is the main reason for drag and heat transfer reduction. Therefore, we may conjecture that some small discrete micelle network structures are formed and concentrated in the buffer layer where the local surfactant concentration is much larger than 30 ppm. The main reason for

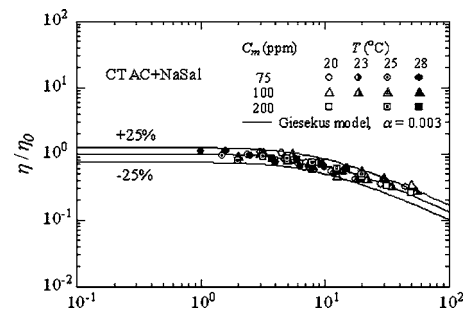


Fig. 8 Least squares fitting result of the measured shear viscosities with the Giesekus model

the surfactant accumulation near the wall is that the shear stress aids the formation of micellar networks. For shear stress less than the critical shear stress, the larger the shear stress, the stronger the networks. The shear stress near the wall is larger than that in the core region for the channel flow, and so surfactants tend to accumulate toward the wall region to form a stronger network. On the other hand, due to the laminar flow in a very narrow gap (about 1 mm) of the double wall Couette cell in the ARES rheometer, the surfactant solution should be more uniform than that in turbulent channel flow. Due to the different flow situation and surfactant distribution in water channel and rheometer, it may be unreasonable to relate the measured DR and HTR performance of an overall 30 ppm surfactant solution flow to the measured rheological properties of the surfactant solution with the same surfactant concentration. Therefore, it is supposed that the critical temperature in the measurements of shear viscosities qualitatively corresponds to that in the measurements of turbulent friction drag and heat transfer coefficient, despite the fact that the surfactant concentration in the rheological measurements is larger than that in the DR and HTR measurements.

Drag-reducing surfactant solutions are very complex systems in terms of rheological properties. As recommended by Lu [19], we should choose a complicated model, the Giesekus model with nonlinear stress terms, to describe the rheological characteristics of these surfactant solutions.

Giesekus [24] derived a constitutive equation as follows:

$$\tau = \tau_s + \tau_p = \tau_p + \eta_s \dot{\gamma} \quad (5)$$

$$\alpha \frac{\lambda}{\eta_p} \tau_p^2 + \tau_p + \lambda \dot{\tau}_p = \eta_p \dot{\gamma} \quad (6)$$

where subscripts s and p represent solvent and surfactant, respectively. To simplify the solution, the contribution from the solvent is set to be zero and we can get the steady shear viscosity solution as

$$\frac{\eta}{\eta_0} = \frac{4(1-\alpha)}{\sqrt{f+1}[\sqrt{f+1} + \sqrt{2(1-2\alpha)}]} \quad (7)$$

where

$$f = \sqrt{1 + 16\alpha(1-\alpha)\lambda^2 \dot{\gamma}^2} \quad (8)$$

There are three parameters in Eqs. (7) and (8), relaxation time λ , zero shear viscosity η_0 , and mobility factor α ($0 \leq \alpha \leq 1$). When the value of α is set to zero, the Giesekus model reduces to the Maxwell model.

Figure 8 shows the least squares fitting results of the measured shear viscosity with the Giesekus model by appropriately adjusting model parameter values for different solution temperatures and concentrations. It can be seen that the prediction of the Giesekus model as plotted by the thick solid line can fit the experimental data well by selecting suitable model parameter values after trial and error. In the temperature range of 20–28 °C and

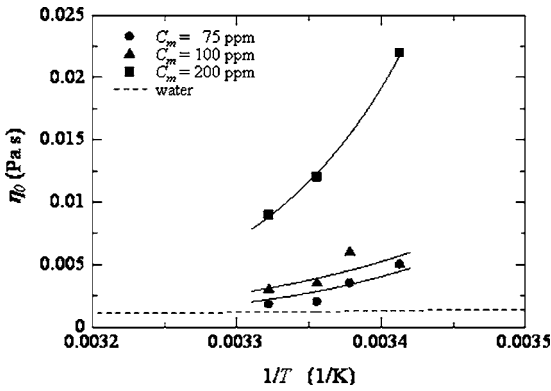


Fig. 9 Zero-shear viscosity η_0 versus temperature T

concentration range of 75–200 ppm, the mobility factor α obtained by fitting is a very small constant of 0.003 and does not change with C_m and T , whereas both the zero shear viscosity η_0 and relaxation time λ are functions of C_m and T . Figure 9 shows η_0 versus inverse T with C_m as a parameter. The data of water indicated by the dashed line are also shown for comparison. We can see that η_0 increases greatly with decreasing T as compared to the gradual change of water. η_0 increases monotonically with C_m . For the highest concentration of 200 ppm, η_0 decreases much more rapidly with increasing T than that for the 75 ppm and 100 ppm cases, resulting in a smaller critical temperature as indicated in Figs. 6(b)–6(d). Figure 10 shows λ versus inverse T with C_m as a parameter. λ increases greatly with decreasing T as η_0 does, but it increases with increasing C_m from 75 ppm to 100 ppm and then decreases with further increasing C_m up to 200 ppm as compared with the monotonic change of η_0 with C_m . The relaxation time $\lambda(=\eta_0/G)$ can be used to describe the viscoelasticity of the surfactant solution, which is infinite for a Hookean elastic solid and zero for a Newtonian viscous liquid. In the present study, the value of λ is in the range of 0.1–1.0 s and the elasticity increases with increasing λ . We can see from Fig. 10 that λ increases with decreasing T . Therefore, the viscoelasticity will increase with decreasing temperature, resulting in the increase of turbulent drag reduction and the corresponding heat transfer reduction. DNS studies of drag-reducing Giesekus fluid flow [11,12] also indicated that the turbulent drag reduction increases with relaxation time λ , which is consistent with the above analysis. The exponential correlations of η_0 and λ with T at $C_m=75, 100,$ and 200 ppm are listed in Table 2.

Figure 11 compares experimental data of shear viscosity with the prediction of the Giesekus model. The values of η_0 and λ for the surfactant solutions with different concentrations and tempera-

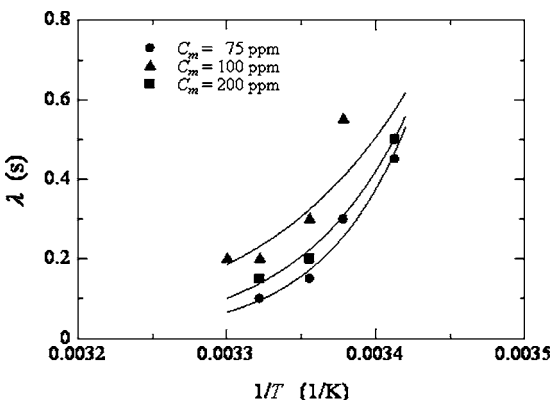


Fig. 10 Relaxation time λ versus temperature T

Table 2 Correlations of η_0 and λ with T for different C_m

C_m (ppm)	η_0 (Pa s)	λ (s)
75	$1.44 \times 10^{-14} \exp(7750/T)$	$7.54 \times 10^{-27} \exp(17400/T)$
100	$7.27 \times 10^{-13} \exp(6680/T)$	$8.95 \times 10^{-16} \exp(10000/T)$
200	$4.11 \times 10^{-17} \exp(9930/T)$	$4.65 \times 10^{-22} \exp(14200/T)$

tures are obtained from the correlations listed in Table 2. For the concentration of 150 ppm, the correlations of η_0 and λ with T are not given, thus linear interpolation is used to get the values of η_0 and λ . Although the correlations are made in the temperature range from 20°C to 28°C, the experimental data of surfactant solutions at $C_m=75, 100,$ and 150 ppm for $T=30^\circ\text{C}$ are also plotted in Fig. 11 for comparison. The values of η_0 and λ are obtained by extrapolation, which results in slightly larger deviation of the experimental data from the prediction of the Giesekus model to within $\pm 27.3\%$.

Thus it seems that the Giesekus model can describe the shear viscosity characteristics of the CTAC/NaSal surfactant solutions at temperatures within 20–30°C and concentrations within 75–200 ppm. The correlations of η_0 and λ can be used for the direct numerical simulation of turbulent drag-reducing CTAC/NaSal surfactant solution flow.

Conclusions

Turbulent friction drag and heat transfer characteristics of very dilute CTAC/NaSal surfactant drag-reducing flow in a two-dimensional channel at various Reynolds numbers and temperatures were experimentally investigated. Shear viscosities of very dilute CTAC/NaSal aqueous solution were measured by an ARES rheometer. The Giesekus model was used for theoretical analyses. The main conclusions were as follows:

- (1) There existed a critical temperature in shear viscosity and turbulent drag and heat transfer measurements, which corresponded to the breakdown of the micelle network structure in surfactant solutions. This phenomenon may be used for active control of DR and HTR by using thermal heating to adjust the temperature of surfactant flow locally.
- (2) From the shear viscosity characteristics and DR and HTR characteristics of the very dilute CTAC/NaSal surfactant solution, the micelle network structure was considered to be affected not only by the solution concentration and temperature but also by the shear stress, which may qualitatively explain the effects of Reynolds number and fluid

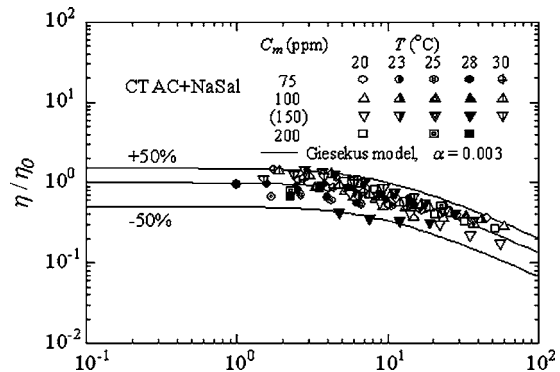


Fig. 11 Comparison of the measured shear viscosities with the prediction of the Giesekus model

temperature and concentration on drag and heat transfer reduction and the peculiar phenomenon for this very dilute surfactant solution that the critical temperature decreases with increasing solution concentration.

- (3) The Giesekus model was found to fit the measured shear viscosity well, and 70% of the measured shear viscosities agreed with the prediction of the Giesekus model to within $\pm 27.3\%$. Model parameters were obtained from the least squares fitting of the measured shear viscosity data with the Giesekus model at different temperatures and concentrations of the surfactant solution. They can qualitatively explain the DR and HTR mechanism and also can be used for direct numerical simulation to clarify the turbulent drag-reducing mechanisms theoretically.

Acknowledgment

This research was partly carried out as a research project of the Center for Smart Control of Turbulence with financial support from the Ministry of Education, Culture, Sports, Science and Technology (MECSST). We are also grateful to NEDO for providing an international research grant for "Development of Practical Drag Reduction Systems for District Cooling Systems" and financial support by the NSFC Fund for Creative Research Groups (No. 50521604).

Nomenclature

- C_m = mass concentration of surfactant solution (ppm)
 c_p = specific heat (J/kg K)
 f = Fanning friction factor, $\tau_w/(0.5\rho U_b^2)$
 G = rigidity modulus (Pa)
 H = channel height (m)
 h = heat transfer coefficient (W/m² K), $h=q_w/(T_w - T_b)$
 j_H = Colburn factor for heat, $St Pr^{2/3}$
 Nu = Nusselt number, hH/κ
 Pr = Prandtl number, $c_p\eta_s/\kappa$
 q = heat flux (W/m²)
 Re = Reynolds number, U_bH/ν
 St = Stanton number, $h/(\rho c_p U_b)$
 T = temperature (°C or K)
 U_b = bulk velocity (m/s)
 W = channel width (m)

Greek Symbols

- α = mobility factor in the Giesekus model
 $\dot{\gamma}$ = shear rate (1/s)
 η = shear viscosity (Pa s)
 η_0 = shear viscosity at zero shear strain rate (Pa s)
 κ = heat conductivity (W/m K)
 λ = relaxation time (s)
 ν = kinematic viscosity (m²/s)
 ρ = density (kg/m³)
 τ = shear stress (Pa)
 $\dot{\tau}$ = time derivative of shear stress (Pa/s)

Subscripts

- b = bulk
 c = critical
 D = hydraulic diameter
 in = inlet
 p = surfactant

s = solvent

w = wall

References

- [1] Toms, B. A., 1948, "Some Observations on the Flow of Linear Polymer Solutions through Straight Tubes at Large Reynolds Numbers," Proc. 1st international. Congress on Rheology, North Holland, Amsterdam, Vol. 2, pp. 135–141.
- [2] Mysels, K. J., 1949, Flow of Thickened Fluids, U.S. Patent 2,492,173.
- [3] White, A., 1967, "Flow Characteristics of Complex Soap Systems," Nature (London), **214**, pp. 585–586.
- [4] Zakin, J. L., Porech, M., Brosh, A., and Warshavsky, M., 1971, "Exploratory Study of Friction Reduction in Slurry Flows," Chemical Engineering Professional Symposium Series, **67**, pp. 85–89.
- [5] Gyr, A., and Bewersdorff, H. W., 1995, *Drag Reduction of Turbulent Flows by Additives*, Kluwer Academic Publishers, The Netherlands.
- [6] Lu, B., Li, X., Zakin, J. L., and Talmon, Y., 1997, "A Non-Viscoelastic Drag-Reducing Cationic Surfactant System," J. Non-Newtonian Fluid Mech., **71**, pp. 59–72.
- [7] Zakin, J. L., Myska, J., and Chara, Z., 1996, "New Limiting Drag Reduction and Velocity Profile Asymptotes for Nonpolymeric Additives Systems," AIChE J., **42**, pp. 3544–3546.
- [8] Kawaguchi, Y., Daisaka, H., Yabe, A., Hishida, K., and Maeda, M., 1997, "Turbulent Characteristics in Transition Region of Dilute Surfactant Drag Reducing Flows," The 11th Symposium on Turbulent Shear Flow, September 8–11, Organizing Committee, Grenoble.
- [9] Li, P. W., Kawaguchi, Y., and Yabe, A., 2001, "Transitional Heat Transfer and Turbulent Characteristics of Drag-Reducing Flow Through a Contracted Channel," Enhanced Heat Transfer, **8**, pp. 23–40.
- [10] Li, P. W., Kawaguchi, Y., Daisaka, Y., Yabe, A., Hishida, A., and Maeda, M., 2001, "Heat Transfer Enhancement to the Drag-Reducing Flow of Surfactant Solution in Two-Dimensional Channel With Mesh-Screen Inserts at the Inlet," ASME J. Heat Transfer, **123**, pp. 779–789.
- [11] Kawaguchi, Y., Tawaraya, Y., Yabe, Y., Hishida, A., and Maeda, M., 1996, "Active Control of Turbulent Drag Reduction in Surfactant Solutions by Wall Heating," ASME 1996 Fluid Eng. Div. Conf., San Diego, CA, July 7–11, ASME, New York, Vol. 2, pp. 47–52.
- [12] Kawaguchi, Y., Segawa, T., Feng, Z., and Li, P., 2002, "Experimental Study on Drag-Reducing Channel Flow with Surfactant Additives-Spatial Structure of Turbulence Investigated by PIV System," Int. J. Heat Fluid Flow, **23**, pp. 700–709.
- [13] Yu, B., Kawaguchi, Y., Takagi, S., and Matsumoto, Y., 2002, "Numerical Investigation on Turbulent Structures in a Drag-Reducing Flow with Surfactant Additives in a 2D Channel-Comparison of Artificial Diffusion Scheme and MINMOD Scheme," The 5th JSME-KSME Fluids Engineering Conference, Nagoya, Japan, November 17–21, JSME, Tokyo.
- [14] Yu, B., and Kawaguchi, Y., 2003, "Effect of Weissenberg Number on the Flow Structure: DNS Study of Drag-Reducing Flow With Surfactant Additives," Int. J. Heat Fluid Flow, **24**, pp. 491–499.
- [15] Clausen, T. M., Vinson, P. K., Minter, J. R., Davis, H. T., Talmon, Y., and Miller, W. G., 1992, "Viscoelastic Micellar Solutions: Microscopy and Rheology," J. Phys. Chem., **96**, pp. 474–484.
- [16] Lin, Z., Zheng, Y., Davis, H. T., Scriven, L. E., Talmon, Y., and Zakin, J. L., 2000, "Unusual Effects of Counterion to Surfactant Concentration Ratio on Viscoelasticity of a Cationic Surfactant Drag Reducer," J. Non-Newtonian Fluid Mech., **93**, pp. 363–373.
- [17] Lin, Z., Lu, B., Zakin, J. L., Talmon, Y., Zheng, Y., Davis, H. T., and Scriven, L. E., 2001, "Influence of Surfactant Concentration and Counterion to Surfactant Ratio on Rheology of Wormlike Micelles," J. Colloid Interface Sci., **239**, pp. 543–554.
- [18] Macias, E. R., Bautista, F., Soltero, J. F. A., Puig, J. E., Attane, P., and Manero, O., 2003, "On the Shear Thickening Flow of Dilute CTAT Worm-Like Micellar Solutions," J. Rheol., **47**, pp. 643–658.
- [19] Lu, B., 1997, "Characterization of Drag-Reducing Surfactant Systems by Rheology and Flow Birefringence Measurements," Ph.D. dissertation, The Ohio State University.
- [20] Kline, S. J., and McClintok, F. A., 1953, "Describing Uncertainties in Single-Sample Experiments," Mech. Eng. (Am. Soc. Mech. Eng.), **75**, pp. 3–8.
- [21] Dean, R. B., 1978, "Reynolds Number Dependence of Skin Friction and Other Bulk Flow Variables in Two-Dimensional Rectangular Duct Flow," ASME J. Fluids Eng., **100**, pp. 215–223.
- [22] Dittus, F. W., and Boelter, L. M. K., 1930, University of California, Berkeley, Publications on Eng., Vol. 2, p. 443.
- [23] Matthys, E. F., 1991, "Heat transfer, Drag reduction, and Fluid Characterization of Turbulent Flow of Polymer Solutions: Recent Results and Research Needs," J. Non-Newtonian Fluid Mech., **38**, pp. 313–342.
- [24] Giesekus, H., 1982, "A Simple Constitutive Equation for Polymer Fluids Based on the Concept of Deformation-Dependent Tensorial Mobility," J. Non-Newtonian Fluid Mech., **11**, pp. 69–109.

Heat Transfer to Small Horizontal Cylinders Immersed in a Fluidized Bed

J. Friedman¹

Department of Mechanical and Industrial Engineering,
Ryerson University, 350 Victoria Street,
Toronto, Ontario, M5B 2K3, Canada
e-mail: jfriedma@ryerson.ca

P. Koundakjian

Department of Mechanical Engineering,
University of Waterloo, 200 University Ave. W.,
Waterloo, Ontario, N2L 3G1, Canada

D. Naylor

D. Rosero

Department of Mechanical and Industrial Engineering,
Ryerson University, 350 Victoria Street,
Toronto, Ontario, M5B 2K3, Canada

Heat transfer to horizontal cylinders immersed in fluidized beds has been extensively studied, but mainly in the context of heat transfer to boiler tubes in coal-fired beds. As a result, most correlations in the literature have been derived for cylinders of 25–50 mm diameter in vigorously fluidizing beds. In recent years, fluidized bed heat treating furnaces fired by natural gas have become increasingly popular, particularly in the steel wire manufacturing industry. These fluidized beds typically operate at relatively low fluidizing rates ($G/G_{mf} < 5$) and with small diameter wires (1–6 mm). Nusselt number correlations developed based on boiler tube studies do not extrapolate down to these small size ranges and low fluidizing rates. In order to obtain reliable Nusselt number data for these size ranges, an experimental investigation has been undertaken using two heat treating fluidized beds; one a pilot-scale industrial unit and the other a lab-scale (300 mm diameter) unit. Heat transfer measurements were obtained using resistively heated cylindrical samples ranging from 1.3 to 9.5 mm in diameter at fluidizing rates ranging from approximately $0.5 \times G_{mf}$ (packed bed condition) to over $10 \times G_{mf}$ using aluminum oxide sand particles ranging from $d_p = 145\text{--}330 \mu\text{m}$ (50–90 grit). It has been found that for all cylinder sizes tested, the Nusselt number reaches a maximum near $2 \times G_{mf}$, then remains relatively steady ($\pm 5\text{--}10\%$) to the maximum fluidizing rate tested, typically $8\text{--}12 \times G_{mf}$. A correlation for maximum Nusselt number is developed.
[DOI: 10.1115/1.2345425]

Keywords: fluidized bed, heat transfer, cylinders

Introduction

Heat transfer to horizontal cylinders immersed in a fluidized bed has been extensively investigated over the last several decades, and has been well summarized by Saxena in Ref. [1]. More recent work has examined local Nusselt number distribution around the circumference of a tube, but has focused on larger diameters [2–4]. Nearly all these investigations have dealt with relatively large cylinders ($d_t > 25$ mm) in the context of boiler tubes immersed in coal-firing fluidized bed combustors, one of the major applications developed in recent decades. Another, less studied application of fluidized beds is as a heat treating medium, which is seeing increasing use in the ferrous metals industry as an alternative to more environmentally hazardous processes using molten salts, oils, or even molten lead [5]. The steel wire industry, in particular, has adopted the fluidized bed heat treating system as a viable alternative to lead-based systems, which are now banned in many jurisdictions, and require extensive and expensive environmental controls in others. These fluidized beds are typically fired by natural gas, which is burned within the bed to provide heat to the system. Most of these systems are used for heat treating low carbon steel wire, as the heat treatment cycle for this material is relatively undemanding, requiring heating the product to just over 700°C , with no specific heating rate or hold time required, and little sensitivity to temperature over- or under-runs. Heat treatment of high carbon steels, on the other hand, requires more stringent control over product temperature and heating rates, as well as controlled quench rates. To date, there have been very

few successful fluidized bed-based systems installed for high carbon steel heat treatment. One of the main challenges in designing these systems has been lack of adequate information on heat transfer rates to cylinders in the size range of 1–8 mm. While there is considerable data available for boiler-tube sized cylinders, correlations developed from this data produce wildly differing results when extrapolated down to small cylinder sizes. The work reported herein is intended to fill this gap and provide reliable data and a model for heat transfer to small cylinders under conditions typically encountered in heat treating fluidized bed systems.

Experimental Method

Two atmospheric pressure fluidized beds have been used in this work. The first, a pilot-scale natural gas-fired unit with an active bed area of 500×1000 mm and capable of operation to 900°C , was used to obtain data under hot conditions. The second, lab-scale unit with a bed area 300 mm in diameter, was operated at ambient temperatures only. However, its smaller size allowed operation using a variety of alumina sand sizes, and at much higher fluidizing rates than the large unit. The pilot-scale unit was capable of operating at up to $2.5 \times G_{mf}$ using $254 \mu\text{m}$ alumina sand (sphericity ≈ 0.7), while the smaller unit was capable of operation to beyond $10 \times G_{mf}$. Figure 1 shows a schematic diagram of the system geometry. Each bed used porous fused alumina hearth tiles as a distributor. The tiles had a porosity of 64%, and a thickness of 50 mm. This type of distributor provides a very even gas distribution, but at low pressure drop and hence low velocity, in contrast to perforated plate distributors which tend to provide high velocity jets at the distributor which encourage bubble formation. As fluidizing air flow increased, the first evidence of fluidization occurred at the smooth walls, where decreased flow resistance allowed some channeling to occur. This was observed at flow rates of approximately $0.9 \times G_{mf}$, where G_{mf} is calculated from the Ergun equation [6]

¹Corresponding author.

Contributed by the Heat Transfer Division of ASME for publication in the JOURNAL OF HEAT TRANSFER. Manuscript received May 31, 2005; final manuscript received March 22, 2006. Review conducted by Jose L. Lage. Paper presented at the 18th International Conference on Fluidized Bed Combustion (FBC2005), May 22–25, 2005, Toronto, Ontario, Canada.

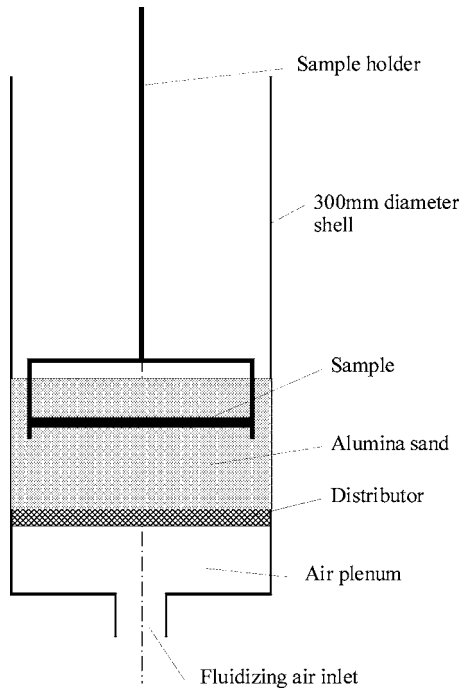


Fig. 1 Schematic cross-section of lab-scale test bed and sample

$$Ar = \left[\frac{150(1 - \epsilon_{mf})}{\phi_s^2 \epsilon_{mf}^3} \right] Re_{mf} + \left[\frac{1.75}{\phi_s \epsilon_{mf}^3} \right] Re_{mf}^2 \quad \text{where}$$

$$Ar = \frac{g \rho_g (\rho_p - \rho_g) d_p^3}{\mu_g^2} \quad (1)$$

and

$$Re_{mf} = \frac{\rho_g d_p U_{mf}}{\mu_g} \quad \text{and} \quad G_{mf} = \rho_g \cdot U_{mf}$$

As air flow increased further, bubbles began to appear randomly through the bed, with full, well-distributed fluidization occurring beyond $1.3 \times G_{mf}$, as illustrated in Fig. 2, which shows pressure at

the top of the distributor as a function of mass flow rate. It should be noted that the Ergun equation predicts a distinct fluidization point. However, in this type of bed where the wall perimeter is large in relation to the bed area, fluidization occurs over a range of air flow rates beginning at the wall, then moving in towards the bed center. While it has long been established that the distributor design has a large influence on heat transfer rates in fluidized beds [7,8] it has also been shown that at higher fluidizing rates, this influence decreases significantly, to the point where heat transfer measurements for a given type of distributor can be considered general. For example, the wall heat transfer data obtained by Sathiyamoorthy et al. [6] using four different distributor grids shows that, at low fluidizing rates (below $2 \times G_{mf}$), convection coefficients vary by over 25% for $70 \mu\text{m}$ alumina particles, but the peak convection coefficients, which occur at higher fluidizing rates, vary by only 5%. Similar results have been noted by Ref. [7] for heat transfer to cylinders.

Heat transfer rates were deduced by resistively heating the cylindrical sample and measuring the steady state temperature difference between the cylinder surface and the bed. The samples used were stainless steel tubes with outside diameters ranging from 1.27 to 9.52 mm, with heated lengths of approximately 250 mm. A similar setup was used in both fluidized beds, using the same sample holder and samples. An Instek regulated direct current (dc) power supply, capable of providing up to 100 A at up to 10 V dc was used to resistively heat the samples. Temperatures were measured using an eight channel IoTech Tempbook 66 data acquisition system and type K thermocouples. Thermocouples were located as follows: one on sample centerline, one at each end of the sample, and one in the bed approximately 30 mm away from the sample. Tests were made using the small fluidized bed at ambient temperature, and using the pilot-scale unit at ambient (to ensure similarity of results between the two beds at similar operating conditions) and at temperatures up to 750°C .

Initially, measurements were made with fine thermocouples (0.127 mm) spot welded to the surface of the sample on centerline, but concerns of errors due to the “fin” effect caused by heat conduction out the thermocouple, particularly for the smaller samples, led to changing the thermocouple location to inside the tube, still on centerline. A simple correction to account for temperature drop from the tube inside wall to the outside wall was used, based on a 1D heat conduction model as shown below. The steady state, 1D conduction equation with generation is given by

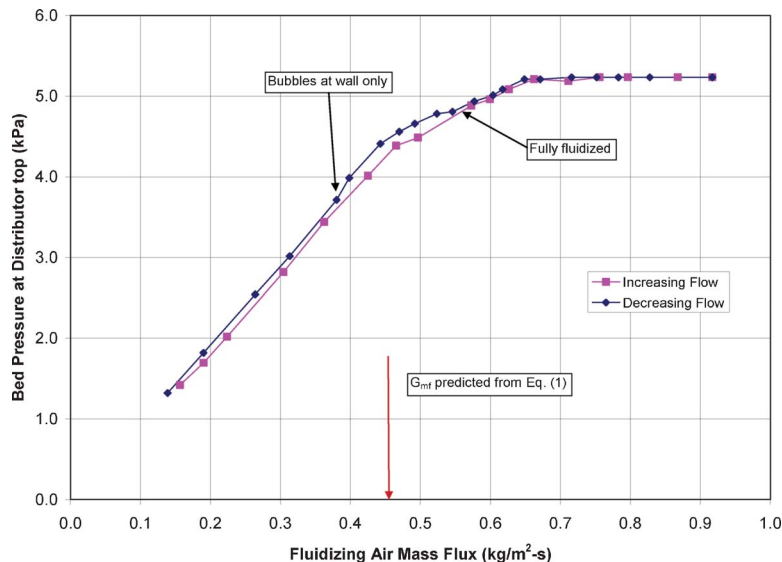


Fig. 2 Bed pressure at the distributor as a function of flow rate for a 70 grit ($200 \mu\text{m}$) bed, 240 mm deep

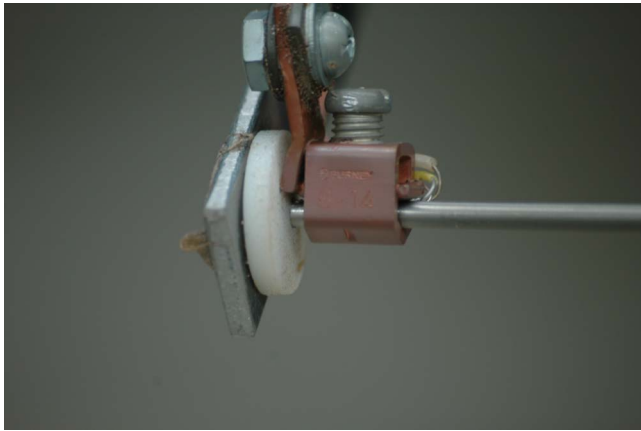


Fig. 3 Terminal assembly

$$\frac{1}{r} \frac{\partial}{\partial r} \left(r \frac{\partial T}{\partial r} \right) + \frac{q'''}{k} = 0 \quad (2)$$

The appropriate boundary conditions are

$$\text{at } r = r_i \quad \frac{\partial T}{\partial r} = 0 \quad \text{no heat transfer to inside of tube}$$

$$\text{at } r = r_i \quad T(r_i) = T_i \quad \text{inside tube surface temperature known}$$

The resulting expression for the outside tube temperature is given by

$$T(r_o) = \frac{-q'''}{4k} (r_o^2 - r_i^2) + \frac{q''' r_i^2}{2k} \ln \left(\frac{r_o}{r_i} \right) + T_i \quad (3)$$

Due to the large currents used to heat the samples, (up to 100 A) large terminal connectors were required, as shown in Fig. 3. These connectors acted as heat sinks, removing heat from the samples at each end. As a result, assuming uniform temperature along the length of the sample was not necessarily a good assumption, particularly for the larger samples where L/d_i was small. In order to account for this, a model was developed that used both the centerline temperature T_o and the measured terminal temperatures T_i . The derivation is similar to the classic fin equation derivation but modified to account for heat generation. The boundary conditions applied were

$$\text{at } x = 0 \quad \frac{\partial T}{\partial x} = 0 \quad \text{symmetry about centerline}$$

$$\text{at } x = \pm \frac{L}{2}$$

$$T\left(\pm \frac{L}{2}\right) = T_i \quad \text{tube temperature known at terminals}$$

The resulting expression for the temperature distribution is

$$T(x) = \left(\theta_i - \frac{q'''}{m^2 k} \right) \frac{\cosh(mx)}{\cosh\left(\frac{mL}{2}\right)} + \frac{q'''}{m^2 k} + T_\infty \quad (4)$$

$$m = \sqrt{\frac{4hd_i}{k(d_o^2 - d_i^2)}} \quad \theta_i = T_i - T_{\text{bed}} \quad (5)$$

Figure 4 shows a plot of sample temperature versus x/L for a 9.53 mm outer diameter \times 7.74 mm inner diameter tube in a 30°C bed, assuming the terminals were at bed temperature. It should be noted that the terminals are quite large due to the high currents involved and will act as effective heat sinks. The assumption of $T_i = T_{\text{bed}}$ should represent the worst case scenario, as end losses increase with decreasing terminal temperature, and bed temperature is the lowest terminal temperature achievable. The calculation was based on a generation rate of 5 MW/m³ and a convection coefficient of 350 W/m² K. As can be seen, the sample temperature is uniform over 90% of its length, with only the end 5% significantly affected by conduction losses. Temperature uniformity is better for smaller tubes.

The heat lost through conduction to the terminals is given by

$$q_t = -kA_c \frac{dT}{dx} \Big|_{x=\pm(L/2)} \quad (6)$$

The energy balance for the sample is therefore

$$VI = 2q_t + \int_{-(L/2)}^{(L/2)} h \pi d_o [T(x) - T_\infty] dx \quad (7)$$

The above equations were solved iteratively by varying h until $T(0)$ matched the measured T_o . It should be noted that the h computed using this expression was generally within 10% of that obtained using the simple expression

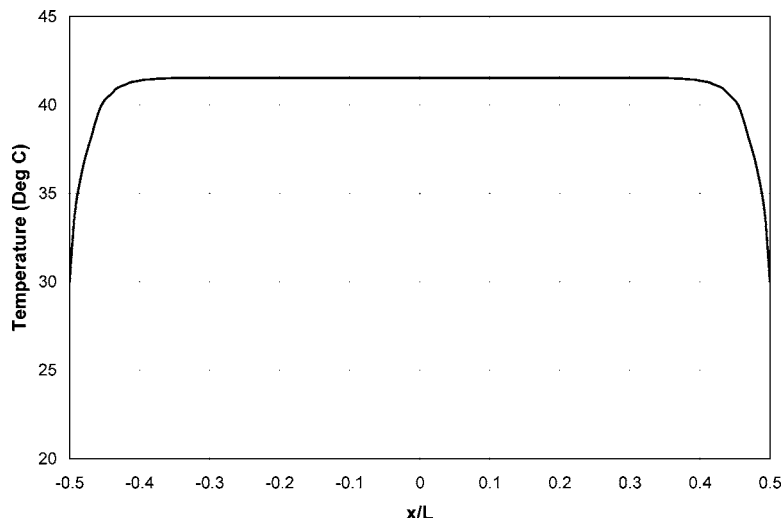


Fig. 4 Sample temperature distribution based on Eq. (4)

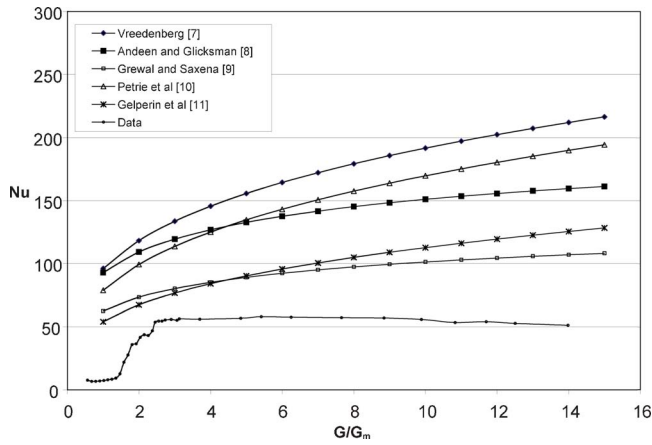


Fig. 5 Standard correlations and data comparison for a 3.18 mm sample in a bed of 200 μm particles

$$h = \frac{VI}{A_o(T_o - T_{\text{bed}})} \quad (8)$$

Heat transfer measurements were made using samples of 1.27, 2.11, 3.18, 4.76, 6.35, 7.94, and 9.52 mm diameter using $d_p = 330, 254, 203, 165,$ and $145 \mu\text{m}$ (50, 60, 70, 80, and 90 grit, respectively) aluminum oxide sand. Fluidizing flow rates were varied from $G/G_{\text{mf}} < 1$ to $G/G_{\text{mf}} > 8-12$, depending on grit size. High temperature heat transfer measurements were done using 60 grit ($254 \mu\text{m}$) sand only, and could only be taken to a maximum fluidizing rate of $G/G_{\text{mf}} \approx 2.5$.

Results and Discussion

Due to the convenience of using the lab-scale fluidized bed for obtaining data, most of the cold data presented herein was obtained using the lab-scale unit, after establishing that heat transfer results were within 5% of each other under similar operating conditions. Only hot test data was obtained using the pilot-scale unit.

Figure 5 shows results for heat transfer measurements from a 3.18 mm diameter sample in $d_p = 203 \mu\text{m}$ (70 grit) sand, as well

as the predicted Nusselt number based on a number of established correlations [9–13] including the Grewal and Saxena correlation [9] listed in Ref. [1] as being the “only one that can be successfully represent all the available data in the literature...” As can be seen in the figure, all the correlations grossly overpredict the heat transfer rate from the sample, and none show the steady plateau apparent in the data. Figure 6 shows typical results for a variety of sample sizes in a $d_p = 203 \mu\text{m}$ (70 grit) bed. As can be seen, beyond approximately $2 \times U_{\text{mf}}$, the Nusselt number remains nearly constant to the maximum fluidizing rates tested. This is not consistent with what is seen for much larger tubes (25 mm and larger), where Nu increases monotonically with fluidizing rate and exhibits no clear maximum [1]. However, the data of Saxena et al. [9], which includes data for 12.7 mm tubes, clearly shows a similar trend to the data presented herein for many of their tests, which used a variety of particle materials and sizes.

Figure 7 shows a plot of mean Nusselt number versus d_t/d_p for $d_p = 145, 203,$ and $330 \mu\text{m}$ (90, 70, and 50 grit sizes). The mean Nusselt number was evaluated as the mean Nusselt number from $G = 2 \times G_{\text{mf}}$ to the maximum flow rate tested for that sample, representing the steady value measured. As can be seen, the relationship is linear for each particle size tested. An effort was made to collapse all the data to a single curve. Dimensional analysis suggests that the Nusselt number will be a function of the following [14]:

$$\text{Nu} = f\left(\text{Ar}, \frac{\rho_p}{\rho_g}, \text{Pr}, \frac{C_{p_s}}{C_{p_g}}, \frac{k_p}{k_g}, \frac{d_t}{d_p}, \frac{G}{G_{\text{mf}}}, \epsilon\right)$$

$$\text{Nu} = \frac{hd_t}{k_g} \quad \text{Ar} = \frac{g\rho_g(\rho_p - \rho_g)d_p^3}{\mu_g^2} \quad (9)$$

Based on our results, the mean Nusselt number does not vary significantly beyond $G/G_{\text{mf}} > 2$, so G can be eliminated from the functional relationship. Also, since ϵ depends on G , it can also be eliminated. Finally, it was found that the data were well correlated by a function of the form

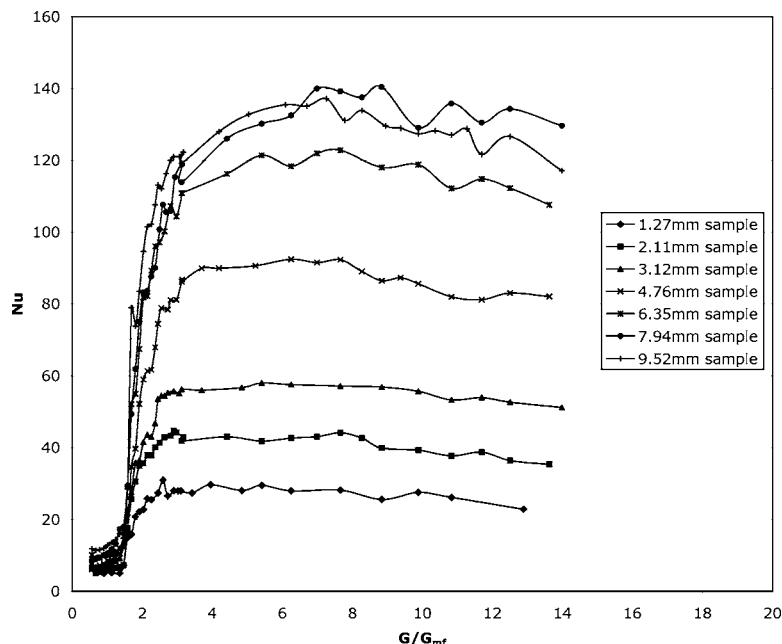


Fig. 6 Nu versus G/G_{mf} for samples in a 70 grit ($200 \mu\text{m}$) bed

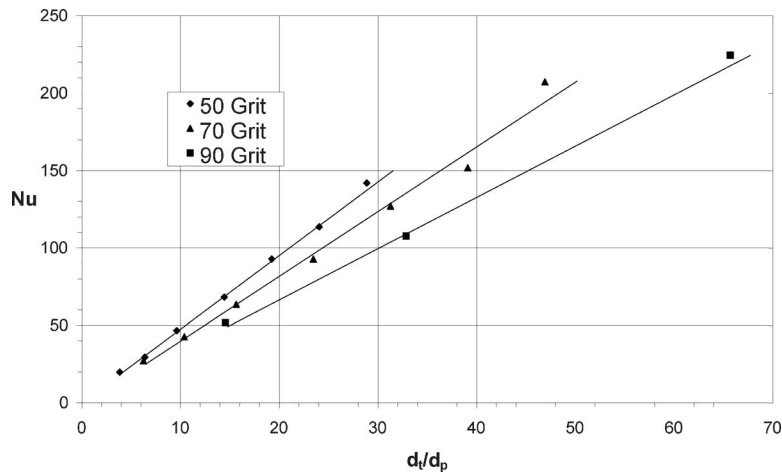


Fig. 7 Mean Nusselt number versus d_t/d_p for different particle sizes

$$Nu_{\text{mean}} = CAr^n \frac{d_t}{d_p} \quad (10)$$

with $C=1.35$ and $n=0.15$. Figure 8 shows a plot of Nu_{mean} for all data versus $Ar^{0.15}d_t/d_p$. Also included on the plot is data from Saxena et al. [9] obtained using a 12.7 mm diameter tube in a variety of particle sizes and materials. As can be seen, the fit is excellent, only beginning to stray where $Ar^n d_t/d_p$ becomes very large (>100). This result is to be expected as it has already been observed that Nusselt number trends for large tubes (and, hence, large d_t/d_p) behave differently than small ones.

Experimental Uncertainties. There are several uncertainty sources in the data presented herein. The fluidized bed heat transfer mechanism, involving bubble formation and particle/gas interactions, is in itself a highly stochastic process such that successive measurements under identical operating conditions will yield somewhat different results. Tests of repeatability show variations on the order of 2–5%, depending on the operating conditions. Another source of uncertainty is caused by the requirement to determine the temperature difference between the sample and bed. While each individual temperature reading may be accurate to within 0.5°C , the temperature difference can be off by a full degree. If the temperature difference is large, this may not be

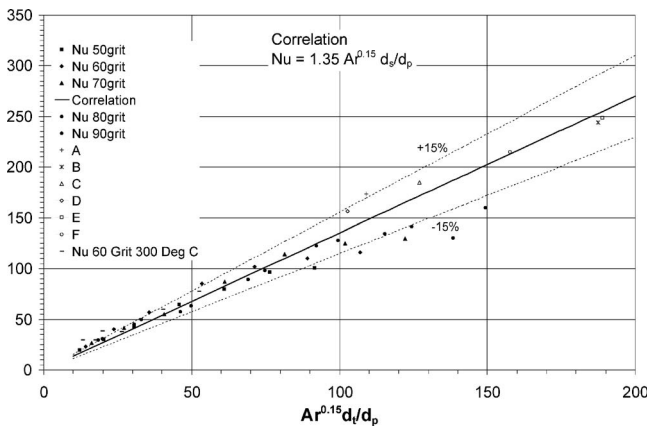


Fig. 8 Equation (10) plotted with all data, as well as data from Grewal and Saxena (see Ref. [1]): (a) Silica sand $d_p=451 \mu\text{m}$, $d_t=12.7 \text{ mm}$, (b) silicon carbide $d_p=178 \mu\text{m}$, $d_t=12.7 \text{ mm}$, (c) silicon carbide $d_p=362 \mu\text{m}$, $d_t=12.7 \text{ mm}$, (d) silica sand $d_p=504 \mu\text{m}$, $d_t=12.7 \text{ mm}$, (e) silica sand $d_p=167 \mu\text{m}$, $d_t=12.7 \text{ mm}$, and (f) alumina sand $d_p=259 \mu\text{m}$, $d_t=12.7 \text{ mm}$

significant, but for larger samples with large current-carrying cross sections and with limited heating current available, the measured temperature difference may only be on the order of 10°C , resulting in a 10% uncertainty. The analysis itself includes some assumptions that may contribute to errors. The analysis assumes a uniform convection coefficient h over the entire length of the sample. However, it is likely that the terminals holding the ends of the sample cause flow disturbances that alter the convection coefficients at the sample ends, though the magnitude of this effect is unknown. Additionally, it has been assumed that no heat is generated in the sample portion that is in the terminals. As the terminals are large cross-section copper, this is likely a good assumption, except right near the point where the sample emerges from the terminals, where some heat will be generated as current funnels into the sample. However, this is not expected to be significant. Other sources of error, such as current and voltage measurements, are not likely to be significant contributors to error, as these values are measured using calibrated instruments that are accurate to better than 1%.

Measurements made in the pilot-scale fluidized bed presented in Fig. 8 (hot conditions) have some uncertainty associated with the limitations of the pilot-scale bed air supply. The air system supplied with this bed can only provide approximately $2.5 \times U_{\text{mf}}$, and so the fluidizing rate range testable is limited. As a result, though the plateau in Nusselt number with flow rate is evident, there is insufficient high flow data to accurately assess the plateau value.

Overall, the level of uncertainty in a given measurement is dependent on conditions such as measured temperature differential, fluidizing rate and other operating parameters, but is expected to be in the range of 15% for cold test data.

Conclusions

Heat transfer to horizontal cylinders has been well studied, but only for cylinders larger than approximately 25 mm. Correlations developed for cylinders of this size range do not extrapolate well for smaller sized cylinders on the order of 1–10 mm diameter. Smaller cylinders exhibit a plateau in Nusselt number that is reached quite rapidly, near $G/G_{\text{mf}}=2$, while larger cylinders show a monotonic increase of Nu with increasing fluidizing gas flow. Data obtained using cylinders ranging from 1.27 to 9.52 mm in fluidized beds using alumina sand ranging from 145 to 330 μm were used to develop a correlation for Nu_{mean} as a function of Ar and d_t/d_p . The resulting expression correlated most data to within 15%, including data reported by Grewal and Saxena [9] for 12.7 mm tubes in a variety of particle materials and sizes.

Acknowledgment

The financial support of NSERC (Natural Sciences and Engineering Research Council of Canada) is acknowledged with thanks. The assistance of Phillip Cowie and Andrew Rawlings of The I.C.E. Group is gratefully acknowledged.

Nomenclature

A_c	= tube cross-sectional area (m^2)
A_o	= outside area of tube (m^2)
Ar	= Archimedes number
C	= factor
Cp_g	= gas specific heat (J/kg K)
Cp_s	= particle specific heat (J/kg K)
d_t	= tube diameter (m)
d_p	= particle diameter (m)
G	= fluidizing gas mass flux ($\text{kg/m}^2 \text{ s}$)
G_{mf}	= fluidizing gas mass flux at minimum fluidizing condition ($\text{kg/m}^2 \text{ s}$)
h	= convection coefficient ($\text{W/m}^2 \text{ K}$)
I	= current through tube (A)
k	= tube thermal conductivity (W/m K)
k_g	= fluidizing gas conductivity (W/m K)
k_p	= particle conductivity (W/m K)
L	= sample length (m)
n	= factor
Nu	= Nusselt number
Nu_{mean}	= mean Nusselt number
Pr	= fluidizing gas Prandtl number
q'''	= volumetric heat generation (W/m^3)
q_t	= heat loss at terminals (W)
r	= radial coordinate (m)
r_i	= tube inner radius (m)
r_o	= tube outer radius (m)
T	= temperature (K or $^{\circ}\text{C}$)
T_{bed}	= fluidized bed temperature (K or $^{\circ}\text{C}$)
T_i	= tube inner temperature (K or $^{\circ}\text{C}$)
T_o	= tube surface temperature (K or $^{\circ}\text{C}$)
T_t	= terminal temperature (K or $^{\circ}\text{C}$)
U	= gas velocity (m/s)

U_{mf}	= minimum fluidizing gas velocity (m/s)
V	= voltage drop across sample (V)
x	= axial coordinate (m)
ε	= bed voidage
ε_{mf}	= bed voidage at minimum fluidization flow
ρ_g	= fluidizing gas density (kg/m^3)
ρ_p	= particle density (kg/m^3)
ϕ_s	= particle sphericity
μ_g	= fluidizing gas viscosity (N s/m^2)
θ_t	= temperature difference (K)

References

- [1] Saxena, S. C., 1989, "Heat Transfer between Immersed Surfaces and Gas-Fluidized Beds," *Adv. Heat Transfer*, **19**, pp. 97–190.
- [2] Li, H.-S., Qian, R.-Z., Huang, W.-D., and Bi, K.-J., 1993, "An Investigation on Instantaneous Local Heat Transfer Coefficients in High Temperature Fluidized Beds—I. Experimental Results," *Int. J. Heat Mass Transfer*, **36**(18), pp. 4389–4395.
- [3] Khan, T., and Turton, R., 1992, "The Measurement of Instantaneous Heat Transfer Coefficients Around the Circumference of a Tube Immersed in a High Temperature Fluidized Bed," *Int. J. Heat Mass Transfer*, **35**(12), pp. 3397–3406.
- [4] Karamavruc, A. I., and Clark, N. N., 1996, "A Correction Factor for One-Dimensional Heat Transfer Coefficients Around a Horizontal Tube in a Fluidized Bed," *Powder Technol.*, **86**, pp. 209–217.
- [5] Crowle, W., 1987, "Annealing Wire in Fluidised Beds," *Wire Ind.*, **54**(644), pp. 455–457.
- [6] Ergun, S., 1952, "Fluid Flow Through Packed Columns," *Chem. Eng. Prog.*, **48**, pp. 89–94.
- [7] Sathiyamoorthy, D., Sridhar Rao, Ch., and Raja Rao, M., 1988, "Effect of Distributors on Heat Transfer from Immersed Surfaces in Gas Fluidised Beds," *Chem. Eng. J.*, **37**, pp. 149–163.
- [8] Grewal, N. S., Saxena, S. C., Dolidovich, A. F., and Zabrodsky, S. S., 1979, "Effect of Distributor Design on Heat Transfer From an Immersed Horizontal Tube in a Fluidized Bed," *Chem. Eng. J.*, **18**, pp. 197–201.
- [9] Grewal, N. S., and Saxena, S. C., 1980, "Heat Transfer Between a Horizontal Tube and a Gas-Solid Fluidized Bed," *Int. J. Heat Mass Transfer*, **23**, pp. 1505–1519.
- [10] Vreedenberg, H. A., 1958, "Heat Transfer Between a Fluidized Bed and a Horizontal Tube," *Chem. Eng. Sci.*, **9**, pp. 52–60.
- [11] Andeen, B. R., and Glicksman, L. R., 1976, "Heat Transfer to Horizontal Tubes in Shallow Fluidized Beds," *ASME Paper 76-HT-67*.
- [12] Petrie, J. C., Freeby, W. A., and Buckham, J. A., 1968, "In-bed Heat Exchangers," *Chem. Eng. Prog.*, **64**(7), pp. 45–51.
- [13] Ainshtein, V. G., and Gel'Perin, 1966, "O Teploobmene Mezhdru Psevdozhzhennym Sloem i Poverkhnost'yu," *Int. Chem. Eng.*, **6**(1), pp. 67–74.
- [14] Molerus, O., and Writh, K. E., 1997, *Heat Transfer in Fluidized Beds*, Chapman and Hall, London.

M. B. Gillespie
Progress Energy,
8202 West Venable Street,
Crystal River, FL 34429
e-mail: mark.gillespie@pgnmail.com

W. Z. Black
e-mail: william.black@me.gatech.edu

C. Rinehart
e-mail: gt1479b@mail.gatech.edu

A. Glezer
e-mail: ari.glezer@me.gatech.edu

George W. Woodruff School of Mechanical
Engineering,
Georgia Institute of Technology,
Atlanta, GA 30332-0405

Local Convective Heat Transfer From a Constant Heat Flux Flat Plate Cooled by Synthetic Air Jets

The effects of a small-scale, rectangular synthetic air jet on the local convective heat transfer from a flat, heated surface were measured experimentally. The synthetic jet impinges normal to the surface and induces small-scale motions by zero-net mass flux, time-periodic entrainment, and ejection of ambient air at frequencies whose periods are far higher than the characteristic thermal time scale. The velocity field between the jet orifice and the target plate is measured in planar cross sections using particle image velocimetry and is related to the local heat transfer from the plate. The present work suggests that synthetic jets can lead to substantial enhancement of the local heat transfer from heated surfaces by strong mixing that disrupts the surface thermal boundary layer. The dependence of the local heat transfer coefficient on the primary parameters of jet motion is characterized over a range of operating conditions.

[DOI: 10.1115/1.2345423]

Keywords: experimental heat transfer, jet impingement, pulsating air jets, oscillatory flow

1 Introduction

The ability to dissipate heat at high flux levels while maintaining relatively low component temperatures is a formidable task facing thermal engineers. The primary example of this challenging problem is the quest to cool microelectronic packages as the level of power dissipation from these systems continues to increase while the size of packages continues to shrink at accelerating rates. Innovative cooling techniques that require minimal power consumption are needed to maintain package junction temperatures at tolerable levels. In the past, natural convection was the preferred mechanism for cooling low-cost consumer devices. As heat dissipation rates have increased, cooling schemes have relied upon fan-induced, global air motion. However, the abrupt increase in recent years of hardware functionality and complexity, and hence, power consumption, has quickly surpassed the cooling limits of natural convection and simply designed forced convection systems. As a result, designers have had to develop new, inexpensive and compact thermal management methods to remove heat from small surfaces.

Limitations in heat transfer from small discrete packages exist because the flow structure generated by the cooling scheme is not often effectively coupled to the larger, global heat removal system. In fact, two important aspects should be considered to improve the heat removal from miniature surfaces. First, the enhancement of surface heat transfer is possible through the exploitation of small-scale vortex motion and through the promotion of local entrainment and mixing of cool ambient air. The increase in heat transfer results from increased turbulence and a reduced thermal boundary layer at the heated surface. Second, the hardware for direct heat removal should scale appropriately with the size of the surface and it should operate with minimal power. This paper reports on small, low-speed, low-power, pulsating jets

that are capable of exploiting small-scale turbulent vortices, and therefore are able to meet the requirements of creating high heat transfer rates on miniature heated surfaces.

1.1 Purpose. Although a few papers have discussed the fluid characteristics of small-scale pulsating jets, they include no data regarding the jets' heat transfer characteristics. This paper presents an experimental investigation of the flow field and heat transfer characteristics of a rectangular, synthetic jet impinging normally on a flat, heated surface. Synthetic jets are a particularly attractive candidate for cooling miniature surfaces like electronic packages because they can affect the heat transfer on extremely small scales and enhance the transport and mixing of the heated fluid. Furthermore, because these jets are zero net mass flux in nature they can be easily integrated into complex geometries, require relatively low operating power, are simple to design and fabricate and, unlike traditional fans or steady jets, they do not require external ducting. Synthetic jets are ideal devices for use where heat removal is required from small, discrete surfaces.

1.2 Background. Since the surface area of the package cannot be easily modified and the maximum temperature difference for heat transfer is clearly limited by the junction temperature of the electronic package and the local ambient temperature, the most effective means of enhancing the local heat transfer from a package is to maximize the local heat transfer coefficient. A number of earlier investigations recognized the advantages and relatively high heat transfer coefficients that can be produced by steady impingement flow involving round jets, slot jets, and arrays of jets [1,2]. In addition, a number of experiments were conducted to characterize the convective heat transfer of impinging steady air jets on flat surfaces [3–6]. In these investigations, the impinging jet Reynolds number was on the order of 1000 to 10,000.

Until recently, the problem of heat transfer between a surface and a pulsating jet had been treated as a steady-state problem. Few studies have been performed with pulsating, impinging jet flows despite their use in cooling, heating, and drying processes. Using air as the heat transfer fluid, experiments measured spatially and temporally averaged heat transfer rates from a flat, isothermal surface that was cooled by a pulsating, circular air jet with $1200 < Re < 12,000$ and $10^{-4} < S_{\omega} < 10^{-2}$ [7]. For the range of variables covered in their investigation, no apparent correlation was found

Contributed by the Heat Transfer Division of ASME for publication in the JOURNAL OF HEAT TRANSFER. Manuscript received March 29, 2005; final manuscript received February 22, 2006. Review conducted by Phillip M. Ligrani. Paper presented at the 2005 ASME Pressure Vessels and Piping Conference (PVP2005), July 17–21, 2005, Denver, CO.

between the Nusselt number and the two dimensionless groups involving the amplitude and frequency of jet pulsation. The authors concluded that the action of a low velocity, pulsed jet had little effect on the thickness of the thermal boundary layer.

In a more recent analysis, an experimental investigation was performed on the effect of flow intermittency on convective heat transfer resulting from a planar water jet impinging on a constant heat flux surface [8]. Enhancement was achieved by briefly and repetitively interrupting the jet flow and thereby halting the development of the hydrodynamic and thermal boundary layers. The authors discovered that enhancements due to intermittency occurred only when the frequency of the intermittency was sufficiently high to maintain a time-averaged thermal boundary layer thickness that was much thinner than the steady-state value. Similar experiments measured the effect of flow pulsations on the local heat transfer characteristics of a large-scale planar air jet [9]. The authors determined that stagnation-point heat transfer in axisymmetric submerged jets was enhanced by a surface renewal effect produced by the impingement of large-scale structures on the boundary layer. Results indicated that pulse amplitude and frequency influenced the size and formation of coherent structures in pulsed flow.

A recent experimental study measured local and instantaneous heat transfer rates from a downward-facing heated plate when cooled with an array of pulsating jets [10]. The jet velocity profile consisted of steady, bulk airflow superimposed with an oscillatory flow with pulsation magnitudes up to 60% of the steady flow values and frequencies up to 65 Hz. The jet Reynolds number of the combined flow based on the orifice diameter ranged between 2500 and 10,000. The authors reported that, as a result of the imposed flow fluctuations, the distribution of convective heat transfer on the surface of the plate became more uniform. However, the overall heat transfer rate from the surface was not significantly enhanced.

While heat transfer by direct impingement of an unsteady jet appears to be an attractive approach to the thermal management of integrated circuits, earlier work in this area has underscored the importance of small-scale flow turbulence and the entrainment of ambient fluid near the surface. Flow pulsations have yielded promising results in laboratory experiments, but their use in practical applications has been hindered by the complexity of existing electronic hardware. Nonetheless, experiments with zero-net mass flux synthetic jets have shown that they are easily integrated into existing electronic equipment [11]. For example, preliminary work has demonstrated the effectiveness of a single jet used to cool an array of power metal-oxide-semiconductor field effect transistor devices [12].

Synthetic jets have the unique property that they are formed from the working fluid in which they are deployed. In contrast to conventional continuous jets or pulsed jets, synthetic jets are able to transfer linear momentum without a net mass injection across the flow boundary. Synthetic jets are created by the time-periodic formation and subsequent advection of a train of counter-rotating vortex pairs. Successive vortex pairs are formed at the edge of the orifice by the time-periodic motion of the diaphragm that bounds the sealed cavity. Away from the orifice, the general features of synthetic jets are similar to conventional continuous jets in terms of cross-stream spreading and the decay of the centerline velocity. However, the details of the near-field flow are substantially different and synthetic jet Reynolds numbers are typically several orders of magnitude smaller than published steady jet data. The time-averaged static pressure in the near-field of a synthetic jet is lower than the ambient pressure because of the suction of fluid into the cavity. In addition, both the stream-wise and cross-stream velocity components reverse their direction during one complete cycle of the diaphragm. The velocity components, as well as the celerity and characteristic length scale of the vortex pairs, can be varied over a broad range by controlling the amplitude and period of diaphragm motion.

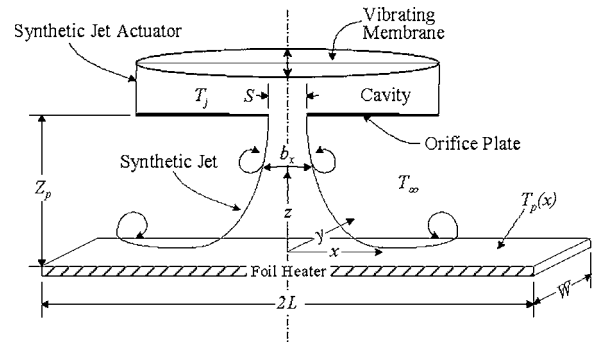


Fig. 1 Synthetic jet actuator with a rectangular orifice of width S and length W , impinging on a foil heater of length $2L$ and width W

Previous studies measured the stream-wise and cross-stream velocity profiles for both rectangular and circular pulsating synthetic jets [11]. Near the orifice, the flow was dominated by time-periodic variations and a vortex-type flow was generated at the edge of the orifice. As the vortex structure progressed downstream, the air transitioned to turbulent flow. The transition process was followed by the development of a fully turbulent jet region that had characteristics similar to a conventional, two-dimensional jet.

2 Experimental Apparatus

2.1 Synthetic Jet Actuator. The experimental synthetic jet consisted of a shallow, cylindrical cavity bounded on one side by an orifice plate and on the other side by a flexible, vibrating membrane (Fig. 1). The orifice plate consisted of a 0.5 mm thick stainless steel plate with a 1.0 mm wide by 25.0 mm long slot, which was fabricated using standard micromachining techniques. The internal volume of the cavity was approximately 6000 mm³. The hydrodynamic impulse required to form each vortex was produced by the time-harmonic motion of a Mylar diaphragm that was driven by a 40 mm diameter electromagnetic actuator. The actuator was powered by an oscillator that produced a sinusoidal voltage signal. Even though a single orifice was used during this study, orifices can be made in a variety of shapes including circular holes and rectangular slots, either of which may be used individually or in an array. When the membrane is driven by a time-harmonic signal, a highly turbulent jet is synthesized from the advection of successive vortex pairs that originate at the orifice; these vortices entrain ambient air into the jet. Unlike a traditional steady jet, synthetic jets produce zero-net mass flux in the plane of the orifice. However, the vortices create net-positive hydrodynamic momentum across the centerline of the jet, which decays as the distance from the orifice increases. The turbulent stagnation-point nature of the synthetic jet has the potential to produce a highly efficient heat transfer process on a surface that is placed nearby.

The apparatus used to measure the local heat transfer coefficients produced by synthetic jets is shown schematically in Fig. 2. The testing facility consisted of two main parts: the base and the support assembly. The nylon base provided an insulating foundation for the guard heater, Teflon[®] substrate, thermocouples, and test heater. The support assembly was affixed to the base and moved the synthetic jet vertically over the test heater such that the centerline of the orifice plate was located directly above the center of the heater. Surrounding the test apparatus was an enclosure that minimized room air currents to ensure quiescent conditions during all tests.

Since the time-averaged velocity of a synthetic jet in the plane of the orifice is zero, a nontraditional definition of the synthetic jet velocity was used to define the Reynolds number. The synthetic

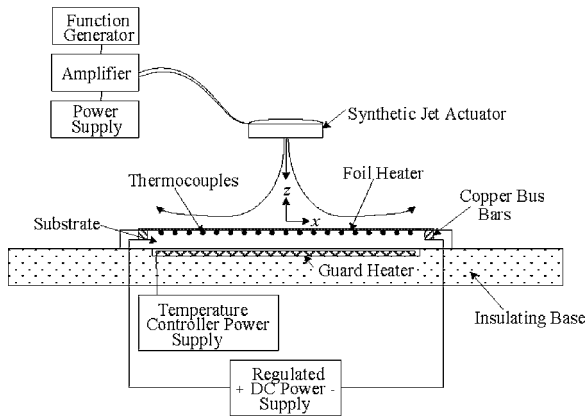


Fig. 2 Schematic of experimental apparatus

jet Reynolds number was based on the orifice width and average jet discharge velocity in the plane of the orifice. The velocity of the synthetic jet was measured using a single element Dantec 55P11 miniature hot wire anemometry probe with a 5 micron diameter, 1.25 mm long platinum-plated tungsten wire sensor. The sensor was placed at the center of the jet orifice flush with the exit plane spanwise along the major axis. The sensor interfaced with a conventional anemometer and data were collected with a personal computer-based data acquisition system at a sampling rate of 50 kHz. The average jet discharge velocity (U_0) was determined by integrating the instantaneous streamwise velocity in the plane of the orifice, $u_o(t)$, over the discharge half of one driving cycle. The result was then averaged over the entire cycle

$$U_0 = \frac{1}{\tau} \int_0^{\tau} u_o(t) dt \quad (1)$$

Hence, the average jet discharge velocity was calculated based only upon the air that was ejected from the slot and subsequently produced the synthetic jet. The Reynolds number was defined as follows:

$$Re = \frac{U_0 S}{\nu} \quad (2)$$

A typical instantaneous velocity profile is shown in Fig. 3 for a synthetic jet frequency of 300 Hz. Results in Fig. 4 show the variation of the jet Reynolds number with actuator driving frequency. The hot-wire anemometry measurements resulted in synthetic jet Reynolds numbers that did not exceed 450 with peak Reynolds number occurring for frequencies between 300 and 400 Hz. Reynolds numbers this low would normally imply lami-

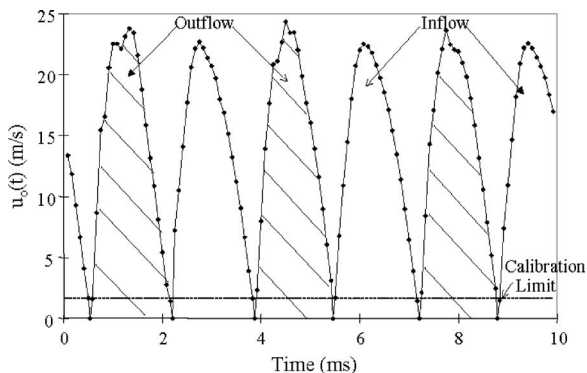


Fig. 3 Time trace of synthetic jet velocity at the orifice ($f = 300$ Hz)

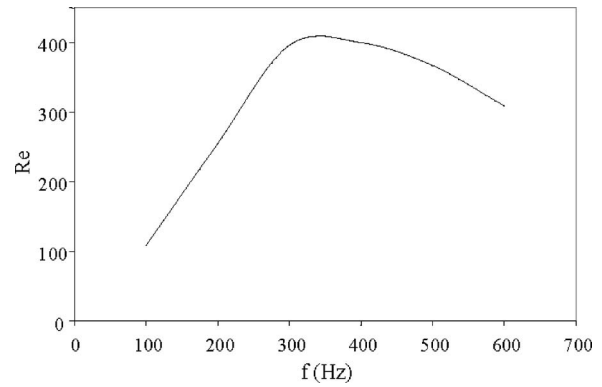


Fig. 4 Variation of jet Reynolds number with frequency

nar flow if steady jets generated them. However, due to the vortices formed at the edge of the orifice plate and the alternating type of flow produced by the vibrating diaphragm, the synthetic jets produced fully turbulent flow that enhanced the heat transfer beyond the expected rate suggested by the relatively low Reynolds numbers.

Measurements of the time-averaged velocity field of both the free and impinging synthetic jet were obtained using particle image velocimetry (PIV) in an enclosed test cell. The optical setup of the PIV system included: a pair of 50 mJ Nd-yttrium-aluminum-garnet lasers with 1 μ s trigger capability, an adjustable lens system that produced a sheet of light with variable thickness and width, and a closed circuit digital camera. Distributions of the two orthogonal velocity components in planar cross sections of the flow field were obtained from successive image pairs of tracer particles using a standard cross-correlation algorithm. The pulsed lasers and the camera were controlled by a dedicated laboratory computer using synchronizing electronic hardware and software that allowed the delay time between successive image pairs to be varied. A typical data record consisted of 1000 image pairs. The time delay between successive images was selected such that the maximum velocity resulted in displacements that were nominally one quarter of the characteristic length of the interrogation domain.

2.2 Heated Test Surface. The heated surface consisted of a thin (0.0254 mm) electrically heated stainless steel foil measuring 75 mm by 20 mm that was mounted on an insulating Teflon[®] substrate (Fig. 2). To ensure that the stainless steel foil experienced a uniform current distribution and uniform heating, the short ends of the foil were attached to copper bus bars using a silver-filled epoxy adhesive. The two bus bars were embedded into the substrate material so that the top surface of the heater remained flat and level. Controlled heating was generated by passing a known electrical current from a regulated direct current power supply through the foil via the copper bus bars. A guard heater was located beneath the substrate to reduce conduction from the back surface of the heater. In addition, a regulated temperature controlled power supply was used to maintain the guard heater at a fixed temperature that was equivalent to the lowest recorded temperature on the heater. In the presence of the guard heater, the heat transfer through the back surface of the heater was less than 6% of the heat convected from the top surface. In comparison, without a guard heater operating, the heat transfer through the back surface of the heated plate was approximately 26% of the total heat convected.

The local temperature distribution of the heated surface was measured using an array of thermocouples that were embedded at discrete locations in the substrate. Small grooves (0.30 mm wide and 0.50 mm deep) for the leads and holes (0.50 mm in diameter) for the beads were machined with a precision milling machine

into the top surface of the substrate. The thermocouples were fabricated from bare, 30-gauge copper and constantan wires (ANSI type-T) using a butt-weld configuration so that a single thermocouple lead could be placed in each groove. Excess weld material was removed from the junction to ensure that the beads were only slightly larger than the diameter of the wire. The thermocouples were covered with a thin layer of electrically insulating lacquer and calibrated in a constant temperature bath of ethylene glycol. Once the thermocouples were inserted into the substrate, a small amount of thermally conducting and electrically insulating paste was applied to each thermocouple junction to provide proper thermal contact with the heater. Because the heater had a high thermal conductivity and it was very thin ($Bi < 0.1$), the vertical temperature gradient through the thickness of the heater was negligibly small. Therefore, the thermocouples located beneath the test heater accurately measured the local surface temperature of the heater.

All thermal data, including the local temperatures on the heater, the temperature of the ambient air, the guard heater temperature, and the total power input to the heater, were recorded with a PC-based data acquisition system. Steady-state data were collected when the average heater temperature changed by less than 1°C over a period of 1 h. Infrared images of the heater surface were also used to provide a qualitative measure of the temperature distributions and the location of the isotherms. The infrared images confirmed that the span-wise temperature variations across the heater were negligible. The thermal time constant of the heater was larger than the characteristic period of the synthetic jet. As a result, for the frequencies used during all tests (i.e., 100–600 Hz), the heated surface experienced a steady cooling effect even though the flow of air over the plate was oscillatory in nature.

The calculated convective heat transfer rate had to account for other modes of heat transfer from the plate because the total power supplied to the heater was not dissipated from the top surface solely by convection. The net rate at which heat was convected from the top surface of the plate (q_{conv}) was determined by first measuring the total electrical heat input to the test heater. Then, the radiative heat transfer from the upper surface of the plate was estimated assuming a gray, diffuse heater surface radiating to black surroundings at ambient temperature. In addition, the electrical input to the heater was corrected for the heat transfer conducted downward through the substrate and for the conduction through electrical leads. Radiative losses were approximately 1% of the total energy input to the heater and conduction losses through metallic leads, including all thermocouples and power leads, did not exceed 16%.

The primary errors associated with the data collected in this experiment originated from the measurements of the local temperatures and the determination of the convective heat transfer rate from the heater. A detailed uncertainty analysis [13] was performed to account for all possible errors. Using this procedure, the uncertainty errors in the measured Nusselt number were determined to be no greater than 8%. Several experiments were duplicated to determine repeatability of the experimental measurements and the values for all local heat transfer coefficients varied by less than the estimated experimental error.

3 The Synthetic Jet Flow Field

3.1 Free Jet. Maps of the time-averaged velocity vectors and vorticity concentrations in an upward-directed free jet (i.e., in the absence of the impingement plane) are shown in Fig. 5. The nominal operating frequency of the jet is 300 Hz, with a jet strength corresponding to $Re \approx 400$. While thermocouple measurements were only performed along the x -axis, variations in fluid flow for such a configuration are not purely two dimensional. In order to better understand the variation in thermal performance versus orifice-to-plate separation distance, observations of the fluid flow in both the x - z and y - z planes are necessary. Hence, the data are

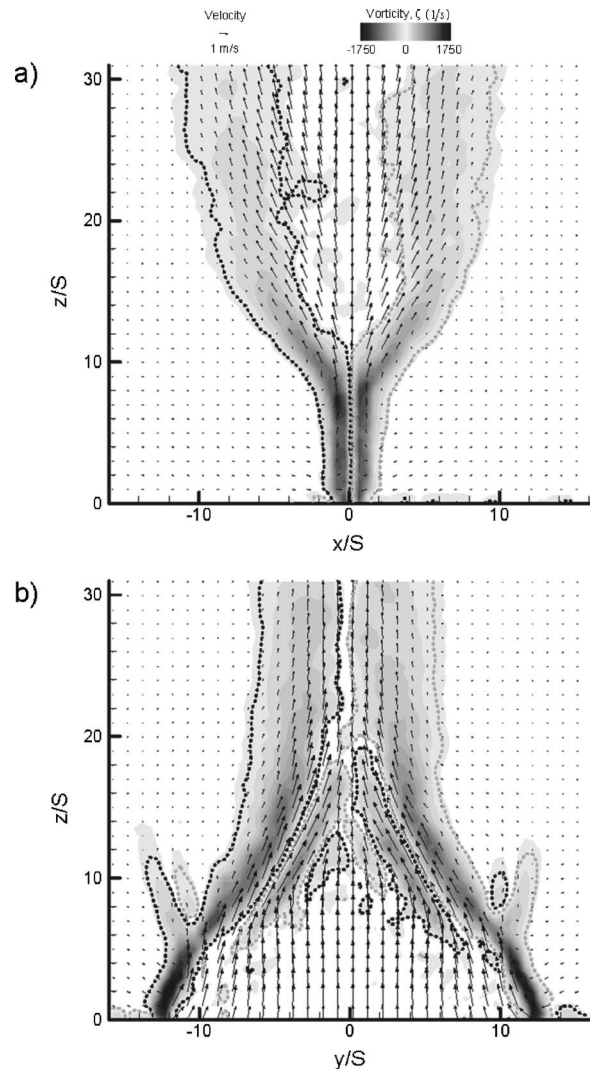


Fig. 5 Velocity field and spanwise vorticity concentrations for a free jet, (a) minor axis, and (b) major axis. Two vorticity contours are marked with dashed lines: $\zeta = \bullet\bullet\bullet\bullet\bullet\bullet 100$, $\bullet\bullet\bullet\bullet\bullet\bullet -100(1/s)$.

measured using PIV in two orthogonal planes along the minor (Fig. 5(a)) and major (Fig. 5(b)) centerlines of the jet orifice (i.e., x - and y -axes, respectively), each with a 31 mm square field of view. Flow entrainment and recirculation in the orthogonal (y - z) plane are directly related to the fluid flow pattern and impinging fluid temperature in the plane of the thermal measurement (i.e., the x - z plane).

One of the most striking features of the mean flow field is the radical change in the cross-stream breadth of the jet in the x - z and y - z planes. By defining the jet width (b) as the central span within which the velocity is greater than one-half the centerline streamwise velocity, several unique aspects of the synthetic jet are revealed by these measurements, presented in Fig. 6(a). In the x - z plane (i.e., along the minor axis), the jet width (b_x) is almost invariant through $z/S \approx 7$, after which it begins to spread such that by $z/S \approx 15$ its cross-stream jet width is equivalent to the jet width in the y - z plane. For $z/S > 18$, the rate of increase in b_x begins to diminish and at the downstream edge of the measurement domain $b_x \approx 14$. In contrast to the jet structure in the x - z plane, the jet width (b_y) decreases monotonically in the y - z plane up to $z/S \approx 18$. Within the measurement domain, the aspect ratio of the jet switches from $b_x/b_y = 0.04$ at $z/S = 0$ to $b_x/b_y = 2.5$ at $z/S = 31$.

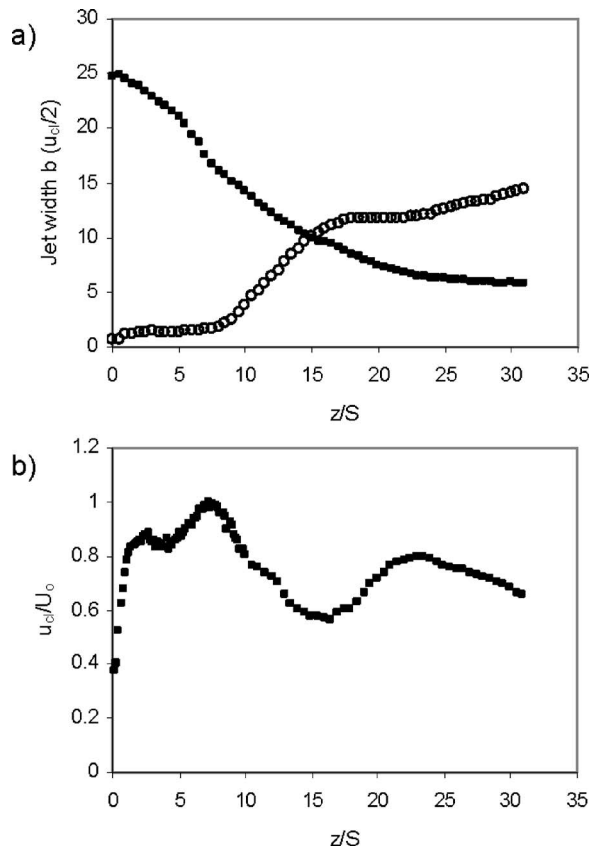


Fig. 6 Streamwise variation of: (a) jet width at 50% of centerline velocity (■major axis b_y , ○minor axis b_x) and (b) normalized centerline velocity

More importantly, the pivotal ratio of $b_x/b_y=1.0$ occurs at $z/S=15$, or the point at which the jet width in the x -axis equals the jet width in the y -axis.

Another remarkable feature of the jet in the near field is the evolution of the time-averaged spanwise vorticity concentrations: ζ_y and ζ_x . While the vorticity concentrations in the x - z plane (ζ_y , Fig. 5(a)) are predominantly of one sense on either side of the jet centerline (i.e., counter-clockwise and clockwise on the left and right side, respectively), the evolution of the jet in the y - z plane (Fig. 5(b)) is substantially different. The initial roll-up of the jet shear layer at either spanwise edge is predominantly single sense. However, at $z/S \approx 5$, vorticity concentrations of the opposite sign appear near the inner edge of the jet shear layers and persist through $z/S \approx 20$, where the decrease in cross-stream spreading of the jet subsides. It should be noted that the appearance of the counter-sense vorticity concentrations at $z/S \approx 5$ is accompanied by “wings” of similar (but weaker) vorticity concentrations near the outer edges of the jet. These wings vanish near $z/S \approx 15$.

While not the focus of the present experiment, it is conjectured that the reason for the narrowing of the jet is associated with the advection dynamics of the high aspect ratio vortex loops that are formed around the circumference of the jet orifice during each actuation cycle. The vorticity concentrations in Fig. 5(b) suggest the presence of out-of-plane vortical motions that are connected with the bending or folding of these high aspect ratio vortex loops that ultimately lead to the changes in the jet aspect ratio. Similar changes in aspect ratio were observed in the near field of rectangular [14] and elliptical [15] conventional jets where the cross-stream major and minor axes switch (or alternate) with streamwise distance such that the jet ultimately becomes round in the far field.

The reduction in the aspect ratio of the jet is accompanied by

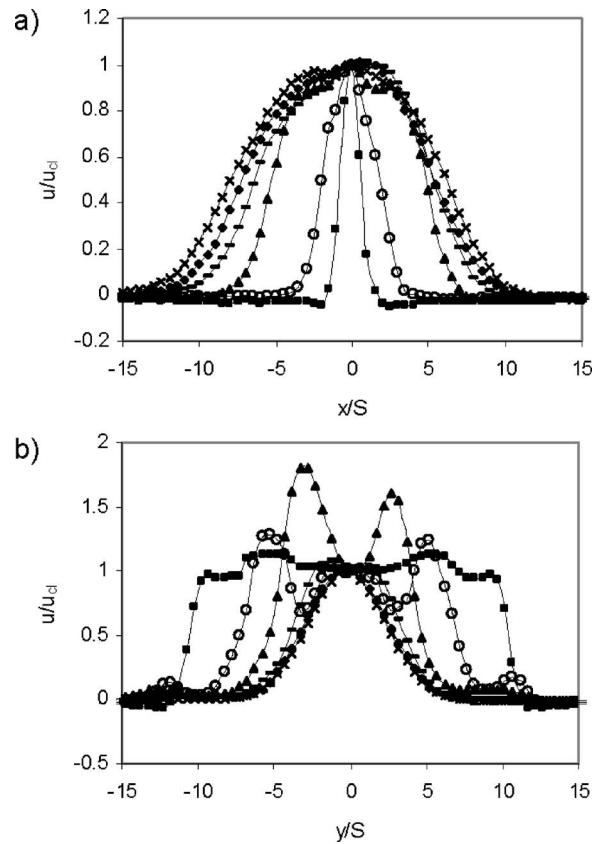


Fig. 7 Cross-stream distributions of streamwise velocity in the free jet, (a) minor axis and (b) major axis. $z/S=$ ■5, ○10, ▲15, ◆20, ◆25, and ×30.

substantial changes in the streamwise variation of the time-averaged centerline velocity. The centerline velocity in the near field of a high-aspect ratio synthetic jet vanishes at the exit plane of the jet and thereafter increases monotonically with streamwise distance [11]. This velocity then reaches a local maximum, which is associated with the coherence of the vortex pairs that form the jet, and ultimately decreases in the far field (approximately as $1/z$). However, owing to rapid loss of coherence of the jet vortices, previous experiments [11] exhibited a streamwise rate of change in the jet aspect ratio that was far lower than in the present jet, which has a lower orifice aspect ratio. The streamwise variation of the normalized centerline velocity for the present experiment is shown in Fig. 6(b). The centerline velocity initially increases rapidly with streamwise distance and has a local peak at $z/S \approx 7$, at which point the jet has narrowed in the y - z plane, but has not yet spread appreciably in the x - z plane (Fig. 6(a)). The ensuing spread in the x - z plane then results in a decrease of the centerline velocity through $z/S \approx 15$, where there is a local minimum, also noted as the point of axis switching. A local peak at $z/S \approx 23$ results when the jet continues to narrow in the y - z plane while remaining relatively constant in the x - z plane. Downstream of $z/S \approx 23$, the rate of spreading in the x - z plane is greater than that of the y - z plane and the centerline velocity decreases thereafter.

The streamwise evolution of the jet is also discerned from normalized cross-stream distributions of the time-averaged streamwise velocity in the x - z and y - z planes (Figs. 7(a) and 7(b), respectively). The distributions in the y - z plane clearly show the narrowing of the jet. The distribution at $z/S \approx 10$ exhibits three major peaks: one on each side of the jet centerline ($y/S \approx \pm 6$) and another lower, central peak. These peaks are associated with the counter-sense vorticity distributions at each spanwise edge of the

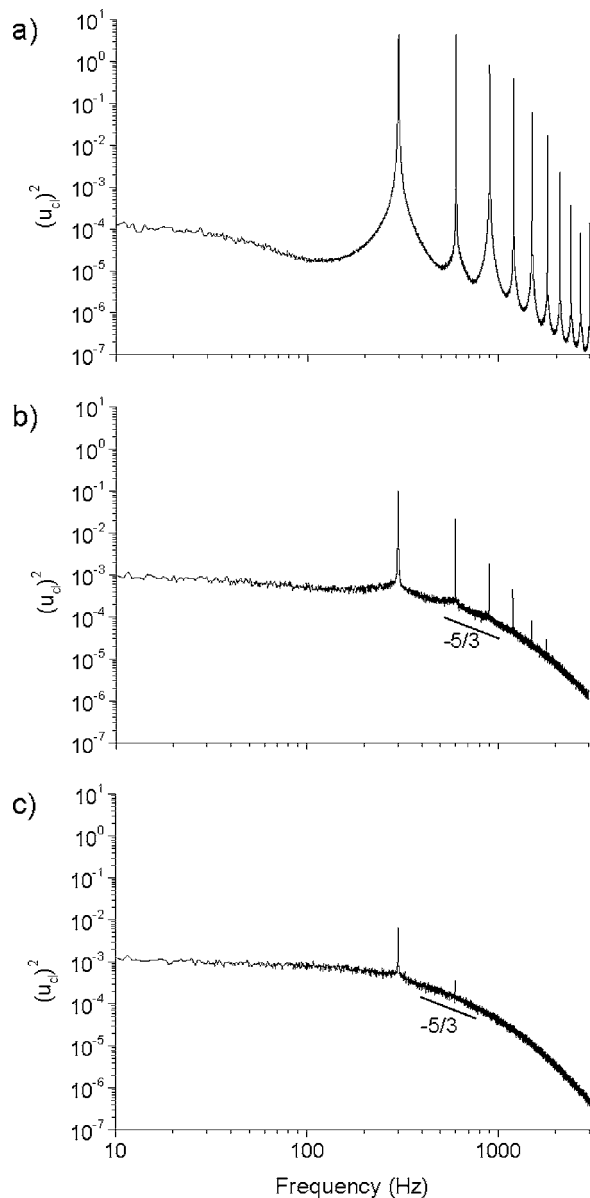


Fig. 8 Power spectra of the jet centerline velocity: (a) $z/S=5$, (b) $z/S=15$, and (c) $z/S=25$

jet. This distribution also shows lower peaks ($y/S \approx \pm 12$) that are associated with the vorticity wings in Fig. 5(b). By $z/S=15$ (the location of axis switching as previously noted) the local central peak disappears and the two other off-center peaks are no longer present by $z/S \approx 25$.

The evolution of vortical structures within the jet is also characterized by spectra of the streamwise velocity measured on the jet centerline at $z/S=5$, 15, and 25 (Figs. 8(a)–8(c), respectively) using hot wire anemometry. Near the jet exit plane ($z/S=5$), the velocity spectrum is entirely dominated by the jet formation frequency (300 Hz) and its higher harmonics. Figure 8(a) illustrates that the spectral components below the formation frequency have relatively little power. The formation of the successive vortices is accompanied by the presence of higher harmonics of the driver frequency; these higher harmonics are artificially strengthened by the rectification of the velocity time trace by the hot wire sensor. However, this rectification subsides farther downstream as the magnitude of the time-averaged velocity increases [11]. By $z/S=15$, the power in spectral components that are below the forma-

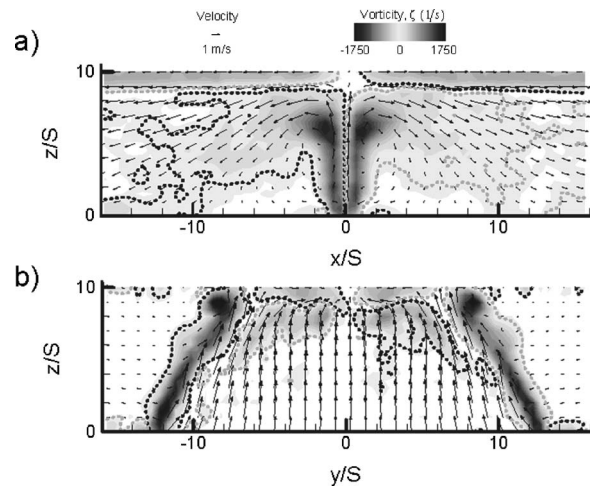


Fig. 9 Velocity field and spanwise vorticity concentrations for jet impinging surface at $Z_p/S=10$, (a) minor axis, and (b) major axis. Two vorticity contours are marked with dashed lines: $\zeta = \bullet\bullet\bullet\bullet\bullet 100, \bullet\bullet\bullet\bullet\bullet -100(1/s)$.

tion frequency increases although this part of the spectrum is featureless and does not exhibit any specific spectral peaks (including subharmonics of the formation frequency). Of particular note is the evolution of the higher end of the spectrum (the spectral decay apparently begins at the formation frequency) that shows an increase in the magnitude of broadband high frequency components, which suggests an increase in the intensity of small-scale motion. The concomitant increase in dissipation apparently leads to the decay of harmonics of the formation frequency above 2000 Hz. Finally, at $z/S=25$, the power spectrum exhibits a clear $-5/3$ slope (evidence of viscous dissipation) and spectral peaks only at the formation frequency and its first harmonic (Fig. 8(c)). The rapid evolution of small-scale motions within the jet indicates strong mixing and thermal dissipation, which are both key factors in applications to small-scale heat removal from solid surfaces.

3.2 Impinging Synthetic Jet. While the discussion in the previous section was limited to a free jet, the primary focus of the present experiment is heat transport by direct, normal impingement of the oscillatory synthetic jet on a solid surface. The velocity field induced by the synthetic jet as it impinges on a solid surface that is parallel to the jet exit plane and can be translated along the z -axis is measured in the x - z and y - z planes using PIV. Time-averaged velocity vectors and distributions of vorticity concentrations are measured at dimensionless orifice-to-plate distances (Z_p/S) of 10, 15, and 20 (Figs. 9–11, respectively). When the plate is placed at $Z_p/S=10$ (i.e., upstream of the axis switching), a clear stagnation region is formed at the impingement zone near the jet centerline. It is interesting to note that in the x - z plane (Fig. 9(a)), the flow along the impingement surface is away from the jet centerline as indicated by velocity vectors and vorticity concentrations within the wall boundary layers. A small recirculating flow domain is also evident on each side of the jet centerline at $z/S \approx 5$. In contrast, the flow in the y - z plane (Fig. 9(b)) indicates that the jet has three stagnation points (on the centerline and at $y/S = \pm 6$). It should be noted that the flow within the jet between the two off-center stagnation points moves toward the centerline and is turned out of y - z plane away from the centerline as shown in the x - z map. These data also suggest that the entrained flow that feeds the jet cavity (along the jet exit plane) and the jet column (along the spanwise edges of the jet) is primarily confined to finite sectors around the y - z plane.

When the impingement plate is placed at $Z_p/S=15$, the flow near the stagnation point changes substantially due to the flow mechanisms associated with the jet axis switching. The PIV image

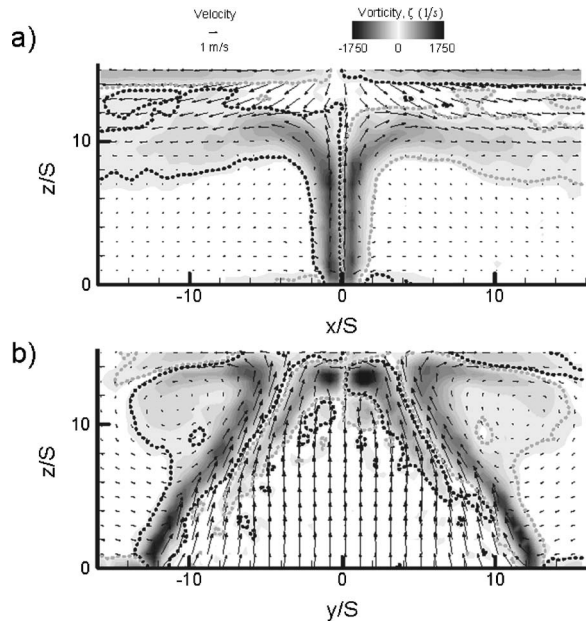


Fig. 10 As in Fig. 9 for $Z_p/S=15$

in the y - z plane (Fig. 10(b)) indicates the formation of a secondary counter rotating vortex pair with a plane of symmetry that nominally coincides with the x - z jet plane. In addition, a secondary vortex pair is formed just below the impingement surface and another stagnation point is evident on the jet centerline at $z/S \approx 12$. The off-center stagnation points that appear in Fig. 9(b) are no longer present and the outer flow (to the right and left of the corresponding spanwise edges of the jet) appears to move away from the jet centerline, although the jet still entrains outer fluid along the exit plane of the jet. The flow that is induced by the

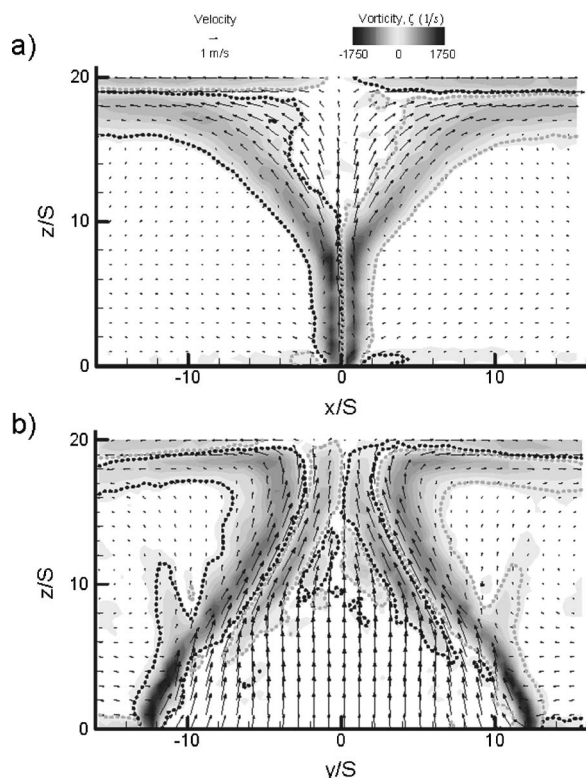


Fig. 11 As in Fig. 9 for $Z_p/S=20$

secondary counter-rotating vortex pair in the y - z plane is also evident in the x - z plane (Fig. 10(a)) where there are two stagnation points on the jet centerline at $z/S=15$ and 12. The stagnation point at $z/S=12$ is formed between the induced downward flow from the impingement surface and the jet flow from below. This flow pattern leads to spanwise ejection of fluid away from the jet centerline. The jet entrains fluid both into the jet cavity and into the jet column as a result of a counter-current flow pattern. The data suggest that the formation of the secondary vortex and the outward jet flow along the surface in both the x - z and y - z planes provide enhanced heat removal from the surface.

Finally, when the impingement plate is placed at $Z_p/S=20$ (i.e., downstream of the axis switching), the secondary vortex is no longer present. The jet exhibits outward flow away from the centerline along the impingement surface in both the x - z (Fig. 11(a)) and y - z (Fig. 11(b)) planes. The flow of expelled air along the impingement surface appears to be balanced by counter-current flow between the plates in both planes of view. At this height it appears that heat transfer from the surface is primarily influenced by the momentum and spreading of the jet before impingement. Investigation of the velocity field of the impinging jet provides insight into the magnitude of the heat transfer from the solid surface, which is discussed in detail in the next section.

4 Heat Transfer

The flow patterns of a synthetic jet that were discussed in the previous section have several basic differences from the flow of steady jets; these differences affect the local heat transfer coefficients. When a steady jet issuing from either a round or rectangular slot impinges normally on a flat surface, the flow pattern can be segregated into three regions: the free jet region, the stagnation region and the wall jet region [16,17]. In the free jet region the jet broadens linearly as it entrains fluid from the surroundings and the jet develops into an approximately Gaussian velocity distribution across the jet profile. Close to the surface, the normal velocity component is slowed and converted into an accelerated tangential component resulting in an area of enhanced heat transfer. As the fluid moves away from the stagnation point, it entrains flow from the quiescent surroundings and it transforms into a decelerated wall jet region. The tangential velocity, which is zero at the stagnation point, accelerates and reaches a maximum value only to decrease as it moves further along the heated surface into the free jet region. The region of maximum flow velocity coincides with a point of maximum local heat transfer coefficient. As a result, the local heat transfer coefficient experienced for a steady slot jet shows a local maximum at the stagnation point and a secondary maximum where the streamwise pressure gradient leads to an increase in the local turbulence levels. The secondary maximum in the heat transfer coefficient is more prevalent when the jet is placed within a few slot widths of the surface and it disappears as the jet is moved further from the heated surface. For a large jet-to-plate spacing, the local heat transfer coefficient decreases monotonically from its peak value at the stagnation point. These steady jet characteristics will be compared to those of the synthetic jet later in this section.

Measurements were carried out to determine the effect of orifice-to-plate spacing (Z_p/S), synthetic jet Reynolds number, and spanwise position (x/S) on the local and average Nusselt numbers for synthetic jets. The apparatus was not designed to investigate the variation in local heat transfer coefficient with the y -axis. Using local plate temperatures, the ambient air temperature and the measured convective heat transfer rate from the heated plate, the local heat transfer coefficient was defined as

$$h_x = \frac{q_{\text{conv}}}{A(T_p - T_\infty)_x} \quad (3)$$

The local Nusselt number was defined as

$$Nu_x = \frac{h_x S}{k} \quad (4)$$

and the average Nusselt number was determined by

$$Nu_{avg} = \frac{1}{L} \int_0^L Nu_x dx = \frac{S}{kL} \int_0^L h_x dx = \frac{h_{avg} S}{k} \quad (5)$$

The study of the velocity profiles in the previous sections indicates that the flow field, much like the flow field produced by a steady jet, can be subdivided into three distinct regimes or fields. In the near-field ($0 < z/S < 7$), the synthetic jet centerline velocity rises to its peak value as the jet width contracts in the y - z plane and remains fairly constant in extent in the x - z plane (Figs. 6(a) and 6(b)). In the intermediate-field ($7 < z/S < 18$), the centerline velocity falls from its peak at $z/S=7$ to its minimum plotted value near $z/S=18$ as the jet width in the x - z plane increases, surpassing that of the y - z plane at $z/S=15$. Finally, in the far-field ($z/S > 18$), the jet velocity rises to a secondary peak and gradually declines as the jet width stabilizes in both planes. The trends in heat transfer coefficients that are described in the following sections can be rationalized by noting the different behavior in each of the three regimes.

The trend in local Nusselt number produced by a synthetic jet is expected to mirror the Gaussian trend known to exist for steady jet impingement on a flat plate for large orifice-to-plate distances [3]. However, the unique flow characteristics of the synthetic jet produce somewhat different trends in local heat transfer that are not expected to parallel those of a traditional steady jet impingement flow. The earlier discussion of steady jet flow characteristics suggests an optimum orifice-to-plate spacing that maximizes the average heat transfer from the surface. If the synthetic jet is placed in the near-field, the ability of the jet to ingest cooler ambient fluid is restricted by the presence of the heated plate. Furthermore, the jet centerline velocity is low in the near-field, as shown in Fig. 6(b). Both of these factors suggest low heat transfer rates in the near-field. In comparison, the strength of the synthetic jet diminishes in the far-field as reflected by the decrease in jet centerline velocity. As a result, the jet is unable to effectively penetrate the surface boundary layer of the heater and its cooling ability is diminished. At intermediate locations between the near- and far-fields, the jet velocity is maximized and the cooling capacity of the jet is increased.

The results shown in Fig. 12 illustrate the local Nusselt number distribution for the synthetic jet in the three flow regimes. Despite the differences in the jet velocity and vorticity concentrations, the Nusselt number curves illustrate that all three flow regimes produce a Gaussian cooling distribution on the surface. Further, the local Nusselt curves show that the greatest heat transfer rates are achieved at a Reynolds number of approximately 400, which corresponds to a nominal synthetic jet frequency of 300 Hz. This frequency provides efficient coupling between the driver and the synthetic jet cavity (Fig. 4).

When the heated plate is placed in the near-field flow regime, the trends in the local heat transfer rates can be correlated to the velocity distributions shown in Fig. 9(a). At such close orifice-to-plate spacing, the centerline velocity of the jet does not decay significantly, so the stagnation point heat transfer rate is fairly pronounced as shown in Fig. 12(a) ($Z_p/S=3.6$). The local heat transfer rate decreases as the speed of the induced flow near the surface diminishes away from the jet centerline. In the near-field, the variation in the local Nusselt number decreases with jet Reynolds number. The curves clearly show that the most efficient cooling occurs when the jet is driven near the fundamental frequency of the driver and cavity ($Re \approx 400$). At other frequencies, the ineffective coupling of the driver and cavity significantly reduces the centerline velocity and corresponding heat transfer capacity.

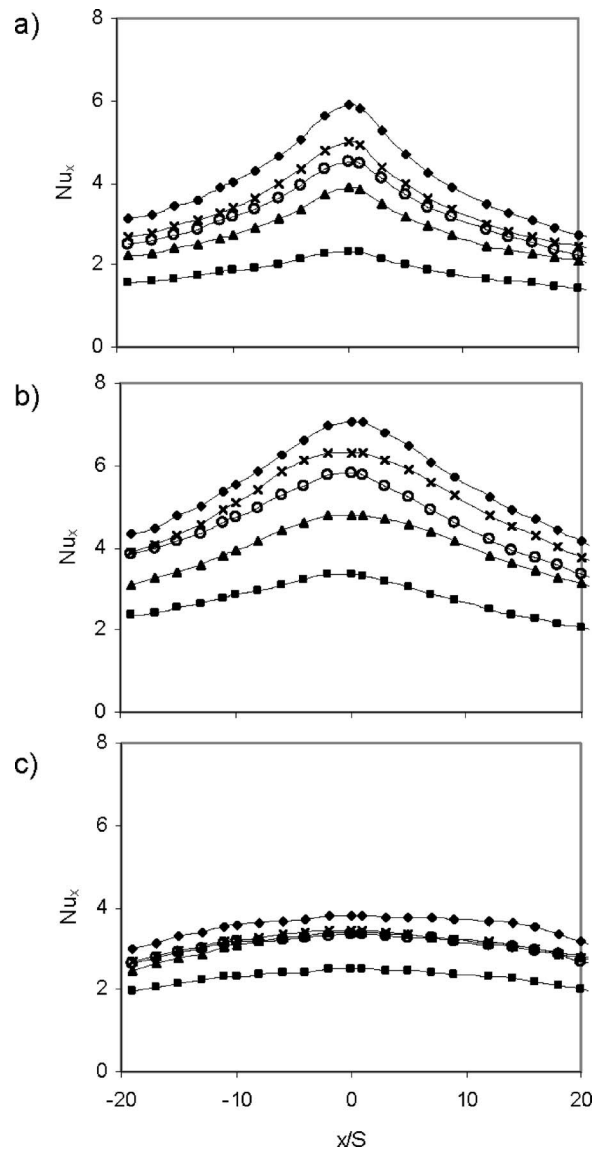


Fig. 12 Spanwise distributions of local time-averaged Nusselt number, $Z_p/S =$ (a) 3.6, (b) 14.5, (c) 22.7. $Re =$ ■ 108, ○ 254, ▲ 309, × 367, and ◆ 396.

In the intermediate-field, stagnation point heat transfer rate increases slightly from its near-field value. Figure 12(b) illustrates the spanwise distribution of local Nusselt number for $Z_p/S=14.5$. The Nusselt numbers are generally larger in value than the near-field case but show a slightly flatter distribution; presumably as a result of increased mixing above the plate (Figs. 9 and 10).

When the heated plate is placed in the far-field regime, local Nusselt number distributions become much flatter and more uniform over the surface of the plate as shown in Fig. 12(c) ($Z_p/S=22.7$). This behavior is expected based on the velocity distribution in the x - z plane (Fig. 11(a)). The stagnation point heat transfer coefficient in the far-field is only about one-half the value it has in the intermediate-field. As before, the maximum Nusselt numbers occur when $Re \approx 400$, although the influence of Reynolds number on local cooling is much less than for the other regimes.

For large distances from the orifice of the jet (far-field), the oscillatory flow of the jet degenerates into a quasi-steady flow with little resemblance to the oscillations that exist at the orifice. Since the thermal time constant of the plate is far greater than the time between flow oscillations, the plate essentially experiences

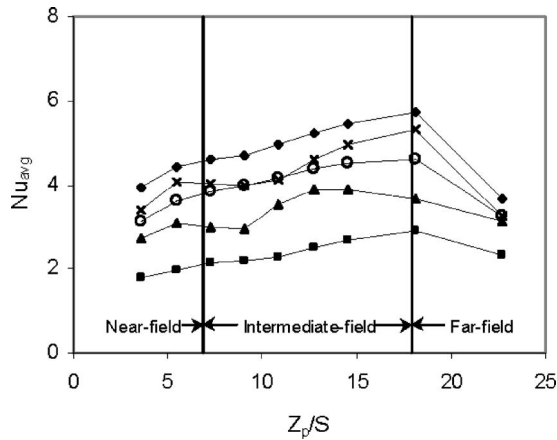


Fig. 13 Variation of the average Nusselt number with orifice-to-plate separation. $Re = \blacksquare 108, \circ 254, \blacktriangle 309, \times 367, \text{ and } \blacklozenge 396$.

steady cooling characterized by the average flow conditions of the synthetic jet, regardless of whether the plate is located in the near-, intermediate-, or far-fields.

Variation of average Nusselt number with jet Reynolds number and orifice-to-plate separation distance is shown in Fig. 13. The data indicate that the average heat transfer rate increases as the location of the plate progresses from the near-field to the intermediate-field and then decreases when the plate moves into the far-field regime. In the near-field, the heated air below the plate is entrained into the synthetic jet, which limits its cooling capability. In comparison, the velocity of the synthetic jet in the far-field is significantly diminished at the point of impact such that the jet is unable to effectively breakdown the thermal boundary layer and cool the heated surface. However, in the intermediate-field, an optimum location exists that produces maximum cooling. The data indicate that the dimensionless separation distance that produces the largest average Nusselt numbers occurs in the range $14 < Z_p/S < 18$ for the conditions of this experiment.

The results in Fig. 14 illustrate the variation of average Nusselt number with synthetic jet frequency at various separation distances. In keeping with jet performance as plotted in Fig. 4, the curves rise to peaks at 300–400 Hz. Again the results reinforce the superior performance of the intermediate-field with peak values at $Z_p/S = 18$ and the overall lowest performance coming in the far-field.

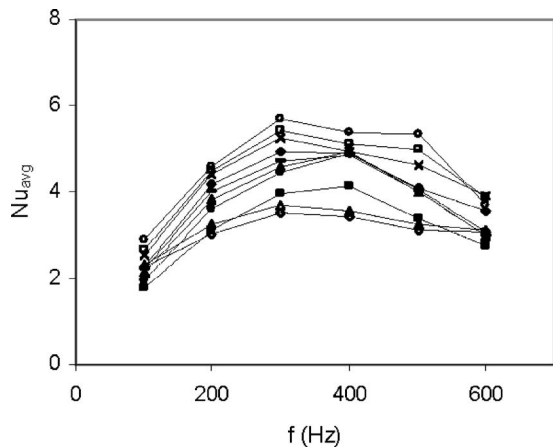


Fig. 14 Variation of the average Nusselt number with synthetic jet frequency. $Z_p/S = \blacksquare 3.6, \bullet 5.4, \blacktriangle 7.3, \text{---} 9.1, \blacklozenge 10.9, \times 12.7, \square 14.5, \circ 18.1, \triangle 22.7, \text{ and } \diamond 45.4$.

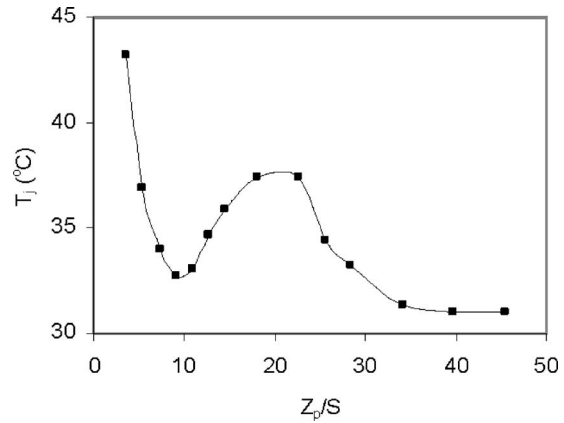


Fig. 15 Variation of air temperature in the synthetic jet actuator cavity, T_j , with orifice-to-plate separation

To this point in the discussion, the heat transfer coefficient of the synthetic jet has been defined in terms of the temperature difference between the plate and ambient air, $(T_p - T_\infty)$. But measurements within the cavity of the jet actuator indicated that the temperature of the impinging jet may be very different from ambient. Therefore it may be more appropriate to define the heat transfer coefficient in terms of the difference between the plate temperature and the jet temperature $(T_p - T_j)$ rather than $(T_p - T_\infty)$. The variation of jet cavity temperature with orifice-to-plate separation distance is shown in Fig. 15. These measurements were performed for a single jet strength and frequency ($Re = 400$ and $f = 300$ Hz).

The great variation witnessed in the jet fluid temperature in Fig. 15 can be attributed to entrainment and recirculation of hot air, as shown in the PIV measurements. At small orifice-to-plate separations, the narrow plate spacing causes uniform entrainment of fluid adjacent to the heated surface. Also, a counter-rotating recirculation vortex-pair dominates the minor axis but dwindles to only small, local zones by $Z_p/S = 10$ (Fig. 9(a)). The average flow here is highly three-dimensional, where the only outlet for impinging flow on the major axis (y - z plane) is via out-of-plane turning to the minor axis (x - z plane). This three-dimensional “pumping” via out-of-plane turning causes the jet temperature to quickly decrease once the minor-axis recirculation diminishes, by $Z_p/S = 10$ thus explaining the observed initial decreasing trend in jet fluid temperature. But then from $Z_p/S = 10$ to about 20, the jet fluid temperature increases as a result of recirculation on the major axis.

PIV measurements shown in Figs. 9–11 explain this temperature increase due to recirculation. The two small, local recirculation vortices observed near the heater plate on the major axis at $Z_p/S = 10$ are much larger by $Z_p/S = 15$. This increase in size causes a great deal of entrained jet fluid to originate near the heater. This trend increases in scale with plate spacing, reaching a recirculation scale that is the full height of the plate spacing by $Z_p/S = 20$. Hence, a local peak exists in the jet fluid temperature at this elevation. As orifice-to-plate spacing approaches $Z_p/S = 30$, the major-axis recirculation cannot maintain strength and ambient fluid becomes the predominant fluid source for the jet. This scenario is similar to a free-jet with little relation between the intake of the jet and exhaust of the impingement.

The corresponding variation of average Nusselt number with separation distance for the case of $Re = 400$ and $f = 300$ Hz is shown in Fig. 16. The figure provides two curves; one calculated for the temperature difference of $T_p - T_\infty$ and the other based on $T_p - T_j$. The results indicate an approximately 20% increase in average Nusselt number for the data range with greater gains in the regions of higher jet fluid temperature.

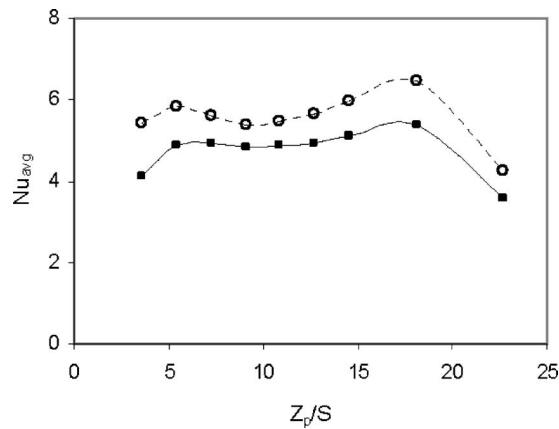


Fig. 16 Comparison of the average Nusselt number based on ambient and cavity temperatures: ■ $(T_p - T_\infty)$, ○ $(T_p - T_j)$

The thermal performance of synthetic jets cannot easily be compared to that of a steady jet because of the dearth of correlations that cover similar ranges of Reynolds numbers. The majority of papers that present heat transfer measurements for steady jets provide correlations for jet Reynolds number on the order of $10^3 - 10^6$, although a recent paper reporting on an analytical study of unsteady jets includes results for Reynolds numbers as low as 300 [18]. Nonetheless, the Reynolds numbers for the present study on the performance of synthetic jets are always less than 500. This low Reynolds number would imply laminar flow if the jet were steady. However, the flow structure in the air downstream of the orifice is fully turbulent, as demonstrated in Figs. 5(a) and 5(b). Therefore, heat transfer rates from synthetic jets incident on a heated surface can be expected to be greater than from a steady jet with an equivalent Reynolds number.

While synthetic jets can provide local heat transfer coefficients that exceed values produced by steady jets with equivalent Reynolds numbers, they also have other advantages over traditional cooling techniques that are used to cool small microelectronic packages. Synthetic jets require no external plumbing or ducting to transport cool air to the heated surface. They require very low levels of power that are typically less than those required to operate small fans or compressors used to produce steady pressurized jets of air. Furthermore, synthetic jets of air do not utilize confined reservoirs, such as those required when liquid jets are used for high heat transfer applications. If high heat fluxes are required, phase change of dielectric liquids can be considered as an option. For example, several investigations have considered both an experimental and analytical approach [19,20] to quantify the heat transfer from a microtextured surface which is cooled by a steady flow of small liquid droplets generated by micromachined nozzles.

5 Conclusions

The flow field induced by a synthetic jet that is produced by a time-harmonically driven membrane is uniquely suitable for small-scale cooling applications as evidenced by distributions of velocity and vorticity that reveal the interactions between the jet and the heated surface. In the present work, a rectangular synthetic air jet first proceeds though an axis switching phase near the slot; then further from the slot, the flow field becomes more fully developed. This flow behavior creates three distinct flow regimes in the near-, intermediate-, and far-fields. Variations in the flow pattern in the three regimes suggest that there is an optimal location for maximum heat transfer from a plate that is cooled by synthetic jets. Flow from the synthetic jet is fully turbulent even at Reynolds numbers far below the critical Reynolds number for

steady jets. The fully turbulent nature of the jet at low velocities can be exploited when small-scale heat transfer is desired.

The present experiments identified optimum jet-to-plate spacings that lead to maximum local Nusselt numbers. Regardless of the separation distance between the jet and heated surface, the trend in the local Nusselt number is Gaussian with the results tending to flatten as the surface is moved farther from the orifice of the synthetic jet. In the near-field the synthetic jet has a tendency to ingest heated air from the thermal boundary layer and the jet velocity is relatively low, causing relatively low heat transfer rates. In the far-field the diminished jet velocity at the surface is unable to effectively penetrate the boundary layer which also leads to low heat transfer rates. For separation distances that place the synthetic jet in the intermediate-flow regime, the increased jet velocity coupled with a more effective mixing with ambient air produced improved local heat transfer rates. Average Nusselt numbers were maximized when the dimensionless plate spacing was between 14 and 18. Furthermore, heat transfer rates were maximized when the jet frequency was close to the resonance frequency of the driver cavity.

Nomenclature

A	= surface area
b_x, b_y	= dimensionless jet width in the x and y directions, respectively
f	= frequency of synthetic jet
h_0	= stagnation point heat transfer coefficient
h_x	= local heat transfer coefficient
k	= thermal conductivity
L	= one-half heated plate length in x direction
Nu_x	= local Nusselt number ($h_x S/k$)
Nu_{avg}	= average Nusselt number ($h_{avg} S/k$)
Nu_0	= stagnation point Nusselt number
P	= heater perimeter
Pr	= Prandtl number ($Pr = \nu/\alpha$)
q_{conv}	= heat convected from the top surface
Ra	= Rayleigh number ($Ra = g\beta\Delta T L_C^3/\nu\alpha$)
Re	= synthetic jet Reynolds number ($Re = U_0 S/\nu$)
S	= width of slot in orifice plate
t	= time
T_∞	= ambient air temperature
T_j	= synthetic jet actuator cavity temperature
$T_p(x)$	= local plate temperature
u	= time-averaged streamwise jet velocity
$u_{cl}(z)$	= time-averaged streamwise jet velocity along streamwise centerline (z -axis)
$u_o(t)$	= instantaneous streamwise synthetic jet velocity in the plane of the orifice
U_0	= average jet discharge velocity in the plane of the orifice
W	= width of heated plate
x	= coordinate along minor axis of jet
y	= coordinate along major axis of jet
z	= coordinate perpendicular to plane of jet
Z_p	= vertical distance between orifice and heated plate
Z_p/S	= dimensionless orifice-to-plate separation distance

Greek Symbols

α	= thermal diffusivity
β	= volumetric thermal expansion coefficient
$(\Delta T)_x$	= local temperature difference
ν	= kinematic viscosity

ζ_x, ζ_y = spanwise vorticity concentrations in the y - z and x - z planes, respectively
 τ = period of the synthetic jet

References

- [1] Martin, H., 1977, "Heat and Mass Transfer Between Impinging Gas Jets and Solid Surfaces," *Advances in Heat Transfer*, Academic Press, New York, Vol. 13, pp. 1–60.
- [2] Jambunathan, K., Lai, E., Moss, M. A., and Button, B. L., 1992, "Review of Heat Transfer Data for Single Circular Jet Impingement," *Int. J. Heat Fluid Flow*, **13**, pp. 106–115.
- [3] Gardon, R., and Cobonpue, J., 1961, "Heat Transfer Between a Flat Plate and Jets of Air Impinging on It," *International Developments in Heat Transfer*, ASME, New York, pp. 454–460.
- [4] Hrycak, P., 1983, "Heat Transfer From Round Impinging Jets to a Flat Plate," *Int. J. Heat Mass Transfer*, **26**(12), pp. 1857–1865.
- [5] Gardon, R., and Akfirat, J. C., 1965, "The Role of Turbulence in Determining the Heat Transfer Characteristics of Impinging Jets," *Int. J. Heat Mass Transfer*, **8**, pp. 1261–1272.
- [6] Hollworth, B. R., and Gero, L. R., 1985, "Entrainment Effects on Impinging Heat Transfer: Part II—Local Heat Transfer Measurements," *ASME J. Heat Transfer*, **107**, pp. 910–915.
- [7] Nevins, R. G., and Ball, H. D., 1961, "Heat Transfer Between a Flat Plate and a Pulsating Impinging Jet," *Proceedings of the 1961 National Heat Transfer Conference*, Vol. 60, pp. 510–516.
- [8] Zumbrunnen, D. A., and Aziz, M., 1993, "Convective Heat Transfer Enhancement Due to Intermittency in an Impinging Jet," *ASME J. Heat Transfer*, **115**, pp. 91–98.
- [9] Mladin, E. C., and Zumbrunnen, D. A., 1994, "Nonlinear Dynamics of Laminar Boundary Layers in Pulsatile Stagnation Flows," *J. Thermophys. Heat Transfer*, **8**(3), pp. 514–523.
- [10] Sheriff, H. S., and Zumbrunnen, D. A., 1999, "Local and Instantaneous Heat Transfer Characteristics of Arrays of Pulsating Jets," *ASME J. Heat Transfer*, **121**, pp. 341–348.
- [11] Smith, B. L., and Glezer, A., 1998, "The Formation and Evolution of Synthetic Jets," *Phys. Fluids*, **10**(9), pp. 2281–2297.
- [12] Thompson, M. R., and Glezer, A., "Cooling of Multi-Chip Modules by Synthetic Jet Impingement," SEMICON West 95, Packaging Technologies, San Francisco, CA, pp. 75–178.
- [13] Gillespie, M. B., 1998, "Local Convective Heat Transfer from Heated Flat Plates Using Synthetic Air Jets," M.S. thesis, G. W. Woodruff School of Mechanical Engineering, Georgia Institute of Technology, Atlanta, GA.
- [14] Wiltse, J. M., and Glezer, A., 1993, "Manipulation of Free Shear Flows Using Piezoelectric Actuators," *J. Fluid Mech.*, **249**, pp. 261–85.
- [15] Ho, C.-M., and Gutmark, E., 1987, "Vortex Induction and Mass Entrainment in a Small-Aspect-Ratio Elliptic Jet," *J. Fluid Mech.*, **179**, pp. 383–405.
- [16] Beltaos, S., 1976, "Oblique Impingement of Circular Turbulent Jets," *J. Hydraul. Res.*, **14**(1), pp. 17–36.
- [17] Gutmark, E., and Wagnanski, I., 1975, "The Planar Turbulent Jet," *J. Fluid Mech.*, **73**, pp. 465–495.
- [18] Chung, Y. M., and Luo, K. H., 2002, "Unsteady Heat Transfer Analysis of an Impinging Jet," *ASME J. Heat Transfer*, **124**, pp. 1039–1048.
- [19] Amon, C. H., Yao, S.-C., Wu, C.-F., and Hsieh, C.-C., 2005, "Microelectromechanical System-Based Evaporative Thermal Management of High Heat Flux Electronics," *ASME J. Heat Transfer*, **127**, pp. 66–75.
- [20] Narumanchi, S. V. J., Amon, C. H., and Murthy, J. Y., 2003, "Influence of Pulsating Submerged Liquid Jets on Chip-Level Thermal Phenomena," *ASME J. Electron. Packag.*, **125**, pp. 354–361.

Self-Preserving Mixing Properties of Steady Round Buoyant Turbulent Plumes in Uniform Crossflows

F. J. Diez

Department of Mechanical and Aerospace
Engineering,
Rutgers, The State University of New Jersey,
Piscataway, NJ 08854-8058
e-mail: diez@rutgers.edu

L. P. Bernal

G. M. Faeth

Department of Aerospace Engineering,
The University of Michigan,
Ann Arbor, MI 48109-2140

The self-preserving mixing properties of steady round buoyant turbulent plumes in uniform crossflows were investigated experimentally. The experiments involved salt water sources injected into fresh water crossflows within the windowed test section of a water channel. Mean and fluctuating concentrations of source fluid were measured over cross sections of the flow using planar-laser-induced fluorescence which involved seeding the source fluid with Rhodamine 6G dye and adding small concentrations of ethanol to the crossflowing fluid in order to match the refractive indices of the source flow and the crossflow. The self-preserving penetration properties of the flow were correlated successfully based on the scaling analysis of Diez, Bernal, and Faeth (2003, ASME J. Heat Transfer, 125, pp. 1046–1057) whereas the self-preserving structure properties of the flow were correlated successfully based on the scaling analysis of Fischer et al. (1979, Mixing in Inland and Coastal Waters, Academic Press, New York, pp. 315–389); both approaches involved assumptions of no-slip convection in the cross stream (horizontal) direction (parallel to the crossflow) and a self-preserving line thermal having a conserved source specific buoyancy flux per unit length that moves in the streamwise (vertical) direction (parallel to the direction of both the initial source flow and the gravity vector). The resulting self-preserving structure consisted of two counter-rotating vortices having their axes nearly aligned with the crossflow direction that move away from the source in the streamwise (vertical) direction due to the action of buoyancy. Present measurements extended up to 202 and 620 source diameters from the source in the streamwise and cross stream directions, respectively. The onset of self-preserving behavior required that the axes of the counter-rotating vortex system be nearly aligned with the crossflow direction. This alignment, in turn, was a strong function of the source/crossflow velocity ratio, u_o/v_∞ . The net result was that the onset of self-preserving behavior was observed at streamwise distances of 10–20 source diameters from the source for $u_o/v_\infty=4$ (the smallest value of u_o/v_∞ considered), increasing to streamwise distances of 160–170 source diameters from the source for $u_o/v_\infty=100$ (the largest value of u_o/v_∞ considered). Finally, the counter-rotating vortex system was responsible for substantial increases in the rate of mixing of the source fluid with the ambient fluid compared to axisymmetric round buoyant turbulent plumes in still environments, e.g., transverse dimensions in the presence of the self-preserving counter-rotating vortex system were 2–3 times larger than the transverse dimensions of self-preserving axisymmetric plumes at similar streamwise distances from the source. [DOI: 10.1115/1.2345424]

Keywords: heat transfer, buoyancy, scaling, dispersion, turbulence

Introduction

Recent studies of the temporal and steady penetration properties of round turbulent puffs, thermals, starting and steady jets, and starting and steady plumes in both still fluids and uniform unstratified crossflows [1–4], and the mixing properties of steady round nonbuoyant turbulent jets in uniform crossflows [5], were extended to consider the mixing properties of steady round buoyant turbulent plumes in uniform unstratified crossflows (denoted “steady turbulent plumes in crossflows” in the following). Interest in steady turbulent plumes in crossflows is motivated by practical applications to the dispersion of harmful releases of heat and substances into atmospheric crosswinds. Similar to the study of the mixing properties of steady turbulent jets in crossflows due to

Diez et al. [5], the present study emphasized flow properties far from the source, where effects of source disturbances are lost, where the flows are largely controlled by their conserved properties, where flow properties approximate self-preserving turbulent flow behavior, and where appropriately-scaled flow properties became independent of the distance from the source. This region is of particular interest because the properties of self-preserving turbulent flows provide a compact presentation of measurements that substantially simplifies the interpretation of flow behavior.

In order to fix ideas, a visualization of a typical steady turbulent plume in crossflow appears in Fig. 1. This flow actually involves the injection of dye-containing salt water normal (the more dense salt water flowing vertically downward) into a fresh water crossflow (flowing from left to right) in a water channel facility. Following past practice [3,4], however, the vertical direction has been inverted to show the flow as an upwardly injected turbulent plume with the source density smaller than the ambient density because most individuals are more familiar with positively buoyant up-

Contributed by the Heat Transfer Division of ASME for publication in the JOURNAL OF HEAT TRANSFER. Manuscript received March 31, 2005; final manuscript received July 7, 2006. Review conducted by Karen Thole.

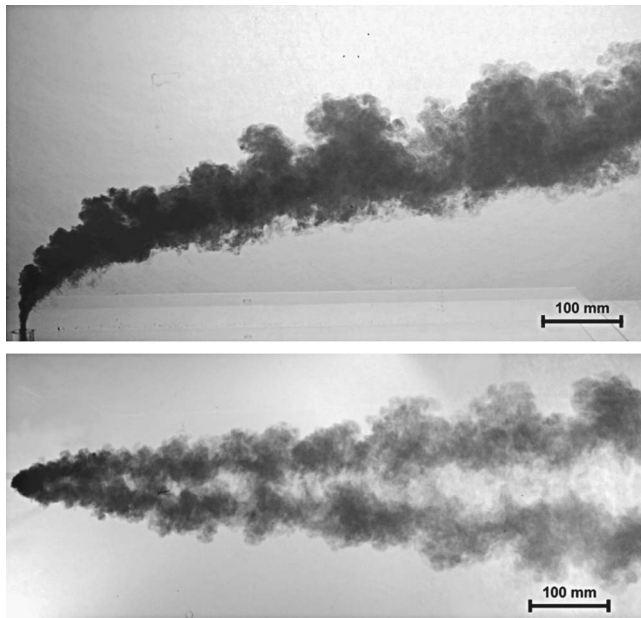


Fig. 1 Visualization of the penetration properties of a steady turbulent plume in a uniform crossflow ($d=6.4$ mm, $Re_o=5000$, $\rho_o/\rho_\infty=1.150$, $Fr_o=223$, $u_o/v_\infty=7$). The upper figure is a side view; the lower figure is a top view.

wardly flowing plumes than with negatively buoyant downwardly flowing plumes. This practice will be adopted throughout the present article. The images appearing in Fig. 1 consist of side and top views of a typical turbulent plume in crossflow obtained when steady flow conditions have been reached. The length scales that appear on the images are appropriate for streamwise (vertical, or in the same direction as the plume source flow) and cross stream (horizontal, or in the same direction as the ambient crossflow) directions. It will be shown later that the streamwise velocities of steady turbulent plumes in crossflows progressively decrease with increasing streamwise distance from the source so that the streamwise velocity eventually becomes small and the trajectory of steady turbulent plumes in crossflows become nearly horizontal far from the source where self-preserving behavior is approached. When this condition is reached, the streamwise penetration of the flow approximates a two-dimensional horizontal line thermal in a still fluid. Then the streamwise motion of the line thermal, retarded along its sides in the streamwise direction by the uniform ambient crossflow, naturally leads to the flow becoming two nearly horizontal counter-rotating vortices whose axes are aligned along the axis of the plume as a whole (and thus are nearly horizontal as well). Evidence for this behavior is provided by the top view of the flow which is the lower image in Fig. 1, where the darker regions associated with the two vortices are separated by a significantly lighter region dominated by the presence of dye-free ambient fluid that is entrained by the vortex system along its plane of symmetry. Another interesting feature of the visualization appearing in Fig. 1 is that turbulent distortions of the lower surface of the flow (the side facing the source) are smoothed out because this region is stable to buoyant disturbances whereas the turbulent distortions of the upper surface of the flow (the side facing away from the source) are enhanced because this region is unstable to buoyant disturbances. Notably, corresponding visualizations of steady turbulent jets in crossflow do not exhibit this behavior but instead exhibit similar degrees of distortion on the lower and upper surfaces (the sides toward and away from the source) of the flow because mechanisms of buoyant stability and instability are absent in this case, see Diez et al. [5]. In order to develop the objectives of the present investigation, earlier studies of turbulent plumes will be discussed next.

The self-preserving properties of turbulent plumes in still fluids have received significant attention in the past, typical reviews and studies of these flows are presented by Rouse et al. [6], Morton et al. [7], Morton [8], Turner [9], Tennekes and Lumley [10], Turner [11], Hinze [12], Seban and Behnia [13], Yih [14], George et al. [15], Chen and Chen [16], Yih and Wu [17], List [18], Papanicolaou and List [19], Papantoniou and List [20], Peterson and Bayazitoglu [21], Dai et al. [22–24], Dai and Faeth [25], and references cited therein. These studies sought the self-preserving scaling rules that describe both the temporal development and the steady properties of turbulent plumes in still fluids. The most recent studies of steady turbulent plumes in still fluids of Dai and co-workers [22–25] show these flows became turbulent within five source diameters from the source whereas self-preserving behavior of flow mixing (structure) properties is only observed at streamwise distances farther from the source than previously thought (e.g., at streamwise distances greater than roughly 80–100 source diameters from the source). On the other hand, recent studies of the penetration properties of steady turbulent plumes in still fluids due to Diez et al. [3,4] suggest that self-preserving behavior for penetration properties is observed much sooner than for structure properties (e.g., at streamwise distances greater than roughly 40–50 source diameters from the source).

Most practical releases of turbulent plumes are exposed to crossflow; therefore, there have been a number of attempts to extend the results just discussed for turbulent plumes in still fluids to corresponding turbulent plumes in crossflows, see Diez et al. [3,4], Fischer et al. [26], Lutti and Brzustowski [27], Andreopoulos [28], Alton et al. [29], Baum et al. [30], Hasselbrink and Mungal [31], Huq and Stewart [32], and references cited therein. These studies generally have shown that motion in the crossflow direction satisfies the no-slip convection approximation and that the deflection of the plume toward the crossflow direction results in the development of a counter-rotating vortex system over the cross section of the flow, as discussed in connection with Fig. 1. Measurements of the mixing structure of these flows, however, generally have been limited to the region near the source where the flow undergoes most of its deflection toward the cross-stream direction. Studies of the potential self-preserving behavior of this flow show that the decay of streamwise velocities with increasing distance from the source is relatively rapid so that the flow eventually becomes nearly aligned with the horizontal direction for all source/crossflow velocity ratios, u_o/v_∞ , i.e., the general appearance of the flow illustrated in Fig. 1 is typical of flows of this type. Thus, self-preserving behavior for these flows eventually involves no-slip convection in the crossflow direction combined with the motion of a line thermal in the streamwise direction, see Diez et al. [3,4] and Fischer et al. [26]. Relationships for the self-preserving transient and steady penetration properties of these flows have been confirmed by measurements, obtaining results similar to corresponding flows in still environments. In particular, the flows become turbulent within five source streamwise diameters from the source and become self-preserving at streamwise distances greater than 40–50 source diameters from the source for $u_o/v_\infty < 35$ [3,4]. On the other hand, the rates of mixing and the structure properties of these flows at self-preserving conditions have not yet received any attention.

Based on the previous observations, the objectives of the present investigation were to extend past work concerning the self-preserving penetration properties of steady turbulent plumes in crossflows [3,4], in order to develop an improved understanding of their self-preserving mixing structure properties, as follows.

1. Measure the self-preserving mixing structure of these flows, including the trajectories of the axes of the counter-rotating vortices, and the distributions of the mean and rms fluctuations of source fluid concentrations within the counter-rotating vortex system, for steady flow and for source and crossflow conditions typical of practical applications.
2. Exploit the new measurements of these flows in order to

evaluate the effectiveness of self-preserving scaling relationships developed by Diez et al. [3,4] for penetration properties (specifically for the penetration properties of the vortex axes that have not been considered before) and by Fischer et al. [26] for flow mixing structure properties, and to determine the empirical parameters associated with the various scaling relationships.

The present description of the research begins with a discussion of experimental methods and the self-preserving scaling properties of the flows; measured scaling results are then described, considering flow penetration properties and flow mixing structure properties, in turn.

Experimental Methods

Test Apparatus. The present experiments adopted methods analogous to the salt/fresh-water modeling experiments for buoyant turbulent flows suggested by Steckler et al. [33]. Somewhat different source and ambient fluids were required, however, for measurements of source flow penetration properties by visualization of a dye-containing source fluid and measurements of source flow mixing structure properties by planar-laser-induced-fluorescence (PLIF) records of a dye-containing source fluid because the latter measurements required matching the indices of refraction of the source and ambient fluids in order to avoid scattering the laser beam away from the buoyant flow. Thus, the source and ambient fluids for the two types of experiments differed as follows: a salt (NaCl) water source containing a red vegetable dye was injected into an unstratified uniform fresh water crossflow for flow visualization measurements of source flow penetration properties, and a salt (sodium phosphate, KH_2PO_4) water source containing Rhodamine 6G dye was injected into an unstratified uniform ethyl-alcohol/water crossflow for matched refractive index PLIF measurements of source flow mixing (structure) properties. The unstratified and uniform crossflow was produced by a water channel facility. The test section of the water channel had cross-section dimensions of 610×760 mm and a length of 2440 mm. The sides and bottom of the test section were constructed of 20 mm thick acrylic and float glass panels, respectively, to provide optical access. The crossflow in the channel was driven by a propeller pump to yield crossflow velocities of 40–300 mm/s. The properties of the crossflow were characterized using a pure water flow as described by Diez et al. [5]. A contraction of ten-to-one (involving a fifth-order polynomial having a zero slope and curvature at the entrance and the exit), flow straighteners, screens, etc., of the water channel combined to yield a flow nonuniformity of less than 1.5% and turbulence intensity levels less than 1%, in the test section.

The source flows had a larger density than the crossflows for present conditions and were injected vertically downward into the channel flow to obtain steady turbulent plumes in crossflows. The source flows passed through smooth round injector tubes having inside diameters of 2.1, 3.2, and 6.4 mm. The source injector tubes had length/diameter ratios of 200, 100, and 50, respectively, to help insure fully developed turbulent pipe flow at the source exit for sufficiently large source Reynolds numbers, as discussed by Wu et al. [34]. The source injector tubes were mounted vertically and discharged roughly 25 mm below the liquid surface. The source injector tubes passed through a plane horizontal Plexiglas plate (508×914 mm in plan dimension $\times 12$ mm thick) with a tight fit. The source injector tube exits were mounted flush with the lower surface of the Plexiglas plate in order to provide well-defined entrainment conditions at the source exit. The source liquid was supplied to the tubes using either a syringe pump (Harvard Apparatus, PHD2000, model 70-2000, with four 150 cm^3 syringes having volumetric accuracies of $\pm 1\%$ mounted in parallel) for small flow rates, or a peristaltic pump (Masterflex L/S Digi-Staltic Dispersion, model 72310-0) with two flow dampers for large flow rates. The pumps were calibrated by collecting liquid for timed intervals.

Penetration Measurements. Observations of dye-containing source liquids were obtained using charge coupled device video cameras similar to earlier studies of the penetration properties of starting and steady turbulent plumes in still and crossflowing fluids [3,4]. A portion of these results for steady turbulent plumes in crossflows will be considered here for completeness. Experimental methods for these measurements are described by Diez et al. [3,4] which should be considered for these details. Experimental uncertainties (95% confidence) of the measurements from the video records were as follows: less than 8% for mean maximum streamwise and cross stream penetration distances and less than 15% for mean maximum radial and half-width penetration distances. Experimental uncertainties of all penetration distances were largely governed by sampling errors due to the irregular turbulent boundaries of the present turbulent flows but also include fundamental accuracies of distance calibrations and measurements. Finally, the PLIF measurements of flow structure were used to find the streamwise distance to the center of the counter-rotating vortex system and the horizontal distance between the axes of the counter-rotating vortices; the experimental uncertainties (95% confidence) of these measurements were less than 8% and 15%, respectively.

Structure Measurements. The PLIF arrangement was similar to the arrangement used by Diez et al. [5] for studies of the structure of steady turbulent jets in crossflows, except for features required to match the refractive indices of the source and crossflowing fluids discussed by Ferrier et al. [35], Alahyari and Longmire [36], and Daviero et al. [37]. The arrangement consisted of a laser, optics for scanning the laser beam across the image area, and a digital camera for recording the image. Rhodamine 6G dye at a concentration of $5.0 \times 10^{-6} \text{ mol}/\ell$ was used for the PLIF signals in the source liquid, see Ferrier et al. [35] for a discussion of the properties of this dye. An argon-ion laser (Coherent Innova 90-4) operated in the single-line mode at 514.5 nm with an optical power of 3200 mW and a beam diameter of 1.5 mm (at the e^{-2} intensity locations) was used to excite the fluorescence.

A mirror located roughly 1000 mm downstream from the imaged cross section of the flow allowed the camera to view the PLIF image. The camera was a Redlakes Inc., model Mega Plus ES 1020. This camera has a 1004×1004 pixel array with a 7.4×7.4 mm active sensor area. The intensity resolution of the pixels was 10-bit which provided 1024 gray levels of the image. A PC-Cam Link frame grabber from Coreco Imaging transferred the camera images to a computer for processing and storage. The images were corrected for vignetting, sweep geometry, attenuation (by water, Rhodamine 6G, sodium phosphate, and ethanol) and background effects as discussed by Ferrier et al. [35]. Finally, the use of potassium phosphate (KH_2PO_4) to increase the density of the source fluid along with an appropriate concentration of ethyl alcohol in the crossflowing water which decreased its density, matched the refractive indices of the source and ambient fluid as discussed by Ferrier et al. [35], Alahyari and Longmire [36], and Daviero et al. [37]. Close control of the temperature differences between the source and ambient fluid, however, was also required for proper matching of refractive indices; this was done using a heater for the source fluid that limited temperature differences between the source and ambient fluids to less than 0.10 K.

The mean and fluctuating concentrations of source fluid were obtained over cross sections of the flow by averaging 4000 images. The experimental uncertainties (95% confidence) were less than 7% and 15% for mean and root-mean-square (rms) fluctuating concentrations, respectively, at each point in the flow. These uncertainties were largely governed by sampling errors due to the finite number of measurements of concentration properties that were averaged at each point in the flow.

Test Conditions. Test conditions for the present experiments considering steady turbulent plumes in crossflow are summarized in Table 1. Due to the modification of source and crossflow prop-

Table 1 Summary of test conditions for steady round buoyant turbulent plumes in uniform crossflows^a

Experiment	Structure properties ^b	Penetration properties ^c
Source fluid	KH ₂ PO ₄ and water	Sodium chloride (NaCl) and water
Crossflowing fluid	CH ₃ CH ₂ OH and water	Water
Source mass solute (% by wt.)	3.6% KH ₂ PO ₄	10% and 20% NaCl
Crossflowing mass solute (% by wt.)	6.6% CH ₃ CH ₂ OH	–
Source dye	Rhodamine 6G	–
Source dye conc. (μ M)	5.0	–
Source fluid density (kg/m ³)	1024	1070 and 1150
Crossflowing fluid density (kg/m ³)	987	998
Index of refraction of source fluid	1.3372	–
Index of refraction of ambient fluid	1.3372	–
Source fluid kinematic viscosity (mm ² /s)	1.05	1.11 and 1.36
Crossflowing fluid kinematic viscosity (mm ² /s)	1.33	1.0
Source diameter (mm)	2.1, 3.2, and 6.4	3.2 and 6.4
Source passage length, L/d	200, 100, and 50	100 and 50
Source flow rate (cm ³ /s)	13–40	7–40
Source Froude number, $(\rho_o u_o^2 / (gd\Delta\rho))^{1/2}$	26–211	6–100
Source Reynolds number, $u_o d / \nu_o$	5000–15,000	2500–15,000
Source/crossflow fluid density ratio, ρ_o / ρ_∞	1.038	1.073 and 1.150
Source/crossflow fluid velocity ratio, u_o / v_∞	19–96	4–26
Streamwise (vertical) penetration distance, $(x_p - x_o) / d$	0–202	0–120
Cross stream (horizontal) penetration distance, $(y_p - y_o) / d$	0–380	0–620

^aPlumes injected vertically downward into uniform crossflows having a 610×760 mm cross section at an ambient pressure and temperature of 99.0±0.5 kPa and 294.05±0.10 K.

^bPotassium-phosphate/water plumes injected into uniform ethanol/water crossflows.

^cSodium-chloride/water plumes injected into uniform fresh water crossflows.

erties in order to match refractive indices for the PLIF measurements, test conditions are summarized separately in Table 1 for the flow penetration and the flow structure measurements. Overall test conditions were as follows: source diameters of 2.1, 3.2, and 6.4 mm; corresponding source passage length/diameter ratios of 200, 100, and 50; source/ambient density ratios of 1.038, 1.073, and 1.150; source/crossflow velocity ratios of 4–96; source Reynolds numbers of 2500–15,000; source Froude numbers of 6–211; streamwise (vertical) penetration distances of 0–202 source diameters; and cross stream (horizontal) penetration distances of 0–620 source diameters.

Scaling Considerations

Conditions for Self-Preservation. The present discussion of scaling for steady turbulent plumes in crossflows addresses three aspects of scaling, in turn: (1) conditions required for self-preservation, (2) self-preserving penetration properties, and (3) self-preserving structure properties. The discussion is limited to the behavior of steady turbulent plumes in crossflows, see Diez et al. [3,4] for consideration of the penetration properties of starting plumes in still and crossflowing fluids.

A parameter that is frequently used to estimate when steady turbulent unconfined flows reach self-preserving behavior is the distance from the effective (virtual) origin of the flow normalized by the source diameter, $(x - x_{os}) / d$, taken to be in streamwise (vertical) direction (parallel to the source flow) for present conditions, where the subscript *os* is used to denote conditions at the virtual origin for a steady plume. This normalized distance is a measure of conditions where distributions of flow properties appropriate for the often confined conditions of a source have adjusted to reach distributions appropriate for an unconfined flow. The value of $(x - x_{os}) / d$ needed for self-preserving behavior depends on the nature of the flow, the properties of the source, and the property for which self-preserving behavior is sought. For example, results for steady turbulent plumes in still fluids suggest that values of $(x - x_{os}) / d$ greater than 40–50 source diameters are needed in order for flow penetration properties to reach self-preserving behavior, whereas values of $(x - x_{os}) / d$ greater than 80–100 are needed

for the structure of flow concentration properties to reach self-preserving behavior based on the observations of Dai [22]. Measurements of steady turbulent jets in still fluids also indicate that the L/d of the source passage, as well as the Reynolds number of the flow through the passage, can have a profound effect on transition to turbulence and, accordingly, on the conditions required for self-preserving behavior to be observed [34]; it is probable that similar behavior would be observed for steady round turbulent buoyant plumes in still fluids. Finally, the crossflow was found to have a strong effect on the conditions required for onset of self-preserving behavior during the present investigation; this effect, and the corresponding flow regime map that identifies conditions required for self-preserving flow, will be discussed subsequently.

Penetration Properties. Scaling relationships for the penetration properties of starting and steady turbulent plumes in crossflows were developed and evaluated successfully based on measurements of dye-containing source liquids as discussed by Diez et al. [4]. The present study extends these results to consider the penetration properties of the axes of the vortices of the counter-rotating vortex system observed for steady turbulent plumes in crossflows based on measurements of flow structure properties using PLIF. Thus, scaling relationships for the penetration properties of the steady turbulent plumes in crossflows during the present investigation are briefly reviewed in the following.

The development of scaling relationships for the penetration (geometrical) properties of steady turbulent plumes in crossflows is discussed by Diez et al. [4]. The configuration of the present steady turbulent plumes in crossflows considered in the following is sketched in Fig. 2. The source flow enters from a round passage normal to the crossflow and flows into an environment having a uniform crossflow velocity. As discussed by Diez et al. [4], the streamwise velocity decays rapidly with increasing streamwise distance for this flow; for example, the streamwise velocity is proportional to $(t - t_{os})^{-1/3}$ when the crossflow velocity is large compared to the streamwise velocity and the steady plume is nearly horizontal, as the self-preserving region is approached far from the source [4]. In addition, the flow approximates no-slip convection in the cross stream direction [3,4]. This behavior im-

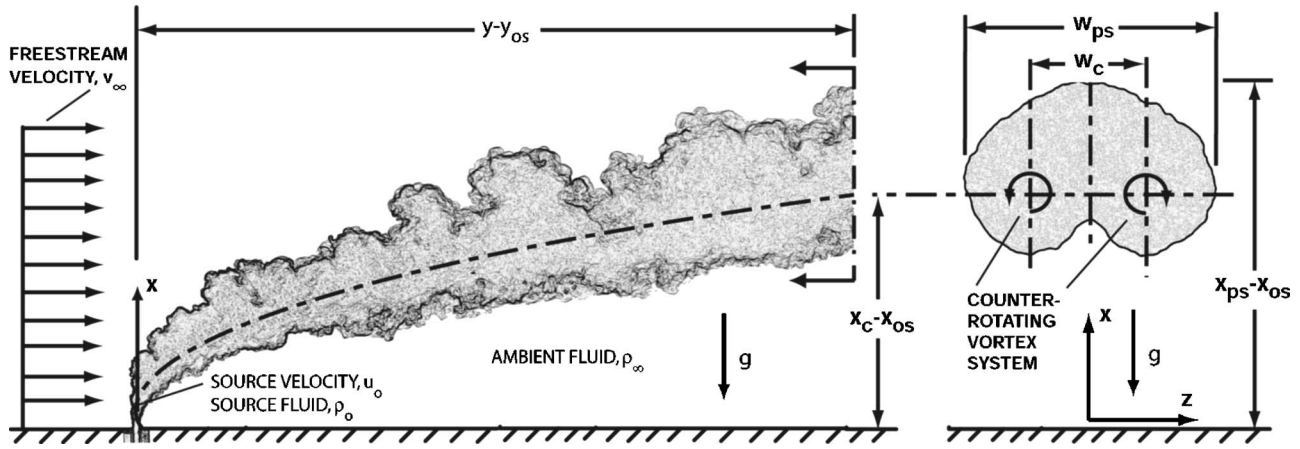


Fig. 2 Sketches of a steady turbulent plume in a uniform crossflow

plies that the plume eventually is deflected so that its axis is nearly aligned with the cross stream direction. At this condition, the initial streamwise source specific buoyancy flux continues to be conserved so that the flow approximates the behavior of a line thermal. Then the streamwise source specific buoyancy flux per unit length of the line thermal causes a counter-rotating pair of vortices to form, leading to a somewhat flattened shape of the flow cross section. The geometrical properties of interest for this flow include the trajectory of the axis of the vortex system, $(x_c - x_{os})/d$, as a function of $(y - y_{os})/d$, after allowing for virtual origins to extend the self-preserving region as near to the source as possible, as well as the separation between the axes of the two counter-rotating vortices, w_c . In addition, the steady penetration properties of the flow are of interest, including the farthest streamwise penetration distance, $x_{ps} - x_{os}$, and the transverse penetration width of the flow, w_{ps} , both as functions of the cross stream distance, $y - y_{os}$.

Major assumptions used to find scaling relationships for the geometrical features of the flow, e.g., the trajectories of the vortex system axis and the counter-rotating vortex axes, as well as the various penetration properties of the flow, are as follows: physical property variations are small as normally considered within the Boussinesq approximation of buoyant flows, i.e., the physical properties of the source and ambient fluids are the same except for modest density differences that are responsible for the effects of buoyancy in the flow; the flows are self-preserving so that effects of source disturbances have been lost; the streamwise source specific buoyancy flux per unit length of the line thermal is conserved; and the properties of both the source and the crossflow are independent of time, i.e., both are steady. As mentioned earlier, the detailed measurements of Diez et al. [4] show that motion in the cross stream direction satisfies the no-slip convection approximation, as follows:

$$(y_p - y_{os})/d = C_{ys}[v_\infty(t - t_{os})/d] \quad (1)$$

where t_{os} is a virtual temporal origin to be selected in order to extend the self-preserving region as near to the source as possible and $C_{ys} = 1$. Finally, the flow in the streamwise direction, after deflection has proceeded for a time and the axis of the counter-rotating vortex system is nearly aligned with the crossflow direction, approximates a line thermal having a conserved streamwise source specific buoyancy flux per unit length that can be expressed as follows:

$$B'_0 = \dot{Q}_0 g |\rho_0 - \rho_\infty| / (\rho_\infty v_\infty) \quad (2)$$

Under these assumptions the penetration of the flow in the streamwise direction is given as follows [4]:

$$(x_{ps} - x_{os})/d = C_{xs}[(t - t_{os})/t^*]^n \quad (3)$$

where t^* is a characteristic time that involves the conserved streamwise source specific buoyancy flux per unit length of the line thermal, as follows:

$$t^* = (d^3/B'_0)^{1/2} \quad (4)$$

where $n = 2/3$. Far from the source in the self-preserving region of the flow, the source diameter is no longer relevant and can be eliminated from Eqs. (1), (3), and (4) to yield

$$(x_{ps} - x_{os})/x_s^* = C_{xs} \quad (5)$$

where

$$x_s^* = [B'_0{}^{1/2}(y - y_{os})/v_\infty]^{2/3} \quad (6)$$

The steady penetration properties of plumes in crossflow are then given as simple ratios with respect to the streamwise distance, as follows:

$$r_{ps}/(x_{ps} - x_{os}) = C_{rs} \quad (7)$$

and

$$w_{ps}/(x_{ps} - x_{os}) = C_{ws} \quad (8)$$

In addition, the properties of the axis of the vortex system as a whole, and the spacing between the axes of the two counter-rotating vortices, as defined in Fig. 2, are given by expressions similar to Eqs. (5), (7), and (8), as follows:

$$(x_c - x_{os})/x_s^* = C_{xcs} \quad (9)$$

and

$$w_c/(x_c - x_{os}) = C_{wcs} \quad (10)$$

Structure Properties. Similar to penetration properties, present considerations of structure properties are limited to steady flows. Analyses to find the self-preserving behavior of the mean and rms fluctuating concentration distributions in self-preserving steady turbulent plumes in crossflows are described by Fisher et al. [26]. The results of these analyses in terms of the present notation are as follows:

$$\bar{c}g(x_c - x_{os})^2/(c_0 B'_0) = F[(x - x_c)/(x_c - x_{os}), z/(x_c - x_{os})] \quad (11)$$

and

$$\bar{c}'g(x_c - x_{os})^2/(c_0 B'_0) = F'[(x - x_c)/(x_c - x_{os}), z/(x_c - x_{os})] \quad (12)$$

The form of Eq. (12) for \bar{c}' is used because it provides a compact notation that avoids defining an additional empirical parameter for

the maximum mean concentration of source fluid over a cross section of the flow, \bar{c}_m .

Results and Discussion

Overview. As noted earlier, even though present flows involved downwardly injected negatively buoyant turbulent plumes in crossflows, plots of the results of these flows have all been inverted to show them as upwardly injected positively buoyant steady turbulent plumes in crossflows, similar to the approach taken for the visualization illustrated in Fig. 1. This was done due to the greater familiarity of most individuals with upwardly flowing plumes.

Flow Regime Map for Self-Preservation. The conditions required to observe self-preserving behavior are influenced by the type of flow being considered, the properties of the source, and the property for which self-preserving behavior is being sought. For the present steady turbulent plumes in crossflows, having relatively long source passages ($L/d \geq 50$) and relatively large source Reynolds numbers ($Re_o \geq 2500$), the most conservative property for the onset of self-preserving behavior was the concentration structure of the flow. Thus, consideration of the range of conditions required for the flow to exhibit self-preserving behavior will be based on the concentration structure of the flow in the following.

In addition to the properties just mentioned, observations during the present investigation indicated that the source/crossflow velocity ratio, u_o/v_∞ , substantially influenced conditions at the onset of self-preserving behavior for the concentration structure of steady turbulent plumes in crossflows. This behavior follows because self-preservation was only observed when the axes of the counter-rotating vortex system were nearly aligned with the crossflow direction. At this condition, the plume was nearly horizontal so that the full effect of the streamwise source specific buoyancy flux of a line thermal could act upon the deflected plume in order to develop the full strength of the counter-rotating vortex system. In turn, conditions when the axes of the counter-rotating vortex system were nearly horizontal were a strong function of u_o/v_∞ . In particular, nearly horizontal alignment of the axes of the counter-rotating vortex system was delayed when u_o/v_∞ was large because a large streamwise distance was required before u_o decayed to a value that was small compared to v_∞ so that the plume could be deflected into the nearly horizontal direction.

Present experimental observations of the onset of self-preserving behavior for the concentration structure of steady turbulent plumes in crossflows were based on mean concentration distributions plotted according to the self-preserving scaling of the flows due to Fisher et al. [26], as shown in Eq. (11). The actual approach involved plotting the mean values of the concentrations according to Eq. (11) for several paths over the cross section of the plumes (along a horizontal line passing through the axes of the two counter-rotating vortices, along the two vertical lines passing through the axis of each vortex, and along a third vertical line in the plane of symmetry of the counter-rotating vortex system). Given these results for a particular value of u_o/v_∞ , the condition was assumed to be self-preserving when the distributions along all these paths did not depart from the average distributions for all the paths over the self-preserving region by more than 5%.

The resulting self-preserving flow regime map for steady turbulent plumes in crossflows is illustrated in Fig. 3. This map was constructed based on tests specifically conducted to determine the onset of self-preservation, with conditions prior to and within the self-preserving region denoted by appropriate symbols. The flow regime map of Fig. 3 shows the developing flow and self-preserving regions of steady turbulent plumes in crossflows in terms of the streamwise distance from the source, $(x_c - x_{os})/d$, for u_o/v_∞ in the range 4–100. Note that values of u_o/v_∞ smaller than 4 were not considered because the plume deflects immediately upon leaving the source tube so that its properties are affected by

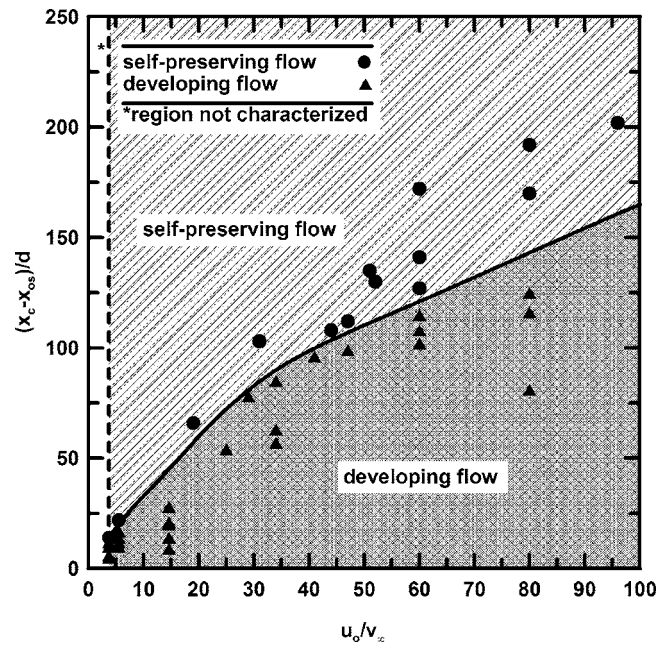


Fig. 3 Flow regime map of the developing flow and self-preserving regions for steady turbulent plumes in crossflows

the walls of the water channel. The tendency for increased values of u_o/v_∞ to delay the onset of self-preserving flow is evident with onset reached at $(x_c - x_{os})/d$ of 10–20 for u_o/v_∞ of 4 (the smallest value of u_o/v_∞ considered) but increasing to 160–170 for u_o/v_∞ of 100 (the largest value of u_o/v_∞ considered.)

Penetration Properties. The penetration properties of starting and steady turbulent plumes in uniform crossflows are considered by Diez et al. [4]. All these results, however, are limited to boundaries of the source fluid flow. Thus, the present measurements of penetration properties extend these results to consider the trajectories of the axes of the vortices of the counter-rotating vortex system of steady turbulent plumes in crossflows which involves properties that depend on the mixing structure of the flow.

The test conditions for present measurements of the properties of steady turbulent plumes in crossflows are summarized in Table 1; a visualization of a typical plume of this nature has already been discussed in connection with Fig. 1. The locations of the axes of the vortices of the counter-rotating vortex system were found by averaging 4000 PLIF images at each streamwise location. The fine details of the dynamics of the mixing pattern of the source and ambient fluids can be seen from the sequence of PLIF images illustrated in Fig. 4. In order to achieve adequate spatial resolution for these PLIF images, the diameter of the laser beam sweeping the cross section of the flow was reduced to 0.5 mm for these images. The time between images was 50 ms, which implies a cross stream distance between images that is relatively large compared to the integral length scales of the flow; therefore, the images illustrated in Fig. 4 are statistically independent. The instantaneous images appearing in Fig. 4 show the largely distorted presence of the two counter-rotating vortices separated near the plane of symmetry by the deeply penetrating ambient fluid of the flow. In addition, the presence of ambient fluid being transported deep into the vortex system of the flow along its plane of symmetry clearly has an important effect on the flow structure, as mentioned earlier in connection with the discussion of the flow visualization of Fig. 1. Finally, by averaging 4000 images, each similar to those illustrated in Fig. 4, at each cross stream test condition, it was possible to locate the axes of the vortices with an experimental uncertainty (95% confidence) of less than 4% of the transverse distance between the vortex axes, w_{cs} .

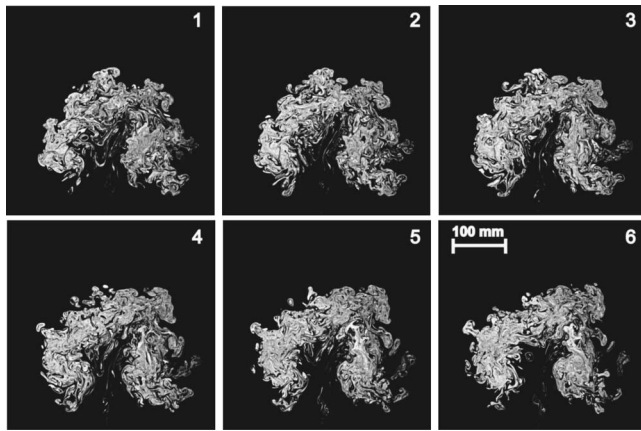


Fig. 4 Instantaneous PLIF images of the cross section of a steady turbulent plume in a uniform crossflow ($d=3.2$ mm, $Re_o=10,000$, $\rho_o/\rho_\infty=1.038$, $Fr_o=223$, $u_o/v_\infty=47$, $(x_c-x_{os})/d=120$, $y/d=98$, and $\Delta t=50$ ms between frames)

Present measurements of the penetration properties of aspects of the concentration structure of steady plumes in crossflow involved the trajectories of the counter-rotating vortex system, $(x_c-x_{os})/x_s^*=(x_c-x_{os})/(B_o^{1/2}(y-y_o)/v_\infty)^{2/3}$, and the normalized spacing between the axes of the two counter-rotating vortices, $w_{cs}/(x_c-x_{os})$, as given by Eqs. (9) and (10). These properties are plotted as a function of the normalized streamwise vortex core penetration distance, $(x_c-x_{os})/d$, in the bottom two plots of Fig. 5. These parameters are rather scattered in the developing flow region at small streamwise distances from the source but eventually approach constant values, $C_{xcs}=1.5$ and $C_{wcs}=0.46$, for self-preserving flow at large streamwise distances from the source. Notably, these measurements in the developing flow region of Fig. 5 generally involve $u_o/v_\infty < 50$ and were obtained for $(x_c-x_{os})/d < 100$, which generally agrees with the developing flow region of the flow regime map of Fig. 3.

Measurements of the penetration properties of the boundaries of the source fluid of steady plumes in crossflow from Diez et al. [4] involved the farthest normalized streamwise penetration distance, $(x_{ps}-x_{os})/x_s^*=(x_{ps}-x_{os})/(B_o^{1/2}(y-y_o)/v_\infty)^{2/3}$, the normalized radial penetration distance, $r_{ps}/(x_{ps}-x_{os})$, and the normalized lateral penetration width, $w_{ps}/(x_{ps}-x_{os})$, as given by Eqs. (5), (7), and (8). These properties are plotted as a function of the normalized streamwise penetration distance, $(x_{ps}-x_{os})/d$, in the top three plots of Fig. 5. These parameters are rather scattered in the developing flow region at small streamwise distances from the source but eventually approach constant values $C_{xs}=1.9$, $C_{rs}=0.36$, and $C_{ws}=0.49$, for self-preserving flow at large streamwise distances from the source. Notably, the measurements in the developing flow region of Fig. 5 generally involve $u_o/v_\infty < 25$ and were obtained for $(x_{ps}-x_{os})/d < 75$, which generally agrees with the developing flow region of the flow regime map of Fig. 3. Thus, the fact that penetration properties of the boundaries of the source fluid reach self-preserving behavior sooner than the penetration properties of aspects of the concentration structure of the plumes in crossflow comes about largely due to the smaller values of u_o/v_∞ that were used during the source fluid penetration tests.

Finally, for convenient reference, the measured parameters associated with the penetration properties of steady turbulent plumes in crossflows are summarized in Table 2. Experimental uncertainties for flow penetration properties (95% confidence) are as follows: less than 5% for C_{xs} , less than 3% for C_{rs} , less than 4% for C_{ws} , less than 18% for x_{os}/d , and less than 5% for both C_{xcs} and C_{wcs} . For comparison, the corresponding parameter values for steady turbulent jets in crossflows from Diez et al. [5] are also

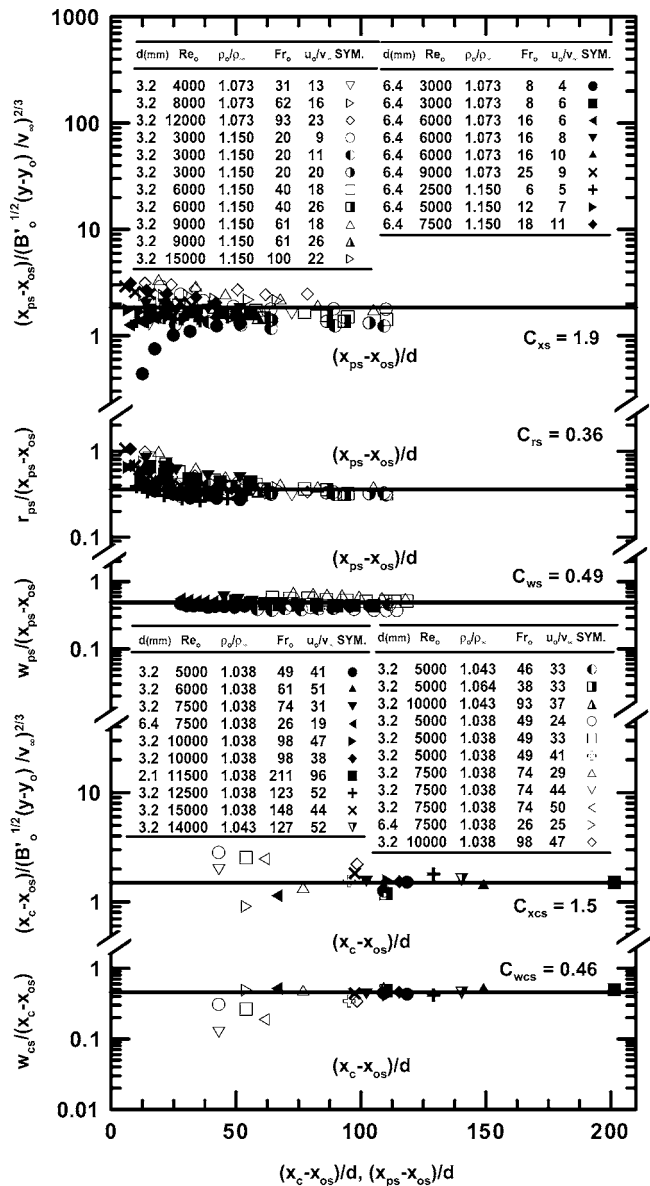


Fig. 5 Streamwise and transverse penetration distances, and the transverse spacing between the vortex axes, in terms of self-preserving variables for steady turbulent plumes in crossflows

Table 2 Summary of empirical parameters for the self-preserving flow and vortex axes penetration properties of steady round turbulent jets and plumes in uniform crossflowing fluids^a

Flow	C_{xs}	C_{rs}	C_{ws}	x_{os}/d
Results for flow penetration properties from Diez et al. [4]:				
Plume	1.9(0.08)	0.36(0.008)	0.49(0.015)	25.6(4.5)
Jet	2.3(0.08)	0.23(0.005)	0.31(0.011)	6.1(2.7)
Flow	C_{xcs}	C_{wcs}	x_{os}/d	
Results for vortex axes penetration properties from Diez et al. [5] and from the present study:				
Plume	1.5(0.06)	0.46(0.013)	0.0	
Jet	1.7(0.08)	0.36(0.017)	0.0	

^aExperimental uncertainties (95% confidence) in parentheses; also $C_{ys}=1$ and $y_{os}=0.0$.

provided in Table 2; the experimental uncertainties (95% confidence) of these parameters for jets are similar to the present values for plumes.

It is of particular interest to compare the values of C_{rs} , C_{ws} , and C_{wcs} for jets and plumes in crossflow because larger values of these parameters imply larger penetration of the source flow into the crossflow, which implies faster rates of mixing. The results in Table 2 show that these parameters are 30–60% larger for plumes than for jets, suggesting increased rates of mixing for the plumes due to their enhanced motion as a result of buoyancy. On the other hand, the streamwise penetration coefficients are larger for jets than plumes, however, these parameters are not directly comparable because the functional forms of x_c^* for these two flows are fundamentally different, see Diez et al. [4].

Finally, the counter-rotating vortex system that develops for steady turbulent plumes in crossflows promotes the mixing properties of the flow as a function of streamwise penetration distance compared to steady turbulent plumes in still fluids where the axis of the flow is aligned with the direction of penetration of the flow. In particular, the penetration of the flow normal to the axis is much greater for steady turbulent plumes in crossflows than for corresponding plumes in still fluids, e.g., $r_{ps}/(x_{ps}-x_{os})$ and $w_{ps}/(x_{ps}-x_{os})$ are 0.36 and 0.49 for present plumes in crossflow whereas $r_p/(x_p-x_o)$ is 0.16 for the measurements of Diez et al. [3] for plumes in still fluids. Thus, penetration of the flow normal to its axis is 2–3 times faster for steady turbulent plumes in crossflows than for similar plumes in still fluids for similar streamwise distances and initial source conditions. Notably, this behavior is qualitatively similar to results observed by Diez et al. [5] for steady turbulent jets in crossflows compared to similar jets in still fluids. This behavior suggests that there is much more effective mixing between the source and the ambient flows when the axes of the source flow are perpendicular to the streamwise direction of penetration, which is the case for steady turbulent plumes and jets in crossflows, than when the axis of the source flow is aligned with the direction of penetration, which is the case for similar plumes and jets in still fluids. This behavior is very similar to numerous other fluid transport configurations where relative motion in crossflow to the axis of the flow is much more effective for promoting transport between two streams than when the direction of relative motion is aligned with the flow axes.

Structure Properties. The development of distributions of mean concentrations of source fluid over cross sectional planes of steady turbulent plumes in crossflows is illustrated in Fig. 6. This plot involves mean and fluctuating concentrations of source fluid plotted according to the self-preserving structure variables of Eqs. (11) and (12) along a horizontal line crossing the flow that intersects the axes of the two counter-rotating vortices for various test conditions including different values of $(x_c-x_{os})/d$. On this plot, results from the developing flow region are designated by open and partially open symbols whereas results for self-preserving flow are shown as dark symbols that represent the average of all the results measured within the self-preserving flow region. Notably, results in the developing flow region of Fig. 6 for both mean and rms fluctuating concentrations were obtained for $u_o/v_\infty=24-50$ and $(x_c-x_{os})/d \leq 62$, which is within the developing flow region of the flow regime map of Fig. 3. Similarly, all results for the self-preserving flow region of Fig. 6 for both mean and rms fluctuating concentrations involve values of u_o/v_∞ and $(x_c-x_{os})/d$ that are within the self-preserving flow region of the flow regime map of Fig. 3. Mean concentrations of source fluid reach a maximum at the vortex axes, somewhat analogous to reaching maximum values of mean concentrations at the axis of steady turbulent plumes in still fluids, see Dai et al. [22]. In contrast, the maximum values of rms concentration fluctuations along these paths reach maximum values at somewhat larger radial distances than the axes of the counter-rotating vortices, which also is analogous to the position where rms concentration fluctuations reach a

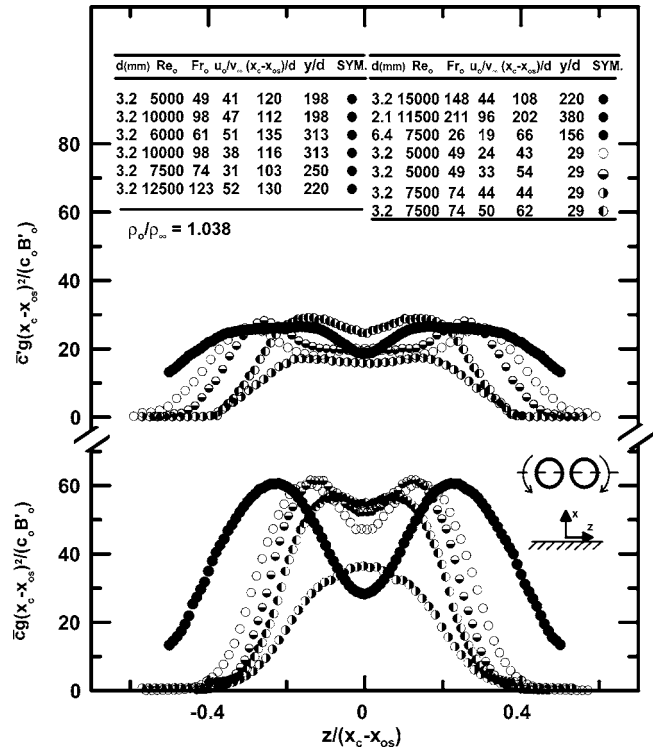


Fig. 6 Plots of the development of mean and fluctuating concentrations of source fluid in terms of self-preserving variables for transverse paths through the vortex axes over the cross section of the flow for steady turbulent plumes in crossflows

maximum in steady turbulent plumes in still fluids, see Dai et al. [22]. Finally, the region between the counter-rotating vortices involves a broad minimum of rms concentration fluctuations, which is caused by the relatively wide region that is dominated by entrainment of ambient fluid between the axes of the vortices seen in the dye visualization image of Fig. 1 and the PLIF images of Fig. 4.

Figures 7 and 8 are illustrations of mean and rms fluctuating concentrations of source fluid plotted according to the self-preserving structure variables of Eqs. (11) and (12). These results are for various paths over the flow cross section (horizontally through the axes of the two counter-rotating vortices, vertically through the axes of the counter-rotating vortices, and vertically along the plane of symmetry of the counter-rotating vortex system). All these results were obtained at test conditions within the self-preserving flow region of the flow regime map of Fig. 3; the averages of these results have been plotted in Figs. 7 and 8. The variations of appropriately scaled mean and rms fluctuations of the concentrations of source fluid for these conditions were well within experimental uncertainties, e.g., less than 11% percent (95% confidence) for $|z|/(x_c-x_{os}) < 0.45$ and $|x-x_c|/(x_c-x_{os}) < 0.40$. Noting that the paths over the cross section of the plumes provide reasonable coverage of the main features of the mixing caused by the counter-rotating vortex system, the next step involved attempting to completely characterize the self-preserving functions $F[\]$ and $F'[\]$ of Eqs. (11) and (12).

The distributions of mean and rms fluctuating concentrations over the cross section of steady turbulent plumes in crossflows in the self-preserving region are quite complex and cannot be reduced to a simple empirical formula similar to that obtained by Dai et al. [22] for steady turbulent plumes in still fluids. Instead, present measurements of mean and rms fluctuating concentrations over cross sections in the self-preserving region were reduced in terms of self-preserving variables and plotted as a function of location in the cross section according to self-preserving stream-

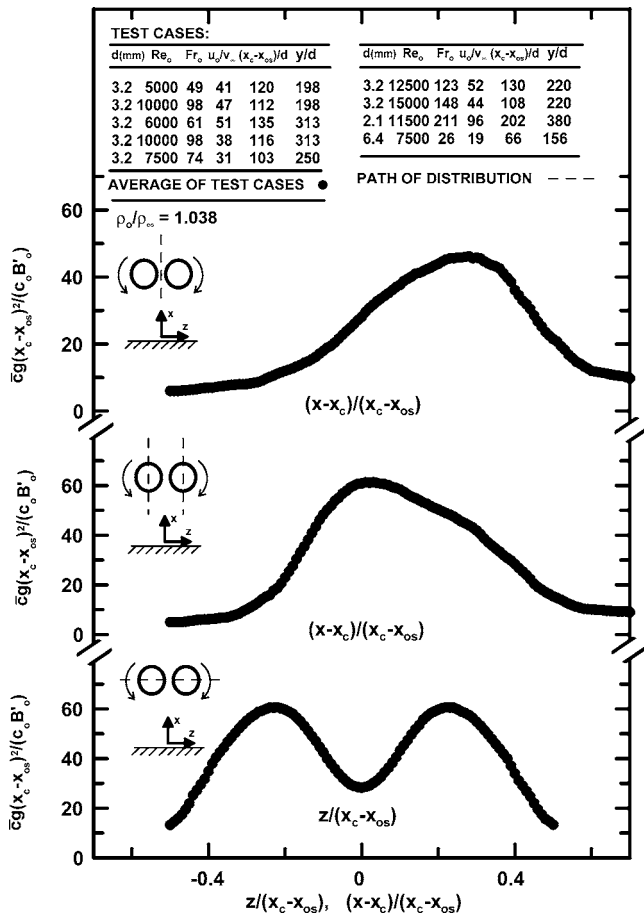


Fig. 7 Plots of mean concentrations of source fluid in terms of self-preserving variables for various vertical and horizontal paths over the cross section of the flow for steady turbulent plumes in crossflows within the self-preserving region

wise and transverse variables indicated by Eqs. (11) and (12), e.g., $(x-x_c)/(x_c-x_{os})$ and $z/(x_c-x_{os})$, respectively. Results of this nature are illustrated in Figs. 9 and 10 for the present measurements. The mean locations of the two axes of the counter-rotating vortex system are shown as white crosses on these plots, for reference purposes. On both plots, the self-preserving scaled values of mean and rms fluctuating concentrations are divided into 12 gray scales, for ranges of mean and rms fluctuating source fluid concentration values in terms of self-preserving variables of 0–70 and 0–35, respectively. The counter-rotating vortex system is seen to contribute to the two-lobed structure of the flow with the entrainment of ambient fluid along the plane of symmetry from the side of the flow opposite to the plume source tending to displace maximum mean concentrations along this plane in the streamwise (upward) direction (i.e., in the direction of penetration of the counter-rotating vortex system). A particularly surprising feature of this flow is its unusually large streamwise and transverse penetration distances of $(x-x_c)/(x_c-x_{os})$ of approximately +0.6 to -0.3 and $z/(x_c-x_{os})$ of approximately ± 0.5 . These values are 2–3 times larger than the corresponding radial dimensions of steady round buoyant turbulent plumes in still fluids, see Dai et al. [22], where $r/(x-x_o)$ is approximately 0.16. In addition, the concentration field for steady turbulent plumes in crossflows decays according to $\bar{c}_m \sim (x-x_{os})^{-2}$, which is slightly faster than for steady turbulent plumes in still fluids which decays according to $\bar{c}_m \sim (x-x_{os})^{-5/3}$ [22]. This highlights the capability of vortex structures in cross-flow to promote effective mixing between source and ambient fluids.

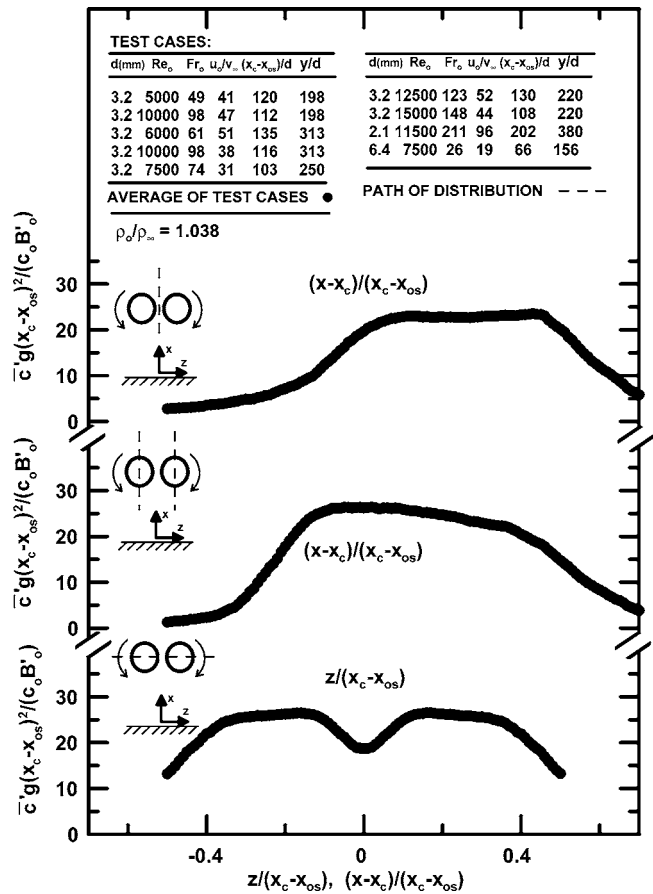


Fig. 8 Plots of rms concentration fluctuations of source fluid in terms of self-preserving variables for various vertical and horizontal paths over the cross section of the flow for steady turbulent plumes in crossflows within the self-preserving region

Conclusions

Scaling relationships for the penetration (geometrical) and structure properties of steady turbulent plumes in crossflows were evaluated based on measurements of the mixing properties of salt water sources injected into fresh water and ethanol/water crossflows. The test conditions involved source exit diameters of 2.1, 3.2, and 6.4 mm, source passage lengths in excess of 50 source exit diameters; source Reynolds numbers of 2500–15,000; source/ambient density ratios of 1.038, 1.073, and 1.150; source Froude numbers of 6–211; source/ambient velocity ratios of 4–96; vertical penetration distances of 0–202 source diameters; and horizontal penetration distances of 0–620 source diameters. Major conclusions of the study are as follows.

(1) The flows became turbulent at streamwise distances of 0–5 source diameters from the source, similar to earlier observations of these flows by Diez et al. [3,4]. The onset of self-preserving behavior required that axes of the counter-rotating vortex system be nearly aligned with the crossflow direction whereas this condition was strongly affected by the source/crossflow velocity ratio, u_o/v_∞ . As a result, self-preserving behavior was observed at streamwise distances greater than 10–20 source diameters from the source for $u_o/v_\infty=4$ (the smallest value of u_o/v_∞ considered), increasing to streamwise distances greater than 160–170 source diameters from the source for $u_o/v_\infty=100$ (the largest value of u_o/v_∞ considered). The detailed flow regime map of the developing flow and self-preserving regions for steady turbulent plumes

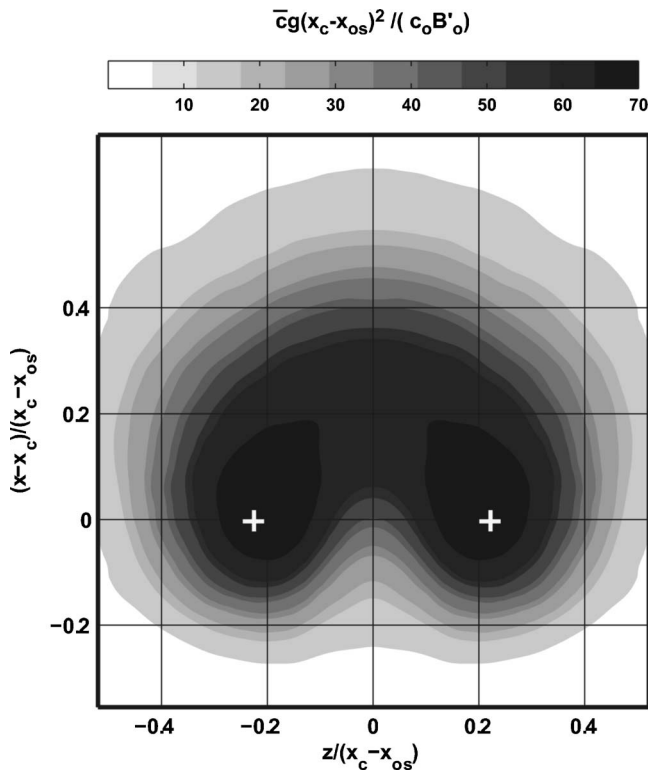


Fig. 9 Contour plots of mean concentrations of source fluid in terms of self-preserving variables over the cross section of the flow for steady turbulent plumes in crossflows within the self-preserving region

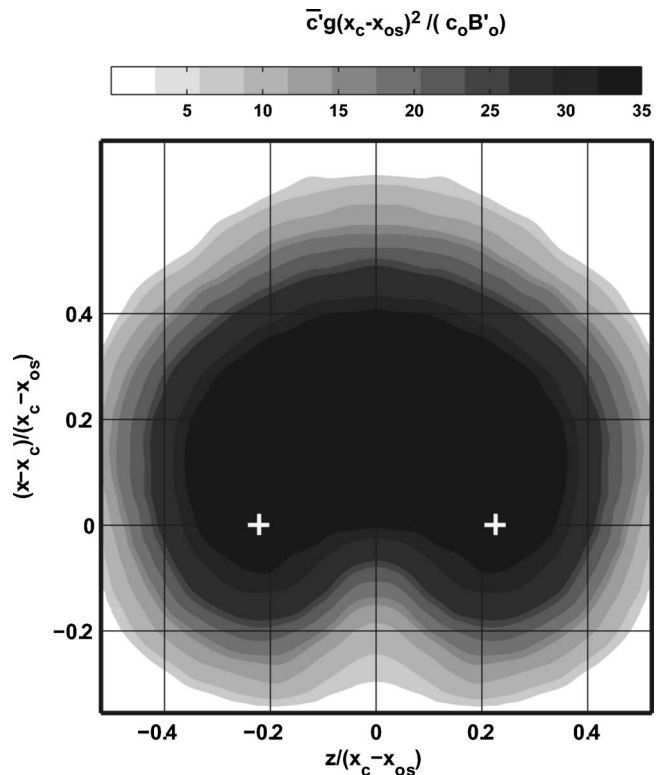


Fig. 10 Contour plots of rms concentration fluctuations of source fluid in terms of self-preserving variables over the cross section of the flow for steady turbulent plumes in crossflows within the self-preserving region

in uniform crossflows of Fig. 3, however, should be consulted for the details of the variation of $(x_{cs} - x_{os})/d$ at the onset of self-preserving behavior as a function of u_o/v_∞ .

(2) Combining the no-slip convection approximation in the cross stream direction with self-preserving scaling for a horizontal line thermal in a still fluid in the streamwise direction yielded good predictions of both steady penetration properties and the steady structure properties (consisting of the mean and rms fluctuations of the concentrations of source fluid) of the flow within the self-preserving region of steady turbulent plumes in crossflows.

(3) The self-preserving structure of steady turbulent plumes in crossflows involves a counter-rotating vortex system whose axes are nearly aligned with the crossflow and thus are nearly horizontal. The nearly crossflow orientation of the axes of the counter-rotating vortex system promotes unusually rapid mixing due to the approximately crossflow motion in the streamwise direction of steady turbulent plumes in crossflows compared to steady turbulent plumes in still fluids where the flow axis is aligned with the streamwise direction, for example: $(r_{ps} \text{ and } w_{ps})/(x_{ps} - x_{os}) = 0.36$ and 0.49 for steady turbulent plumes in crossflow compared to $r_p/(x_p - x_s) = 0.16$ for steady turbulent plumes in still fluids. The rapid onset of self-preserving behavior for plumes in crossflow at small values of u_o/v_∞ , where the axes of the counter-rotating vortex system becomes aligned with the crossflow almost immediately upon leaving the source and the onset of self-preserving behavior is observed at streamwise distances of 10–20 source diameters from the source, provides further evidence of unusually rapid mixing due to the crossflow motion of the plume, e.g., steady turbulent plumes in still fluids where mixing is limited to the longitudinal direction only exhibit self-preserving behavior at streamwise distances greater than 80–100 source diameters from the source, see Dai et al. [22].

The observations of conclusion (3) from the present study of steady turbulent plumes in crossflows, combined with similar observations of conclusion (4) from Diez et al. [5] for an earlier study of steady turbulent jets in crossflows, highlight the enhanced mixing and transport that occur when the geometry involves crossflow rather than parallel flow; this behavior is familiar from many areas of fluid mechanics, e.g., the response of hot wires mainly to crossflow rather than coflow and the highly effective primary breakup properties of nonturbulent fluid jets subjected to crossflow rather than coflow, among others.

Acknowledgment

This research was supported by the United States Department of Commerce, National Institute of Standards and Technology, Grant No. 60NANB1D0006, with H. R. Baum of the Laboratory for Building and Fire Research serving as Scientific Officer. The assistance of R. Jolly and D. Zock, both students in the Undergraduate Research Opportunity Program (UROP) of the University of Michigan, in carrying out the experiments is gratefully appreciated.

Nomenclature

- B'_o = source specific buoyancy flux per unit length of a line thermal, Eq. (2)
- c = concentration of source fluid
- C_{rs} = radial penetration coefficient for steady plumes in crossflow, Eq. (7)
- C_{wcs} = vortex core spacing coefficient for steady plumes in crossflow, Eq. (10)
- C_{ws} = transverse penetration coefficient for steady plumes in crossflow, Eq. (8)

C_{xcs} = streamwise penetration coefficient of the axis of the vortex system for steady plumes in crossflow, Eq. (9)
 C_{xs} = streamwise penetration coefficient for steady plumes in crossflow, Eq. (5)
 C_{ys} = cross stream penetration coefficient for steady plumes in crossflow, Eq. (1)
 d = source diameter
 Fr_o = source Froude number, $(\rho_o u_o^2 / (gd|\Delta\rho|))^{1/2}$
 g = acceleration of gravity
 L = source passage length
 \dot{Q}_o = volumetric rate of injection of source fluid
 r = streamwise penetration normal to flow axis in a vertical plane
 Re_o = source Reynolds number, $u_o d / \nu_o$
 t = time
 t^* = self-preserving time scale, Eq. (4)
 u = streamwise (vertical) velocity parallel to the source flow
 v = cross stream (horizontal) velocity in the direction of plume deflection
 w_c = transverse separation of the vortex axes normal to the flow axis in a plume cross-sectional plane, Fig. 2
 w_{ps} = transverse penetration normal to the flow axis in a plume cross-sectional plane for steady plumes, Fig. 2
 x = streamwise (vertical) distance relative to the source, Fig. 2
 x_c = streamwise (vertical) distance from the jet source to the horizontal axis of the vortex system, Fig. 2
 x_s^* = streamwise characteristic distance for a steady flow, Eq. (6)
 y = cross-stream (horizontal) distance relative to the source in the direction of plume deflection, Fig. 2
 z = transverse distance relative to the source in a plume cross-sectional plane, Fig. 2
 Δt = time between PLIF images of the flow
 ν = kinematic viscosity
 ρ = density

Subscripts

c = vortex axis
 m = maximum concentration
 p = maximum penetration location
 s = steady-state flow property
 o = source value or virtual origin location
 ∞ = ambient value

Superscripts

$(\bar{\quad})$ = time-averaged mean value
 $(\overline{\quad})'$ = rms fluctuating value

References

- [1] Sangras, R., Kwon, O. C., and Faeth, G. M., 2002, "Self-Preserving Properties of Unsteady Round Nonbuoyant Turbulent Starting Jets and Puffs in Still Fluids," *ASME J. Heat Transfer*, **124**, pp. 460–469.
- [2] Diez, F. J., Sangras, R., Kwon, O. C., and Faeth, G. M., 2003, "Self-Preserving Properties of Unsteady Round Nonbuoyant Turbulent Starting Jets and Puffs in Still Fluids," *ASME J. Heat Transfer*, **125**, pp. 204–205.
- [3] Diez, F. J., Sangras, R., Faeth, G. M., and Kwon, O. C., 2003, "Self-Preserving Properties of Unsteady Round Turbulent Plumes and Thermals in Still Fluids," *ASME J. Heat Transfer*, **125**, pp. 821–830.
- [4] Diez, F. J., Bernal, L. P., and Faeth, G. M., 2003, "Round Turbulent Thermals, Puffs, Starting Plumes and Starting Jets in Uniform Crossflow," *ASME J. Heat*

- Transfer*, **125**, pp. 1046–1057.
- [5] Diez, F. J., Bernal, L. P., and Faeth, G. M., 2005, "Self-Preserving Mixing Properties of Steady Round Nonbuoyant Turbulent Jets in Uniform Crossflows," *ASME J. Heat Transfer*, **127**, pp. 877–887.
- [6] Rouse, H., Yih, C. S., and Humphreys, H. W., 1952, "Gravitational Convection from a Boundary Source," *Tellus*, **4**, pp. 201–210.
- [7] Morton, B. R., Taylor, G. I., and Turner, J. S., 1956, "Turbulent Gravitational Convection from Maintained and Instantaneous Sources," *Proc. R. Soc. London, Ser. A*, **A234**, pp. 1–23.
- [8] Morton, B. R., 1959, "Forced Plumes," *J. Fluid Mech.*, **5**, pp. 151–163.
- [9] Turner, J. S., 1969, "Buoyant Plumes and Thermals," *Annu. Rev. Fluid Mech.*, **1**, pp. 29–44.
- [10] Tennekes, H., and Lumley, J. L., 1972, *A First Course in Turbulence*, MIT Press, Cambridge, MA, pp. 113–124.
- [11] Turner, J. S., 1973, *Buoyancy Effects in Fluids*, Cambridge University Press, Cambridge.
- [12] Hinze, J. O., 1975, *Turbulence*, 2nd Ed., McGraw-Hill, New York, pp. 724–734.
- [13] Seban, R. A., and Behnia, M. M., 1976, "Buoyant Turbulent Jets in Unstratified Surroundings," *Int. J. Heat Mass Transfer*, **19**, pp. 1197–1204.
- [14] Yih, C.-S., 1977, "Buoyant Turbulent Plumes," *Phys. Fluids*, **20**, pp. 1234–1237.
- [15] George, W. K. Jr., Alpert, R. L., and Tamanini, F., 1977, "Turbulence Measurements in an Axisymmetric Buoyant Plume," *Int. J. Heat Mass Transfer*, **20**, pp. 1145–1154.
- [16] Chen, C. J., and Chen, C. H., 1979, "On Prediction and Unified Correlation for Decay of Vertical Buoyant Jets," *ASME J. Heat Transfer*, **101**, pp. 532–537.
- [17] Yih, C.-S., and Wu, F., 1981, "Round Buoyant Laminar and Turbulent Plumes," *Phys. Fluids*, **24**, pp. 823–830.
- [18] List, E. J., 1982, "Turbulent Jets and Plumes," *Annu. Rev. Fluid Mech.*, **14**, pp. 189–212.
- [19] Papanicolaou, P. N., and List, E. J., 1988, "Investigation of Round Vertical Buoyant Turbulent Jets," *J. Fluid Mech.*, **195**, pp. 341–391.
- [20] Papanioniou, D., and List, E. J., 1989, "Large Scale Structure in the Far Field of Buoyant Jets," *J. Fluid Mech.*, **209**, pp. 151–190.
- [21] Peterson, J., and Bayazitoglu, Y., 1992, "Measurements of Velocity and Turbulence in Vertical Axisymmetric Isothermal and Buoyant Plumes," *ASME J. Heat Transfer*, **114**, pp. 135–142.
- [22] Dai, Z., Tseng, L.-K., and Faeth, G. M., 1994, "Structure of Round, Fully-Developed, Buoyant Turbulent Plumes," *ASME J. Heat Transfer*, **116**, pp. 409–417.
- [23] Dai, Z., Tseng, L.-K., and Faeth, G. M., 1995, "Velocity Statistics of Round, Fully-Developed Buoyant Turbulent Plumes," *ASME J. Heat Transfer*, **117**, pp. 138–145.
- [24] Dai, Z., Tseng, L.-K., and Faeth, G. M., 1995, "Velocity/Mixture-Fraction Statistics of Round Self-Preserving Buoyant Turbulent Plumes," *ASME J. Heat Transfer*, **117**, pp. 918–926.
- [25] Dai, Z., and Faeth, G. M., 1996, "Measurements of the Structure of Self-Preserving Round Buoyant Turbulent Plumes," *ASME J. Heat Transfer*, **118**, pp. 493–495.
- [26] Fischer, H. B., List, E. J., Koh, R. C., Imberger, J., and Brooks, N. H., 1979, *Mixing in Inland and Coastal Waters*, Academic Press, New York, pp. 315–389.
- [27] Lutti, F. M., and Brzustowski, T. A., 1977, "Flow Due to a Two-Dimensional Heat Source with Cross Flow in the Atmosphere," *Combust. Sci. Technol.*, **16**, pp. 71–87.
- [28] Andreopoulos, J., 1983, "Heat Transfer Measurements in a Heated Jet-Pipe Flow Issuing Into a Cold Cross Stream," *Phys. Fluids*, **26**, pp. 3200–3210.
- [29] Alton, B. W., Davidson, G. A., and Slawson, P. R., 1993, "Comparison of Measurements and Integral Model Predictions of Hot Water Plume Behavior in a Crossflow," *Atmos. Environ., Part A*, **27A**, pp. 589–598.
- [30] Baum, H. R., McGrattan, K. B., and Rehm, R. G., 1994, "Simulation of Smoke Plumes from Large Pool Fires," *Proc. Combust. Inst.*, **25**, pp. 1463–1469.
- [31] Hasselbrink, E. F., and Mungal, M. G., 1998, "Observations on the Stabilization Region of Lifted Non-Premixed Methane Transverse Jet Flames," *Proc. Combust. Inst.*, **27**, pp. 1167–1173.
- [32] Huq, P., and Stewart, E. J., 1997, "Measurements of Density Fluctuations in Steady, Buoyant Plumes in Crossflow," *Atmos. Environ.*, **31**, pp. 1677–1688.
- [33] Steckler, K. D., Baum, H. R., and Quintiere, J. G., 1986, "Salt Water Modeling of Fire Induced Flows in Multicomponent Enclosures," *Proc. Combust. Inst.*, **21**, pp. 143–149.
- [34] Wu, P.-K., Miranda, R. F., and Faeth, G. M., 1995, "Effects of Initial Flow Conditions on Primary Breakup of Nonturbulent and Turbulent Round Liquid Jets," *Atomization Sprays*, **5**, pp. 175–196.
- [35] Ferrier, A. J., Funk, D. R., and Roberts, P. J. W., 1993, "Application of Optical Techniques to the Study of Plumes in Stratified Fluids," *Dyn. Atmos. Oceans*, **20**, pp. 155–183.
- [36] Alahyari, A., and Longmire, E. K., 1994, "Particle Image Velocimetry in a Variable Density Flow: Application to Dynamically Evolving Microburst," *Exp. Fluids*, **17**, pp. 434–440.
- [37] Daviero, G. I., Roberts, P. J. W., and Maile, K., 2001, "Refractive Index Matching in Large-Scale Stratified Experiments," *Exp. Fluids*, **31**, pp. 119–126.

Effect of Surface Radiation on Multiple Natural Convection Solutions in a Square Cavity Partially Heated from Below

El Hassan Ridouane¹

Department of Mechanical Engineering,
The University of Vermont,
Colchester Ave,
201 Votey,
Burlington, VT 05405
e-mail: eridouan@cems.uvm.edu

Mohammed Hasnaoui

Department of Physics,
LMFE,
Faculty of Sciences Semlalia,
Marrakech, Morocco

A numerical study of natural convection with surface radiation in an air filled square enclosure with a centrally heated bottom wall and cooled upper wall is presented. The vertical walls and the rest of the bottom wall are assumed to be insulated. The problem is studied for Rayleigh numbers Ra , ranging from 10^3 to 4×10^6 and surfaces emissivity ϵ , varying from 0 to 1. The governing equations, written in terms of stream function-vorticity formulation, are solved using a finite difference approach. It is found that, under these heating/cooling conditions, three different steady-state solutions are possible in the ranges of the parameters considered. Results are presented detailing the occurrence of each steady-state solution and the effect of Ra and ϵ on its range of existence. It is found that the surface radiation alters significantly the existence ranges of the solutions. For each solution, convective and radiative contributions to the global heat transfer are also quantified for various Ra and ϵ . The influence of the heated surface dimension on the fluid flow and thermal patterns is also presented by comparing the present results against those obtained by the authors in an earlier study within a square cavity totally heated from below. [DOI: 10.1115/1.2345429]

1 Introduction

Natural convection in enclosures has been extensively studied both numerically and experimentally. In numerical studies, natural convection in enclosures represents one of the simplest multiple-scale, coupled nonlinear fluid flow problems and provides a convenient vehicle for the development of new analyses and new numerical algorithms. Among the various enclosures, the rectangular cavity is the most extensively studied since many engineering applications may be accommodated to this geometry. These include solar collector cavities, air flow in rooms and other structures in the habitat domain such as cavity walls and double pane windows, cooling of electronic devices, and others. The study of natural convection coupled with radiation still constitutes an attractive challenge for researchers working experimentally and numerically on the subject. The effect of surface radiation on natural convection is known to be significant, even at room temperature, in air-filled cavities with walls maintained at prescribed temperatures [1–4].

Most of the numerical studies previously reported in the literature have considered one of the vertical walls heated and the other one cooled with horizontal insulated walls. By using air as a working fluid, Balaji and Venkateshan [5] showed that surface radiation leads to a reduction of the convective component which decreases monotonically with the emissivity. However, this reduction is, in general, largely compensated by the radiative transfer between the walls of the cavity. Hence, the net effect of radiation leads to an increase of the overall heat transfer across the enclosure when the emissivity of the hot wall is greater than 0.229. Two years later, the same authors [6] proposed general correlations for convection and radiation Nusselt numbers for different emissivities of the walls. Good agreement between the numerical data and the correlations was observed; the maximum difference being

within 6%. Akiyama and Chong [7] studied the problem of coupled natural convection and radiation in a square enclosure filled with air and having gray surfaces. Their results showed that the surface radiation has an important influence on the temperature distribution and flow patterns in the cavity, especially at high Rayleigh numbers. The average convective Nusselt number increases by increasing Ra , but only limited variations were observed when the emissivity was varied. On the other hand, the average radiative Nusselt number rises quickly as the emissivity increases.

Using the finite volume method, Mezrhab and Bchir [8] studied the heat transfer by radiation and natural convection in an air-filled square enclosure with a vertical partition of finite thickness and varying height. Numerical solutions were obtained for $N_r = 30$ in conjunction to different Rayleigh numbers varying up to a maximum of 10^8 . Mahapatra et al. [9] reported a finite element solution on the interaction of surface radiation and variable property laminar natural convection in a differentially heated square cavity. The presence of radiation was observed to affect the thermal stratification in the core region of the cavity and leads to the instability in the thermal and flow fields characterized by the divergence of the numerical code at high values of Ra and ϵ . In addition, the limiting value of the temperature difference ($T'_H - T'_C$) below which the process of heat transfer by convection dominates over surface radiation was determined. The phenomenon of laminar natural convection coupled with radiation in a rectangular enclosure with two incomplete partitions was studied numerically in the case of a large temperature difference by Han and Baek [10], assuming that the partitions are very thin, adiabatic, and radiatively opaque. More recently, Colomer et al. [11] analyzed the natural convection phenomenon coupled with radiant exchange in a three-dimensional differentially heated cavity. The problem was solved for a transparent medium showing that radiation contributes to increase significantly the heat transfer. More importantly, for a given Plank number and a constant reference temperature ratio, the contribution of radiation remains almost impervious in a designated range of Rayleigh numbers. A comparison between the

¹Corresponding author.

Contributed by the Heat Transfer Division of ASME for publication in the JOURNAL OF HEAT TRANSFER. Manuscript received July 29, 2005; final manuscript received May 16, 2006. Review conducted by Jose L. Lage.

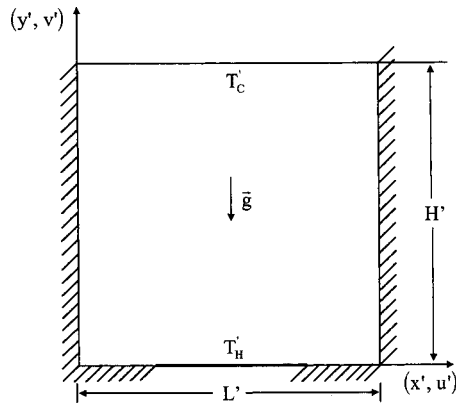


Fig. 1 Schematic of the physical system

results of two-dimensional model and those obtained in the mid-plane of a long rectangular enclosure was presented and a good agreement was achieved between both solutions.

A very limited number of laboratory experiments have been conducted for coupled natural convection and radiation in rectangular enclosures differentially heated. One experiment reported in the literature involving two cases corresponding to highly emissive ($\epsilon=0.85$) and highly polished ($\epsilon=0.05$) walls was reported by Ramesh and Venkateshan [12]. A Wollaston prism interferometer was used to perform the heat transfer measurements along the hot wall. Later, Ramesh et al. [13], using the same experimental method, analyzed the effect of boundary conditions on natural convection in a square enclosure with surface radiation. The authors applied nearly adiabatic boundary conditions at the horizontal walls within a deviation of about 3%. Results of the experiments were compared with those obtained numerically with a finite volume method and reasonable agreement was observed. Deviations from experiments were within 9% for the mean convective Nusselt number and within 5% for the mean radiative Nusselt number.

When the heating/cooling scenario switches from vertical to horizontal walls, Hasnaoui et al. [14] have proved numerically the existence of multiple steady-state solutions in the absence of radiation in a rectangular cavity partially heated from below. Recently, while studying coupling between radiation and natural convection in a square cavity entirely heated from below, Ridouane et al. [15,16] proved also that the multiplicity of solutions is possible. The effect of radiation on the existence range of each type of solution was analyzed in the case of a square cavity having walls with equal [15] or different [16] emissivities.

A detailed review of the archival literature on fluid dynamics and heat transfer reveals that the impact of radiation on the multiplicity of solutions induced inside a square enclosure partially heated from below has not been investigated so far. Of course, its physical features in modifying the structure and heat transfer as well as the existence ranges of these solutions are not yet understood. In view of this shortcoming, the objective of the present study is to fill this gap carrying out numerical simulations of the heated airflow in a square cavity partially heated from below. The results obtained within the partially heated enclosure will be compared to those obtained by the authors in an earlier work within a totally heated square enclosure (Ridouane et al. [15]). Streamlines and isotherms are presented in the case of a cavity partially heated.

2 Theoretical Model

The physical system, sketched in Fig. 1, consists of incompressible air trapped inside a square enclosure of height H' . To initiate the natural convection airflow in the closed space, a hot temperature is prescribed at the central portion of the bottom wall, over a

length of $H'/2$, and a cold temperature is imposed to the horizontal upper wall. The vertical walls and the remaining portions of the bottom wall are thermally insulated from the surrounding.

2.1 Governing Equations. The simultaneous effects of the density, dynamic viscosity, specific heat capacity, and thermal conductivity of the air changing with temperature are assumed to be negligible. Correspondingly, the standard Boussinesq approximation is adopted and all fluid properties are assumed to be constant and evaluated at the reference temperature T'_0 . The fluid flow is assumed to be laminar, two dimensional, and the viscous dissipation is neglected due to low velocities. Under these assumptions and using vorticity-stream function formulation, together with the energy equation, the Navier-Stokes equations for a Newtonian fluid can be written in dimensionless form as follows:

$$\frac{\partial \Omega}{\partial t} + \frac{\partial(u\Omega)}{\partial x} + \frac{\partial(v\Omega)}{\partial y} = \text{Pr} \left(\frac{\partial^2 \Omega}{\partial x^2} + \frac{\partial^2 \Omega}{\partial y^2} \right) - \text{Pr Ra} \frac{\partial T}{\partial x} \quad (1)$$

$$\frac{\partial T}{\partial t} + \frac{\partial(uT)}{\partial x} + \frac{\partial(vT)}{\partial y} = \frac{\partial^2 T}{\partial x^2} + \frac{\partial^2 T}{\partial y^2} \quad (2)$$

$$\frac{\partial^2 \Psi}{\partial x^2} + \frac{\partial^2 \Psi}{\partial y^2} = -\Omega \quad (3)$$

$$u = \frac{\partial \Psi}{\partial y}; \quad v = -\frac{\partial \Psi}{\partial x} \quad (4)$$

$$(x, y) = \left(\frac{x'}{H'}, \frac{y'}{H'} \right); \quad (u, v) = \left(\frac{u'H'}{\alpha}, \frac{v'H'}{\alpha} \right)$$

where

$$(t, T) = \left(\frac{t' \alpha}{H'^2}, \frac{(T' - T'_C)}{(T'_H - T'_C)} \right); \quad (\Psi, \Omega) = \left(\frac{\Psi'}{\alpha}, \frac{\Omega' H'^2}{\alpha} \right) \quad (5)$$

are the nondimensional variables.

2.2 Boundary Conditions. The velocity boundary conditions are based on the assumption that the walls are rigid and impermeable and that the trapped air does not sleep on the walls. In terms of stream function, this assumption can be translated to $\Psi=0$ at all surfaces. The temperature boundary conditions are established with a prescribed hot temperature T'_H at the hot portion of the bottom wall and a prescribed cold temperature T'_C at the cold upper wall. On the other hand, the temperature of the insulated vertical walls and the rest of the bottom wall results from a surface energy balance considering that the net radiative heat flux arriving to the surface equals the heat flux transferred from the surface to the surrounding air

$$\frac{\partial T}{\partial x} + N_r Q_r = 0 \quad \text{for the insulated vertical surfaces}$$

$$\frac{\partial T}{\partial y} + N_r Q_r = 0 \quad \text{for the insulated elements of the bottom surface}$$

In these energy balances, the radiative heat transfer between the surfaces (left term of the equality) is modeled assuming a nonparticipating medium to radiation, infinite surfaces in the third direction, and grey-diffuse surfaces with identical emissivity value. The assumption of the infinite surfaces ignores the radiation out of the ends of the cavity in the direction perpendicular to the paper.

Notice that the vorticity boundary conditions are obtained using the well-known formulas of Woods [17].

2.3 Radiosity Formulation. The nondimensional radiosity equation for the i th element on each wall is given by

Table 1 Grid independence in the case of S_1 for various Ra and ϵ

Ra	ϵ	Mesh	Ψ_{\max}	Ψ_{\min}	Nu_{conv}	Nu_{rad}	Nu
2×10^6	0	61×61	106.95	-11.23	6.98	0	6.98
		81×81	106.06	-10.93	6.92	0	6.92
		101×101	105.65	-10.81	6.90	0	6.90
6.7×10^5	0.5	61×61	57.04	-5.31	4.44	4.77	9.22
		81×81	56.91	-5.25	4.36	4.71	9.08
		101×101	56.85	-5.24	4.33	4.68	8.97
3×10^5	1.0	61×61	37.09	-2.69	3.38	8.21	11.60
		81×81	36.88	-2.62	3.32	8.16	11.45
		101×101	36.77	-2.59	3.31	8.14	11.39

$$G_i = (1 - \epsilon_i) \sum_{S_j} F_{ij} G_j + \epsilon_i \left(\frac{T_i}{\theta} + 1 \right)^4 \quad (6)$$

In the above equation, the summation over the surface element S_j is to be taken for all the elements of the boundary with which the element i can interact radiatively. The view factors F_{ij} between the elements i and j are determined using Hottel's crossed string method [18]. The dimensionless radiant heat flux Q_r is then calculated by the expression

$$Q_r = \epsilon_i \left[\left(1 + \frac{T_i}{\theta} \right)^4 - \sum_j F_{ij} G_j \right] \quad (7)$$

2.4 Heat Transfer Relations. The average heat transfer coefficients h_{cv} for convection and h_{rad} for radiation can be represented in dimensionless form by the proper Nusselt numbers. The average normalized Nusselt numbers along the horizontal active walls are respectively calculated as

$$Nu_{\text{cv}} = \frac{Q_{\text{cv}}}{Q_{\text{cd}}} = \frac{1}{Q_{\text{cd}}} \int_{\text{wall}} \left. \frac{\partial T}{\partial y} \right|_{y=0,1} dx \quad (8)$$

$$Nu_{\text{rad}} = \frac{Q_{\text{rad}}}{Q_{\text{cd}}} = \frac{1}{Q_{\text{cd}}} \int_{\text{wall}} N_r Q_r |_{y=0,1} dx \quad (9)$$

Here, Q_{cd} is the dimensionless heat transfer by pure conduction calculated by the same expression as Q_{cv} in the conduction regime. Hence, the total average Nusselt number would be written in additive form as

$$Nu = Nu_{\text{cv}} + Nu_{\text{rad}} \quad (10)$$

3 Numerical Model

3.1 Solution Procedure. The system of governing equations together with the associated boundary conditions are solved numerically using a classical finite difference method. In the discretization of the governing equations, an implicit scheme, based on the ADI method (alternating direction implicit), was used to obtain a system of coupled algebraic equations that must be solved simultaneously. Each time step is achieved in two time steps and with this manner, the ADI method treats implicitly one direction each half time step and leads to tridiagonal systems that can be solved efficiently by using TDMA (tridiagonal matrix algorithm).

The first and second derivatives were evaluated by means of central differences and the time derivatives by a forward difference. The vorticity transport and energy equations were written in conservative form for the nonlinear convective terms in order to preserve conservative properties. The Poisson equation was solved later by the point successive over-relaxation method

Table 2 Grid independence in the case of S_2 for $Ra=8 \times 10^4$ and $\epsilon=1.0$

Mesh	Ψ_{\max}	Ψ_{\min}	Nu_{conv}	Nu_{rad}	Nu
61×61	10.88	-11.63	2.32	5.63	7.95
81×81	10.66	-11.88	2.26	5.69	7.96
101×101	10.53	-12.03	2.28	5.70	7.98

(PSOR). To solve the system of discretized equations and their respective boundary conditions, an algorithm of solution using Fortran 90 is implemented.

3.2 Numerical Code Validation. In the absence of thermal radiation, the numerical code was validated against the results of the benchmark results of De Vahl Davis [19], in terms of average Nusselt number and maximum stream function obtained in the case of a cavity differentially heated. Good agreement was observed in the range of the Rayleigh numbers considered; the maximum differences being 2.69% and 0.84%, respectively, in terms of Nu and Ψ_{\max} . When surface radiation is considered, the results of the numerical code were tested against those obtained by Akiyama and Chong [7] by comparing the average convective Nusselt number at the hot wall for Ra varying in the range [10^3 , 10^6]. Differences within 0.62% and 2.3% were observed for $\epsilon=0$ and 1, respectively. The numerical code was also validated with results obtained by Ramesh et al. [13] in terms of temperature profiles calculated along the adiabatic horizontal walls of a differentially heated square cavity. The agreement between the plotted temperature profiles was excellent.

The accuracy of the numerical results was checked through numerous detailed tests on the grid size effect. Important parameters such as maximum values of stream function and convective and radiative average Nusselt numbers were calculated for several grids and thereafter compared. The grid for the results reported in this paper is chosen such that the maximum relative changes in terms of Ψ_{\max} , Ψ_{\min} , Nu_{cv} , Nu_{rad} , and Nu, were, respectively, within 4.4, 4.6, 2.5, 1.9, and 2.78% for each emissivity and for the highest values of Rayleigh. This collection of results is summarized in Tables 1–3 respectively for the solutions of S_1 , S_2 , and S_3 types. Based on the numerical experiments, the computational mesh that renders grid independent solutions is 61×61 uniform segments.

4 Results and Discussion

Fluid motion was set up in the square cavity by heating the central part of the bottom wall over a length $H'/2$ (half of the bottom walls length) with a uniform temperature T'_H while maintaining the upper wall at a uniform cold temperature T'_C . The remaining part of the bottom wall together with the vertical walls were assumed thermally insulated from the surrounding. The thermophysical properties of the air ($Pr=0.71$) were evaluated at the reference temperature $T'_0=341.3$ K, while the temperature ratio was fixed at $\theta=T'_0/(T'_H-T'_C)=5.604$. The numerical simulations were performed for Rayleigh number and emissivity of the surfaces varying in the ranges $10^3 \leq Ra \leq 4 \times 10^6$ and $0 \leq \epsilon \leq 1$, respectively. The influence of these parameters on the multiplicity

Table 3 Grid independence in the case of S_3 for $Ra=2 \times 10^6$ and $\epsilon=0.1$ ($\epsilon \leq \epsilon_c$)

Mesh	Ψ_{\max}	Ψ_{\min}	Nu_{conv}	Nu_{rad}	Nu
61×61	49.63	-53.77	4.60	1.35	5.96
81×81	47.79	-51.64	4.56	1.33	5.89
101×101	47.51	-51.36	4.55	1.33	5.88

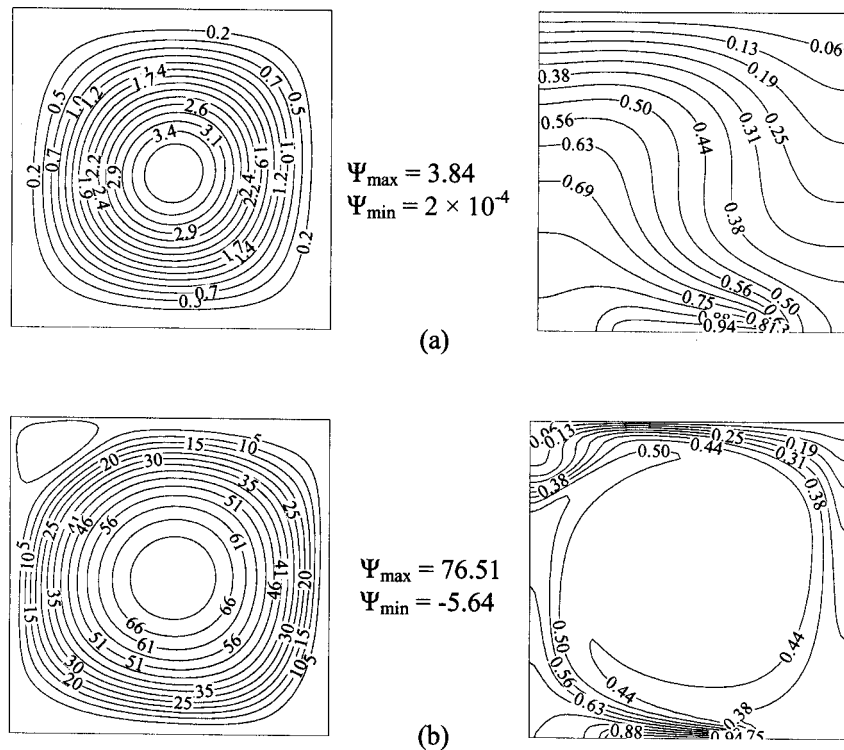


Fig. 2 Streamlines and isotherms obtained in the case of S_1 for $\varepsilon=0$: (a) $Ra=5 \times 10^3$ and (b) $Ra=10^6$

of solutions and also on their existence ranges was among the main objectives of this study. In previous studies, the existence of three possible steady-state solutions, excluding their solution images through plan mirrors, was proved numerically in similar geometries both in the absence (Hasnaoui et al. [14]) and in the presence (Ridouane et al. [15]) of surface radiation. These solutions will be named hereafter S_1 , S_2 , and S_3 . The discussion of the results is divided into three sections. Each section is focused on the effects of the aforementioned parameters on the flow structure, critical values characterizing transitions from a steady-state solution to another or to the unsteady regime, as well the convective and radiative contributions to the global heat transfer across the cavity. The results are compared to those obtained by the authors in an earlier work within a square cavity totally heated from below (Ridouane et al. [15]). This will shed some light on the effect of the heated length of the bottom wall on the flow and thermal fields in an air-filled square cavity.

4.1 Solution of S_1 Type. In the absence of surface radiation, streamlines and isotherms, obtained for relatively low and high Rayleigh numbers, are presented in Figs. 2(a) and 2(b). For $Ra = 5 \times 10^3$, streamlines of Fig. 2(a) (on the left) show that the flow is organized in a single vortex rotating in the clockwise direction. The corresponding isotherms show weak convection effect; they characterize a situation for which the conduction regime is still dominating. The vortex moves warm fluid from the hot element along the left insulated vertical wall which results in higher temperature gradients at the left part of the cavity. At higher Rayleigh number, Fig. 2(b) shows, for $Ra=10^6$, that the increase of Ra leads to the appearance of a secondary vortex located in the upper left corner of the cavity. This secondary flow, turning in the trigonometric direction, is engendered by the viscous effects. In addition to the new vortex location, the strength of the main cell is also increased as indicated by the magnitude of the extreme values of Ψ , which leads to more complex structure of the isotherms. High temperature gradients are observed near the active walls whereas the core region of the cavity is isothermal indicating the predomi-

nance of convection at this Rayleigh number value. For the sake of differentiation with the other solutions, this solution is referred to as a solution of S_1 type. The buoyant flow corresponding to S_1 remains steady for a wide range of Ra ($10^3 \leq Ra \leq 2.3 \times 10^6$). Above the upper value of Ra in this range, a pitchfork bifurcation occurs and the flow pattern becomes bi-cellular of S_3 type (see Sec. 4.3 for more details).

For $Ra=10^5$, streamlines and isotherms are presented in Figs. 3(a)–3(c), respectively, for $\varepsilon=0, 0.5$, and 1 to illustrate the effect of the emissivity on the flow characteristics in the case of S_1 . By increasing the emissivity, the intensity of the main vortex (Ψ_{\max}) is reduced while that of the secondary flow (Ψ_{\min}) is enhanced. Qualitatively, the changes observed in the flow structure are characterized by the flatness of the extreme streamlines of the main cell, just behind the left upper corner, indicating that the increase of ε precipitates the appearance of the secondary vortex and supports it. In addition, the associated thermal fields reveal some interesting aspects; the increase of ε leads to a better homogenization of temperature inside the cavity and engenders a significant qualitative change on the temperature distribution inside the cavity.

In the case of S_1 (unicellular flow), the increase of the Rayleigh number up to a critical value leads to a supercritical pitchfork bifurcation characterizing a transition towards a bicellular flow of S_3 type for $\varepsilon \leq 0.1$. However, a transition toward oscillatory regimes is observed for $\varepsilon > 0.1$. The critical values of Rayleigh, Ra_c , at which these transitions are observed, are summarized in Table 4 for various values of ε . It can be seen from this table that Ra_c decreases by increasing the emissivity of the walls. This result is a consequence of the presence of the secondary vortex, favored by the increase of ε as it is confirmed by the streamlines of Fig. 3. Comparison of Ra_c corresponding to both cavities partially heated (PH) and totally heated (TH) from below is given in Fig. 4 for ε varying in its wide range. For a given ε , the transition toward the unsteady flows is precipitated in the case of the partial heating and for both heating conditions, Ra_c decreases by increasing ε . This

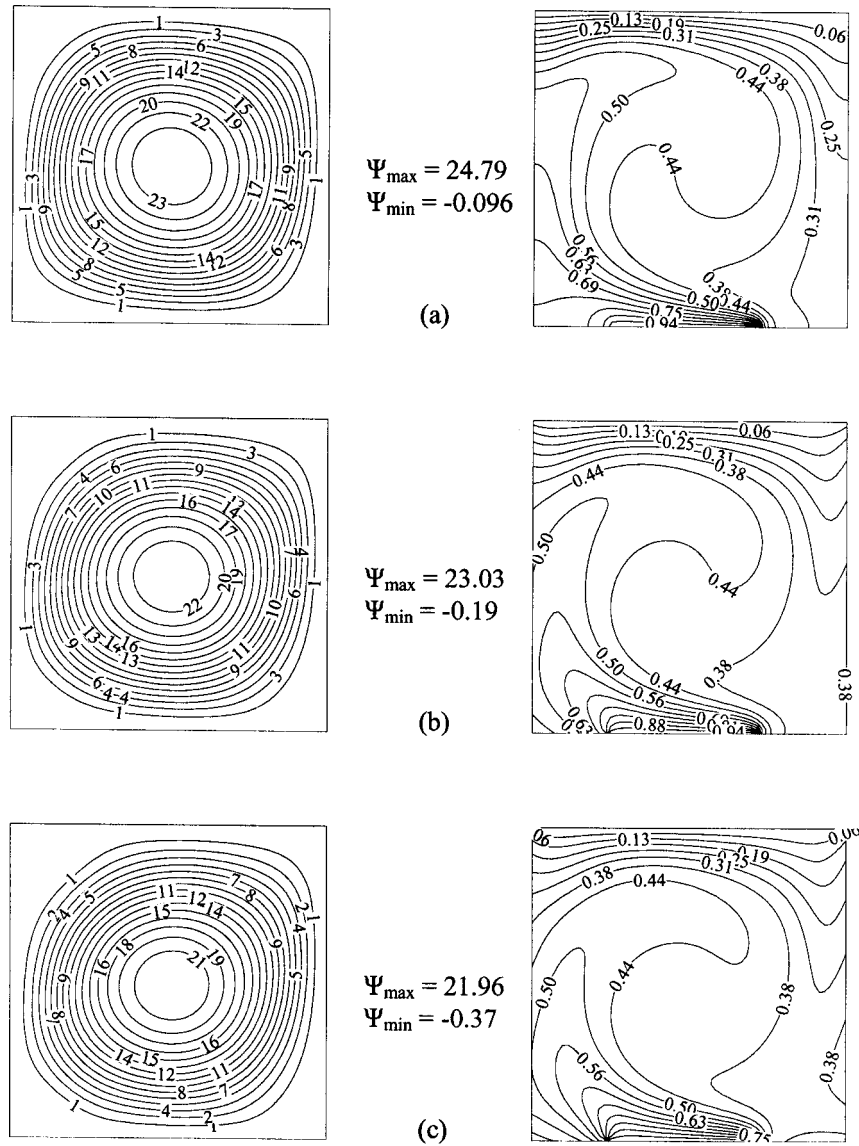


Fig. 3 Emissivity effect on the S_1 patterns at $Ra=10^5$: (a) $\varepsilon=0$, (b) $\varepsilon=0.5$, and (c) $\varepsilon=1.0$

means that the existence range of S_1 in its steady form is notably reduced by increasing ε . The gap between the two curves is also reduced for relatively high emissive walls ($\varepsilon \geq 0.6$), indicating that the effect of the heated length on the Ra_c is more pronounced in the subinterval ($0.1 \leq \varepsilon \leq 0.6$).

The response of the mean Nusselt number Nu to the increase of the Rayleigh number is displayed in Fig. 5 for selected values of ε corresponding to polished, moderately, and highly emissive walls ($\varepsilon=0, 0.5$, and 1). It is seen from the figure that Nu in-

Table 4 Critical values of Ra characterizing the transition of S_1 toward the oscillatory regime for various ε

ε	Ra_c
0.0	2.3×10^6
0.2	1.4×10^6
0.5	6.8×10^5
0.8	4.15×10^5
1.0	3.3×10^5

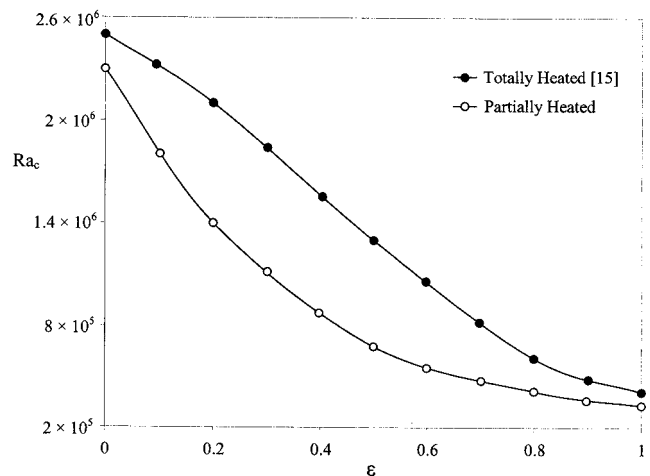


Fig. 4 Variations of Ra_c with the emissivity for both partially and totally heated cavities

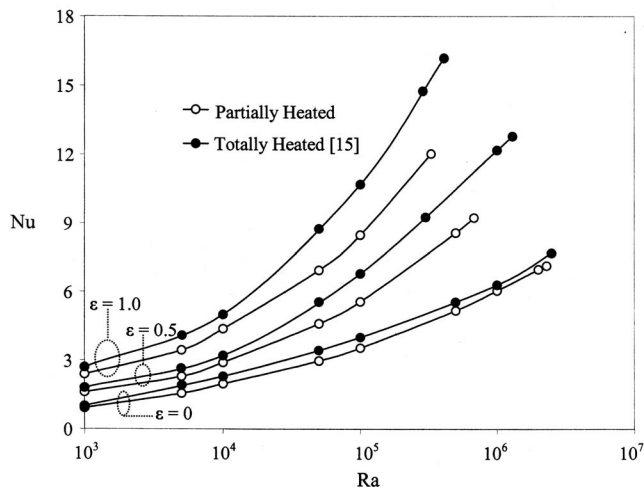


Fig. 5 Comparison of the global Nusselt numbers obtained for both heating conditions in the case of S_1

increases monotonically with Ra and ε , and the effect of the latter is more pronounced at high values of Ra . Figure 5 also emphasizes the effect of the heated area on the overall quantity of heat, transferred from the hot wall to the fluid medium, by presenting the variations of Nu versus Ra and ε corresponding to the cavity totally heated [15]. For a fixed ε , the Nu curve representative of the PH cavity lies underneath its counterpart curve of the TH cavity. The difference between the two curves is minimal at low Ra ; when the process of heat transfer is dominated by conduction. However, as Ra increases, the natural convection dominates over the conduction and this separation climbs up gradually. In addition, for a fixed Ra , it is seen that this difference grows also with the emissivity ε .

The contribution of radiation Nu_{rad} to the overall heat transfer, characterized by Nu , is quantified for different values of Ra and ε

Table 5 Percent of radiation contribution to Nu in the case of S_1

ε	10^3	5×10^3	10^4	5×10^4	10^5	5×10^5	10^6
0.2	21.01	21.73	22.77	23.07	23.75	26.54	28.07
0.5	41.61	43.39	45.51	46.73	47.66	50.81	—
0.8	55.34	60.26	61.55	61.9	62.41	—	—
1.0	62.76	65.93	67.96	68.77	69.45	—	—

and the obtained results are presented in Table 5. From the latter, it can be deduced that the heat transfer becomes dominated by radiation for $\varepsilon > 0.5$. More precisely, the radiation contributes only by about 20–30% for $\varepsilon = 0.2$. In contrast, the contribution of radiation for $\varepsilon = 1$ surpasses 62% for all values of Ra . Moreover, for a fixed value of ε , this contribution increases slightly with Ra .

4.2 Solution of S_2 Type. The solution of S_2 type, is illustrated in Fig. 6 for two values of Ra in the absence of the walls radiation ($\varepsilon = 0$). In Fig. 6(a), the flow structure, obtained for $Ra = 2 \times 10^5$, is symmetrical with respect to the midplane of the cavity. The flow rises in the central region of the enclosure (hot stream) and falls along each insulated vertical wall (cold stream) creating mirror image structures that rotate clockwise in the right half and counterclockwise in the left half of the cavity. Both vortices rotate with the same strength $\Psi_{ext} = 19.73$. The corresponding isotherms show an important heat transfer between the active horizontal walls and the working fluid, mainly in the regions where the hot ascending stream and the cold descending stream enter in contact with these walls. By increasing gradually Ra from $Ra = 2 \times 10^5$, the boundary layer gets thinner and the vortices strengths grow as a result of the higher fluid velocities which contributes to increase the overall heat transfer. This tendency is maintained as long as the Rayleigh number value increases below the critical value $Ra_2 = 3.6 \times 10^5$. Above this threshold value of Ra , the flow becomes oscillating in the range $[Ra_2, Ra_3]$ where $Ra_3 = 9.8 \times 10^5$. Further increase of Ra

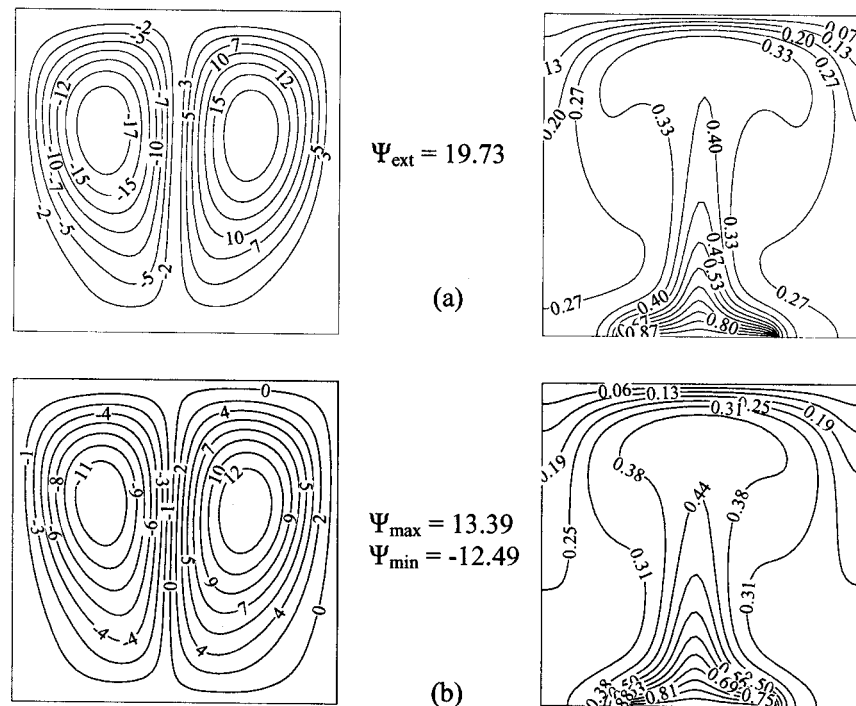


Fig. 6 Streamlines and isotherms obtained in the case of S_2 for $\varepsilon = 0$: (a) $Ra = 2 \times 10^5$ and (b) $Ra = 9.3 \times 10^4$

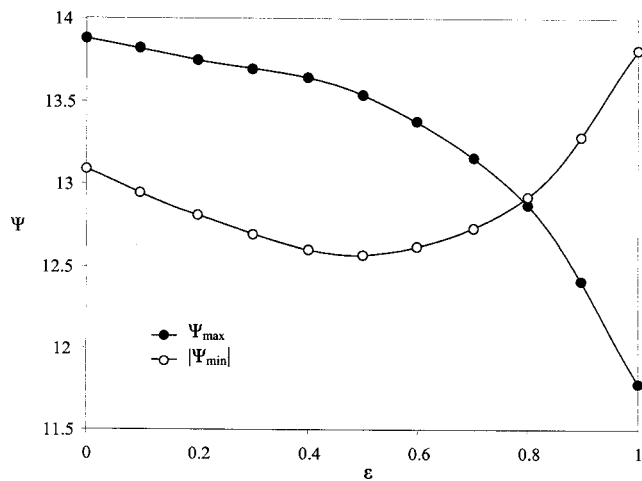


Fig. 7 Extremum values of the stream function for the S_2 type solution as a function of walls emissivity at $Ra=10^5$

from Ra_3 leads to a steady-state solution of S_1 type while a decrease of this parameter from $Ra=2 \times 10^5$, leads to an increase of the size of one vortex to the detriment of the other one; breaking up the symmetry of the solution. This behavior is amplified as the value of Ra is reduced until the latter reaches another critical value $Ra_1=9.3 \times 10^4$. Below Ra_1 , the solution of S_2 type disappears and the flow patterns becomes unicellular of S_1 type. The bi-cellular asymmetrical solution of S_2 type is illustrated in Fig. 6(b) for $Ra=Ra_1$ where a slight but a visible asymmetry can be observed.

To illustrate the effect of the emissivity on the bicellular flow characteristics, the value $Ra=10^5$ was selected. For this particular value of Ra , the solution S_2 remains steady for the whole range of ϵ . Maximum and minimum values of Ψ (Ψ_{\max} and Ψ_{\min}), characterizing, respectively, the strengths of the right clockwise and left counterclockwise vortices, are plotted against the emissivity ϵ in Fig. 7. At low values of ϵ , the strength of the clockwise vortex Ψ_{\max} is higher than its counterpart Ψ_{\min} of the counterclockwise vortex resulting in a nonsymmetrical flow structure. The increase of ϵ is accompanied by a decrease of both $|\Psi_{\min}|$ and Ψ_{\max} until $\epsilon = 0.5$, for which the minimum of $|\Psi_{\min}|$ is reached. Above this threshold value of ϵ , the $|\Psi_{\min}|$ curve climbs up gradually while Ψ_{\max} continues to decrease with an increasing rate. The intersection of the two curves occurs around $\epsilon = 0.8$. At this particular point, the solution becomes symmetrical with respect to the mid-plane but the symmetry does not stay longer; it is destroyed quickly by any increase of ϵ above 0.8. Then, the counterclockwise vortex expands toward the center of the cavity pushing the other vortex to the right part of the cavity. This tendency is enhanced by increasing ϵ towards unity.

The radiation effect on the critical values of Ra (Ra_i , $i=1, 2, 3$), characteristic of the bi-cellular flow of S_2 type, are listed in Table 6. It is to notice that the solution S_2 was obtained in a small range $[Ra_1, Ra_2]$ of Ra which is depending on ϵ . An unsteady convection, characterized by sustained periodic oscillations, was ob-

Table 6 Critical Rayleigh numbers corresponding to S_2

ϵ	Ra_1	Ra_2	Ra_3
0.0	9.3×10^4	3.6×10^5	9.8×10^5
0.2	2×10^4	1.6×10^5	6.5×10^5
0.5	1.5×10^4	1.7×10^5	6.4×10^5
0.8	1.5×10^4	1.4×10^5	8×10^5
1.0	1.5×10^4	1.2×10^5	—

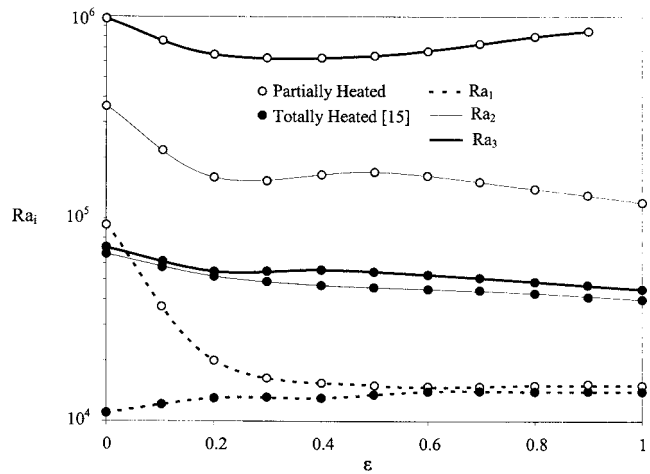


Fig. 8 Variations of Ra_i ($i=1, 2, 3$) with ϵ for both partially and totally heated bottom wall

served in the range $[Ra_2, Ra_3]$. For $Ra < Ra_1$ or $Ra > Ra_3$, the flow becomes unicellular of S_1 type excluding the case of $\epsilon=1$ for which, sustained periodic oscillations are observed for $Ra > Ra_2$ and the solution becomes chaotic for higher Ra numbers. The variations of these critical values of Ra versus ϵ are depicted in Fig. 8 and compared with those of TH cavity [15]. It is seen from this figure that the existence range of S_2 is smaller in the case where the cavity is totally heated compared to the partial heating case and, globally, both ranges $[Ra_1, Ra_2]$ and $[Ra_2, Ra_3]$ of Ra are significantly reduced when the lower boundary is totally heated. For the last case also, Ra_2 and Ra_3 are lower than those corresponding to the partial heating conditions for which the transition toward the oscillating convection is retarded compared to the former case. The examination of the Ra_1 curves shows that the radiation effect on the variation of Ra_1 is significant only in the range $[0, 0.3]$ of ϵ . Outside this range, the effect of the walls radiation becomes limited on Ra_1 and the difference between the Ra_1 curves, corresponding to both heating conditions, is limited.

The combined effect of Ra and ϵ on the overall heat transfer is illustrated in Fig. 9 where the plots are limited to the ranges of Ra for which the steady-state solution of S_2 type exists. These ranges are strongly dependent on the selected values of ϵ and the heating conditions. For all values considered for ϵ , the variations of Nu , plotted against Ra , are characterized by linear variations with different slopes. In Fig. 9, the results corresponding to the cavity totally heated [15] are also included for comparison purposes. Physically, a decrease in the heated area results in a decrease of the quantity of heat transferred from the hot surface to the fluid. Consequently, for a given ϵ , Nu corresponding to the total heating is higher than that obtained in the case of a partial heating in the ranges of Ra where S_2 exists for both heating conditions. However, the reduction by 50% of the heated area is accompanied by only a maximum reduction of 16% as relative difference in terms of Nu . In addition, the existence range of S_2 corresponding to the partial heating becomes larger in the presence of radiation while the opposite is seen in pure thermal natural convection ($\epsilon=0$). The quantitative contribution of radiation to the overall heat transfer is summarized in Table 7 for various Ra and ϵ . It is seen that the contribution of radiation is rather controlled par the parameter ϵ and stays almost unaffected by the Rayleigh number. Hence, the contribution of radiation increases by increasing ϵ to reach a maximum of 69.89% for $\epsilon=1$ and $Ra=1.5 \times 10^4$.

4.3 Solution of S_3 Type. When the Rayleigh number is gradually increased, in the absence of radiation effect ($\epsilon=0$), the unicellular flow of S_1 type is maintained until the reach of a critical value $Ra_c=2.3 \times 10^6$. Above this threshold, a transition toward

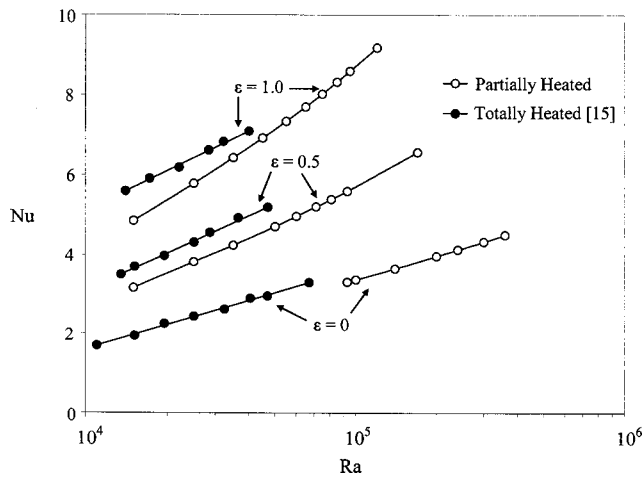


Fig. 9 Comparison of the global Nusselt numbers obtained for both heating conditions in the case of S_2

another steady-state solution occurs. The latter is bicellular, characterized by the presence of two horizontal vortices (one above the other). Figure 10(a) illustrates this type of solution, hereafter referred to as a solution of S_3 type, for $Ra=4 \times 10^6$. Each vortex is in contact with only one active wall. The structure of the isotherms shows that the heat is transferred from the heated element to the lower vortex, then from the lower vortex to the upper one, and finally from the latter to the cold wall as testified by the presence of sharp gradients near the active walls and between the vortices. In addition, the central part of each half of the cavity, containing the horizontal vortices, is isothermal. An increase of Ra above Ra_c is favorable to S_3 as long as Ra remains lower than another critical value $Ra_6=4 \times 10^6$, above which a transition toward an oscillatory regime is observed. It is useful to point out that, any decrease of Ra in the range $[Ra_c, Ra_6]$ with the use of initial conditions favorable to S_3 , leads to a steady solution of S_3

Table 7 Percent of radiation contribution to Nu in the case of S_2

ε	Ra	1.5×10^4	2.5×10^4	3.5×10^4	5×10^4	7.5×10^4	9.3×10^4	1.2×10^5
0.2	—	—	24.42	23.84	23.59	23.91	24.27	25.26
0.5	48.73	46.59	46.22	46.28	46.44	47.14	48.40	—
0.8	63.11	60.93	60.47	60.40	60.64	61.20	61.96	—
1.0	69.89	67.87	67.34	67.34	67.62	67.90	68.23	—

type. By decreasing Ra below Ra_c and using initial conditions favorable to S_3 , a new transition happens at $Ra < Ra_5=4 \times 10^5$. This transition is to the unicellular flow of S_1 type and occurs via an oscillatory regime of S_3 type in the range $[Ra_4, Ra_5]$. Figure 10(b) presents streamlines and isotherms for $Ra=Ra_5=4 \times 10^5$ just before the transition. Compared to Fig. 10(a), the strength of the vortices is reduced and the thickness of the boundary layers is larger.

When the surface radiation is considered, the solution of S_3 type is obtained only in a small range of ε . In fact, there exists a critical value $\varepsilon_c=0.1$ of ε above which, the solution S_3 disappears. Special efforts have been devoted to determine this critical value with 5% as maximum relative error. The tests were conducted by decreasing ε from 1 toward 0.1 with very small steps when necessary but it was found that this kind of solution does not exist at any intermediate value of ε between 1 and 0.1 even at $\varepsilon=0.105$. Therefore, the existence range of this solution, $[Ra_5, Ra_6]$, is highly affected by the emissivity; this range of Ra is reduced from $[4 \times 10^5, 4 \times 10^6]$ at $\varepsilon=0$ to $[1.65 \times 10^6, 2 \times 10^6]$ at $\varepsilon=0.1$. Note that $\varepsilon_c=0.22$ in the case of a cavity totally heated from below [15], and this critical value of ε is reduced to 0.1 in the case of the PH. In fact, the reduction of the heated surface length is accompanied by a reduction of the range of ε corresponding to the existence of S_3 . Table 8 illustrates the critical values Ra_i ($i=4, 5, 6$) characterizing different events observed in the case of S_3 for $\varepsilon=0$ and 0.1. It can be seen from this table that the radiation tends

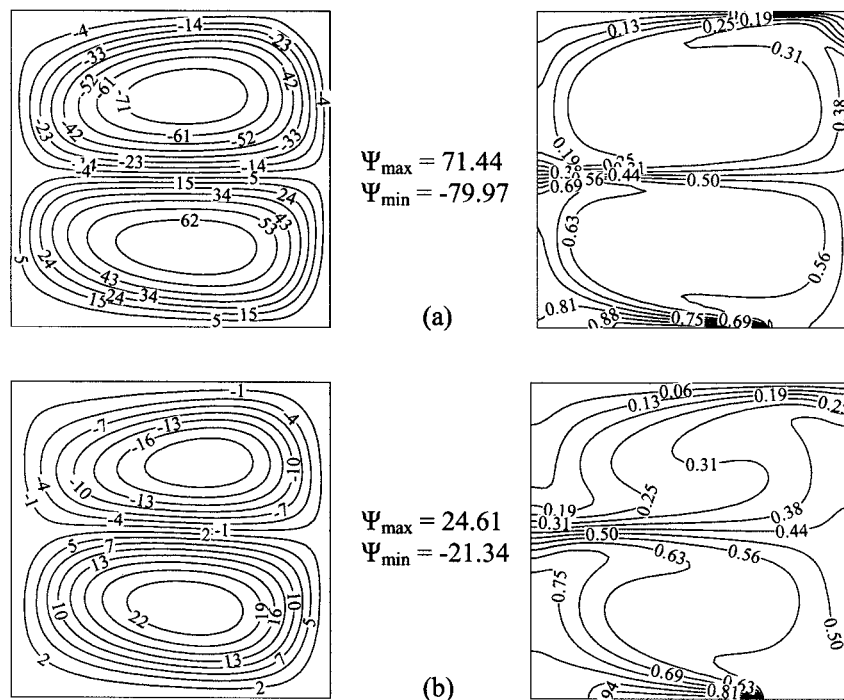


Fig. 10 Streamlines and isotherms obtained in the case of S_3 for $\varepsilon=0$: (a) $Ra=4 \times 10^6$ and (b) $Ra=4 \times 10^5$

Table 8 Critical values of Rayleigh corresponding to S_3

ε	Ra_4	Ra_5	Ra_6
0.0	3.4×10^5	4×10^5	4×10^6
0.1	1.65×10^6	1.65×10^6	2×10^6

to reduce the intervals between these critical values. At $\varepsilon=0.1$, Ra_4 and Ra_5 are identical and the transition from S_3 to S_1 occurs without oscillations.

The heat transfer results corresponding to S_3 are depicted in Fig. 11 for both heating conditions using the results of [15] for the cavity totally heated. The variations of Nu are characterized by a monotonous increase with Ra in the existence range of S_3 and, for both values of the emissivity, Nu corresponding to the TH cavity is higher than that of the PH cavity. In addition, the effect of ε on the global heat transfer is significant in spite of the fact that the highest value used for this parameter is small to ensure the obtaining of S_3 for both heating conditions. An interesting feature that can be deduced from this figure concerns the existence range of S_3 which is largely reduced in the case of the PH cavity. This deduction is attributed to the fact that the reduction of the surface heating does not support the horizontal structure of the cells and it is expected that the flow structure of S_3 type would disappear when the length of the heated element reaches some critical value (not determined here). The heat transfer engendered by S_3 is dominated by convection since its existence range is restricted to low values of ε . The contribution of radiation to the overall heat transfer is summarized in Table 9 for $\varepsilon=\varepsilon_c=0.1$. This contribution does not change with the Rayleigh number and stays around 22.5%.

5 Conclusions

Numerical results for laminar natural convection with surface radiation in an air-filled square enclosure partially heated from below are presented for wide ranges of both the Rayleigh number and the surface emissivity. Equations of mass, momentum, and energy have been solved using constant properties and Boussinesq

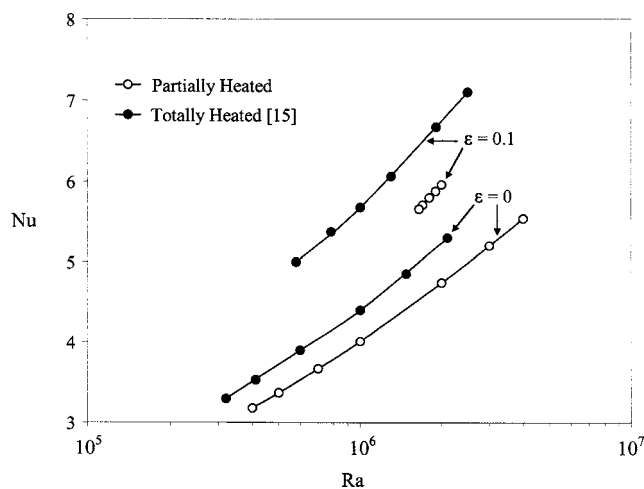


Fig. 11 Comparison of the global Nusselt numbers obtained for both heating conditions in the case of S_3

Table 9 Percent of radiation contribution to Nu in the case of S_3 for $\varepsilon=0.1$ ($\varepsilon \leq \varepsilon_c$)

Ra	2×10^6	1.9×10^6	1.8×10^6	1.7×10^6	1.65×10^6
% radiation	22.43	22.50	22.58	22.62	22.65

approximation. The effect of surface radiation on the multiple solutions obtained in the pure natural convection regime ($\varepsilon=0$) and also on the transition from a steady-state solution to another or to the oscillatory regime is investigated. In the absence of surface radiation, three steady-state solutions have been obtained using appropriate initial perturbations. Unicellular flow of S_1 type is found to exist over a wide range of Ra, while bicellular flows of S_2 and S_3 types have been obtained at relatively low and high values of Ra, respectively. When the surface radiation is considered, the solutions of S_1 and S_2 types are obtained for different values of the emissivity but their existence ranges in terms of Ra is reduced as ε is increased. For the solution of S_3 type, there exists a critical value of the emissivity $\varepsilon_c=0.1$, above which the solution of S_3 type disappears. The transition from S_2/S_3 to S_1 occurs via an oscillatory regime in the range $[Ra_2, Ra_3]/[Ra_4, Ra_5]$ which is strongly dependent on ε . The transition from S_2 to S_1 ($Ra < Ra_1$) or from S_1 to S_3 ($Ra > Ra_c$ and $\varepsilon \leq \varepsilon_c$) occurs suddenly without any oscillations. In terms of heat transfer variations, the global Nusselt number Nu increases monotonically with Ra. For fixed Ra and ε ($\varepsilon \leq \varepsilon_c$), the solution of S_3 type is found to generate less heat than S_1 and S_2 and the percent differences go up to 33% and 24% at $\varepsilon=0$ and 0.1, respectively. The influence of the heated area of the bottom is also presented and characterized by smaller existence ranges of S_1 and S_3 and a larger existence range of S_2 when the heated area is reduced from TH to PH cavity. Also, the critical value of ε , ε_c , is reduced from 0.22 within TH cavity to 0.1 within PH cavity.

Nomenclature

- $F_{i,j}$ = view factor between segments i and j
- g = acceleration of gravity, m/s^2
- G_i = dimensionless radiosity of segment i , Eq. (6)
- h = average heat transfer coefficient, $W/K m^2$
- H' = height of cavity, m
- L' = width of cavity, m
- N_r = conduction-radiation number, $N_r = \sigma T_0^4 H' / \lambda (T_H' - T_C')$
- Nu = mean Nusselt number, Eq. (10)
- PH = refers to a cavity partially heated from below
- Pr = Prandtl number; $Pr = \nu / \alpha$
- Q_r = dimensionless radiative heat flux, Eq. (7)
- Ra = Rayleigh number, $Ra = g\beta(T_H' - T_C')H'^3 / (\nu\alpha)$
- t = dimensionless time
- T = dimensionless temperature, $T = (T' - T_C') / (T_H' - T_C')$
- T_0' = reference temperature, $T_0' = (T_H' + T_C') / 2$
- TH = refers to a cavity totally heated from below
- u, v = dimensionless velocities in x and y directions
- x', y' = horizontal and vertical coordinates, m

Greek Letters

- α = thermal diffusivity, m^2/s
- β = coefficient of thermal expansion, $1/K$
- ε = surface emissivity
- λ = thermal conductivity, $W/K.m$
- ν = kinematic viscosity, m^2/s
- ρ = density, kg/m^3
- θ = temperature ratio, $\theta = T_0' / (T_H' - T_C')$
- σ = Stefan-Boltzmann constant, $\sigma = 5.67 \times 10^{-8} W m^2 K^4$
- Ω = dimensionless vorticity
- Ψ = dimensionless stream function

Subscripts

- c = critical value
- C = cold
- cd = conduction

cv = convection
 H = hot
max = maximum value
min = minimum value
rad = radiation

Superscript

' = dimensional variables

References

- [1] Chong, L. C., Yang, K. T., and Lloyd, J. R., 1983, "Radiation-Natural Convection Interactions in Two-Dimensional Complex Enclosures," *J. Heat Transfer*, **105**(1), pp. 89–95.
- [2] Webb, B. W., and Viskanta, R., 1987, "Analysis of Radiation-Induced Natural Convection in a Rectangular Enclosure," *J. Thermophys. Heat Transfer*, **1**(2), pp. 146–153.
- [3] Siegel, R., and Howell, J. R., 1981, *Thermal Radiation Heat Transfer*, 2nd ed., McGraw-Hill, New York.
- [4] Modest, M. F., 2003, *Radiative Heat Transfer*, 2nd ed., Academic Press, CA.
- [5] Balaji, C., and Venkateshan, S. P., 1993, "Interaction of Surface Radiation with Free Convection in a Square Cavity," *Int. J. Heat Fluid Flow*, **14**(3), pp. 260–267.
- [6] Balaji, C., and Venkateshan, S. P., 1994, "Correlations for Free Convection and Surface Radiation in a Square Cavity," *Int. J. Heat Fluid Flow*, **15**(3), pp. 249–251.
- [7] Akiyama, M., and Chong, Q. P., 1997, "Numerical Analysis of Natural Convection with Surface Radiation in a Square Enclosure," *Numer. Heat Transfer, Part A*, **31**, pp. 419–433.
- [8] Mezrhab, A., and Bchir, L., 1999, "Radiation-Natural Convection Interactions in Partitioned Cavities," *Int. J. Numer. Methods Heat Fluid Flow*, **9**(1), pp. 186–203.
- [9] Mahapatra, S. K., Sen, S., and Sarkar, A., 1999, "Interaction of Surface Radiation and Variable Property Natural Convection in a Differentially Heated Square Cavity—A Finite Element Analysis," *Int. J. Numer. Methods Heat Fluid Flow*, **9**(4), pp. 423–443.
- [10] Han, C. Y., and Baek, S. W., 2000, "The Effect of Radiation on Natural Convection in a Rectangular Enclosure Divided by Two Partitions," *Numer. Heat Transfer, Part A*, **37**, pp. 249–270.
- [11] Colomer, G., Costa, M., Consul, R., and Oliva, A., 2004, "Three Dimensional Numerical Simulation of Convection and Radiation in a Differentially Heated Cavity Using the Discrete Ordinates Method," *Int. J. Heat Mass Transfer*, **47**, pp. 257–269.
- [12] Ramesh, N., and Venkateshan, S. P., 1999, "Effect of Surface Radiation on Natural Convection in a Square Enclosure," *J. Thermophys. Heat Transfer*, **13**(3), pp. 299–301.
- [13] Ramesh, N., Balaji, C., and Venkateshan, S. P., 1999, "Effect of Boundary Conditions on Natural Convection in an Enclosure," *Int. J. Transp. Phenom.*, **1**, pp. 205–214.
- [14] Hasnaoui, M., Bilgen, E., and Vasseur, P., 1992, "Natural Convection Heat Transfer in Rectangular Cavities Partially Heated from Below," *J. Thermophys. Heat Transfer*, **6**(2), pp. 255–264.
- [15] Ridouane, E. H., Hasnaoui, M., Amahmid, A., and Raji, A., 2004, "Interaction Between Natural Convection and Radiation in a Square Cavity Heated from Below," *Numer. Heat Transfer, Part A*, **45**, pp. 289–311.
- [16] Ridouane, E. H., Hasnaoui, M., and Campo, A., 2006, "Effects of Surface Radiation on Natural Convection in a Rayleigh-Benard Square Enclosure: Steady and Unsteady Conditions," *Heat Mass Transfer*, **42**, pp. 214–225.
- [17] Woods, L. C., 1954, "A Note on Numerical Solution of Fourth Order Differential Equations," *Aeronaut. Q.*, **5**, pp. 176–184.
- [18] Hottel, H. C., and Sarofim, A. F., 1967, *Radiative Heat Transfer*, McGraw-Hill, New York.
- [19] De Vahl Davis, G., 1983, "Natural Convection of Air in a Square Cavity: A Benchmark Numerical Solution," *Int. J. Numer. Methods Fluids*, **3**, pp. 249–264.

Radiative Properties of Dense Fibrous Medium Containing Fibers in the Geometric Limit

R. Coquard

Ph.D. Student
Centre Scientifique et Technique du Bâtiment
(CSTB),
24 rue Joseph FOURIER,
38400 Saint Martin d'Hères,
France
e-mail: r.coquard@cstb.fr

D. Baillis

Assistant Professor
Centre de Thermique de Lyon (CETHIL),
UMR CNRS 5008,
Domaine Scientifique de la Doua,
INSA de Lyon,
Bâtiment Sadi Carnot,
9 rue de la Physique,
69621 Villeurbanne Cedex,
France

The aim of this paper is to investigate the dependent regime in dense fibrous materials with size parameters ranging in the geometric optics limit. We use a method based on a Monte Carlo procedure which permits one to identify the radiative properties of dispersed media. This method is applied to materials made of opaque or semitransparent randomly oriented long circular cylinders representing the fibers. The results permit us to investigate the limit of validity of independent scattering hypothesis and to analyze the evolution of the extinction coefficient, scattering albedo and phase function of the fibrous material with the porosity and the reflecting properties of the particles when the shadowing effect due to geometric sized objects is not negligible. We also propose a correlation to estimate the radiative properties in dependent regime from the results of the independent scattering hypothesis. Thereafter, the radiative characteristics obtained are compared to those predicted by previous authors. [DOI: 10.1115/1.2345426]

Keywords: fibrous media, radiative properties, geometric optics limit, dependent regime

1 Introduction

Heat transfer in fibrous materials and, more generally, in porous media, is a complex problem given that, in this kind of medium, different modes of transfer generally occur simultaneously. In particular, radiative heat transfer could contribute significantly to the total heat flux when the density of the media is relatively low. That is the reason why the problem of radiative heat transfer in dispersed media has been widely studied. Some extensive reviews were carried out by Viskanta and Mengüç in 1989 [1], and by Baillis and Sacadura in 2000 [2].

The key problem is then to determine the equivalent radiative properties of the porous medium characterizing its interaction with radiation. These properties are: the absorption coefficient, the scattering coefficient, and the scattering phase function which describes the angular repartition of the radiation scattered by the medium. The principle of the standard modeling techniques designed to determine these properties is to liken the porous material to an arrangement of particles of given shapes and sizes which permit one to reproduce the porous structure as faithfully as possible. In the case of fibrous materials, we can cite as examples the work of Lee [3], Jeandel et al. [4] on silica fibers or Milos and Marschall [5] on rigid fibrous ceramic insulation. In these studies, the authors considered that the material is made of an arrangement of infinite circular cylinders which can be randomly oriented or have particular orientations. Generally, it is also assumed that the distance between two neighboring fibers is sufficiently important to consider that they scatter radiation independently. The radiative properties of the fibrous medium could then be calculated by simply adding the contributions of all the particles forming the porous structure.

The independent scattering hypothesis gives accurate results when it is applied to highly porous materials. However, for dense porous materials, it breaks down due to two fundamental mechanisms:

- The near-field effect arising when the distance between two neighboring particles is not sufficient to consider

that their interactions with radiation are punctual and that they behave as if they were alone.

- The far-field effect resulting from the constructive/destructive interference between waves scattered by neighboring particles.

The limits of applicability of the theory of independent scattering in dispersed media have been experimentally investigated since the beginning of the 1970s by several authors, including Hottel et al. [6], Ishimaru and Kuga [7], and Brewster [8]. Brewster [8] and Yamada et al. [9] proposed a single criterion based on the value of the dimensionless number c/λ . Their results indicated that no dependent effect occurs as long as $c/\lambda > 0.3$ or 0.5 .

The studies on dependent scattering concerned especially beds of spherical particles. Kumar and Tien [10] proposed an analytical model to evaluate the dependent absorption and extinction characteristics of a homogeneous system of randomly positioned scattering spheres lying in the Rayleigh scattering regime (size parameter $x \ll 1$). Singh and Kaviany [11] examined dependent scattering in packed beds of large-size particles (geometric optics domain) by carrying out Monte Carlo simulations. They showed that the independent scattering theory could fail for systems with low porosity even when the c/λ criterion is satisfied and that dependent scattering can be significant even for porosities as high as 0.935. They also proposed a correlation in which the dependent characteristics for a bed of opaque spheres are obtained from their independent characteristics by scaling the optical thickness while leaving the albedo and the phase function unchanged. Coquard and Baillis [12] also conducted a study on dependent regime in packed beds of large spheres based on a Monte Carlo procedure. Their results were in close agreement with that of the correlation of Kaviany. Kamiuto [13] has proposed a heuristic correlated-scattering theory for packed beds consisting of relatively large spheres. Finally, other authors such as Jones et al. [14] and Baillis and Sacadura [15] studied experimentally the dependent scattering in packed beds.

With regards to fibrous materials, only few studies have been interested in the dependent scattering regime. Lee [16] developed formulations of radiative propagation through a medium of closely spaced parallel fibers at oblique incidence based on Maxwell's equations which take into account near field and far field effects. He demarcated the domains of dependent and independent

Contributed by the Heat Transfer Division of ASME for publication in the JOURNAL OF HEAT TRANSFER. Manuscript received June 13, 2005; final manuscript received March 3, 2006. Review conducted by Walter W. Yuen. Paper presented at the European Conference on Thermophysical Properties (ECTP) 2005.

scattering as a function of refractive index, diameter, and volume fraction of fibers. However, the study was restricted to parallel fibers. Kumar and White [17] examined the scattering properties of woven fibrous and then developed another approach to take into account the far-field effect in the case of normal incidence on parallel fibers. Nevertheless, they did not analyze the near-field effect and their approach was restricted to fibers lying in the Rayleigh scattering regime (size parameter $x \ll 1$).

The purpose of this work is to study the dependent regime in dense fibrous materials made of randomly oriented circular cylinders with diameter much greater than the wavelength of the radiation considered. Given the very large size parameter of these fibers, we assume that the distance between two neighboring particles (interparticle clearance) is large enough, when compared to the wavelength, to consider that the far-field interference effect is negligible even for low porosity. Moreover, the interaction of radiation with the fiber can be treated using the geometric optics laws. The radiative properties of materials with various porosities, fiber diameter, and optical properties are calculated using an identification method based on a three-dimensional ray tracing procedure similar to that presented by Coquard and Baillis for beds of opaque spheres [12] or beds of spheres containing an absorbing and scattering medium [18]. This method takes into account the shadowing effects due to the geometric sized objects. The results permit us to investigate the limit of applicability of independent scattering theory and to study the evolution of the extinction coefficient, scattering albedo, and scattering phase function of fibrous media made of opaque diffusively reflecting fibers or semitransparent specularly reflecting fibers. In each case, the results are compared to those from the independent scattering hypothesis and to the results of Lee [16].

2 Description of the Method

2.1 Hypotheses. Several hypotheses are employed in order for our method to be applicable. First, we assume that the diameter D_{fiber} of the cylindrical fibers composing the material is much greater than the wavelength λ of the thermal radiation studied (size parameter $x = 2 \cdot \pi \cdot R_{\text{fib}} / \lambda \gg 1$) and that the refractive index is not extremely small ($x \cdot |\tilde{n} - 1| \gg 1$). Thus, the radiation/matter interaction could be treated using the geometric optics laws.

Moreover, the influence of diffraction on the radiative heat transfer is neglected. Indeed, the diffraction phase function for large particles is predominantly oriented in the forward direction and diffracted rays are very close to transmitted rays. We then assume, here, that diffraction can be neglected and treated as transmission.

Given that the medium is made of randomly positioned and randomly oriented fibers, we also assume that the radiative properties calculated are independent of the azimuth angle (azimuthal symmetry).

Finally, we consider different types of fibers:

- Large opaque diffusely reflecting fibers: the reflectivity of the particle is the same whatever the direction of the incident ray is and the rays intercepted by a surface element of a particle could be reflected in all directions of the hemisphere with the same probability. The diffuse reflectivity is equal to the hemispherical reflectivity $\bar{\rho}$ of the solid phase contained in the particle. Moreover, all the rays which are not reflected are absorbed by the fiber.
- Large semitransparent and specularly reflecting fibers: the specular reflectivity strongly depends on the complex refractive index $\tilde{n} = n - i \cdot k$ of the solid phase as well as on the angle α between the incident ray and the normal to the surface. We only take into account dielectric fibers (imaginary part $k \ll$ real part n). The direction of the reflected θ_{refl} and refracted θ_{refr} rays (see Fig. 1) are given by Snell's laws: $\theta_{\text{refl}} = \alpha$ and $n_2 \cdot \sin(\theta_{\text{refr}})$

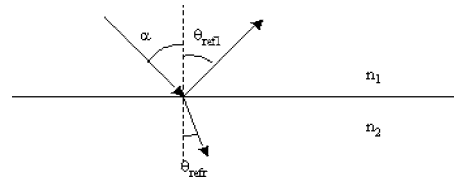


Fig. 1 Reflection and refraction at the interface between air and particles

$= n_1 \cdot \sin(\alpha)$ and the monochromatic specular reflectivity $\rho_\lambda(\alpha, n)$ is calculated by the Fresnel relations [19]

$$\rho_\lambda(\alpha, n) = \frac{1}{2} \frac{\sin^2(\alpha - \theta_{\text{refr}})}{\sin^2(\alpha + \theta_{\text{refr}})} \left[1 + \frac{\cos^2(\alpha + \theta_{\text{refr}})}{\cos^2(\alpha - \theta_{\text{refr}})} \right] \quad (1)$$

Moreover, the absorption coefficient of the semitransparent material is obtained from the complex refractive index by

$$\kappa_\lambda = 4\pi \cdot k / \lambda \quad (2)$$

and the evolution of the radiative energy of a ray traveling along a distance L in the semitransparent medium is $1 - e^{-(\kappa_\lambda \cdot L)}$.

2.2 Principle of the Method. The method has been described in previous papers [12,18] concerning the radiative properties of beds of opaque spherical particles. We briefly recall it here and lay stress on the difference encountered when the method is applied to fibrous materials. The principle of the method is to determine the values of the extinction coefficient β_{fib} , the scattering albedo ω_{fib} , and the scattering phase function $P_{\text{fib}}(\theta)$ of the homogeneous isotropic absorbing and scattering medium that best match the radiative behavior of an arrangement of infinite circular cylinders representing the fibrous material. The method is decomposed in several stages:

First, we generate a large arrangement of randomly positioned and randomly oriented long circular cylinders of given radius R_{fib} representing the fibrous material studied.

Then, a Monte Carlo procedure starts and the path of rays, starting in random points of the fibrous material and with random starting directions, are tracked until they leave an integrating sphere of radius R_{sphere} centered on the starting point (see Fig. 2). The tracked rays can pass through the sphere without striking any particle. They can also undergo reflections or refractions (for semitransparent fibers) at the surface of the fibers or be absorbed inside the particle before leaving the sphere. The probability for a ray striking a fiber to be reflected is directly related to the diffuse reflectivity $\bar{\rho}$ in the case of opaque diffusely reflecting fibers or to the specular reflectivity $\rho_\lambda(\alpha, n)$ for semitransparent fibers. In this latter case, the distance traveled by rays inside the particle before

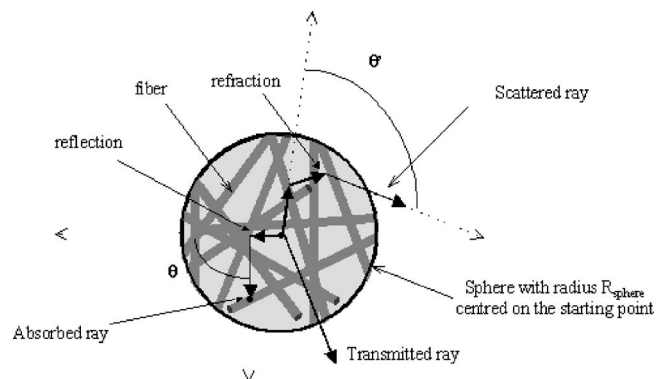


Fig. 2 Monte Carlo procedure in the sphere of radius R_{sphere}

being absorbed depends on the absorption coefficient of the material forming the fibers which is calculated from the imaginary refractive index and the radiation wavelength (see equation). Each time a ray is scattered (reflected and/or refracted) by a particle, the angle θ' between the incident direction and the direction of the ray after having been deviated by the fiber is memorized. Moreover, when rays leave the sphere after one or several scatterings, the angles θ between the starting and scattered directions are also memorized (Fig. 2).

For a great number of rays, the Monte Carlo procedure permits one to compute four parameters which entirely describe the radiative behavior of the fibrous medium:

- **Trans**: the proportion of the starting energy leaving the sphere without being intercepted (transmitted rays)
- **Sca**: the proportion of starting energy leaving the sphere after one or several reflections or refractions (scattered rays)
- **$E(\theta')$** : the average angular repartition of the energy scattered outside the sphere of radius R_{sphere} . In practice, the repartition is discretized for $\theta'_0=0^\circ, \theta'_1=1^\circ, \dots, \theta'_{180}=180^\circ$. Then, all the rays leaving the sphere with an angle θ' comprised between $\theta'_i-0.5^\circ$ and $\theta'_i+0.5^\circ$ are regrouped in $E(\theta'_i)$ except for $i=0$ ($0^\circ < \theta' < 0.5^\circ$) and $i=180$ ($179.5^\circ < \theta' < 180^\circ$)
- **$S(\theta)$** : the average angular repartition of the rays scattered (reflected and/or refracted) by the particles. This repartition is obtained by memorizing every reflecting or refracting angle each time a fiber reflects or refracts a ray. As for $E(\theta')$, in practice, the repartition is discretized for $\theta_0=0^\circ, \theta_1=1^\circ, \dots, \theta_{180}=180^\circ$.

If we assimilate the arrangement of fibers to a homogeneous isotropic absorbing and scattering medium, the extinction coefficient could be determined directly from the parameter Trans (see [12,18])

$$\exp(-\beta_{\text{fib}} \times R_{\text{sphere}}) = \text{Trans} \Leftrightarrow \beta_{\text{fib}} = -\text{Ln}(\text{Trans})/R_{\text{sphere}} \quad (3)$$

Regarding the scattering phase function of the bed $P_{\text{fib}}(\theta)$, we showed in [12] that it is related to the angular repartition $S(\theta)$ which actually represents the probability for an incident ray to be scattered in a direction making an angle comprised between $\theta-0.5^\circ$ and $\theta+0.5^\circ$ with the incident direction. We have

$$P_{\text{fib}}(\theta_i) = S(\theta_i)/d\omega(\theta_i) \quad \text{with} \quad d\omega(\theta_i) = 2\pi \sin(\theta_i) \Delta\theta_i = 2\pi \sin(\theta_i) \times 2\pi/360 \quad \text{and then}$$

$$P_{\text{fib}}(\theta_i) = \frac{S(\theta_i)}{\sin(\theta_i) \times \frac{\pi^2}{90}} \quad \text{for } i=0 \dots 180 \quad (4)$$

The scattering phase function is then normalized to have

$$\frac{1}{4\pi} \sum_{i=0}^{180} P_{\text{fib}}(\theta_i) \times 2\pi \sin(\theta_i) d\theta_i = 1 \quad (5)$$

Finally, as regards the scattering albedo of the bed, it could not be determined directly. To solve the problem, we apply the same Monte Carlo procedure to an homogeneous, isotropic absorbing and scattering medium having an extinction coefficient $\beta = \beta_{\text{fib}}$, a scattering phase function $P(\theta) = P_{\text{fib}}(\theta)$, and a varying albedo ω . We then compute the parameters Trans_{ho} , Sca_{ho} , and $E_{\text{ho}}(\theta')$ which have the same significance as before but now concern the isotropic absorbing and scattering medium. An iterative process is then applied in order to determine the value of ω for which $\text{Sca}_{\text{ho}} = \text{Sca}$. We then have, for the homogeneous absorbing and scattering medium associated with the bed

$$\text{Trans}_{\text{ho}} = \text{Trans}, \quad \text{Sca}_{\text{ho}} = \text{Sca}, \quad S_{\text{ho}}(\theta) = S(\theta)$$

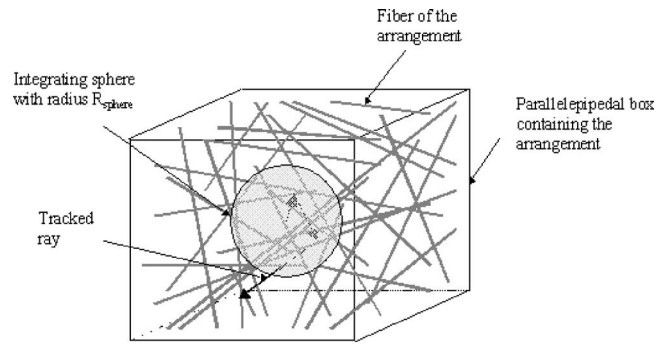


Fig. 3 Monte Carlo procedure in the parallelepipedal box containing the arrangement $\bar{n}=3.0-0.0001.i$

2.3 Generation of the Fibrous Medium. Our program permits one to obtain fibrous media with varying porosities. The arrangement of circular cylinders representing the fibrous material is comprised in a finite large parallelepipedal box (see Fig. 3). The program generates fibers by choosing random point in the box and random directions which respectively correspond to a point of the symmetry axis and the direction of the symmetry axis of the fiber. This point and this direction as well as the diameter are sufficient to entirely define the fiber. Each time a fiber is generated, we check that it does not intersect any other previously generated one, otherwise, its coordinates are erased and a new one is randomly chosen. Different types of arrangement can be generated:

- First, we create arrangements of circular cylinders with infinite length. Then, all the fibers generated go through the entire parallelepipedal box. In this manner, random fibrous media with porosities ranging from 1 to 0.9 could be generated. However, it is not possible to obtain media with porosities lower than approximately 0.9.
- In order to generate arrangements with lower porosities, we also create media made of fibers with finite length. Thus, during the generation of the arrangement, if a new generated infinite fiber intersects a previously generated one, its length is limited in order to avoid the intersection. Nevertheless, in order to still represent a fiber, the generated cylinder must have a minimum length which is arbitrarily fixed to $10 \cdot R_{\text{fib}}$. This second type of arrangement could appear farther from reality than the previous one. However, in real dense fibrous media, the material has generally been compressed and the fibers are no longer perfectly straight. Their macroscopic structure is then relatively close to that of the second type of arrangement. The media generated by this manner permit one to cover a large range of porosity from 1 to 0.75.

2.4 Choice of the Radius R_{sphere} . The radius R_{sphere} of the integrating sphere in which the Monte Carlo procedure takes place is an important parameter of the method. In the previous study on beds of spherical particles containing an absorbing and scattering medium [18], we discussed the influence of R_{sphere} on the results and showed that it must be much greater than the characteristic size of the particles in order for the method to be valid. On the other hand, for beds of opaque spherical particles [12], the radiative properties identified proved to be independent of R_{sphere} as long as $R_{\text{sphere}} > d + R_{\text{part}}$, where d is the distance between the center of two neighboring spherical particles. In the case of fibrous materials, we carried out the numerical simulation for different values of R_{sphere} and analyzed its influence on the identified radiative properties. The variations of the calculated extinction coefficient β_{fib} with R_{sphere} for arrangements of infinite fibers with $R_{\text{fib}}=100 \mu\text{m}$ and $\epsilon=0.8871$ or $\epsilon=0.9498$ are depicted in Fig. 4. In Fig. 5, we have depicted the evolution of the average angular repartition $S(\theta_i) = P_{\text{fib}}(\theta_i) \times \sin(\theta_i) \times \pi^2/90$ with R_{sphere} for a fi-

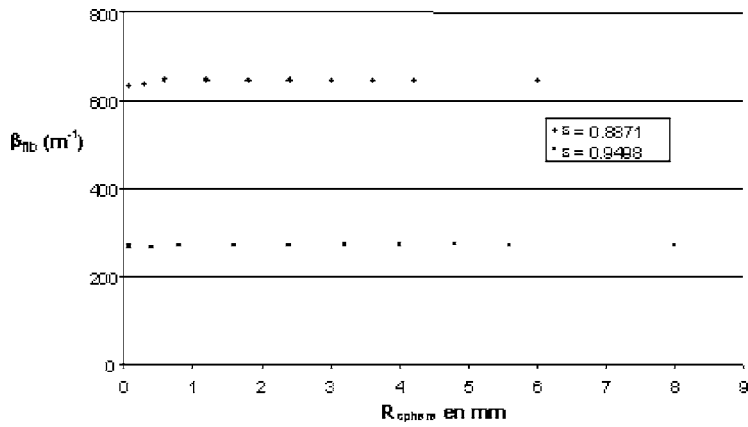


Fig. 4 Evolution of the calculated extinction coefficient with R_{sphere} for arrangements of infinite fibers with $R_{\text{fib}}=0.1$ mm and different porosities

brous material with porosity 0.751, $R_{\text{fib}}=100 \mu\text{m}$, and different reflecting properties. In this figure, the direction $\theta=0^\circ$ corresponds to the x axis. All the calculations were conducted using a number of tracked rays n_{tr} comprised between $2 \cdot 10^5$ and $1 \cdot 10^6$.

One can notice that, whatever the porosity of the fibrous medium considered, the radius of the integrating sphere of the Monte Carlo procedure has almost no influence on the identified extinction coefficient β_{fib} . Moreover, we remark that this extinction coefficient is independent of the optical properties (opaque/semitransparent) of the fibers.

With regards to the identified phase function, the remarks are different. Indeed, R_{sphere} has a strong influence on the angular repartition $S(\theta)$ when the Monte Carlo procedure is applied to media made of semitransparent fibres. As can be seen in Fig. 4, when R_{sphere} is the same order of magnitude as the characteristic size of the fibers (R_{fib}), $S(\theta)$ varies strongly with R_{sphere} , whereas it tends to a fixed repartition when R_{sphere} becomes much greater than this characteristic size. On the other hand, in the case of opaque fibres, $S(\theta)$ does not vary with R_{sphere} .

This observation could be explained by the fact that during the Monte Carlo computation for semitransparent fibers, the rays refracted by the particles can travel inside the fibers. Thus, some of them can leave the integrating sphere while they are still present inside a fiber and the angular repartition $S(\theta)$ does not take them into account as they have not left the particle. $S(\theta)$ then favors the rays reflected by the particles to the detriment of the refracted rays. When R_{sphere} is the same order of magnitude as R_{fib} , the proportion of rays leaving the integrating sphere while they are still in a fiber is not negligible and varies with R_{sphere} and thus, the phenomenon previously described has a significant influence on $S(\theta)$. When $R_{\text{sphere}} \gg R_{\text{fib}}$, this proportion is nearly null and the influence of the phenomenon is negligible. On the other hand,

when the method is applied to media composed of opaque fibers, all the rays hitting a fiber are reflected or absorbed and, thus, the phenomenon previously described does not occur. That is the reason why $S(\theta)$ is the same whatever R_{sphere} .

These observations permit one to conclude that, in order for the identification method to be valid, the radius R_{sphere} must be much greater than the characteristic size of the fibers when the Monte Carlo is applied to semitransparent fibers. However, the choice of R_{sphere} also has a strong influence on the computation time and the accuracy of the identification. Thus, given that the Monte Carlo procedure uses random generated numbers to determine the path of the rays, the angular repartition $S(\theta)$ undergoes fluctuations. The greater R_{sphere} is, the less pronounced these fluctuations are. Indeed, when R_{sphere} is large, the number of reflection and refraction undergone by the rays before leaving the sphere is more important than for small values of R_{sphere} and thus the shape of the angular repartition is smoother. Then, the radius R_{sphere} used for the calculation must not be too small. On the other hand, if R_{sphere} is too large, the parameter Trans and Sca calculated by the Monte Carlo procedure become very small and the identified values of β_{bed} and ω_{bed} become less precise. Moreover, an increase in the value of R_{sphere} causes an important increase in the computation time. For each fibrous material, we then have chosen a value of R_{sphere} which respects the condition $R_{\text{sphere}} \gg R_{\text{fib}}$ for semitransparent fibers and represents a good compromise between the two antagonists phenomenon.

3 Results

The identification of the radiative properties has been conducted for arrangements of infinite and finite fibers and for semi-

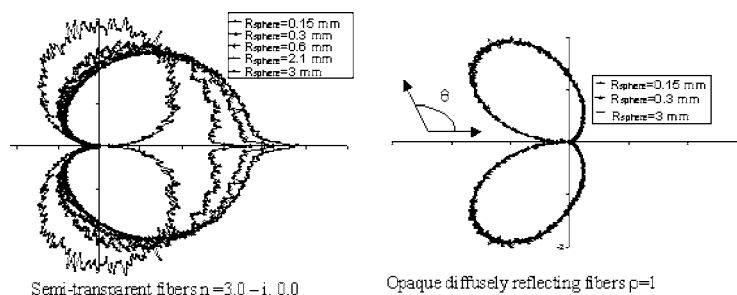


Fig. 5 Evolution of the average angular repartition $S(\theta)$ with R_{sphere} for an arrangement of finite fibers with $R_{\text{fib}}=0.1$ mm a porosity $\epsilon=0.751$ and different reflecting properties

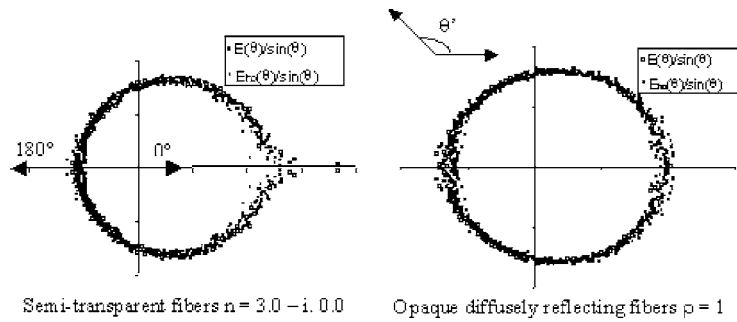


Fig. 6 Comparison of the angular repartitions $E(\theta)/\sin(\theta)$ and $E_{ho}(\theta)/\sin(\theta)$ by an arrangement of finite fibers with porosity $\epsilon = 0.7965$ with different reflecting properties and the associated homogeneous absorbing and scattering media

transparent or opaque fibers. The results have been obtained by carrying out several Monte Carlo procedures ($n_{tr} = 10^6$) for each arrangement of fiber.

3.1 Validity of the Method. We have seen in Sec. 2.2 describing the principle of the method, that, for the homogeneous absorbing and scattering medium associated with the bed whose radiative properties have been identified, we have

$$\text{Trans}_{ho} = \text{Trans}, \quad \text{Sca}_{ho} = \text{Sca}, \quad S_{ho}(\theta) = S(\theta).$$

However, in order to check that the radiative properties of this medium exactly represent the radiative behavior of the fibrous material, we must compare the angular repartitions of energy scattered away from the sphere during the Monte Carlo procedure by the fibrous material and by the associated homogeneous absorbing and scattering medium. Indeed, $E(\theta)$ and $E_{ho}(\theta)$ must be very close to each other. Thus, we have depicted in Fig. 6 the angular repartitions $E(\theta)/\sin(\theta)$ and $E_{ho}(\theta)/\sin(\theta)$ for a fibrous material with porosity 0.7965 (finite fibers) made of opaque purely reflecting ($\bar{\rho} = 1$) or semitransparent ($\bar{n} = 3.0 - i.0.0$) fibers. The values of R_{sphere} used for the two calculations are, respectively, $R_{\text{sphere}} = 40 \times R_{\text{fib}}$ and $R_{\text{sphere}} = 60 \times R_{\text{fib}}$. In both figures, the points in the lower half of the curve are simply repeated points from the upper half.

As can be seen, in both cases $E(\theta)$ and $E_{ho}(\theta)$ are very close to each other. The fluctuations observed are mainly due to the Monte Carlo procedure which generates random numbers to determine the path of the rays. These fluctuations are more pro-

nounced for the directions close to 0° and 180° for which the solid angle is small and then the energy collected during Monte Carlo procedure is small. They could be noticeably reduced by increasing the number of rays which would also increase the computation time. Thus, we can conclude that the behavior of the homogeneous absorbing and scattering medium whose radiative properties have been calculated using our method match the radiative behavior of the fictive fibrous material very well.

3.2 Evolution of the Extinction Coefficient β_{fib} .

3.2.1 Limit of the Independent Scattering Theory. As explained in Sec. 1, when independent scattering hypothesis is valid, the fibers composing the material individually interact with radiation as if they were alone. Thus, if we neglect diffraction, the extinction efficiency of each fiber is equal to 1 whatever its optical properties. The extinction coefficient from independent scattering theory β_{ind} is simply calculated by adding the geometric shadow of each fiber comprised in an elementary volume of material. Moreover, if the particles are randomly oriented, the average geometric shadow S_{fib} (m^2) of a fiber of length L and diameter R_{fib} is calculated by averaging over all the possible orientations and is given by

$$S_{\text{fib}} = L \times 2 \cdot R_{\text{fib}} \times \int_{\theta=0}^{\pi/2} \cos^2(\theta) \cdot d\theta = \frac{\pi}{4} \times L \times 2 \cdot R_{\text{fib}} \quad (6)$$

Then, if all the fibers have the same radius R_{fib} , we have

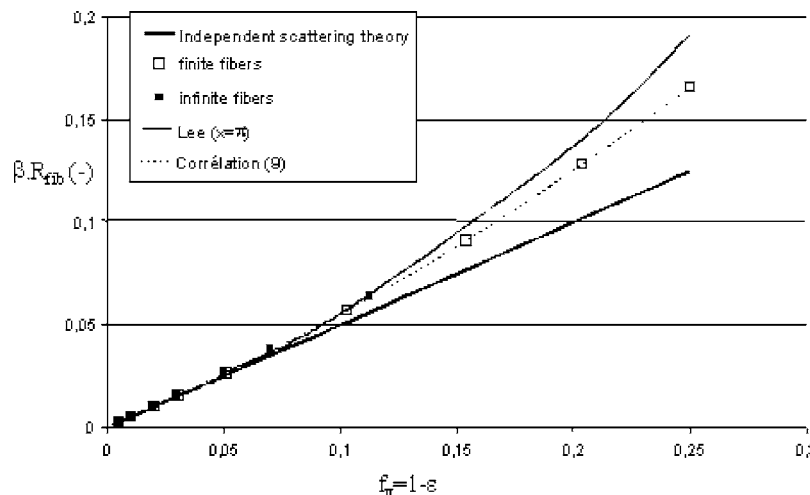


Fig. 7 Evolution of the dimensionless extinction coefficient $\beta_{\text{fib}} \cdot R_{\text{fib}}$ calculated by the different method

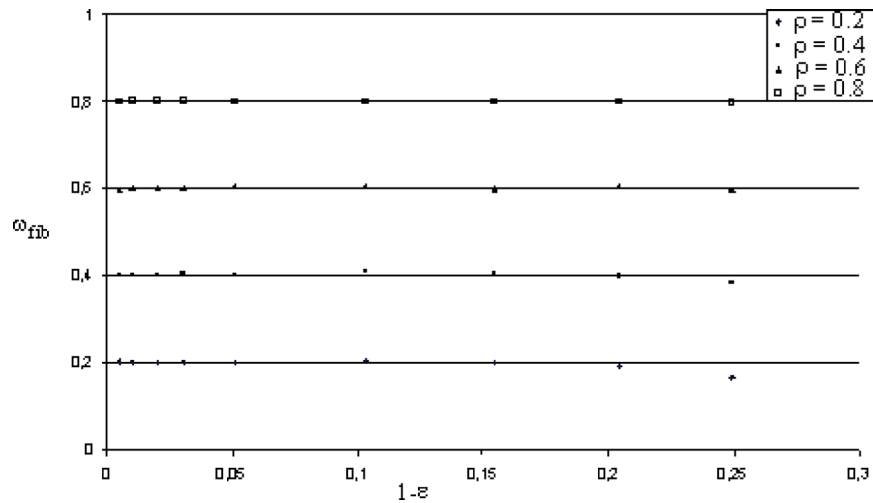


Fig. 8 Evolution of the calculated albedo with the porosity of the material for opaque fibers with different reflectivities

$$\beta_{\text{ind}} = L_{\text{fib}} \times R_{\text{fib}} \times \frac{\pi}{2} \quad (7)$$

where L_{fib} (m/m^3) is the total length of the fibers in an elementary volume of fibrous material. L_{fib} is related to the porosity ϵ and the radius R_{fib} of the fibers by

$$L_{\text{fib}} \times \pi \cdot R_{\text{fib}}^2 = 1 - \epsilon = f_v \Leftrightarrow L_{\text{fib}} = \frac{1 - \epsilon}{\pi \cdot R_{\text{fib}}^2} \quad \text{and then}$$

$$\beta_{\text{ind}} = \frac{1 - \epsilon}{\pi \cdot R_{\text{fib}}^2} \times R_{\text{fib}} \times \frac{\pi}{2} = \frac{1 - \epsilon}{2 \cdot R_{\text{fib}}} \Leftrightarrow \beta_{\text{ind}} \cdot R_{\text{fib}} = \frac{1 - \epsilon}{2} \quad (8)$$

Regarding the calculated extinction coefficient β_{fib} of the fibrous materials, the results of the Monte Carlo procedure also reveal that, as for β_{ind} , it only depends on the porosity ϵ of the material and on the radius R_{fib} and, especially, that it is independent of the optical properties of the particles. This is not surprising given that all the rays hitting a particle are deviated by reflection or refraction whatever the optical properties of the fibers. Moreover, we remark that, for a given porosity, the extinction coefficient is proportional to $(R_{\text{fib}})^{-1}$. We then have chosen to study the evolution of the dimensionless number $\beta \times R_{\text{fib}}$ which only depends on the porosity of the arrangement. The results of our numerical method for the two types of arrangement (finite or infinite fibers) as well as the results of the independent scattering hypothesis are depicted in Fig. 7. The accuracy of the numerical results has been estimated from the amplitude of the fluctuations of the dimensionless extinction coefficient calculated from the different Monte Carlo procedures. It proves to be always lower than 1.0%.

We remark that the dimensionless extinction coefficient $\beta \cdot R_{\text{fib}}$ calculated by our method rapidly increases when the volume fraction of fibers increases. This evolution is nonlinear contrary to the evolution predicted by the independent scattering theory.

As expected, for fibrous media with high porosities, the results obtained using our method are close to the results of the independent scattering theory.

However, the relative difference between the two methods increases rapidly when the porosity decreases. Indeed, we notice that the independent scattering theory tends to underestimate the dimensionless extinction coefficient. This observation is valid for fibrous materials made of infinite or finite fibers. Besides, the difference between the results for the two different kinds of arrangements is almost null.

The relative difference between the extinction coefficient calculated by our method and the independent scattering assumption

exceeds 4% when the porosity is lower than approximately 0.95. This difference reaches 16% when the porosity is approximately 0.75. In this case, the use of independent scattering theory then leads to important errors in radiative transfer calculations.

If we define the dependent scattering regime by $\beta/\beta_{\text{ind}} > 1.1138$, in accord with a criterion given by Hottel et al. [13], dependent scattering occurs as soon as the porosity of the bed is lower than approximately 0.89. Comparing this lower limit with that obtained in [12] for beds of large opaque spherical particles using the same method, we notice that dependent scattering is more restricting in this latter case (lower limit ≈ 0.94 for opaque spherical particles). In order to quantify analytically the influence of dependent scattering, we propose a correlation which permits one to estimate the extinction coefficient when shadowing effects are significant from the extinction coefficient when independent scattering occurs as a function of $f_v = 1 - \epsilon$

$$\frac{\beta_{\text{fib}}}{\beta_{\text{ind}}} = -11.9 \cdot (1 - \epsilon)^3 + 6.2 \cdot (1 - \epsilon)^2 + 0.486 \cdot (1 - \epsilon) + 1 \quad (9)$$

As can be seen in Fig. 7, this formula perfectly fits the results stemming from the Monte Carlo procedure.

3.2.2 Comparison With Previous Studies. As has been previously explained in Sec. 1, very few studies have already been interested in dependent scattering in fibrous materials. Actually, Lee [16] was the only author who has estimated quantitatively the dependent scattering phenomenon in this kind of porous media. Its studies were not restricted to geometric optics but concerned the whole range of size parameter x and took into account near-field effect and far-field effect as well. However, he only considered materials composed of aligned fibers and carried out its calculations for fibrous materials with a maximum size parameter $x = \pi$. For this size parameter, the optic geometrics laws could not be assumed as an exact approximation of the radiation-matter interaction. Nevertheless, we could compare qualitatively the results of the dimensionless extinction coefficient for parallel fibers ($x = \pi$) at normal incidence given by Lee [16] in the form of the dimensionless parameter $\beta_{\text{dep}}/\beta_{\text{ind}}$ with those obtained using our method. The results are shown in Fig. 7.

We notice that the results of the method developed by Lee are in relatively good agreement with our results. Especially, they predict an increase of the extinction coefficient due to the dependent scattering phenomenon like our approach. Furthermore, if we use the criterion previously proposed to demark the independent and dependent scattering regimes, the lower limit of the porosity

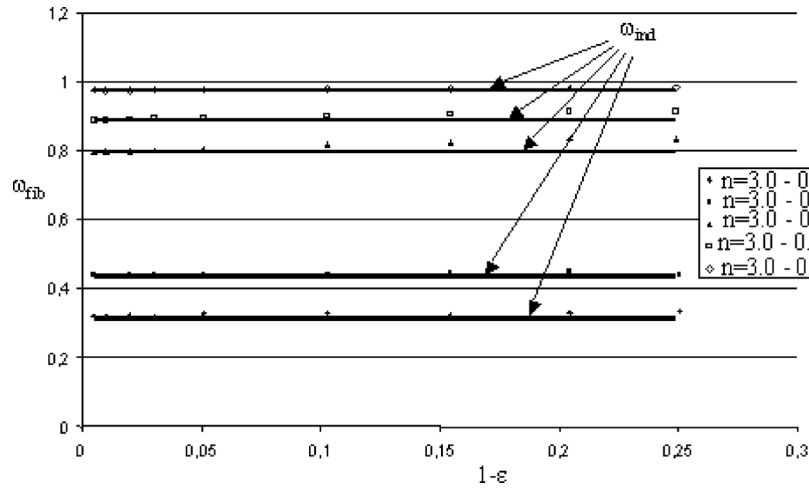


Fig. 9 Evolution of the calculated albedo with the porosity of the material for semi-transparent fibers with different refractive index

is quiet similar. However, we remark that for dense fibrous media, the dimensionless extinction coefficient of Lee is somewhat greater than the one predicted by our approach. This difference may be explained by the fact that the results of Lee were obtained assuming a normal incidence whereas, at oblique incidence, which is the majority case for randomly oriented fibrous materials, the influence of dependent scattering is less pronounced, as shown by Lee [16].

3.3 Evolution of the Scattering Properties $\omega_{bed}/\omega_{ind}$ and $P_{bed}(\theta)$. In this section, we choose to study the evolution of the normalised albedo $\omega_{bed}/\omega_{ind}$ in order to compare the evolution of the albedo for particles with different reflecting properties. For opaque diffusely reflecting particles, the albedo of one particle $\omega_{part} = \omega_{ind}$ is equal to its hemispherical reflectivity $\bar{\rho}$ given that all the rays which are not reflected by the fibers are absorbed. On the other hand, for semitransparent fibers, it depends on the complex refractive index and on the wavelength λ studied. It can be calculated by carrying out a ray-tracing procedure on a randomly oriented isolated fiber and by calculating the proportion of incident energy which has been scattered by the particle. For the cases shown in Fig. 9 ($\lambda = 10 \mu m$, $\tilde{n} = 3.0 - i.5 \cdot 10^{-5}$; $\tilde{n} = 3.0 - i.10^{-4}$; $\tilde{n} = 3.0 - i.5 \cdot 10^{-4}$; $\tilde{n} = 3.0 - i.10^{-3}$; $\tilde{n} = 3.0 - i.5 \cdot 10^{-3}$, and $\tilde{n} = 3.0 - i.10^{-2}$), we, respectively, have $\omega_{ind} = 0.9874$, $\omega_{ind} = 0.9753$; $\omega_{ind} = 0.8859$; $\omega_{ind} = 0.7942$; $\omega_{ind} = 0.4343$, and $\omega_{ind} = 0.3125$.

With regards to the phase function from independent scattering assumption, the literature [19] gives an analytical solution for large opaque diffusely reflecting particles

$$P_{ind}(\theta) = \frac{8}{3\pi} (\sin \theta - \theta \cos \theta) \quad (10)$$

For semitransparent specularly reflecting fibers, in order to determine $P_{ind}(\theta)$, we used the same ray-tracing procedure applied to isolated randomly oriented fibers and computed the repartition of rays scattered in each direction making an angle θ with the incident direction. As for $S(\theta)$ calculated during the Monte Carlo procedure (Sec. 2.2), in practice, the phase function is discretized in 181 directions i $\theta_0 = 0^\circ$, $\theta_1 = 1^\circ$, ..., $\theta_{180} = 180^\circ$. Then, all the rays scattered by the particle with an angle θ comprised between $i^\circ - 0.5^\circ$ and $i^\circ + 0.5^\circ$ are regrouped in $P_{ind}(\theta_i)$ except for $i=0$ ($0^\circ < \theta < 0.5^\circ$) and $i=180$ ($179.5^\circ < \theta < 180^\circ$).

The evolution of $\omega_{bed}/\omega_{ind}$ with the porosity for materials made of opaque and semi-transparent fibers are depicted in Figs. 8 and 9. The evolution of $P_{fib}(\theta)$ with ϵ for opaque fibers ($\bar{\rho} = 0.8$) is depicted in Fig. 10 whereas, for semitransparent particles, for a legibility purpose, we choose to represent the variation of

$P_{fib}(\theta) \times \sin(\theta)$ in Fig. 11. We only show the results obtained using arrangements of finite fibers as the results obtained with infinite particles are almost identical. The scattering phase functions stemming from the independent scattering theory are also shown. As for the extinction coefficient, this results have been obtained using several Monte Carlo procedures ($ntirs = 2 \cdot 10^5$) for each arrangement of fibers.

The analysis of the theoretical results concerning the albedo ω_{fib} and phase function $P_{fib}(\theta)$ clearly indicates that shadowing effects have almost no influence on the scattering properties of fibrous materials. Indeed, we notice that, even when the porosity of the material decreases and reaches relatively small values, the albedo and phase function remain unchanged and equal to the properties from independent scattering hypothesis. These observations are valid for opaque and semitransparent fibers as well. It can be noted that the same trend have been observed for beds or packed beds of opaque spherical particle [11].

Concerning the calculated phase function, the fluctuations observed are mainly due to the Monte Carlo procedure which generates random numbers to determine the path of the rays. These fluctuations are more pronounced for the directions close to 0° and 180° for which the solid angle, and thus, the energy collected during Monte Carlo procedure is small. They could be noticeably reduced by increasing the number of rays which would also increase the computation time. For opaque fibers, the phase function obtained by our Monte Carlo procedure reproduces the characteristic shape of the phase function given by Eq. (10) for large

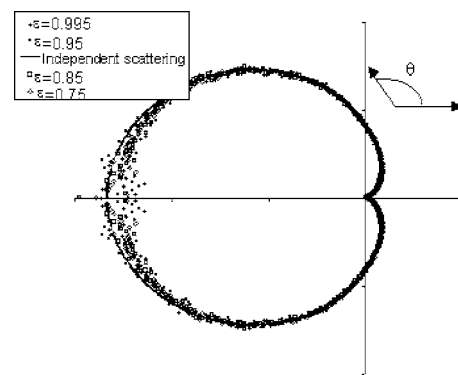


Fig. 10 Evolution of the calculated scattering phase function $P_{fib}(\theta)$ with the porosity for medium made of opaque fibers with $\rho = 0.8$

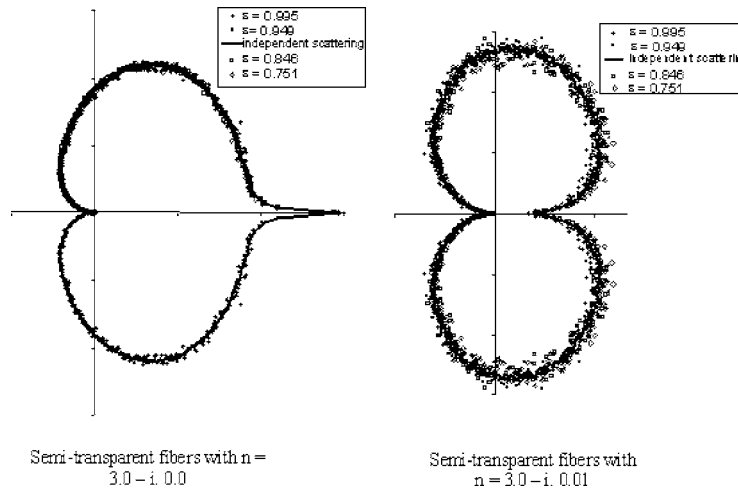


Fig. 11 Evolution of $P_{\text{fib}}(\theta) \cdot \sin \theta$ with the porosity for semi-transparent fibers with different complex refractive index

opaque diffusely reflecting particles. This phase function is the same whatever the reflectivity $\bar{\rho}$. For semitransparent nonabsorbing fibers with $n=3.0$, we notice that $P_{\text{fib}}(\theta)$ is dominated by forward scattering (asymmetry factor $g=0.37$) as the rays refracted by the fibers are more important than reflected ones. Thus, if the real part n of the refractive index increased, forward scattering would be less predominant. The imaginary part of the refractive index also has an influence on the phase function $P_{\text{fib}}(\theta)$ as shown in Fig. 11. Actually, the absorption of the radiant energy by the fibers tend to attenuate forward scattering (asymmetry factor $g=0.16$ for $k=0.01$) given that most of the rays traveling inside the fibers and which are absorbed would, otherwise, be refracted.

4 Conclusion

In this paper, we have used the innovative method of prediction of radiative properties presented in [12] to analyze the dependent phenomenon in dense porous materials made of large randomly oriented fibers ranging in the geometric optics limit. This method has been originally developed for beds and packed beds of opaque spherical particles and was adapted to fibrous media. Given that it is based on a Monte Carlo procedure, it permits taking into account the shadowing effects due to the geometric sized fibers. The method has been applied to fictitious fibrous materials with porosities ranging from 1 to 0.75 and with different absorbing and reflecting properties. The limit of validity of the independent scattering theory has been investigated and proves to be noticeably different than for beds of opaque particles. We also propose an analytical correlation predicting the evolution of the extinction coefficient with the porosity of the material. This correlation could be very useful for researchers who would like to estimate quickly the influence of shadowing effects on a heat transfer calculation for example. Regarding the scattering properties (albedo and phase function), the results of the method reveals that dependent regime due to shadowing effects has almost no influence on these properties.

The variations of the extinction coefficient obtained were also compared to the few other theoretical results given by Lee for a size parameter $x = \pi$. The agreement is globally satisfactory.

Although it is strictly limited to materials made of fibers with large size parameters which are not currently encountered, the conclusions of the study seem to us very interesting given that there have been relatively few studies which have already dealt with dependent regime in fibrous media.

Finally, our method could be of great interest given that it could be easily extended to particulate media ranging in the geometric optics limit and for which the morphology is known (cellular materials, etc.).

Nomenclature

- c = average interparticle clearance (m)
- $d\omega(\theta'_i)$ = the solid angle around direction θ'_i
- D = random generated number
- $f_v = 1 - \epsilon$ = solid volume fraction
- $\tilde{n} = n - i.k$ = refractive index of the particle
- L_{fib} = total length of the fibers per unit volume of fibrous material (m/m^3)
- $P(\theta)$ = scattering phase function
- R_{fib} = radius of cylindrical fibers (m)
- R_{sphere} = radius of the integrating sphere (m)
- S_{fib} = average geometric shadow of a fiber (m^2)
- x = size parameter of the particle ($x = 2 \cdot \pi \cdot R_{\text{fib}}/\lambda$)

Greek Symbols

- λ = wavelength (m)
- β = extinction coefficient (m^{-1})
- κ = absorption coefficient (m^{-1})
- ω = scattering albedo (-)
- ϵ = porosity (-)
- α = angle between intercepted ray and the normal to the surface of the particle (rad)
- θ' = angle between the starting ray and the ray scattered away from the sphere (rad)
- θ = angle between rays intercepted and rays scattered by the particle (rad)
- $\rho_\lambda(\alpha, n)$ = reflectivity of the specularly reflecting fibers
- $\bar{\rho}$ = hemispherical reflectivity

Subscript

- fib = of the fiber
- refl = reflected
- refr = refracted
- sphere = of the sphere
- ind = from independent scattering theory
- ho = isotropic and homogeneous absorbing and scattering medium

References

- [1] Viskanta, R., and Menguc, M. P., 1989, "Radiative Transfer in Dispersed Media," *Appl. Mech. Rev.*, **42**(9), pp. 241–259.
- [2] Baillis, D., and Sacadura, J. F., 2000, "Thermal Radiation Properties of Dispersed Media: Theoretical Prediction and Experimental Characterisation," *J. Quant. Spectrosc. Radiat. Transf.*, **37**, pp. 327–363.
- [3] Lee, S. C., 1996, "Scattering of Fibrous Media Containing Parallel Fibers," *ASME J. Heat Transfer*, **118**(4), pp. 931–936.
- [4] Jeandel, G., Boulet, P., and Morlot, G., 1993, "Radiative Transfer Through a Medium of Silica Fibres Oriented in Parallel Planes," *Int. J. Heat Mass Transfer*, **36**(2), pp. 531–536.
- [5] Milos, F. S., and Marshall, J., 1997, "The Calculation of Anisotropic Extinction Coefficients for Radiation Diffusion in Rigid Fibrous Ceramic Insulation," *Int. J. Heat Mass Transfer*, **40**, pp. 627–634.
- [6] Hottel, H. C., Sarofim, A. F., Dalzell, W. H., and Vasalos, I. A., 1971, "Optical Properties of Coatings, Effect of Pigment Concentration," *AIAA J.*, **9**, pp. 1895–1898.
- [7] Ishimaru, A., and Kuga, Y., 1982, "Attenuation Constant of a Coherent Field in a Dense Distribution of Particles," *J. Opt. Soc. Am.*, **72**, pp. 1317–1320.
- [8] Brewster, M. Q., 1983, "Radiative Heat Transfer in Fluidized Bed Combustors," ASME Paper No. 83-WA/HT-82.
- [9] Yamada, Y., Cartigny, J. D., and Tien, C. L., 1986, "Radiative Transfer with Dependent Scattering by Particles: Part 2-Experimental Investigation," *J. Heat Transfer*, **108**, pp. 614–618.
- [10] Kumar, S., and White, S. M., 1990, "Dependent Absorption and Extinction of Radiation by Small Particles," *J. Heat Transfer*, **112**, pp. 178–185.
- [11] Singh, B. P., and Kaviany, M., 1991, "Independent Theory Versus Direct Simulation of Radiation Heat Transfer in Packed Beds," *Int. J. Heat Mass Transfer*, **34**, pp. 2869–2882.
- [12] Coquard, R., and Baillis, D., 2004, "Radiative Characteristics of Beds of Spheres Containing an Absorbing and Scattering Medium," *J. Thermophys. Heat Transfer*, **18**(2), pp. 178–186.
- [13] Kamiuto, K., 1990, "Correlated Radiative Transfer in Packed Sphere Systems," *J. Quant. Spectrosc. Radiat. Transf.*, **43**, pp. 39–43.
- [14] Jones, P. D., McLeod, D. G., and Dorai-Raj, D. E., 1991, "Correlation of Measured and Computed Radiation Intensity Exiting a Packed Bed," *J. Heat Transfer*, **113**, pp. 94–102.
- [15] Baillis, D., and Sacadura, J. F., 2002, "Directional Spectral Emittance of a Packed Bed: Influence of the Temperature Gradient in the Medium," *J. Heat Transfer*, **124**, pp. 904–911.
- [16] Lee, S. C., 1994, "Dependent vs Independent Scattering in Fibrous Composites Containing Parallel Fibers," *J. Thermophys. Heat Transfer*, **8**, pp. 641–646.
- [17] Kumar, S., and White, S. M., 1995, "Dependent Scattering Properties of Woven Fibrous Insulations," *J. Heat Transfer*, **117**, pp. 160–166.
- [18] Coquard, R., and Baillis, D., 2005, "Radiative Characteristics of Beds of Spheres Containing an Absorbing and Scattering Medium," *J. Thermophys. Heat Transfer*, **19**, pp. 226–234.
- [19] Siegel, R., and Howell, J. R., 1981, *Thermal Radiation Heat Transfer*, Hemisphere, New York.

Jason M. Porter
 Mechanical Engineering Department,
 The University of Texas at Austin,
 1 University Station C2200,
 Austin, TX 78712

Marvin E. Larsen
 Sandia National Laboratories MS 0836,
 Albuquerque, NM 87185

J. Wesley Barnes

John R. Howell
 e-mail: jhowell@mail.utexas.edu

Mechanical Engineering Department,
 The University of Texas at Austin,
 1 University Station C2200,
 Austin, TX 78712

Metaheuristic Optimization of a Discrete Array of Radiant Heaters

The design of radiant enclosures is an active area of research in radiation heat transfer. When design variables are discrete such as for radiant heater arrays with on-off control of individual heaters, current methods of design optimization fail. This paper reports the development of a metaheuristic thermal radiation optimization approach. Two metaheuristic optimization methods are explored: simulated annealing and tabu search. Both approaches are applied to a combinatorial radiant enclosure design problem. Configuration factors are used to develop a dynamic neighborhood for the tabu search algorithm. Results are presented from the combinatorial optimization problem. Tabu search with a problem specific dynamic neighborhood definition is shown to find better solutions than the benchmark simulated annealing approach in less computation time.

[DOI: 10.1115/1.2345430]

Introduction

Radiative Enclosure Design. The design of enclosures where radiation is the dominant mode of heat transfer has been addressed in numerous studies [1–5]. Applications are found in industry, including silicon wafer manufacturing, annealing processes, paint curing, and solar collectors. In the design of radiant enclosures two basic components are of primary interest: heaters and a design surface. The heaters are the source of thermal radiation, and are often composed of lamps, inductively heated elements, or a flame. The surface that requires heating is the design surface. The objective of designing radiant heating enclosures is to change various parameters within the enclosure to obtain the desired conditions on the design surface.

Traditionally, when solving radiation enclosure problems, each surface within an enclosure requires one known boundary condition, either temperature or heat flux. When designing radiant enclosures, neither the temperature nor heat flux of the heaters is typically known. Either the temperature or the heat flux of the heaters must be initialized to some value and the solution reached through iteration. This is the forward formulation of the design problem. When many heaters are present, each with independent control, an optimal solution is difficult to find by iteration alone.

Another approach uses an inverse formulation of the problem in which the temperature and heat flux on the design surface are both specified without specifying a priori either the temperature or heat flux of the heaters [1,2]. The heater settings that result in the specified design surface conditions are then found through regularization. The set of equations relating the unknown radiosities at each heater surface to the known temperatures and heat fluxes on the design surface is given by [6]:

$$\varepsilon_k \sum_{j=1}^N F_{k-j} q_{o,j} = \varepsilon_k \sigma T_k^4 - q_k \quad 1 \leq k \leq M \quad (1)$$

Writing Eq. (1) for all elements on the design surface results in M equations in N unknowns where N is the total number of surface

elements in the enclosure and M is the number of surface elements on the design surface. This set of equations can then be solved by regularization to find the radiosities of the heaters.

Another approach to solving radiant enclosure design problems is non-linear programming [3]. This method uses forward solution strategies and information about the gradients in the solution to arrive at an optimal design. The forward formulation governing energy exchange within the enclosure is [6]:

$$\sum_{j=1}^N [\delta_{kj} - (1 - \varepsilon_k) F_{k-j}] q_{o,j} = \varepsilon_k \sigma T_k^4 \quad 1 \leq k \leq N \quad (2)$$

$$\sum_{j=1}^N (\delta_{kj} - F_{k-j}) q_{o,j} = q_k \quad 1 \leq k \leq N \quad (3)$$

Equation (3) calculates heat fluxes from the radiosities calculated in Eq. (2). The forward formulation requires that either the temperature or the radiosity at each surface in the enclosure is specified. The system of equations can then be solved by matrix inversion or relaxation. In non-linear programming, gradient information is calculated for the problem and used to find the unknown temperatures and radiosities in Eq. (2).

Metaheuristics. In both regularization and non-linear programming, the unknown temperatures and radiosities are required to be continuous. Design problems with heaters that can only be in discrete positions or have discrete power levels require optimization methods with discrete or combinatorial capability. Unlike continuous optimization, combinatorial optimization problems have a fixed number of possible solutions. When the total number of solutions is small, an exhaustive search of all possible solutions can be conducted. An exhaustive search calculates the value of an appropriate objective function for all solutions and returns the best possible solution (the global optimum). However, as the number of discrete variables increases, the total number of solutions to evaluate quickly becomes prohibitive. In the case study presented in this paper, for example, an exhaustive search would require 2^{63} objective function calculations.

A class of optimization methods known as metaheuristics has been successfully applied to combinatorial optimization problems with large solution spaces [7,8]. Metaheuristics have also been applied to a limited number of radiation design problems [4,5].

Contributed by the Heat Transfer Division of ASME for publication in the JOURNAL OF HEAT TRANSFER. Manuscript received August 24, 2005; final manuscript received March 23, 2006. Review conducted by Bakhtier Farouk. Paper presented at the 2005 ASME Heat Transfer Summer Conference (HT2005), July 15, 2005–July 22, 2005, San Francisco.

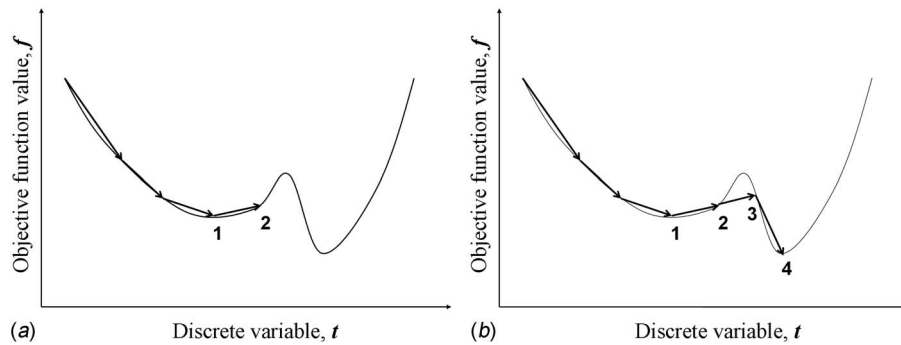


Fig. 1 An illustration of a minimization problem with two local minima. (a) The algorithm proceeds following a direction of decreasing f until the local minimum at point 1 is reached. Moving to point 2 requires accepting a solution with a higher value of f . (b) Only after accepting solutions 2 and 3 with increasing f values does the algorithm find solution 4, the global minimum.

Metaheuristic methods apply specific *searching rules* to strategically search a solution space to find feasible solutions. The searching rules are typically based on trends in calculated values of the objective function. We have developed two metaheuristics, simulated annealing (SA) and tabu search (TS), for application to a discrete radiant heating enclosure design problem.

Simulated Annealing. The algorithm used for probabilistic acceptance of solutions in SA was developed by Metropolis in 1953 as a model for annealing processes in metals and later adapted by Kirkpatrick to be used in metaheuristic optimization [9,10]. In annealing, given sufficient time, atoms within the metal align themselves in the lowest energy state. Kirkpatrick's realization that annealing theory could be applied to optimization led to the following model used in the SA algorithm:

$$P = \exp \frac{-\Delta f}{\theta} \quad (4)$$

where P is the probability of accepting a solution (storing it in memory as the new incumbent solution in the search process) with a higher objective function value than the currently stored solution, Δf is the difference between the stored and current objective function values, and θ is a search parameter set by the designer. The parameter θ is analogous to a slow reduction in temperature during an annealing process. Periodically during the search, θ is reduced according to:

$$\theta_{\text{new}} = \beta \theta_{\text{old}} \quad (5)$$

$$\beta = \left(\frac{\theta_f}{\theta_s} \right)^{\frac{1}{\Theta-1}} \quad (6)$$

where β is a reduction factor and Θ is the total number of reductions desired during the optimization. The parameter θ begins at a high initial value θ_s and is reduced each time a fixed number of new designs have been evaluated. This continues until θ reaches θ_f . Each reduction of θ in Eq. (5) reduces the probability, P , that a worse solution will be accepted.

The algorithm begins by evaluating the objective function for an initial solution that has been randomly selected or chosen by intuition. Subsequent solutions are found by randomly perturbing variables and repeating the objective function calculation. If the new solution is better than the previous, the new solution automatically replaces the previous solution. If the new solution is worse than the previous solution, a random number is chosen between 0 and 1 and compared with the probability of accepting a worse solution, P , calculated in Eq. (4). If the random number is less than this probability, the new (worse) solution is accepted; if

not, it is discarded. After a defined number of new solutions, Φ , have been evaluated, θ is decreased, lowering the probability of accepting a worse design as the algorithm proceeds.

The motivation for accepting worse solutions is illustrated in Fig. 1. Beginning at the left of Fig. 1(a) the algorithm accepts solutions with decreasing f values until it reaches point 1 which is a local minimum in the solution space. To move to point 4 in Fig. 1(b) solutions with increasing f values need to be accepted. Higher levels of θ allow the algorithm to escape local minima and traverse more of the solution space. As θ is decreased, the algorithm will evaluate more solutions near the local minimum before the probability calculated in Eq. (4) allows an escape from the local minimum. Because simulated annealing relies on a probabilistic creation of new solutions and a probabilistic escape from local minima, the algorithm often returns to solutions it has already evaluated. Preventing this redundancy in the search can help an algorithm find better solutions in fewer computations.

Tabu Search. A method that is able to escape local minima and avoid repetitive visits to previous solutions was developed by Fred Glover in the 1980s and is called *tabu search* [11,12]. Tabu search remembers attributes of previously visited solutions and prevents future moves from returning to solutions with these attributes; these moves are thus forbidden or tabu. Tabu search has several key components:

1. solution representation
2. neighborhood definition
3. candidate list structure
4. memory structure

A *solution representation* allows solutions to be conveniently stored in computer memory. A *neighborhood* is a subset of solutions in the solution space that is defined relative to the current incumbent solution. Neighbor solutions are explored at each iteration of the algorithm. A *move* transforms the incumbent solution into one of the neighbor solutions. For computational considerations, when large neighborhoods are present, a *candidate list* composed of a subset of the neighborhood may be defined and only neighbor solutions in that list will be considered. The best non-tabu neighbor solution considered becomes the new incumbent solution. Neighbor solutions are tabu when they possess one or more *tabu attributes* stored in a *memory structure*. The memory structure is created by first, designating as tabu a specific attribute of the incumbent solution, and second, storing this tabu attribute in the memory structure. When an attribute is made tabu, it remains tabu for *tabu tenure* additional iterations after which the

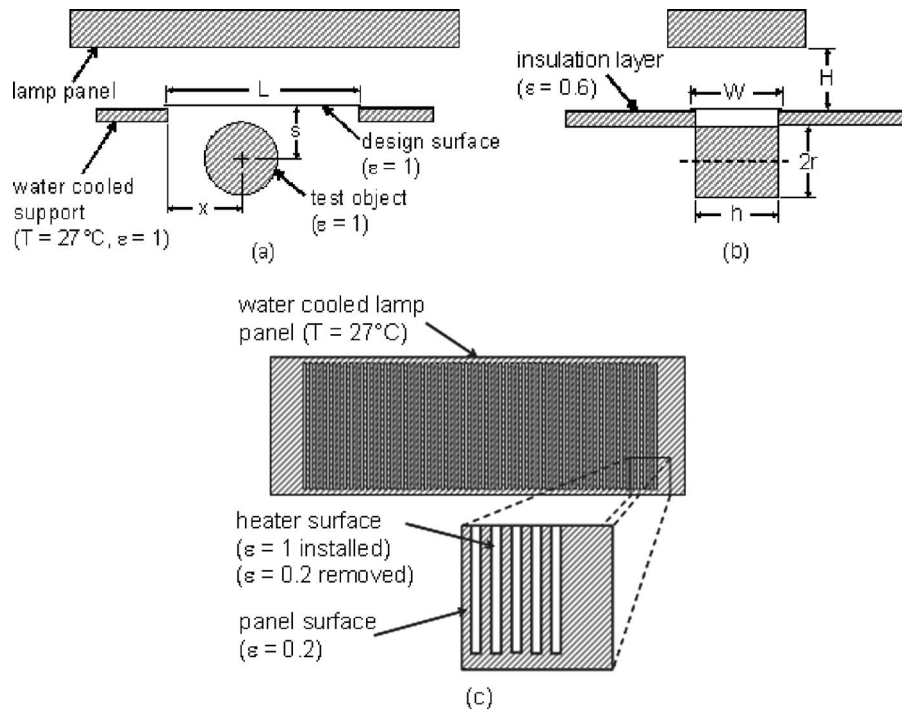


Fig. 2 Schematic of the fire simulation experimental setup. (a) The object (cylinder) is located beneath the design surface (thin metal plate). (b) The length of the cylinder, h , is equal to the width of the opening in the water cooled support. (c) Bottom view of the water cooled lamp panel. The lamps are modeled as strip heaters with variable emissivities corresponding to the state of the heater.

attribute is no longer tabu. These concepts will be explained in greater detail in the case study section.

Case Study: Heater Placement Problem

Fire Simulation Experiments. Certain fire safety studies utilize radiant heating to simulate actual fire environments. The experimental test setup used in this study has discretely placed heaters that heat a thin black metal plate (called a shroud) which in turn radiates to a test object (Fig. 2). The lamp panel has slots for up to 63 lamps that are powered at the same voltage, and controlled using a single thermocouple on the plate surface. Typically, 0.6–1.2 cm of the heated plate’s edges rest on an insulation layer, and the exposed portion of the heated plate radiates to the test object beneath. Plate surface temperatures over 1000°C are routinely achieved during experiments.

A uniform plate temperature is desired for the fire simulation studies. To achieve this, lamps are placed in the panel in a configuration that heats the plate most evenly. The temperature uniformity is affected by the location, size, and radiative properties of the test object. Because of the object-plate interaction, a uniform heat flux on the thin plate usually will not result in a uniform temperature. A heat transfer model was developed by Larsen for the radiant heat test to help technicians determine a priori how certain lamp configurations affected temperature profiles on the plate [13].

The Optimization Model. The heat transfer model developed by Larsen was simplified for this optimization by removing time dependence and conduction heat transfer. Energy exchange between the design surface and the test object was added to the model. These changes were made for two reasons: our intent was to develop optimization strategies for radiation dominated problems, and considering only radiation dramatically reduced solution times. The geometry and positioning of the different elements of the fire simulation experiment are shown in Fig. 2 and Table 1.

The temperatures of the environment, the lamp panel, and the cooling plate were fixed at 27°C. The desired temperature of the heated plate was set at 1000°C and the test object had a uniform constant temperature of 900°C. The heat transfer from the heated plate to the object and environment was calculated using configuration factors from [14]. The lamps were modeled as strip heaters on the bottom surface of the lamp panel (Fig. 2). All installed heaters had the same power level. The total power to the heaters was calculated iteratively by enforcing conservation of energy on the design surface. A single set of configuration factors for the system is sufficient, as the set of finite areas treated remain constant even as heaters are added or subtracted. A strip representing an installed heater has unit emissivity and an imposed heat flux boundary condition. The same strip representing an unoccupied heater position has a lower emissivity and a specified temperature boundary condition.

Table 1 Temperatures and dimensions used in the optimization problem

L [m]	W [m]	H [m]	T_{DS} °C	x_{center} [m]	r [m]	s [m]	T_{TO} °C
0.457	0.203	0.152	1000	0.152	0.102	0.152	900

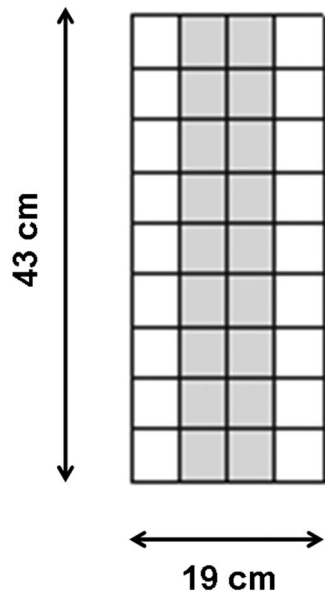


Fig. 3 Elements on the plate that exchange energy with the test object: the objective function only considered flux errors for the center elements of the plate (shaded)

Solution Representation. Heaters in each position have a specified emissivity and net heat flux which result in heater temperature distributions consistent with the current state of the system. Before optimizing the problem a solution representation was constructed that was concise yet captured all of the essential elements of the solution. The optimization routine passed a list of the heaters that were to be turned on for the current objective function calculation. A Boolean list was used to represent the heaters in the model. If an entry in the list was set to 1, the heater in this position was considered to be installed and the corresponding emissivity and boundary condition was updated in the model.

Objective Function. The heat transfer problem is solved using the forward solution approach, where the heater settings are stipulated and the conditions on the design surface are calculated. The difference between the calculated and desired heat flux distributions on the design surface is used in the objective function of the optimization. The optimization of this problem is essentially one dimensional along the length, L , of the design surface (Fig. 2). This is because the heater lengths cannot be changed, and the height, H , of the heaters above the shroud is not considered as a variable in this optimization. The design objective is to distribute lamps along the length of the panel optimally. In the lateral direction, along an individual lamp length, the local heat flux is constant. It was found that including heat flux errors over the entire width of the design surface yielded a less discerning object function than when just the errors adjacent to the centerline were used (Fig. 3). From symmetry, the heat flux errors in both of these rows of elements are identical.

Because conservation of energy is enforced globally on the plate, negative flux errors ($q_{calc,k} < q_{desired,k}$) along the edge elements require positive flux errors along the center elements. Using an objective function that only considers the magnitude of the flux errors in the center elements prevents the objective function from approaching zero. To avoid this, the objective function was normalized by the mean flux error in the considered plate elements. The final objective function, f , is:

$$f = \sqrt{\frac{1}{A_{DS,C}} \sum_{k=1}^{N_{DS,C}} (q_{calc,k} - q_{desired,k} - q_{avg})^2 \Delta x \Delta y} \quad (7)$$

with the average heat flux, q_{avg} given by:

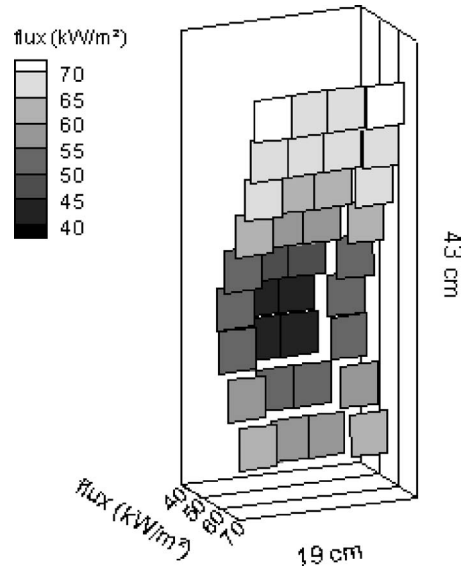


Fig. 4 Desired flux distribution used for the SA and TS optimization. The minimum flux is found to be centered over the location of the test object (Fig. 2).

$$q_{avg} = \frac{1}{N_{DS,C}} \sum_{k=1}^{N_{DS,C}} (q_{calc,k} - q_{desired,k}) \quad (8)$$

where $N_{DS,C}$ is the number of design surface elements considered, $A_{DS,C}$ is the corresponding aggregate area of these elements, $q_{calc,k}$ is the calculated flux to discrete element k on the design surface, $q_{desired,k}$ is the desired flux to discrete element k on the design surface, and $\Delta x_k \Delta y_k$ is the elemental area of element k . The average heat flux, q_{avg} , normalizes the objective function about the average heat flux error of the elements. The desired heat flux, $q_{desired,k}$, is calculated from the energy exchange between the heated plate and the test object. The desired heat flux distribution used in the objective function calculation is plotted in Fig. 4.

SA Combinatorial Radiation Optimization

Neighborhood Selection. As previously described, SA uses random moves and probabilities to search the solution space. In this application, the SA algorithm randomly toggled two heaters in the Boolean list. Two random numbers were generated between 1 and 63. The Boolean state at these two positions on the list was changed from 1 to 0 for a removal, or from 0 to 1 for an insertion. The following three possibilities were considered: two heaters were inserted, two heaters were removed, or one heater was removed and one heater was inserted. The last case represents a swap. The probability of moves represented by each of these three cases resulting in an accepted solution depends upon the incum-

Table 2 SA parameters used for all five of the benchmark solutions

SA parameters	
Initial value of θ	10,000
Final value of θ	100
Max non-improving stages	5
Number of levels for θ	10
At each stage	
Max iterations	1000
Max non-improving iterations	500

Table 3 Optimization results for the benchmark simulated annealing method

Run	Iterations to best	Objective function value
...	...	W/m ²
1	5269	688
2	5768	712
3	8714	616
4	9820	469
5	1390	704
Avg	6192	638
stdev	3302	102

bent solution. If many of the heaters are installed, it is more likely to remove heaters; if few heaters are installed, it is more likely to install heaters.

Optimization Parameters. The overall optimization time was strongly dependent upon the values of the SA parameters θ_s , θ_f , Φ , and Θ . The parameters chosen for the benchmark SA solution are in Table 2. The initial search parameter value was large enough to ensure diversity in the search, while the final search parameter value was set low enough to ensure that the solution space surrounding the final solution was explored thoroughly. If five consecutive stages (different θ values) were completed without any improvement in the best solution found, the search was terminated. If 500 consecutive solutions were explored within a stage without improving the best solution found, the next stage was begun. This is done because the current stage has reached a steady state condition, and further iterations at the same temperature level will probably not improve upon the best solution. This procedure saves computation. All parameters were set to values that were found to produce the best solutions. No rigorous study of parameter settings was performed, however.

Simulated Annealing Results. The benchmark SA algorithm was executed five times using different seeds in the random number generator. The results are shown in Table 3. Since SA is a probabilistic algorithm, results can only be represented as averages. There is no guarantee that the same solution will be found twice. The results for the five SA optimizations show that the average number of iterations to the best solution was 6192. The best solution found during the entire search was stored. A maximum of 10,000 iterations was set for the benchmark cases studied. As with other metaheuristics, better solutions are typically found by increasing the number of iterations. The average minimum objective function value of the five executions of the code was 638 W/m², with a minimum value of 469 W/m² found in execution 4.

Each solution from the benchmark SA was unique and sub-optimal. To illustrate the solutions, two plots are presented. The error plot of solution 4 is shown in a 3D graph to illustrate the uniformity of the considered design surface elements (shaded) relative to the entire design surface (Fig. 5). Plots showing the design surface elements with the superimposed heater positions for all five of the best solutions found are in Fig. 6.

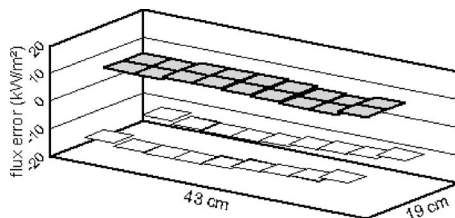


Fig. 5 A 3D plot of the elemental flux error for run 4. The uniformity along the length of the design surface is far better than that along its width.

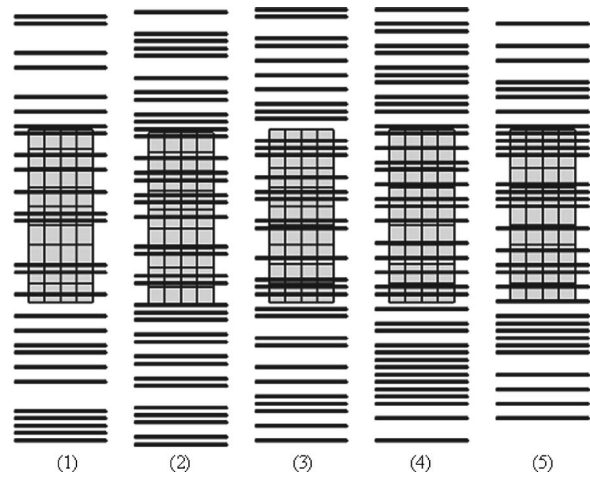


Fig. 6 A side by side comparison of the best heater positions found using the SA algorithm

Although there are not clear similarities between the solutions presented in Fig. 6, it can be generalized that heaters are installed more densely at the ends of the plate, and more sparsely near the test object location. It is also worth noting that the heaters located very far from the design surface may not add to the uniformity of the solution. A penalty function for excess heaters could be developed, but it is often very difficult to determine weighting factors for penalty functions. This was not attempted in this study.

TS Combinatorial Radiation Optimization

As presented in the overview of the TS method, a candidate list of solutions is generated at each iteration of the TS optimization. The next solution is forced to be within this list, so there is no mechanism for solution rejection as in SA. We can, however, accept worse designs, if only worse solutions are present in the candidate list. Populating the candidate list with good solutions becomes a key factor to the success of the algorithm. An intelligent search is needed that deterministically searches the solution space topology. This intelligent search is based on the formulation of an intelligent dynamic neighborhood selection strategy. Using *dynamic neighborhood selection* allows for several different neighborhoods to be utilized during the search.

Neighborhood Selection. In developing the TS algorithm, it became evident that radiation heat transfer has a search neighborhood already embedded in the problem formulation: configuration factors. Given an elemental surface area of interest, configuration factors can give an ordinal rank to every other elemental surface area in the problem. It is immediately known which heaters most strongly influence the surface of interest. We used this feature of

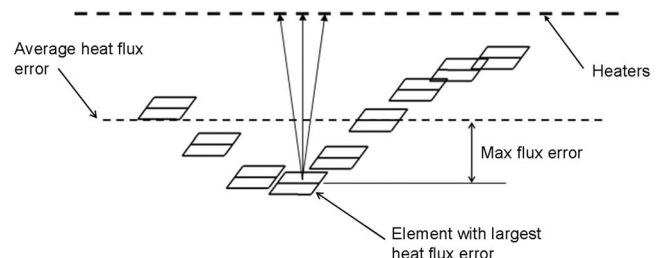


Fig. 7 A search neighborhood based on elements with maximum flux error and the heaters that exchange the most energy with them

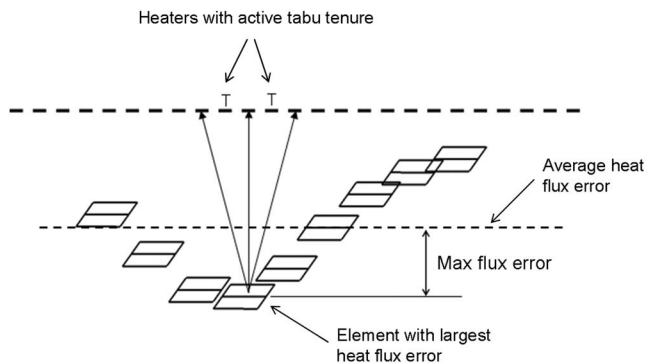


Fig. 8 Coarse search neighborhood with tabu restrictions. The three heaters chosen from the ordered list cannot be tabu.

radiation heat transfer to form an intelligent search neighborhood.

Coarse Neighborhood. To use configuration factors we first needed to identify a surface of interest. We chose the design surface element with the largest absolute value of heat flux error. To determine which heaters to change first, a list of all 63 heaters was generated. Each heater in this list was ordered according to increasing configuration factor from the heater to the surface of interest. This is illustrated in Fig. 7.

The coarse neighborhood identifies moves of *high influence*. When performed, high influence moves have a strong relative effect upon the objective function value. The heaters most likely to strongly influence the design surface element of interest were selected first. In this way the search is focused in a neighborhood that needs the most improvement.

The ordered list of heaters for each design surface element could include all 63 heaters or some candidate list subset. Computational considerations indicated that the latter method was appropriate. Hence, the first K heaters are chosen from this list and all 2^K different heater configurations are generated and evaluated. The best non-tabu solution found from the 2^K configurations is chosen. The tabu attribute used in this optimization was the heater's position. If changing one of the K heater's settings is currently tabu, that heater was ignored in the consideration of neighboring solutions. This is illustrated in Fig. 8 for the case of K equal to 3. In Fig. 8 the design surface elements are plotted showing the heat flux error of each element. The element with the largest heat flux error is the surface element for which the heaters are listed. The heaters with a T above them have active tabu tenures. These are not among the three heaters selected. There is a possibility that there are not K non-tabu heaters to choose from the list. When this happens, the design surface element with the next largest value of flux error is chosen, another list of heaters is selected, and heaters are chosen until K non-tabu heaters are found.

Fine Neighborhood. The coarse neighborhood tabu search rapidly reduced the objective function. However, after a certain number of iterations, the algorithm stopped improving significantly. To improve upon solutions found using the coarse search, a fine neighborhood was defined. Because of the discrete nature of this

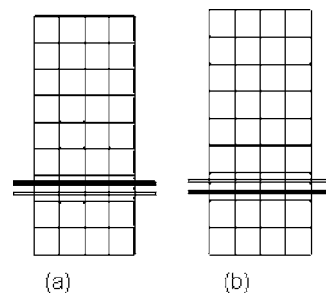


Fig. 9 Illustration of heater positions above the plate. The black heater is installed in both (a) and (b). Swapping the position of two adjacent heaters has a fine tuning effect on the optimization.

radiation problem, removing or adding a heater that is near or over the plate has a drastic impact on the calculated heat flux. In addition, the coarse mesh chosen for the plate to reduce solution time made the problem less sensitive to heater location.

For two adjacent heaters, the heat flux to an elemental design surface beneath those heaters will not experience a large difference in heat flux depending on which of the two heaters is installed. This is illustrated in Fig. 9. Two things are important in the neighborhood selection: first, that a swap move (toggling two adjacent heaters, one off and one on) will have a fine tuning effect upon the optimization, and second, that during the coarse neighborhood search, not every heater needs to be considered. If every other or every third heater position is ignored in the initial search, the solution space is vastly reduced, and the coarse search is done more efficiently. The fine search performs swap moves that consider all heater positions, including those ignored during the coarse search.

Another region of the solution space that may be missed during the coarse search includes heater positions far away from the design surface. These heater positions will be far down on the list of heater positions generated based on configuration factors, and will have a small likelihood of selection. Nearly all of the best designs found using SA included heaters at these outer positions. Incorporating these heaters into the search may be necessary to find the best solutions. These positions were stored in a list including heaters 1–15 and heaters 48–63. Every 5th iteration of the fine search used heaters from this list to form a candidate list. The coarse and fine search neighborhoods are listed in Table 4 and illustrated by general heater position in Fig. 10.

Memory Structure. An adaptive memory structure was implemented for the TS optimization. Adaptive tabu search (ATS) was developed in operations research applications several years ago [15]. In ATS, the tabu tenure (or the number of iterations for which a move is considered tabu) changes adaptively during the search. This incorporates a diversification and intensification strategy into the search. When the new solution found by an iteration of the algorithm is improving, the tabu tenure is reduced by one. This allows for a more thorough search of the solution space near the incumbent solution. When a non-improving solution is found, the tabu tenure is increased by one. This forces the algorithm to

Table 4 Three move neighborhoods selected for the TSDN optimization. A toggle move toggles between two states: installed and not installed.

	Move type	Selection criterion	Ordering
Coarse	Toggle	Max design surface flux error	Largest configuration factors are first
Fine	Adjacent swap	Max design surface flux error	Largest configuration factors are first
	Toggle	Only outer heaters: 1–15, 48–63	Heaters closest to plate are considered first

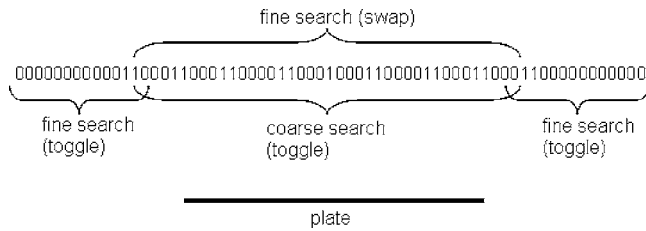


Fig. 10 Illustration of the general heater positions considered in the fine and coarse neighborhoods. A toggle move switches the state of the heater considered between on (1) and off (0). A swap move turns one heater on and one adjacent heater off.

move from the current solution subspace being explored as more moves become tabu. A maximum and minimum tabu tenure length is fixed so that the tabu tenure will not grow too large or too small. Because the tabu attribute was heater position, when a heater in the incumbent solution was changed (toggled or swapped), that heater could not be changed for tabu tenure iterations.

Dynamic Neighborhood. The TS algorithm began with the same initial solution as the benchmark SA algorithm. Initially, the coarse neighborhood was used to search the solution space with every-other heater position considered for toggle moves. This was done until a maximum number of iterations was completed with no improvement in the best solution found. The maximum number of iterations was chosen to be sufficiently large to ensure that the algorithm had indeed reached steady state. The fine neighborhood search then began by considering adjacent swaps, initialized with the best solution found during the coarse search. These swaps were ordered according to the largest design surface flux error and the configuration factors of the installed heaters (Fig. 8). After five iterations of the fine search the outer heaters were toggled as discussed previously.

The fine search can also reach steady state, so we added another level of intensification and diversification. After a maximum number of iterations of the fine search was completed without improvement of the best solution found, the coarse search was again implemented and initialized with the best solution found. This time, however, the maximum number of non-improving solutions was reduced to three. This allowed the search to be quickly diversified by performing several high influence moves using the coarse search neighborhood. The fine search was then repeated. The algorithm was terminated after a fixed number of iterations. The results of the TS optimization are presented next.

TS Results. The results from the TS implementation with both the coarse and fine neighborhood searches along with the intensification and diversification strategy described above are presented in Table 5.

Notice that no repeated runs are necessary since the TS algorithm is deterministic; the same results are found each time the code is executed. The TS algorithm with the dynamic neighborhood (TSDN) algorithm reached an objective function value of 440.8 W/m^2 . This was a 31% relative improvement on the average SA results of 638. It reached this solution in 2666 objective

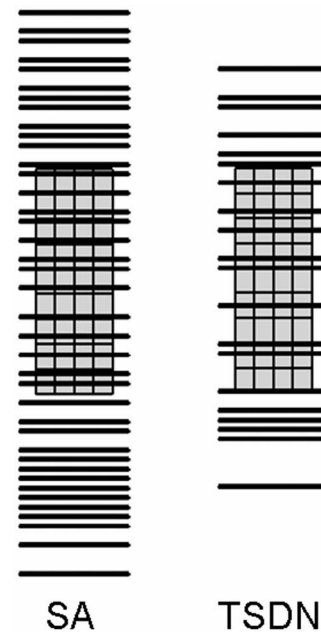


Fig. 11 Comparison of heater positioning for the best SA solution (469.3 W/m^2) and the TSDN solution (440.8 W/m^2)

function evaluations. This was a 57% relative improvement on the SA algorithm of 6192. The SA and TS codes were executed on the same computer (Dell Power Edge server with two 2.0 Ghz processors). The same objective function was used for both the TS and SA codes. Each objective function calculation took approximately 0.6 s to compute.

By comparing the best solution found from the SA algorithm with the solution found using the TSDN algorithm (Fig. 11) we see that the TSDN solution used fewer heaters to achieve a better solution. This is a beneficial consequence of the intelligent neighborhood selection. The closest heater positions are explored first, then the heater positions further from the plate. In the SA algorithm, all 63 heaters are considered simultaneously. This allows for high and low influence moves to be evaluated continuously throughout the search, but also tends to populate more heater positions. Comparing the flux error distributions for both solutions reveals that the two solutions are very similar (Fig. 12). However, SA only reached this solution once, and it took 9820 objective function calculations; TSDN reaches this solution every time in 2666 objective function calculations ($3\frac{1}{2}$ times faster).

By reducing the number of heaters searched during the coarse search to every third heater, further improvement was found (Table 6). Letting the benchmark SA algorithm run for 100,000 iterations revealed a best solution of 359 W/m^2 , but this solution was not reached repeatedly. By running the TSDN with every third heater considered, two previously unfound best solutions were found during the same execution with the best solution of 291.1 W/m^2 , far surpassing any previously found solutions. This

Table 5 Results from the TS algorithm with the dynamic neighborhood (TSDN). The max and min tabu tenure was set to 8 and 3 respectively. All candidate lists were composed of 31 solutions. A heater list size of 20 was used, with only odd numbered heaters considered.

Total Objective Function Calculations	Max Moves	Moves to best	Objective function calculations to best	Improvement on SA average	Time to best s	Objective Function value W/m^2	Improvement on SA average
15,469	500	86	2,666	57%	1631	440.8	31%

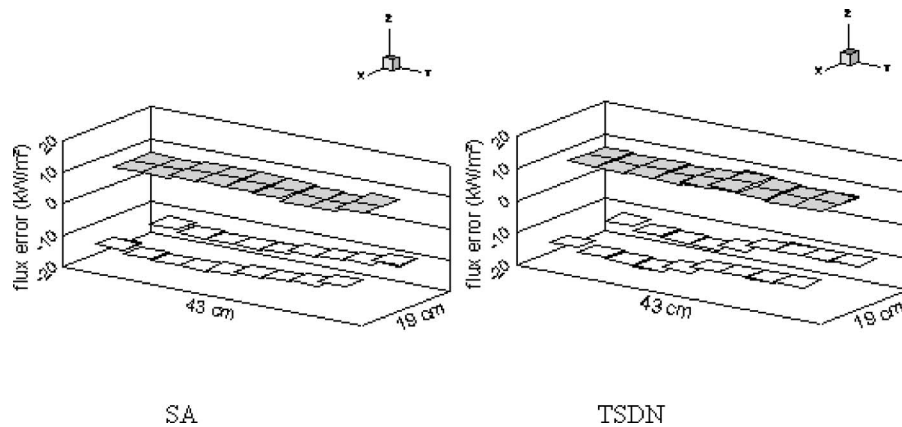


Fig. 12 Comparison 3D plots of the flux error for the best SA solution (469.3 W/m²) and the TSDN solution (440.8 W/m²)

solution is compared with the best SA solution in Fig. 13. It appears in Table 6 that this best solution took longer to find than the benchmark SA. This is because the SA algorithm was unable to find similar solutions for comparison.

The search results for both methods are plotted on a single graph in Fig. 14. In this graph SA appears to do better than TSDN until the number of objective function calculations exceeds 600. From around calculation 600 to around calculation 7600, TSDN is superior to SA. Most of the solutions found using TSDN are better than the best solutions found by SA within this interval. Notice the peaks in the TSDN search. These correspond to the coarse neighborhood search or diversification. Following each peak is a valley corresponding to the fine search neighborhood or intensification. Comparing this to SA, diversification is evident early in the search (many high data points) with intensification later in the search (fewer high data points).

Conclusions

The heater placement problem demonstrated the strengths of metaheuristic optimization when applied to discrete solution spaces with multiple local minima. Choosing the best metaheuristic for a specific combinatorial problem is important. In this study, tabu search was superior to simulated annealing. This is probably

because of the adaptive intensification and diversification of the search. In SA, diversification occurs early when the annealing temperature is high, and intensification happens late in the search as the search parameter is lowered (Fig. 14). Through probabilistic acceptance of non-improving solutions SA can traverse many local minima, but local minima are not explored thoroughly until late in the search. This results in many local minima being visited, but not thoroughly explored. In contrast, TS intensifies at each local minima found (by the adaptive tabu tenure memory structure) and only diversifies when the solutions stop improving. Because SA is sensitive to many of the parameters used, choosing the best parameter settings required many code executions, adding further computation time. Tabu search with adaptive memory structure and dynamic neighborhood selection was much less sensitive to parameter settings.

Neighborhood Selection Guidelines. Adding an additional level of intensification and diversification through a dynamic neighborhood selection was key to the success of the TS algorithm in the case study. This additional level of diversification incorporated problem specific information. This is an advantage of using tabu search. In the case study, we found that toggle moves close to the design surface had a significant effect upon the ob-

Table 6 Results from the TS algorithm with the dynamic neighborhood (TSDN). The max and min tabu tenure was set to 8 and 3, respectively. All candidate lists were composed of 31 solutions. A heater list size of 20 was used, with every third heater considered during the coarse search. Results in the top row are an intermediate solution; bottom row is final best solution.

Total objective function calculations	Max moves	Moves to best	Objective function calculations to best	Improvement on SA average	Time to best, s	Objective function value, W/m ²	Improvement on SA average
...
15,376	500	109	3255	47%	2002	435.9	32%
15,376	500	238	7254	-17%	4437	291.1	54%

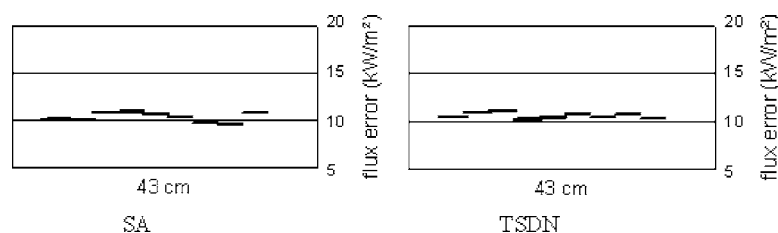


Fig. 13 Results comparison along the centerline of the design surface for the best SA (469 W/m²) and best TSDN (291 W/m²) solutions found

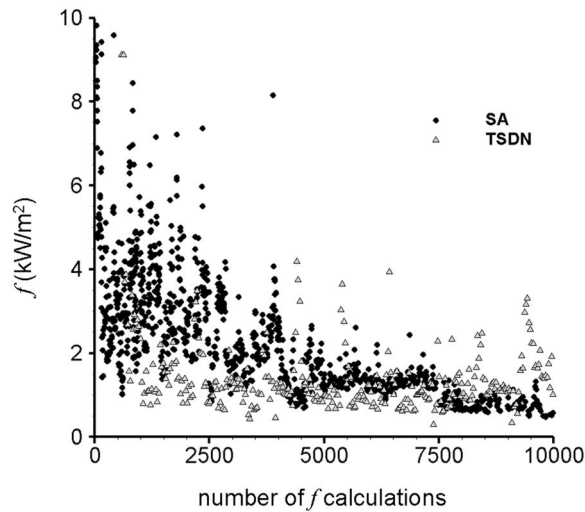


Fig. 14 A comparison of the SA (469 W/m^2) and TSDN (291 W/m^2) searches. Candidate solutions (TSDN) and rejected solutions (SA) are not shown due to the large number of data points required.

jective function. Toggle moves were performed during the coarse search phase of the optimization. Swap moves and toggle moves far from the design surface had a smaller effect on the objective function. These moves were used during the fine search phase. These two search phases formed the dynamic neighborhood. Considering only a subset of the heaters during the coarse search phase further improved search efficiency.

Applications. Metaheuristic optimization is an alternative to non-linear programming or regularization in radiation dominated heat transfer design problems. When all design variables are continuous, regularization and non-linear programming methods are preferred due to the reduced number of iterations required. However, when designs require discrete variables, the complexity of the problem precludes gradient information, or regularization results in infeasible solutions, metaheuristics are a reliable alternative. By exploiting the memory structure and incorporating dynamic neighborhoods into the search, tabu search was shown to be successful in optimizing radiation heat transfer design problems.

Areas for Future Research. Although metaheuristics are most valuable in combinatorial optimization, they have also found broad application in continuous problems (two cases of this are found in [4,5]). Discretizing the solution space of a continuous optimization problem results in a combinatorial optimization problem. This also reduces the solution space. Instead of a simple toggle move, the power to specific heaters could be incremented upward or downward based on the sign and possibly the magnitude of the flux error on the design surface elements. By using this approach, fully continuous transient radiation problems can be optimized using the powerful memory structure and dynamic neighborhood of tabu search.

Nomenclature

A	= area
b	= bottom surface of design surface (shroud)
F	= configuration factor
f	= objective function
H	= height of heaters above design surface (shroud)
h	= height of cylinder (test object)
K	= number of heaters in TS candidate sublist
L	= length of design surface (shroud)

N	= total number of differential surfaces
M	= number of design surface elements
P	= probability of accepting a solution (SA)
Q	= heat transfer
q	= heat flux
r	= radius of cylinder
s	= distance separating the test object axis from the design surface
SA	= simulated annealing
T	= absolute temperature
t	= top surface of design surface (shroud)
TS	= tabu search
TSDN	= tabu search with a dynamic neighborhood
W	= width of design surface (shroud)

Subscripts

avg	= average (mean) heat flux
C	= considered in objective function calculation
calc	= calculated
desired	= desired value of calculation
DS	= design surface
env	= environment
f	= final
i	= incident
insulation	= insulation layers in radiation model
j, k	= surface descriptors
$j-k$	= from surface j to surface k
max	= maximum
min	= minimum
new	= new θ level (SA)
o	= outgoing
object	= test object (cylinder) beneath design surface
old	= previous θ level (SA)
s	= start
TO	= test object

Symbols

β	= reduction factor used to calculated levels of θ (SA)
δ_{kj}	= Kronecker delta
Δ	= differential change
ε	= emissivity
Φ	= number of new solutions evaluated at each level of θ (SA)
θ	= search parameter analogous to annealing temperature (SA)
Θ	= number of levels of θ (SA)
σ	= Stephan-Boltzmann constant

References

- [1] Daun, K., Erturk, H., Gamba, M., and Hosseini Sarvari, M., 2003, "The Use of Inverse Methods for the Design and Control of Radiant Sources," *JSME Int. J., Ser. B* **46**(4), pp. 470–478.
- [2] Franca, F., Howell, J. R., Ezekoye, O., and Morales, J., 2002, "Inverse Design of Thermal Systems," *Advances in Heat Transfer*, J. P. Hartnett and T. F. Irvine, eds., 36, Academic Press, San Diego, pp. 1–110.
- [3] Daun, K. J., Morton, D. P., and Howell, J. R., 2003, "Geometric Optimization of Radiant Enclosures Containing Specular Surfaces," *ASME J. Heat Transfer*, **125**, pp. 845–851.
- [4] Li, H. Y., and Yang, C. Y., 1997, "A Genetic Algorithm for Inverse Radiation Problems," *Int. J. Heat Mass Transfer*, **40**, pp. 1545–1549.
- [5] Kim, K. W., and Baek, S. W., 2004, "Inverse Surface Radiation Analysis in an Axisymmetric Cylinder Enclosure Using a Hybrid Genetic Algorithm," *Numer. Heat Transfer, Part A*, **46**, pp. 367–381.
- [6] Siegel, R., and Howell, J. R., 2002, *Thermal Radiation Heat Transfer*, 4th ed. Taylor and Francis, New York, pp. 276–277.
- [7] Van Laarhove, P. J. M., Aarts, E. H. L., and Lenstra, J. K., 1992, "Job Shop Scheduling by Simulated Annealing," *Oper. Res.*, **40**(1), pp. 113–125.
- [8] Chiang, W. C., and Russell, R. A., 1996, "Simulated Annealing Metaheuristics

- for the Vehicle Routing Problem With Time Windows," *Ann. Operat. Res.*, **63**, pp. 3–27.
- [9] Metropolis, N., Rosenbluth, A., Rosenbluth, M., Teller, A., and Teller, E., 1953, "Equation of State Calculations by Fast Computing Machines," *J. Chem. Phys.*, **21**, pp. 1087–1092.
- [10] Kirkpatrick, S., Gelatt, C. C., Jr., and Vecchi, M. P., 1983, "Optimization by Simulated Annealing," *Science*, **220**(4598), pp. 671–680.
- [11] Glover, F., 1986, "Future Paths for Integer Programming and Links to Artificial Intelligence," *Comput. Oper. Res.*, **5**, pp. 533–549.
- [12] Glover, F., 1989, "Tabu Search—Part I," *ORSA J. Comput.*, **1**(3), pp. 191–206.
- [13] Larsen, M., and Porter, J., 2005, "Theory and Experimental Validation of SPLASH," Sandia Report No. SAND 2005-2947, Sandia National Laboratories.
- [14] Howell, J. R., 2005, "B-32: Element on Plane to Exterior of Right Circular Cylinder of Finite Length. Plane Does Not Intersect Cylinder," online catalogue of view factors maintained on the World Wide Web at <http://www.me.utexas.edu/~howell/sectionb/B-32.html>.
- [15] Barnes, J. W., and Chambers, J. B., 1995, "Solving the Job Shop Scheduling Problem Using Tabu Search," *IIE Trans.*, **27**, pp. 257–263.

Photon Monte Carlo Simulation for Radiative Transfer in Gaseous Media Represented by Discrete Particle Fields

Anquan Wang
Mem. ASME

Michael F. Modest¹
Fellow ASME
e-mail: mfm6@psu.edu

Department of Mechanical and Nuclear
Engineering,
Pennsylvania State University,
University Park, PA 16802

Monte Carlo ray-tracing schemes have been developed for the evaluation of radiative heat transfer for problems, in which the participating medium is represented by discrete point masses, such as the flow field and scalar fields in PDF Monte Carlo methods frequently used in combustion modeling. Photon ray tracing in such cases requires that an optical thickness is assigned to each of the point masses. Two approaches are discussed, the point particle model (PPM), in which the shape of particle is not specified, and the spherical particle model (SPM) in which particles are assumed to be spheres with specified radiation properties across their volumes. Another issue for ray tracing in particle fields is the influence region of a ray. Two ways of modeling a ray are proposed. In the first, each ray is treated as a standard volume-less line. In the other approach, the ray is assigned a small solid angle, and is thus treated as a cone with a decaying influence function away from its centerline. Based on these models, three different interaction schemes between rays and particles are proposed, i.e., line-SPM, cone-PPM and cone-SPM methods, and are compared employing several test problems.

[DOI: 10.1115/1.2345431]

1 Introduction

Among radiative transfer models, Monte Carlo ray tracing (MCRT) can be applied to problems of arbitrary difficulty with relative ease [1]. The MCRT method directly simulates the physical processes, i.e., emission, absorption, scattering, and reflection, from which the radiative transfer equation is derived.

In the standard Monte Carlo method a ray carrying a fixed amount of energy is emitted and its progress is then traced until it is absorbed at a certain point in the participating medium or at the wall, or until it escapes from the enclosure. As many researchers have pointed out [2–6], this method is inefficient when the walls are highly reflective and/or the medium is optically thin so that most photon bundles exit the enclosure without any contribution to the statistics. Modest [4,5] applied the concept of energy partitioning to alleviate this problem. In this method the energy carried by a ray is not absorbed at a single point, but rather is attenuated gradually along its path until its depletion or until it leaves the enclosure. The locally absorbed fraction of the ray's energy contributes to the heat exchange rates of subvolumes along the ray's path. This method was also called "absorption suppression" by Walters and Buckius [6]. A large variety of problems of great complexity can be simulated with reasonable efficiency using either standard or energy partitioning methods in forward Monte Carlo simulations, when overall knowledge of the radiation field is desired.

The MCRT method has been applied to all aspects of radiative heat transfer [7,8]. In applications without a participating medium, ray tracing is relatively simple. However, in many high-temperature applications, such as combustion problems, participating media play a key role. A major difficulty is the evaluation of the optical thickness that a ray passes through, since the temperature and concentration fields tend to be highly inhomogeneous and turbulent. In traditional treatments the turbulence of tempera-

ture and concentrations is regarded as an uncoupled process from radiation, using mean temperature and concentrations to evaluate the radiative intensities and properties [9]. However, many experimental and numerical studies have demonstrated that radiative fluxes can be underestimated by a factor of up to 3, if mean temperature and concentration fields are employed [10,11]. Therefore, turbulence-radiation interactions have been considered in many recent combustion calculations. The treatment of turbulence-radiation interactions is not a trivial task because of the nonlinear coupling of temperature, species concentrations, and radiative intensities. Among various treatments of turbulence-radiation interactions, the joint-probability-density-function (joint-PDF) methods, such as the velocity-composition PDF [12] and the composition PDF [13] methods, are the most advanced and promising methods. In such methods, a particle Monte Carlo method [14] is frequently used to solve the transport equation of the joint PDF, in which the flow is represented by a sufficiently large number of discrete particles (point masses) evolving with time. In such flow fields, to apply the Monte Carlo method for radiation calculations, traditional continuum ray-tracing models are no longer useful. No work appears to have been done to date to implement MCRT in media represented by discrete particle fields, which is the aim of the present paper.

While spectral variations of the absorption coefficient are an important aspect of radiation calculations, it is not the purpose of this paper to discuss spectral models. Therefore, the discussion will be limited to gray media, but the same analysis can readily be applied to nongray media.

2 Ray-Particle Interaction Models

To simulate the radiative transfer process by ray tracing in a discrete particle field, the interaction between infinitesimal point masses and infinitesimally thin photon rays needs to be modeled. This can be done by assigning effective volumes to the point masses, by assigning an influence volume to the ray's trajectory, or a combination of both. In this section, several particle models and ray models are developed first, followed by photon emission and absorption algorithms based on these models.

¹To whom all correspondence should be addressed.

Contributed by the Heat Transfer Division of ASME for publication in the JOURNAL OF HEAT TRANSFER. Manuscript received October 3, 2005; final manuscript received March 21, 2006. Review conducted by Bakhtier Farouk.

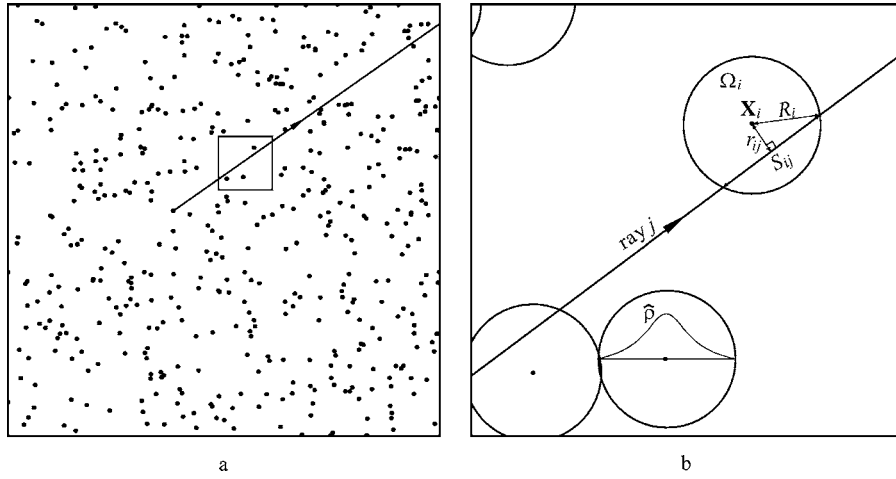


Fig. 1 (a) PPM representation of a 2D medium; (b) SPM representation of a sub-region in (a)

2.1 Particle and Photon Ray Models

2.1.1 Point Particle Model (PPM). In this model, particles are treated as point masses, i.e., they carry an amount of mass without a specific shape at a certain spatial location as shown in Fig. 1(a), which is a 2D particle field. The only geometric information known about the particles is their position vector. However, particles do have a nominal volume, which may be calculated from their thermophysical properties such as pressure and temperature. For example, if the ideal gas assumption is adopted, the nominal volume may be computed as

$$V_{o,i} = \frac{m_i R T_i}{p_i} \quad (1)$$

where m_i is the mass carried by particle i , T_i is its temperature, p_i is its total pressure, and R is the gas constant. To enforce consistency in the discrete particle representation of the medium, the overall nominal volume of all particles should be the same as the actual geometric expanse of the medium. As a consequence, one may regard the nominal volume of a particle as its real volume.

The point particle model only contains the particle information that the original discrete particle field contains. It does not employ any other assumption and, therefore, it will not induce any inconsistency. The disadvantage of this model is that it is difficult to determine the interaction of a photon ray with a volume without shape.

2.1.2 Spherical Particle Model. In this method, each point-mass m_i has a spherical influence region Ω_i , surrounding it as shown in Fig. 1(b). The mass is distributed to its influence region according to a density profile,

$$\hat{\rho}_i(\mathbf{x}) = \begin{cases} \rho_{o,i} W_{3D}\left(\frac{|\mathbf{x} - \mathbf{x}_i|}{R_i}\right), & |\mathbf{x} - \mathbf{x}_i| < R_i \\ 0, & |\mathbf{x} - \mathbf{x}_i| \geq R_i \end{cases} \quad (2)$$

where \mathbf{x}_i is the spatial location vector of the point-mass i , R_i is its influence radius, $\rho_{o,i}$ is the nominal density calculated by

$$\rho_{o,i} = \frac{m_i}{V_{o,i}} = \frac{p_i}{R T_i} \quad (3)$$

and W_{3D} is a spherically symmetric weight function which decays from the center along radial directions and satisfies the condition

$$\int_{\Omega_i} W_{3D}\left(\frac{|\mathbf{x} - \mathbf{x}_i|}{R_i}\right) d\mathbf{x} = V_{o,i} \quad (4)$$

so that the total mass in the influence region is equal to the point mass. In this method, particles are assigned a spherical volume (influence region) with varying density, and overlapping other particles in the domain. This is called the *spherical particle method* (SPM).

One may adjust the size of influence region and the mass distribution of particles by employing different weight functions. Larger influence radii lead to more particle overlap and spatial gradients may be smoothed out. On the other hand, smaller influence radii result in smaller particle volumes, making it more difficult to interact with rays. The simplest possible weight function is

$$W_{3D}\left(\frac{|\mathbf{x} - \mathbf{x}_i|}{R_i}\right) = 1 \quad (5)$$

i.e., the density is constant in the influence region and its volume is the same as the nominal volume of the particle. The particles can then be regarded as constant density spheres with a radius determined by their nominal volumes,

$$R_i = \left(\frac{3V_{o,i}}{4\pi}\right)^{1/3} \quad (6)$$

This model will be termed the *constant density sphere* (CDS) model. The overall density at an arbitrary position is the sum of density contributions from all nearby particles. Some locations may be influenced by more than one particle, while some other locations may not be in the influence region of any particle, i.e., there is a void in these places. Therefore, this model cannot recover a continuous density medium as shown in Fig. 1(b) and Fig. 2. Figure 1(b) is a small portion of the CDS representation of the 2D field given in Fig. 1(a) (if variable density were employed, the R_i would be larger, resulting in substantial overlap, even in this region of few particles). A location with lots of void space was chosen for simplicity in Fig. 1(b). In order to show particle locations in a plane, a 2D rather than 3D particle field is depicted. Figure 2 shows the density distribution on a cross-section of a 3D CDS representation of a homogeneous medium of unity density.

2.1.3 Line Ray Model. In this model, a ray is simply treated as a volume-less line and energy propagates one-dimensionally along the line. This is the standard model for ray tracing in continuous media. Since such rays are not designed to have a specific volume,

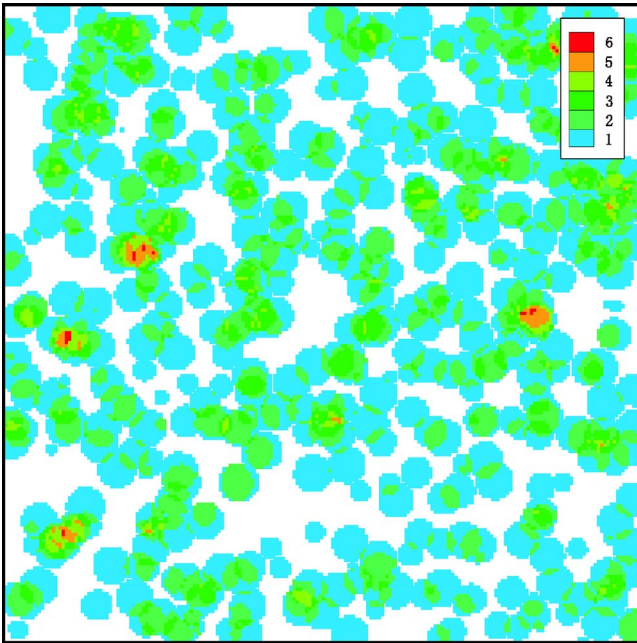


Fig. 2 Relative density distribution on a cross section of a 3D CDS representation for a homogeneous medium

they are not able to interact with point masses. Therefore, this model requires volumetric particle models for radiative transfer simulations.

2.1.4 Cone Ray Model. Physically, a photon bundle consists of many millions of individual photons, occupying a small solid angle. Thus, to model the volume of a ray, one may assign a small solid angle to the ray and treat it as a cone. Energy is assumed to propagate axisymmetrically along the cone, with its strength decaying in the radial direction normal to the cone axis, similar to the weight function assigned to particle density in Eq. (2), but in 2D. For a ray emitted at \mathbf{x}_o into a direction given by a unit direction vector $\hat{\mathbf{s}}$, the intensity at location \mathbf{x} in the ray can then be modeled as

$$I(s, r) = I_o(s) W_{2D}[r/R_c(s)] \quad (7)$$

where $s = (\mathbf{x} - \mathbf{x}_o) \cdot \hat{\mathbf{s}}$ is the distance from the emission location to a point on the ray axis, r is the distance from a point to the ray axis on a plane normal to the axis, $I_o(s)$ is the intensity at the ray

center, and $R_c(s)$ is the local influence radius of the cross-section as depicted in Fig. 3. W_{2D} is a normalized two-dimensional center-symmetric profile which satisfies

$$\int_0^1 W_{2D}(r') 2r' dr' = 1 \quad \text{and} \quad r' = r/R_c \quad (8)$$

Again, many weight functions are possible, ranging from $W_{2D} = 1$ to Gaussian decay. A popular Gaussian-like weight function is provided here [15] as

$$W_{2D}(r') = \frac{60}{7} \begin{cases} \frac{1}{3} - 4r'^2 + 4r'^3, & 0 \leq r' < \frac{1}{2} \\ \frac{4}{3}(1 - r')^3, & \frac{1}{2} \leq r' < 1 \\ 0, & r' \geq 1 \end{cases} \quad (9)$$

Physically, the distribution of energy emitted from a point is isotropic in all directions. Different rays from the same point may overlap if rays have a volume. The Gaussian decay of energy along the radial direction provides a smoother overlap than a uniform energy distribution across the cone cross section. Since in this model the ray has a specific volume, volume-less particles can be intercepted by the ray, and this model can work together with the point particle model.

2.2 Emission From a Particle. We now focus on the implementation of Monte Carlo methods for the simulation of radiative transfer in particle-based media, i.e., how photon bundles are emitted from the particle field, how they are traced, and how they interact with other particles.

A small gas volume emits energy uniformly into all directions. In Monte Carlo simulations, the total energy is divided into a number of photon bundles (rays), which are released into random directions. In a physical gas volume the emitted energy comes from every point in the volume. If the medium is represented by discrete particles, emission takes place inside these particles. Thus, depending on the optical thickness of the particle, and the point and direction of emission, some of the emitted energy may not escape from the particle due to self-absorption. If the particle is optically thin, the self-absorption of emission is negligible and the total emission from particle i is calculated from [1]

$$Q_{\text{emi},i} = 4\kappa_{\rho,i} m_i \sigma T_i^4 \quad (10)$$

where $\kappa_{\rho,i}$ is the density-based Planck-mean absorption coefficient at particle temperature T_i , σ is the Stefan-Boltzmann constant, and m_i is the mass. If self-absorption is considered and the particle is

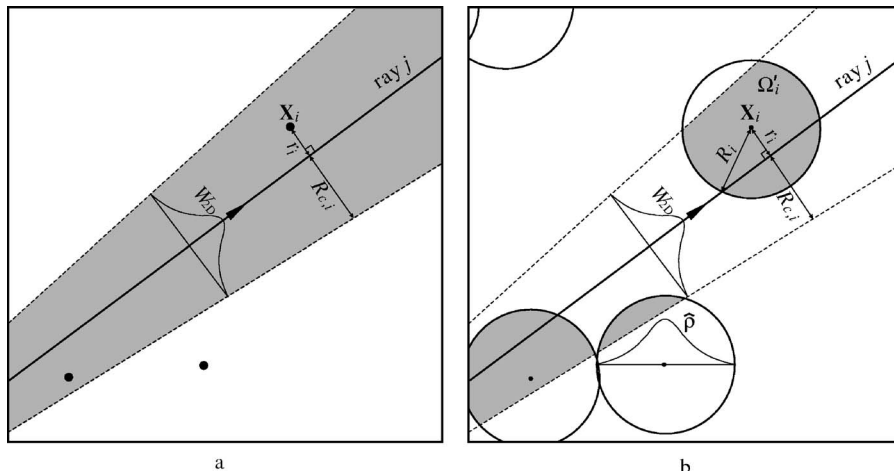


Fig. 3 (a) Cone-PPM scheme; (b) Cone-SPM scheme

assumed to be a constant density sphere, the total emission from a sphere is obtained from [1]

$$Q_{\text{emi},i} = 4\pi R_{o,i}^2 \sigma T_i^4 \left\{ 1 - \frac{1}{2\tau_{o,i}^2} [1 - (1 + 2\tau_{o,i})e^{-2\tau_{o,i}}] \right\} \quad (11)$$

where $R_{o,i} = (3V_{o,i}/4\pi)^{1/3}$ is the nominal spherical radius of particle i and $\tau_{o,i} = \rho_{o,i}\kappa_{\rho,i}R_{o,i}$ is the optical thickness of the spherical volume based on the nominal radius. In the point particle model, the shape of a particle is arbitrary, but Eq. (11) is still a good approximation of total emission from such a particle. If more than one ray is emitted from a particle, the sum of initial energy carried by all rays must be equal to the total emission calculated from Eq. (10) or Eq. (11), depending on whether self-absorption is neglected.

2.3 Absorption Models. The basic task of simulating the absorption of a photon bundle in a medium described by a point particle field is the evaluation of the optical thickness that a ray traverses along its path. This is achieved by modeling the interaction between the ray and the particles that it encounters. Based on different models employed for rays and particles, several schemes for absorption simulation may be obtained.

2.3.1 Line-SPM Scheme. In this scheme, the ray is treated as a line and the spherical particle model (SPM) is employed for the particles as shown in Fig. 1(b). The contribution of particle i to the optical thickness that ray j passes through is computed as

$$\Delta\tau_{ij} = \int_{S_{ij}} \hat{\rho}_i[\mathbf{x}(s)]\kappa_{\rho,i} ds \quad (12)$$

where s is the ray path coordinate as in Eq. (7), S_{ij} is the intersection of ray j and the influence region of particle i , $\kappa_{\rho,i}$ is the density-based absorption coefficient of particle i at its own temperature, and $\hat{\rho}_i$ is the local density of particle i as indicated in Fig. 1(b). If the constant density sphere (CDS) model is employed, the mass of the particle is distributed uniformly across its influence region and Eq. (12) can be simplified to

$$\Delta\tau_{ij} = 2\rho_{o,i}\kappa_{\rho,i}\sqrt{R_i^2 - r_{ij}^2} \quad (13)$$

where $\rho_{o,i}$ is the nominal density defined in Eq. (3), R_i is the influence radius, and r_{ij} is the distance from the center of particle i to ray j , as indicated in Fig. 1(b). Since Eq. (13) has a very simple form, its implementation can be very fast.

The total optical thickness that ray j passes through is simply the summation of the contributions from the individual particles it interacts with,

$$\tau_j = \sum_{i \in I_j} \Delta\tau_{ij} \quad (14)$$

where I_j denotes all the particles intersected by ray j .

2.3.2 Cone-PPM Scheme. If the ray is modeled as a cone, it is possible to let it interact with point particles. The energy change of a conical ray, when it traverses over a small distance ds in a continuous medium, is

$$dE(s) = - \int_0^{R_c} \kappa ds I(r) 2\pi r dr = - \bar{\kappa} ds \int_0^{R_c} I(r) 2\pi r dr = - E(s) \bar{\kappa} ds \quad (15)$$

where $E(s)$ is the plane-integrated energy over the cone cross-section at axial location s , κ is the local absorption coefficient, $\bar{\kappa}(s)$ is the plane-averaged absorption coefficient, and $R_c(s)$ is the local radius of the cross-section. From Eqs. (15), (7), and (8), the plane-averaged absorption coefficient can be derived as

$$\bar{\kappa} = \frac{\int_0^{R_c} \kappa I r dr}{\int_0^{R_c} I r dr} = \frac{\int_0^1 \kappa I r' dr'}{\int_0^1 I r' dr'} = \frac{\int_0^1 \kappa W_{2D} 2r' dr'}{\int_0^1 W_{2D} 2r' dr'} = \int_0^1 \kappa W_{2D} 2r' dr' \quad (16)$$

Therefore, the total optical thickness that the ray passes through along its path S is

$$\tau = - \ln \frac{E(s)}{E(0)} = - \int_S \frac{dE}{E} = \int_S \bar{\kappa} ds = \int_S \int_0^1 \kappa W_{2D} 2r' dr' ds = \int_S \int_0^{R_c} \frac{\kappa W_{2D}}{\pi R_c^2} 2\pi r dr ds = \int_V \frac{\kappa W_{2D}}{\pi R_c^2} dV \quad (17)$$

where V is the volume that the ray covers in its path.

In discrete particle fields as shown in Fig. 3(a) the absorption coefficient is represented by a set of delta functions,

$$\kappa = \sum_i \kappa_i V_i \delta(\mathbf{x} - \mathbf{x}_i) \quad (18)$$

Integration over V yields

$$\tau = \sum_{i \in I} \frac{\kappa_i W_i V_i}{\pi R_{c,i}^2} = \sum_{i \in I} \frac{\kappa_{\rho,i} W_i m_i}{\pi R_{c,i}^2} \quad (19)$$

where I denotes all the particles enclosed by the cone. For point particles, the particle weight is a point weight in the energy distribution, i.e.,

$$W_i = W_{2D}(r_i/R_{c,i}) = W_{2D}(r'_i) \quad (20)$$

where r'_i is the distance from particle i to the cone axis, normalized by the local cone radius $R_{c,i}$.

2.3.3 Cone-SPM Scheme. In the most advanced scheme, the ray is treated as a cone, and the particle is given a specific shape and a density distribution may exist across its volume, as shown in Fig. 3(b). In this case, the weight function and absorption coefficient cannot be separated from the volume integral in the optical thickness evaluation. The total optical thickness passed through by a ray is obtained as

$$\tau = \sum_{i \in I} \kappa_{\rho,i} \int_{\Omega'_i} \frac{\hat{\rho}_i W_{2D}[r/R_c(s)]}{\pi R_c^2(s)} d\mathbf{x} \quad (21)$$

where Ω'_i is the intersection of the particle influence region and the ray, r is the distance from a location in Ω'_i to the cone axis and $R_c(s)$ is the local cone radius at this location. Since the solid angle of the ray is small, $R_c(s)$ can be regarded as constant in a single particle, i.e., the small cone segment interacting with a particle can be treated as a small cylinder. Then the local radius $R_c(s) \equiv R_{c,i}$ can be separated from the integral,

$$\tau \approx \sum_{i \in I} \frac{\kappa_{\rho,i}}{\pi R_{c,i}^2} \int_{\Omega'_i} \hat{\rho}_i(\mathbf{x}) W_{2D}(r/R_{c,i}) d\mathbf{x} \quad (22)$$

For constant-density spherical particles this reduces to

$$\begin{aligned} \tau &= \sum_{i \in I} \frac{\kappa_i}{\pi R_{c,i}^2} \int_{\Omega'_i} W_{2D}(r/R_{c,i}) d\mathbf{x} \\ &= \sum_{i \in I} \frac{\kappa_i}{\pi R_{c,i}^2} \int_{r_{\min}}^{r_{\max}} W_{2D}(r/R_{c,i}) A_i(r) dr \\ &= \sum_{i \in I} \frac{\kappa_i R_{c,i}}{\pi} \int_{r'_{\min}}^{r'_{\max}} W_{2D}(r') A'_i(r') dr' \end{aligned} \quad (23)$$

where $r' = r/R_{c,i}$ is the normalized distance from a point in Ω'_i to the cylinder (cone) axis, r'_{\min} is the normalized closest distance and r'_{\max} is the farthest. All points of the same distance r' are part of a cylindrical shell $A_i(r')$ around the cone axis, and its normalized form can be evaluated as

$$A'_i(r') = \frac{A_i(r')}{R_{c,i}^2} = \begin{cases} 4r'^{3/2}r_i'^{1/2}\alpha^{1/2}E(1/\alpha), & r' \leq R'_i - r'_i \\ 8r'^{3/2}r_i'^{1/2}[2E(\alpha) - \beta K(\alpha)], & r' > R'_i - r'_i \end{cases} \quad (24)$$

where $r'_i = r_i/R_{c,i}$ is the normalized distance from the particle center to the cylinder axis, $R'_i = R_i/R_{c,i}$ is the normalized radius of particle i , K and E are complete elliptic integrals of the first and second kind [16], and

$$\alpha = [R_i'^2 - (r' - r'_i)^2]/4r'r'_i$$

$$\beta = [(r' + r'_i)^2 - R_i'^2]/2r'r'_i \quad (25)$$

If we define

$$f_i = \frac{1}{\pi} \int_{r'_{\min}}^{r'_{\max}} W_{2D}(r') A'_i(r') dr' \quad (26)$$

Eq. (23) can be rewritten as

$$\tau = \sum_{i \in I} \kappa_i R_{c,i} f_i \quad (27)$$

Rather than making costly evaluations during the simulation, Eq. (26) can easily be tabulated as a function of the two dimensionless parameters r'_i and R'_i .

3 Sample Calculations

In order to evaluate and compare the performance of the different schemes for Monte Carlo ray tracing in media represented by statistical particles, one-dimensional radiative heat transfer problems in a nonscattering gray gaseous medium are studied. Two media will be considered: a 1D gas slab bounded by two infinitely large, parallel, cold, black walls and a gas sphere surrounded by a cold black wall. The thickness of the slab is fixed at $L=10$ cm and the radius of the sphere is $R=5$ cm. The temperature and density (or absorption coefficient) may vary across the slab thickness or along the sphere radial direction. The resulting radiative heat flux at the boundary ($x=0, L$ for slab; $r=R$ for sphere) can be evaluated exactly through numerical integration [1].

In the slab problem, the 1D medium is simulated by repeating a gas cube, each with equal side lengths of 10 cm in the two infinite dimensions. A single gas cube is then taken as the computational domain in the Monte Carlo simulation. In the sphere problem, the computational domain is the gas sphere itself. The continuous gas medium in both problems is represented by a number of discrete gas particles randomly placed inside the computational domain. The mass of particles can be equally sized or have a distribution function. For computational efficiency, a mesh of cubic cells is laid on top of the computational domain because the ray-tracing algorithm on smaller cubic cells is simpler and more efficient. The same cubic-cell mesh is used for the sphere problem as well, by first identifying a $D \times D \times D$ cube enclosing the sphere, then dividing the cube into cubic cells, where $D=2R$ is the diameter of the sphere. In the slab problem each of the cells contains a number of gas particles, while in the sphere problem some cells at the corners of the mesh may contain no particles, because they may be outside the spherical computational domain. If the point particle model (PPM) is employed, it can be assumed that each particle is completely enclosed by a single cell, since the shape of particles is not specified. However, if the spherical particle model (SPM) is employed, the cells contain not only the particles with their center in it, but also parts of particles from neighboring cells.

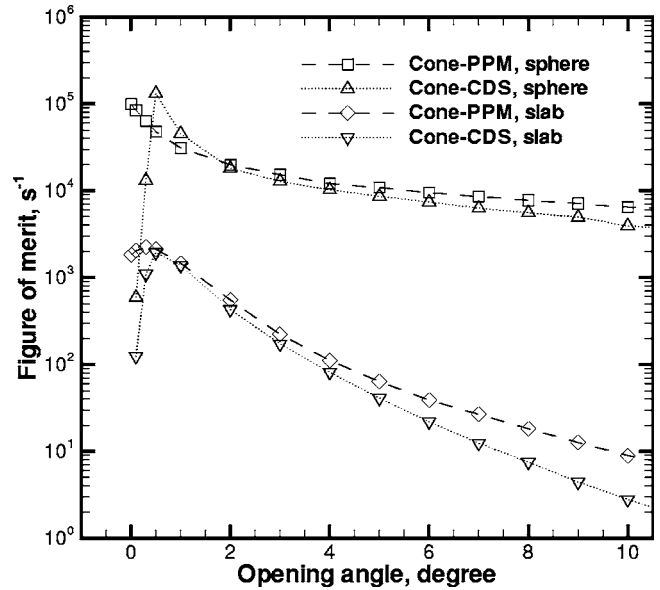


Fig. 4 Figure of merit (FoM) of cone ray models at different cone opening angles; $50 \times 10,000$ equally sized particles; 1 ray/particle; homogeneous medium

Thus, a scheme must be developed to avoid having the ray interact with a single particle more than once, since a single particle may belong to multiple cells.

When the cone ray model is adopted for ray tracing, the opening angle (the angle between the cone axis and its lateral surface) needs to be chosen. Larger opening angles result in more particles caught by the ray, requiring more CPU time per ray. At the same time, larger opening angles reduce the statistical scatter (i.e., reduce the number of required photon bundles for a given desired standard deviation), while also smoothing gradients that may exist in the solution. In turbulent flow fields large opening angles, therefore, may smooth out the turbulence. The “figure of merit” (FoM) of a Monte Carlo simulation is defined as [17]

$$\text{FoM} = \frac{1}{\epsilon^2 t}, \quad \epsilon = \left(\frac{1}{S} \sum_{s=1}^S (q_s/q^0 - 1)^2 \right)^{1/2} \quad (28)$$

where ϵ is the root-mean-square (rms) relative error of the simulation and t is the simulation time. In the current work, the error of 50 simulations is adopted for ϵ ($S=50$); q_s is the simulation result of radiative flux at the boundary and q^0 is the exact solution found in Chapter 9 of Ref. [1]. A good Monte Carlo simulation should have a high FoM score. Figure 4 shows FoM scores for different opening angles. The gas slab or sphere was represented by 10,000 randomly distributed, equally sized particles, each of which emits all its energy into a single random direction. Temperature and absorption coefficient are uniform and, thus, the smoothing effect of larger cone angles is not an issue. The mesh in use contains $5 \times 5 \times 5 = 125$ cubic cells. As seen from Fig. 4, for this one-dimensional problem 1 deg is the optimal opening angle, which can achieve high accuracy as well as high CPU efficiency. Although smaller opening angles required less computational time, their errors were larger, because they could not interact with enough particles. Similar results were also obtained for other temperature and absorption coefficient profiles. Therefore, for all the following simulations in this paper, an opening angle of 1 deg is chosen, whenever the cone ray model is employed.

Another factor that can affect the simulation speed is the number of particles per cell. When a ray is traced, the cells that it travels through are identified first. Then all particles in those cells are checked for interaction with the ray. For a finer mesh, the number of particles per cell is smaller and, thus, a smaller number

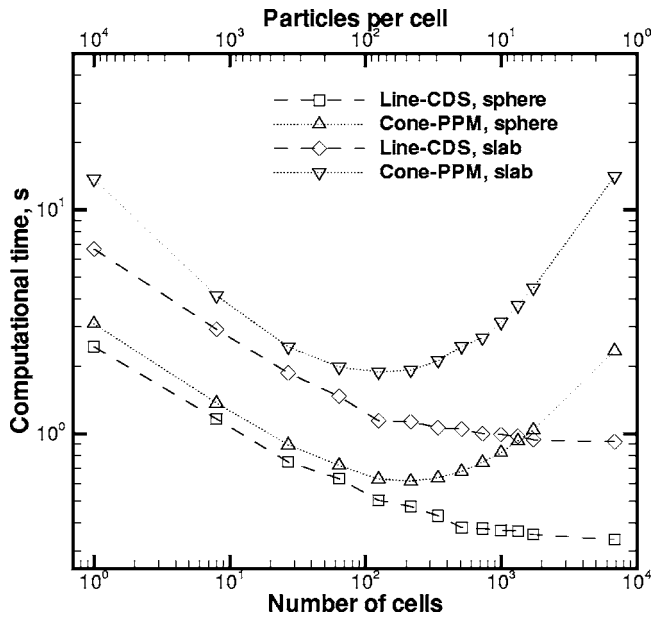


Fig. 5 Computational time at different particle number densities; $50 \times 10,000$ equally sized particles; 1 ray/particle; homogeneous medium

of particles are checked during ray tracing. However, more cells must be searched. Thus, finer meshes tend to reduce the time spent on checking particles for their interaction with a ray, but increase the overhead related to cell searching and recording. Therefore, an optimal value of the number of particles per cell may exist. Figure 5 shows the computational time for different cell sizes, keeping the total number of particles in the domain constant. Results for the cone-CDS scheme are not shown to retain readability, and are essentially the same as those for the cone-PPM scheme, since both schemes share the same algorithm except for the particle weight, which has only a very small impact on computational time. From Fig. 5 it is seen that no optimal cell size exists for the line-CDS scheme; the computational time decreases consistently with decrease of cell size. Therefore, the optimum value for the number of particles per cell is 1 particle/cell, which has been verified for up to 100,000 particles in the domain. For cone schemes, however, an optimal value was found to be around 50 particles/cell in both the slab and the sphere problems. In the line scheme rays are one-dimensional lines. The number of cells that a ray intersects is proportional to the number of cells in one dimension, i.e., the cubic root of the number of cells in the 3D computational domain. Doubling the number of cells in each dimension, the number of cells to be searched is doubled, but the number of particles to be checked for interaction becomes only one-eighth of the original number. In cone schemes, on the other hand, rays are assigned a volume. The number of cells that a ray intersects increases rapidly with increase of the number of cells. If the cell size is too small, the speed-up gained by checking fewer particles cannot compete with the overhead related to cell searching and recording and, thus, an optimal cell size exists for cone schemes.

Several combinations of temperature profiles and absorption coefficient profiles have been tested as listed in Table 1, with different cases numbered in Table 2. In those profile equations x and L denote the x position and the slab thickness in the slab problem, and the r variable and the sphere radius in the sphere problem. The three absorption schemes have been implemented and compared with exact solutions of boundary fluxes for all nine cases. Table 3 shows the corresponding root-mean-square (rms) relative error of 50 simulations in each case, in which the gas cube or sphere is represented by 10,000 equally sized random particles, each of which emits all its energy in a single ray into a random

Table 1 Temperature and absorption coefficient profiles

Temperature profiles, K	
const	$T(x) = T_o$
linear	$T(x) = T_o + (x/L)(T_L - T_o), \quad T_L/T_o = 2$
sine	$T(x) = T_o + T_A \sin(2\pi x/L), \quad T_L/T_o = 0.5$
Absorption coefficient profiles, cm^{-1}	
const	$\kappa(x) = 0.1$
linear	$\kappa(x) = 0.01 + 0.99(x/L)$
sine	$\kappa(x) = 0.55 + 0.45 \sin(2\pi x/L)$

direction. Since the slab has two boundaries, the result shown here is the averaged error of both boundaries. As shown in Table 3, the three absorption schemes have the same level of accuracy, especially in the slab problem. In the sphere problem the cone-PPM scheme achieves much better accuracy than the line-CDS scheme, but this improvement of accuracy comes at a cost of increased CPU time. As expected, the cone-CDS scheme has slightly better accuracy than the cone-PPM scheme, however, this also comes at a cost in slightly increased CPU time. Therefore, the three absorption schemes are essentially equivalent.

It is worth noting that the discrete particle representation of a continuous medium inevitably introduces a bias on radiation calculations when the density field cannot be recovered exactly. In the current sample problems the random distribution of particles inevitably generates fluctuations on the original homogeneous density fields, as shown in Fig. 2. Table 4 shows relative errors and standard deviations of all nine cases for the sphere problem. The negative sign attached to all errors indicates that the particle representation tends to underpredict the boundary flux. If the magnitude of the error is larger than or comparable with the standard deviation, the bias introduced by the particle representation is the major source of error. The bias is not so prominent in the slab problem as in the sphere problem, which can be seen from Fig. 6, which shows the variation of rms error with respect to the number of rays each particle emits. The particles are all of the same size and only the result of Case (1) is provided for clarity. The relation follows the inverse-square-root law in the slab problem, indicating that standard deviation is the major source of rms error. In contrast, the relation does not follow the inverse-square-root law in the sphere problem, indicating that bias is an important contributor to the error. Similarly, Fig. 7 shows the relation between the rms error and the number of particles, with which the medium in

Table 2 Case numbering

Case	(1)	(2)	(3)	(4)	(5)	(6)	(7)	(8)	(9)
T	const	const	const	linear	linear	linear	sine	sine	sine
κ	const	linear	sine	const	linear	sine	const	linear	sine

Table 3 Percentage rms errors of radiative fluxes at boundaries; $50 \times 10,000$ particles; 1 ray/particle; 125 cells; uniform particle mass

Case No.	Line-CDS		Cone-PPM		Cone-CDS	
	Slab	Sphere	Slab	Shpere	Slab	Sphere
(1)	1.621	1.148	1.509	0.702	1.516	0.564
(2)	1.574	1.044	1.542	0.783	1.498	0.574
(3)	1.821	0.730	1.729	0.664	1.733	0.536
(4)	1.975	1.258	1.974	0.899	1.880	0.741
(5)	2.027	1.191	1.986	0.969	1.935	0.758
(6)	1.784	0.807	1.837	0.778	1.782	0.680
(7)	2.098	1.115	2.000	0.852	2.007	0.771
(8)	1.798	1.006	1.798	0.838	1.787	0.702
(9)	2.341	1.352	2.180	1.346	2.191	1.273

Table 4 Percentage errors and standard deviations of radiative fluxes at the boundary in the sphere problem; $50 \times 10,000$ particles; 1 ray/particle; 125 cells; uniform particle mass

Case No.	Line-CDS		Cone-PPM		Cone-CDS	
	Error	STD	Error	STD	Error	STD
(1)	-1.113	0.288	-0.637	0.298	-0.487	0.288
(2)	-1.003	0.293	-0.722	0.305	-0.495	0.295
(3)	-0.564	0.468	-0.454	0.490	-0.262	0.473
(4)	-1.149	0.517	-0.730	0.530	-0.533	0.520
(5)	-1.066	0.537	-0.799	0.553	-0.536	0.542
(6)	-0.516	0.627	-0.461	0.633	-0.273	0.629
(7)	-0.841	0.739	-0.329	0.794	-0.223	0.746
(8)	-0.800	0.617	-0.548	0.640	-0.341	0.620
(9)	-0.495	1.271	-0.302	1.325	-0.048	1.286

the gas cube is represented. Again, it is observed that the relation follows the inverse-square-root law for the slab problem but not for the sphere problem. The bias is caused by the representation of a homogeneous or gradually varying density field by a fluctuating density field. In turbulent flow simulations the inhomogeneous particle field is assumed to provide a snapshot of a turbulent medium, and no bias exists.

The effect of varying particle size was also investigated. In the slab problem a linear distribution of particle mass along the x direction is considered, i.e.,

$$m(x) = m_o + (m_L - m_o)(x/L) \quad (29)$$

where m_o and m_L are the values of particle mass at the two boundaries $x=0$ and $x=L$. Because the probability distribution $P(x)$ associated with particle mass distribution $m(x)$ is inversely proportional to $m(x)$, the following random number relation holds for the x coordinate of random particle positions

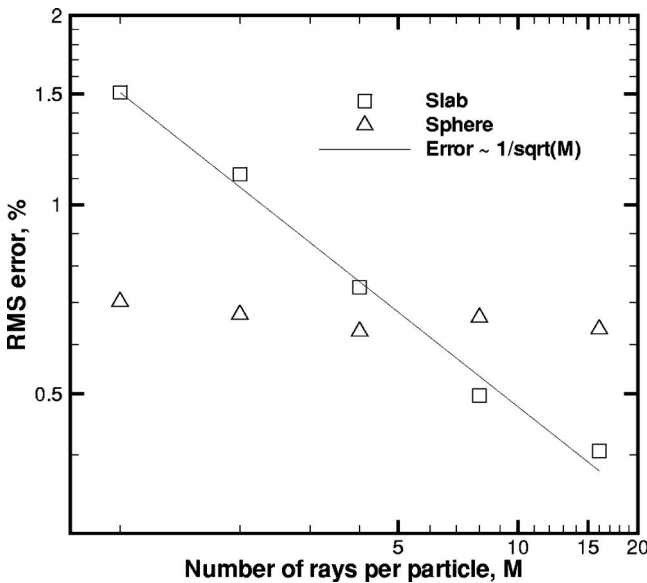


Fig. 6 Averaged boundary flux error versus number of rays per particle; cone-PPM scheme; $50 \times 10,000$ particles; uniform particle mass; Case (1)

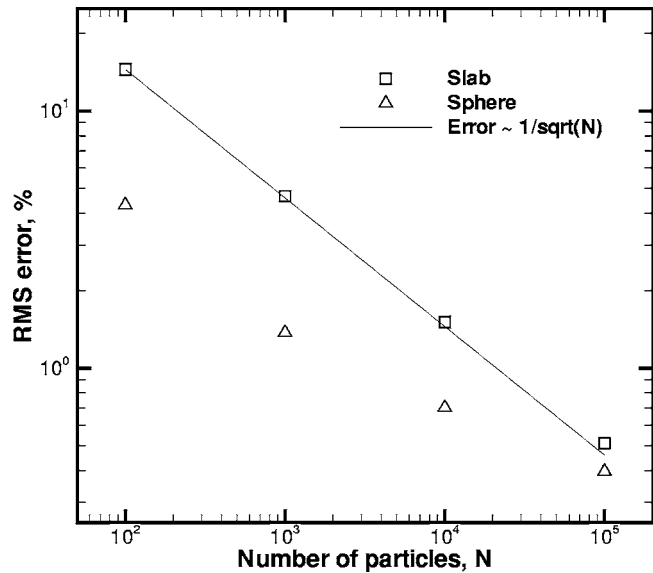


Fig. 7 Averaged boundary flux error versus number of particles in computation domain; cone-PPM scheme with one ray per particle; $50 \times N$ particles; uniform particle mass; Case (1)

$$\eta_x = \frac{\int_0^x P(x)dx}{\int_0^L P(x)dx} = \frac{\int_0^x 1/m(x)dx}{\int_0^L 1/m(x)dx} = \frac{\int_0^x [m_o + (m_L - m_o)(x/L)]^{-1} dx}{\int_0^L [m_o + (m_L - m_o)(x/L)]^{-1} dx} \quad (30)$$

where η_x is a random number uniformly distributed in $[0, 1)$. After carrying out the integrations and rearranging, one obtains

$$x = \frac{(m_L/m_o)^{\eta_x} - 1}{(m_L/m_o) - 1} L \quad (31)$$

where (m_L/m_o) is the mass ratio of particles at $x=L$ to that at $x=0$. Since there is no variation in the y and z directions, the y and z coordinates of particle positions can be readily generated as

$$y = \eta_y L, \quad z = \eta_z L \quad (32)$$

where η_y and η_z are two additional independent random numbers uniformly distributed in $[0, 1)$. Figure 8 shows a 2D CDS representation with a linear particle mass distribution for a homogeneous medium.

Table 5 gives the results for the linear particle mass distribution. For all nine cases, the random number sequence used in the generation of particle position and emission direction is the same as in the uniform mass cases. Again, the three absorption schemes all achieve the same level of accuracy. Comparing Table 5 to 3, it is observed that the difference caused by varying the particle masses is fairly small considering that particle mass across the domain varies by a factor of 1000. It is also noticed that the error at $x=L$ is larger than at $x=0$. This is because particles are larger near that boundary, but still emit only one ray per particle as do the smaller particles near the boundary at $x=0$. It also explains why errors for the linear temperature profile are higher than for other profiles. In that scenario larger particles are at higher temperatures and the importance of emission from larger particles is even more crucial to the simulation result.

4 Summary

For radiative heat transfer simulations using Monte Carlo ray tracing in media represented by discrete particle fields it is important to find ways to model the interaction between point masses

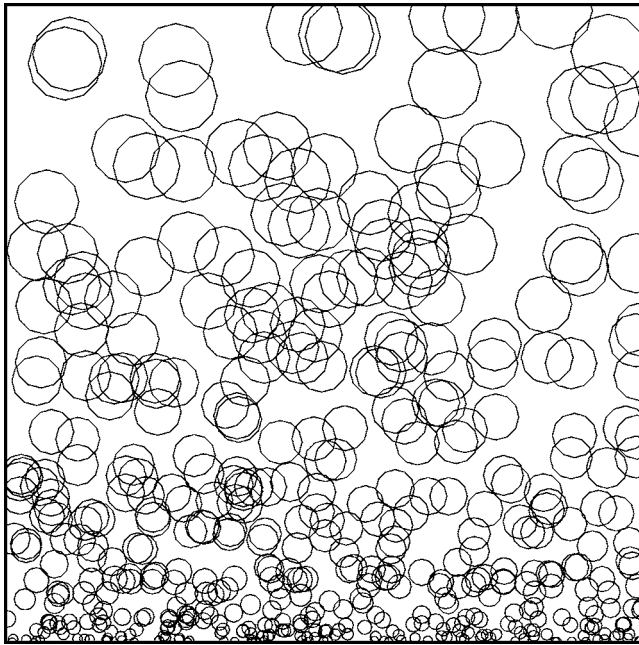


Fig. 8 2D CDS representation with linear mass distribution for a homogeneous medium

and photon rays. In the point particle model (PPM) the shape of particles is not presumed in order to avoid any inconsistency with the underlying particle field. As a result, this method is limited to applications, in which the ray has a shape and volume. In the spherical particle model (SPM) particles are assumed to be spheres. As a special case, in the constant density sphere (CDS) model the density is assumed to be constant across the entire particle volume. Although it is easy to interact spheres with a ray, this model introduces some inconsistencies. For example, it cannot recover continuous medium properties due to the existence of particle overlap and voids.

In the line ray model for photon bundles, rays are simply treated as volume-less lines and energy propagates one-dimensionally along those lines. In the cone ray model each ray is assigned a small solid angle, and is thus treated as a cone; energy propagates two-dimensionally. The strength of the ray may vary across the cross-section of the cone through a given weight function. Since the ray has a volume, it is possible to have the ray interact with volume-less particles directly. Thus, three schemes for the interaction between ray and particles, i.e., line-CDS, cone-PPM and cone-CDS schemes, have been proposed and examined in two one-dimensional radiative heat transfer problems with various temperature and absorption coefficient profiles. It was shown that all three schemes achieved comparable levels of accuracy. For

Table 5 Percentage rms errors of radiative fluxes at slab boundaries; 50×10,000 particles; 1 ray/particle; volume ratio: $m_L/m_o=1000$

Case No.	Line-CDS		Cone-PPM		Cone-CDS	
	$x=0$	$x=L$	$x=0$	$x=L$	$x=0$	$x=L$
(1)	1.896	3.378	1.958	3.173	1.956	3.123
(2)	2.795	3.671	2.864	3.675	2.862	3.685
(3)	1.863	2.234	1.985	2.162	1.939	2.146
(4)	4.050	4.332	3.956	4.493	3.656	4.513
(5)	4.584	4.740	4.623	4.947	4.581	4.910
(6)	3.748	3.990	3.727	4.025	3.596	4.009
(7)	2.174	4.412	2.225	3.593	2.208	2.819
(8)	2.398	3.647	2.522	3.016	2.481	2.905
(9)	2.377	2.487	2.443	2.471	2.396	2.417

the cone approaches, an optimal opening angle was found, and a most efficient number of particles per cell exists. For the line approach, computational speed increases consistently with decrease of the number of particles per cell.

Acknowledgment

This research has been sponsored by National Science Foundation under Grant No. CTS-0121573.

Nomenclature

A	= cylindrical shell
I	= emission intensity; particles enclosed by ray
L	= thickness of gas slab; side length of computational domain
Q_{emi}	= total energy emitted from a particle
R	= particle influence radius; gas constant
R_c	= local radius of cone
S	= ray path; number of simulations
T	= temperature
V_o	= nominal volume of particle
W	= weight function
m	= particle mass
p	= total pressure
q	= heat flux
q^o	= exact solution of heat flux
r	= distance to axis of conical ray
r'	= normalized distance to ray axis, r/R_c
s	= axial distance from emission point
\mathbf{x}	= location vector
Ω	= particle influence region
Ω'	= particle influence region intercepted by ray
κ	= linear absorption coefficient
κ_ρ	= density-based absorption coefficient
η	= random number
ρ_o	= nominal density of particle
$\hat{\rho}$	= density profile in particle influence region
τ	= optical thickness

Superscripts

' = quantity normalized by local cone radius R_c

Subscripts

i = particle

j = ray

s = simulation

2D,3D = dimension of weight function

References

- [1] Modest, M. F., 2003, *Radiative Heat Transfer*, 2nd ed., Academic, New York.
- [2] Heinsch, R. P., Sparrow, E. M., and Shamsundar, N., 1973, "Radiant Emission From Baffled Conical Cavities," *J. Opt. Soc. Am.*, **63**(2), pp. 152–158.
- [3] Shamsundar, N., Sparrow, E. M., and Heinsch, R. P., 1973, "Monte Carlo Solutions—Effect of Energy Partitioning and Number of Rays," *Int. J. Heat Mass Transfer*, **16**, pp. 690–694.
- [4] Modest, M. F., and Poon, S. C., 1977, "Determination of Three-Dimensional Radiative Exchange Factors for the Space Shuttle by Monte Carlo," ASME paper No. 77-HT-49.
- [5] Modest, M. F., 1978, "Determination of Radiative Exchange Factors for Three Dimensional Geometries With Nonideal Surface Properties," *Numer. Heat Transfer*, **1**, pp. 403–416.
- [6] Walters, D. V., and Buckius, R. O., 1992, "Monte Carlo Methods for Radiative Heat Transfer in Scattering Media," in *Annual Review of Heat Transfer*, Vol. 5, Hemisphere, New York, pp. 131–176.
- [7] Howell, J. R., 1998, "The Monte Carlo Method in Radiative Heat Transfer," *ASME J. Heat Transfer*, **120**(3), pp. 547–560.
- [8] Farmer, J. T., and Howell, J. R., 1998, "Monte Carlo Strategies for Radiative Transfer in Participating Media," in *Advances in Heat Transfer*, 34, J. P. Hartnett, and T. F. Irvine, eds., Academic, New York.
- [9] Viskanta, R., and Mengüç, M. P., 1987, "Radiation Heat Transfer in Combustion Systems," *Prog. Energy Combust. Sci.*, **13**, pp. 97–160.
- [10] Faeth, G. M., Gore, J. P., Chuech, S. G., and Jeng, S. M., 1989, "Radiation From Turbulent Diffusion Flames," in *Annual Review of Numerical Fluid Mechanics and Heat Transfer*, 2, Hemisphere, Washington, D.C., pp. 1–38.

- [11] Kounalakis, M. E., Gore, J. P., and Faeth, G. M., 1988, "Turbulence/Radiation Interactions in Nonpremixed Hydrogen/Air Flames," In Twenty-Second Symposium (International) on Combustion, The Combustion Institute, pp. 1281–1290.
- [12] Mazumder, S., and Modest, M. F., 1999, "Turbulence–Radiation Interactions in Nonreactive Flow of Combustion Gases," *Int. J. Heat Mass Transfer*, **121**, pp. 726–729.
- [13] Li, G., and Modest, M. F., 2002, "Application of Composition PDF Methods in the Investigation of Turbulence–Radiation Interactions," *J. Quant. Spectrosc. Radiat. Transf.*, **73**(2–5), pp. 461–472.
- [14] Pope, S. B., 1985, "PDF Methods for Turbulent Reactive Flows," *Prog. Energy Combust. Sci.*, **11**, pp. 119–192.
- [15] Liu, G. R., and Liu, M. B., 2003, *Smoothed Particle Hydrodynamics—A Mesh-free Particle Method*, World Scientific, Singapore.
- [16] Abramowitz, M., and Stegun, I. A., eds., 1965, *Handbook of Mathematical Functions*, Dover, New York.
- [17] Lewis, E. E., and Miller, W. F., Jr., 1984, *Computational Methods of Neutron Transport*, Wiley, New York.

Measurement and Modeling of Condensation Heat Transfer Coefficients in Circular Microchannels

Todd M. Bandhauer

Modine Manufacturing Company,
Racine, WI 53403

Akhil Agarwal

Srinivas Garimella

e-mail: srinivas.garimella@me.gatech.edu

GWW School of Mechanical Engineering,
Georgia Institute of Technology,
Atlanta, GA 30332-0405

*A model for predicting heat transfer during condensation of refrigerant R134a in horizontal microchannels is presented. The thermal amplification technique is used to measure condensation heat transfer coefficients accurately over small increments of refrigerant quality across the vapor-liquid dome ($0 < x < 1$). A combination of a high flow rate closed loop primary coolant and a low flow rate open loop secondary coolant ensures the accurate measurement of the small heat duties in these microchannels and the deduction of condensation heat transfer coefficients from measured UA values. Measurements were conducted for three circular microchannels ($0.506 < D_h < 1.524$ mm) over the mass flux range $150 < G < 750$ kg/m² s. Results from previous work by the authors on condensation flow mechanisms in microchannel geometries were used to interpret the results based on the applicable flow regimes. The heat transfer model is based on the approach originally developed by Traviss, D. P., Rohsenow, W. M., and Baron, A. B., 1973, "Forced-Convection Condensation Inside Tubes: A Heat Transfer Equation For Condenser Design," *ASHRAE Trans.*, **79**(1), pp. 157–165 and Moser, K. W., Webb, R. L., and Na, B., 1998, "A New Equivalent Reynolds Number Model for Condensation in Smooth Tubes," *ASME, J. Heat Transfer*, **120**(2), pp. 410–417. The multiple-flow-regime model of Garimella, S., Agarwal, A., and Killion, J. D., 2005, "Condensation Pressure Drop in Circular Microchannels," *Heat Transfer Eng.*, **26**(3), pp. 1–8 for predicting condensation pressure drops in microchannels is used to predict the pertinent interfacial shear stresses required in this heat transfer model. The resulting heat transfer model predicts 86% of the data within $\pm 20\%$. [DOI: 10.1115/1.2345427]*

Keywords: condensation, microchannel, phase change, heat transfer coefficient

Introduction

Microchannels are increasingly being used in industry to yield compact geometries for heat transfer in a wide variety of applications. Considerable literature exists on single-phase flow, pressure drop, and heat transfer in microchannels, as can be seen in some recent reviews of the literature [1–4]. Similarly, boiling and evaporation (pool boiling and convective boiling) in microchannels have also been studied due to the interest in heat removal at high heat fluxes in the electronics cooling industry. But limited research has been conducted on flow regimes, and the measurement of pressure drop and heat transfer coefficients during condensation in microchannel geometries, i.e., in the submillimeter range of hydraulic diameters. The prominence of studies on boiling and evaporation to date can be attributed to the electronics cooling industry's need to remove high heat fluxes through vaporization from compact devices that must be maintained at relatively low temperatures while being not readily accessible or conducive to the installation of large and complex cooling systems. However, the ultimate rejection of these large heat duties through compact condensers has not been addressed adequately. It should be noted that such compact condensers have been designed and used for some years by the automotive industry, whose air-conditioning condensers consist of rectangular tubes with multiple parallel microchannels cooled by air flowing across multilouver fins. The

microchannels used in these condensers often have hydraulic diameters in the 0.4–0.7 mm range, although an understanding of the fundamental condensation phenomena in these heat exchangers is just beginning to emerge. A fundamental understanding of condensation at the microscales will yield far reaching benefits not only for these industries, but also for other as-yet untapped applications such as portable personal cooling devices, hazardous duty and high ambient air conditioning, and medical/surgical devices, to name a few.

The essential issue and research challenge in microscale condensation is that two-phase flow mechanisms and flow regime transitions in these small channels are considerably different from those found in the more conventional larger diameter tubes. This is because of significant differences between large round tubes and the smaller noncircular tubes in the relative magnitudes of gravity, shear, and surface tension forces, which determine the flow regime established at a given combination of liquid and vapor-phase velocities. Coleman and Garimella experimentally demonstrated and interpreted these differences in flow mechanisms and transitions for air-water flows [5] as well as for the condensation of refrigerants [6,7]. Because heat transfer coefficients and two-phase pressure drops depend on the corresponding flow patterns, it is reasonable to expect that heat transfer coefficients in microchannels may not be predicted adequately by the existing correlations for larger diameter tubes. Having established the pertinent flow mechanisms and transition criteria for the condensation of refrigerants in microchannels, Garimella et al. developed experimentally validated models for pressure drops during intermittent condensing flows in circular [8] and noncircular [9] microchannels. In addition, they developed a model for conden-

Contributed by the Heat Transfer Division of ASME for publication in the *JOURNAL OF HEAT TRANSFER*. Manuscript received June 17, 2005; final manuscript received March 7, 2006. Review conducted by Satish G. Kandlikar. Paper presented at the 3rd International Conference on Microchannels and Minichannels (ICMM2005), June 13–15, 2005, Toronto, Ontario, Canada.

sation pressure drop in annular flow [10], and further extended it to a comprehensive multiregime pressure drop model [11] for circular microchannels. The present work continues this effort by focusing on the measurement and modeling of condensation heat transfer in circular microchannels.

Prior Work

There is very little prior information available on condensation heat transfer coefficients at small D_h , therefore, a brief review of the literature on condensation heat transfer in tubes with $D_h < 7$ mm is presented here. Breber et al. [12] developed a four flow “zone” map for $4.8 < D < 50.8$ mm and recommend a Nusselt-type heat transfer correlation for the wavy and stratified zone, while the Traviss et al. [13] correlation was recommended for all other zones. Dobson et al. [14] presented condensation heat transfer data for R-12 and R-134a flowing inside a 4.57 mm tube for $75 < G < 600$ kg/m² s, which spanned the wavy, annular, and annular-mist flow regimes. They provided semiempirical correlations for the wavy and annular flow regimes distinguished by the criteria proposed by Soliman [15,16], and found that the condensation heat transfer coefficient h was a function of saturation temperature. Yang and Webb [17,18] experimentally investigated and modeled condensation of R-12 in plain and microfin tubes with $D_h = 2.637$ and 1.564 mm, respectively, and found that the Shah [19] correlation overpredicted the data, while the Akers et al. [20] correlation showed better agreement, except at high mass fluxes, where it also overpredicted the data. Dobson and Chato [21] found G and x to be the dominant influences on h in tubes with $3.14 < D < 7.04$ mm for several refrigerants and blends, and could not definitively discern an influence of surface tension for this diameter range. For gravity-driven condensation ($G < 500$ kg/m² s and $Fr < 20$), they accounted for film condensation at the top of the tube, and liquid pool forced-convective condensation at the bottom. Their model predictions did not agree with the data for the small diameter (3.14 mm) tube due to the large uncertainty in the data because of small heat transfer rates. For the annular flow regime ($G > 500$ kg/m² s, or $Fr > 20$ and $G < 500$ kg/m² s), a Martinelli parameter-based multiplier to the Dittus-Boelter correlation was introduced. Moser et al. [22] presented an equivalent Reynolds number model for condensation h prediction, which was based on the Akers et al. [20] model, which assumes that the condensing h could be calculated using a modified single-phase heat transfer coefficient for an equivalent liquid flow. Their correlation predicted data for tubes with $3.14 < D < 20$ mm for several refrigerants better than the models of Shah [19] and Traviss et al. [13]. Hurlburt and Newell [23] developed condensation h and ΔP models for annular flow for $3 < D < 10$ mm using an empirical interfacial shear relationship by Asali et al. [24] and compared their predictions with the data of Sacks [25] and Dobson [26]. Their h model was presented as a piecewise function of the film thickness spanning the viscous, buffer, and turbulent layers, and tended to underpredict the R-11 ΔP while overpredicting the R-12 and R-22 ΔP , which suggested that the interfacial shear model needs to be improved, especially as the liquid-vapor density ratio decreases away from air-water mixtures (i.e., higher pressure refrigerants).

Thus, gravity-driven condensation (not particularly relevant to surface-tension dominated flows in microchannels) and annular flow condensation in larger D_h have received attention in the literature. Annular flow models have included approaches based on the interfacial shear originated as early as 1951 by Carpenter and Colburn [27] and modified by numerous other researchers, notably, Soliman et al. [28] who corrected the momentum contribution, Chen et al. [29] who modified their vertical annular flow correlation to apply it to horizontal flow, and many others. Two-phase multipliers or the use of two-phase equivalent Re in single-phase correlations have also been employed [22,14,19,20,30]. Yet another category of studies uses boundary layer analyses for an-

ular flow [13,21,23]. Representative numerical analyses of annular flow condensation have included studies by Chitti and Anand [31], Guo and Anand [32], and Ibrahim [33]. For annular flow with liquid entrainment in the vapor core, homogeneous and mist flow correlations [15,34,35] offer some alternatives.

During the past year, some investigators have developed analytical approaches for addressing condensation heat transfer in triangular [36] and square [37] microchannels. For film condensation of R134a in horizontal 1-mm triangular channels, Wang and Rose [36] assumed that the condensate was in laminar flow, and developed one of the first models that accounts for surface tension, shear stress, and gravity. They were able to predict and substantiate the varying condensate flow pattern across the cross section as well as along the length of the channel. Thus, they were able to model the corresponding variations in heat transfer coefficient. Using a similar approach, Wang et al. [37] developed a model for film condensation of R134a in square, horizontal, 1-mm microchannels. Because these papers account for the three primary governing influences in microchannel condensation, they provide a good start for the modeling of phenomena specific to microchannels. Furthermore, the respective forces can be “switched on or off” to understand their respective significances.

In another recent study, Cavallini et al. [38] conducted measurements of heat transfer coefficients and pressure drops during condensation of R134a and R410A inside multiple parallel 1.4-mm D_h channels. The test section was divided into three separate segments to provide quasilocal pressure drops and heat transfer coefficients. They deduced the frictional pressure drop from the measured drop in saturation temperature and found good agreement between the data for R134a and the correlations of Friedel [39], Zhang and Webb [40], Mishima and Hibiki [41], and Mueller-Steinhagen and Heck [42]. All of these correlations were found to overpredict the R410A data, however. Their heat transfer coefficients were obtained from wall temperature measurements, and they found that the available models in the literature [22,20,40,43–45] underestimated their results, particularly at high values of mass flux. They attributed these differences to the much higher gas velocities in their experiments where mist flow might prevail, whereas the available correlations are primarily for annular flow in larger diameter tubes.

Shin and Kim [46] used a technique that matched the outlet temperature of an electrically heated air stream with that of a similar air stream heated by condensing refrigerant R134a to measure small, local condensation heat transfer rates. Circular and square channels with $0.5 < D_h < 1$ mm were tested for the mass flux range $100 < G < 600$ kg/m² s at 40°C. For circular and square channels, they found that most of the available models and correlations discussed above [13,22,19,20,26,28,30] underpredict their data at the low mass fluxes, which they deemed to be the important range for engineering applications. The agreement with these correlations improved somewhat at the higher mass fluxes. Although they found no significant effect of the heat flux, they noted that at lower mass fluxes, square channels had higher heat transfer coefficients than those for circular channels, whereas the reverse was true for high mass fluxes. No satisfactory explanation was provided for these trends.

It is clear from the above discussion that there is no reliable model for the prediction of condensation heat transfer coefficients in small diameter channels. The preponderance of studies on condensation has been on annular flows in large diameter tubes. Even the recent studies on ~ 1 mm channels, while employing innovative experimental techniques, have primarily reported heat transfer coefficients that are in considerable disagreement with the available models; these new data have as yet not resulted in any models specific to micro- and mini-channels. The present study, therefore, undertakes the measurement of local condensation heat transfer coefficients over a wide range of G and x for circular microchannels ($0.506 < D < 1.524$ mm).

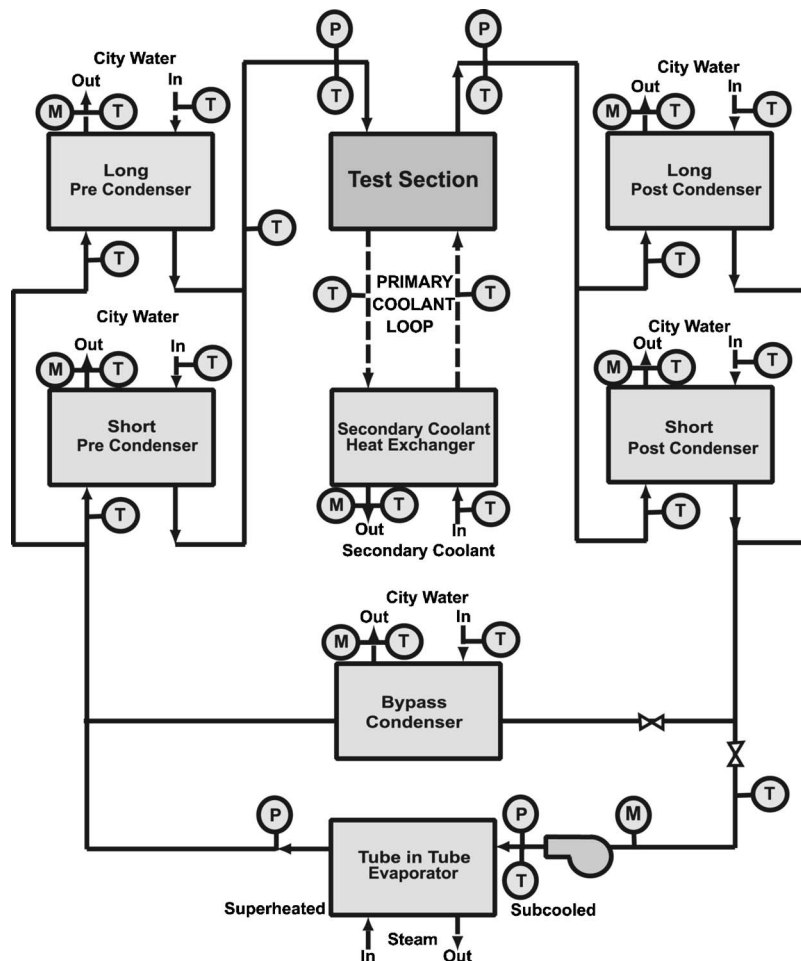


Fig. 1 Schematic of the test facility

Experimental Approach and Data Analysis

The two-phase test facility (Fig. 1) used in earlier work by this group for flow visualization [6,7] and pressure drop measurement [8,9] was also used for the heat transfer experiments, with appropriate modifications. The facility and the experimental procedures are described in extensive detail in those papers; therefore, only a brief summary is provided here. Subcooled liquid refrigerant is pumped through a tube-in-tube evaporator, in which steam is used to boil and superheat the refrigerant. The superheated vapor is partially condensed to the desired quality using a set of water-cooled precondensers. Refrigerant exiting the precondensers enters the test section, which is a counterflow water-cooled heat exchanger containing the test channels. The two precondensers, with their different heat transfer surface areas, and variable cooling water flow rates help establish a wide range of refrigerant conditions at the test section inlet. The set of postcondensers downstream of the test section was used to completely condense and subcool the refrigerant. An energy balance on the precondenser yielded the refrigerant quality at the test section inlet, while a similar energy balance on the post condenser provided the refrigerant quality at the test section outlet. The average of the test section inlet and outlet qualities represented the quality for the data point being measured.

Coriolis mass flow meters ($\pm 0.15\%$ uncertainty for the refrigerant, and $\pm 0.2\%$ uncertainty for the coolant) were used for the measurement of refrigerant and coolant flow rates. Cooling water flow rates were measured using banks of rotameters with a maximum uncertainty of $\pm 2\%$. Pressure transducers with uncertainties

of $\pm 0.25\%$ of the span were used to measure refrigerant pressures. All temperatures were measured using Platinum Resistance Temperature Detectors (RTDs).

The test sections were fabricated as flat tubes with multiple extruded parallel channels. Three such tubes, with an effective heat transfer length of 0.3048 m and an upstream development length of 0.102 m were brazed together (Fig. 2), with refrigerant flowing through the center tube, and coolant flowing in counterflow through the top and bottom tubes. This method of using multiple parallel channels ensured that the refrigerant flow rates used were large enough to be adequately controlled and measured, with accurate heat balances around the test loop.

For the measurement of local heat transfer coefficients as a function of quality across the vapor-liquid dome, small Δx values are required in the test section; therefore, the heat duties at the mass fluxes of interest are relatively small. Calculating this heat duty from the test section inlet and outlet quality measurements would result in considerable uncertainties because this would involve the difference between two similar x values. Therefore, the heat duty must be measured on the coolant side, which must in turn be based on large ΔT s to minimize uncertainties. Ensuring large ΔT s requires low coolant flow rates. However, this makes the coolant-side thermal resistance the dominant resistance in the test section, making it difficult to deduce the refrigerant-side resistance from the measured test section overall thermal conductance (UA).

Garimella and Bandhauer [47] resolved these conflicting requirements for the accurate measurement of heat duty, and the

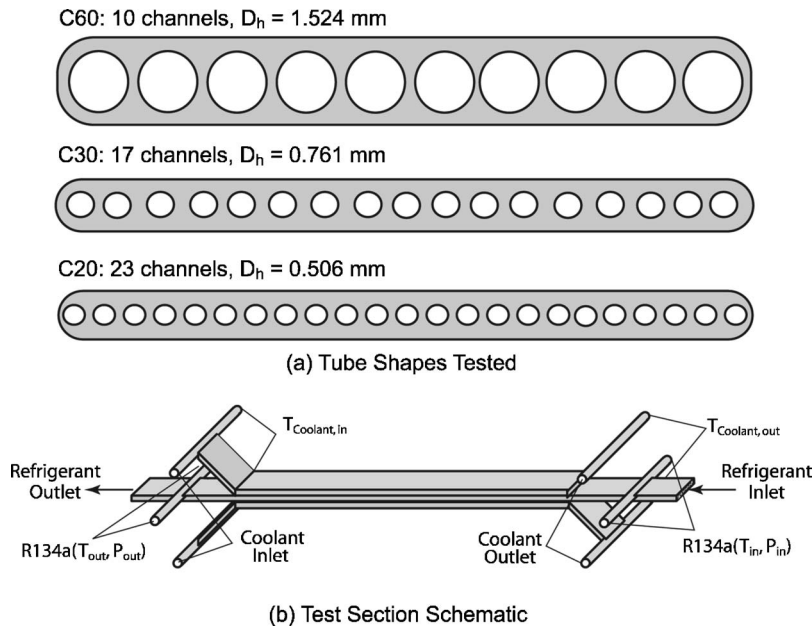


Fig. 2 Test section and tubes tested

refrigerant heat transfer coefficients, by developing a thermal amplification technique that decoupled these two issues. Thus, as shown in Fig. 1, the test section is cooled using water flowing in a closed (primary) loop at a high flow rate to ensure that the condensation side presents the governing thermal resistance. Heat exchange between this primary loop and a secondary cooling water stream at a much lower flow rate is used to obtain a large temperature difference, which is in turn used to measure the condensation duty. The secondary coolant flow rate is adjusted as test conditions change to maintain a reasonable ΔT and also small heat duties in the test section.

Multiple layers of low conductivity phenolic foam insulation and small temperature differences between the primary coolant and the ambient minimize the heat loss from the primary loop to the ambient. Also, the heat addition to this loop is minimized by using a recirculation pump with an extremely low heat dissipation rate, which was calculated from the pump curves supplied by the manufacturer. With the pump heat dissipation and the ambient heat loss being small fractions of the secondary loop duty, the test section heat load is relatively insensitive to these losses and gains. It should also be noted that the ambient heat loss term compensates for the heat gain due to pump heat dissipation. Local heat transfer coefficients are therefore measured accurately in small increments for the entire saturated vapor-liquid region. Additional details of this thermal amplification technique are provided in the paper by Garimella and Bandhauer [47].

The thermal amplification provided by this technique resulted in uncertainties typically as low as $\pm 2\%$ in the measurement of the secondary loop heat duty even at the small heat transfer rates of interest in this study. Combining the errors in the secondary loop duty, the pump heat addition, and the ambient heat loss (even with a highly conservative uncertainty of $\pm 50\%$ assumed for these terms), the test section heat duty was typically known to within a maximum uncertainty of $\pm 10\%$. With the refrigerant heat duty known, the condensation heat transfer coefficient was determined using the applicable thermal resistances. The coolant-side resistance was determined from correlations available in the *Handbook of Single-Phase Convective Heat Transfer* [48]. The large coolant flow rate and the enhancement in surface area (indirect area of about 4.7 times the direct area at an efficiency of 73.2%) provided by the coolant port walls on both sides of the microchannel tube resulted in high refrigerant-to-coolant resistance ratios (between 5

and 30). With this high resistance ratio, even an uncertainty of $\pm 25\%$ in the tube-side heat transfer coefficient did not appreciably affect the refrigerant-side heat transfer coefficient. For much of the data in this study, the uncertainties in condensation heat transfer coefficients were within about 20%. Representative heat transfer coefficients deduced from the data for a microchannel with $D_h = 0.761$ mm are shown in Fig. 3, along with the respective uncertainties. Methods for obtaining the qualities and their respective uncertainties were discussed in detail in earlier papers on flow visualization and pressure drops in these channels [11,7–9]. For the channels under consideration, the uncertainties in the measured qualities were between 2.5 and 9.1 percent, with an average uncertainty of 5.0 percent across the test matrix.

Discussion

The data for the three circular microchannels tested over the mass flux range $150 < G < 750$ kg/m² s are shown in Fig. 4 (including the data for the 0.761 channel that were presented in Fig.

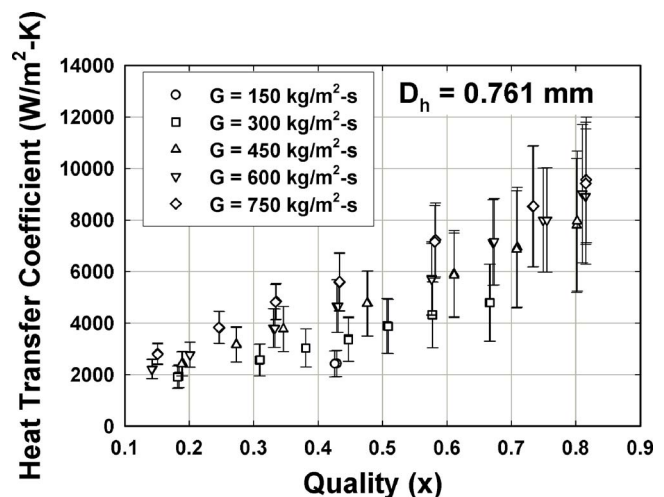


Fig. 3 Representative heat transfer coefficients and uncertainties, $D_h = 0.761$ mm

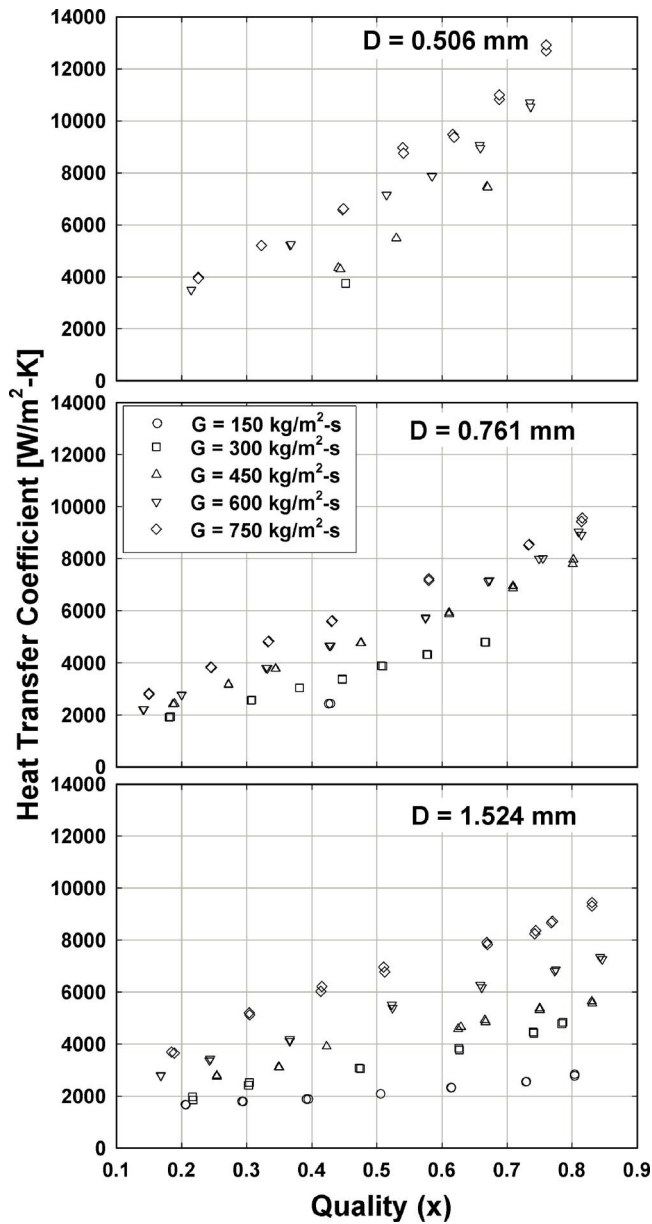


Fig. 4 Measured heat transfer coefficients

3) without error bands to facilitate identification and discussion of the trends. This figure illustrates the effects of mass flux, quality, and channel diameter on the heat transfer coefficient. It should be noted that some of the variations in heat transfer coefficient seen in this figure may be attributed to deviations from the nominal mass flux at each data point. In general, the heat transfer coefficient increases with increasing mass flux and quality, and decreasing diameter (please note that the trends pertaining to the effect of diameter can also be seen more clearly in Fig. 9, presented in a subsequent section, along with the predictions of the model developed in this study). For $G=300 \text{ kg/m}^2 \text{ s}$, the heat transfer coefficient increases with decreasing D_h for $x > 0.45$. For $x < 0.45$, heat transfer coefficients are very similar for $D_h=0.761$ and 1.524 mm (only one point, with a large Δx , could be taken at this nominal mass flux, about $320 \text{ kg/m}^2 \text{ s}$, for $D_h=0.506$ mm due to the somewhat large uncertainties at this low flow rate). The h values for $D_h=0.761$ mm are about 10% higher than the data for $D_h=1.524$ mm for $x > 0.45$. For $G=450 \text{ kg/m}^2 \text{ s}$, the effect of D_h becomes significant for $x > 0.45$, with almost no effect seen for $x < 0.45$. The h for $D_h=0.761$ mm for $0.45 < x < 0.65$ are about

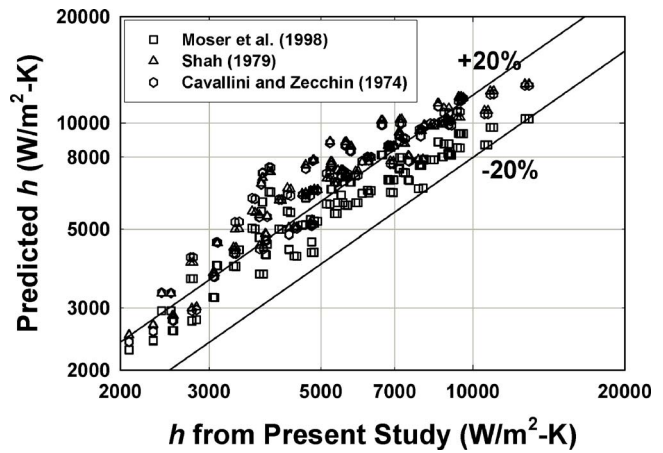


Fig. 5 Comparison of data from present study with two-phase-multiplier based correlations

20% higher than those for $D_h=1.524$ mm, while h for $D_h=0.506$ mm are between 10% and 15% higher than those for $D_h=0.761$ mm within this same quality range. For $x > 0.65$, h for $D_h=0.761$ mm are about 40% higher than those for $D_h=1.524$ mm. However, due to the low log-mean temperature differences (LMTDs) for these points (caused by a very large overall UA), the uncertainties for the $D_h=0.761$ mm case are higher. Similarly, h for $D_h=0.506$ mm are about 10% higher than those for $D_h=0.761$ mm, but are known only to within 35% for $x > 0.65$. Similar trends are seen for $G=600 \text{ kg/m}^2 \text{ s}$, but the trends for $G=750 \text{ kg/m}^2 \text{ s}$ are somewhat different. For this highest mass flux, very little difference exists between $h(0.761 \text{ mm})$ and $h(1.524 \text{ mm})$ for all x . However, the heat transfer coefficients for $D_h=0.506$ mm are between 20% and 40% higher than for the other two diameters for $x > 0.5$. The uncertainties in these h for $D_h=0.506$ mm are higher, particularly at large values of x , which may indicate that not all of this difference can be attributed to the effect of D_h . In summary, h increases between 10% and 40% for $x > 0.45$ as D_h is reduced from 1.524 mm to 0.506 mm. This effect is more prominent for a decrease in D_h from 0.761 mm to 0.506 mm.

The data from this study are compared with the available literature in Figs. 5–7. For clarity of presentation and ease of discussion, these comparisons are grouped in terms of the bases used by the existing correlations. (Comparisons with gravity driven models are not presented, because based on the flow visualization

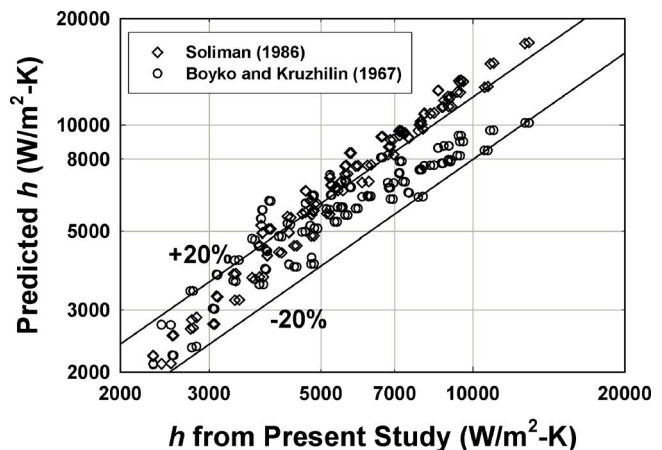


Fig. 6 Comparison of data from present study with predictions of homogeneous flow models

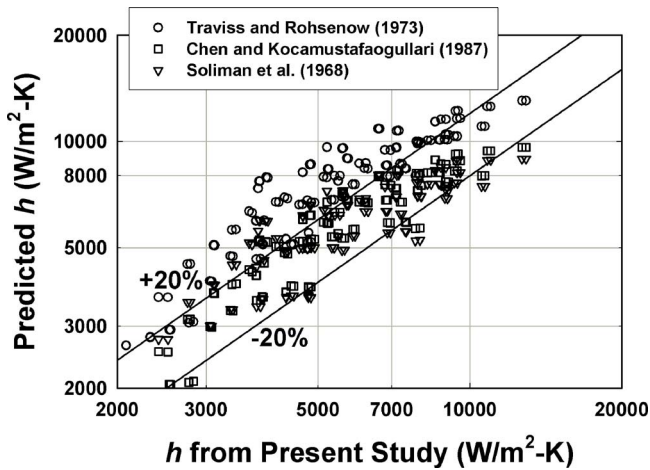


Fig. 7 Comparison of data from present study with boundary layer annular flow treatments

results of Coleman and Garimella [6,7], almost no data in the present study are in the stratified wavy flow regime.) Figure 5 shows correlations that use a two-phase multiplier approach plotted against the data from the present study. The Cavallini and Zecchin [30] and Shah [19] correlations are modifications to the Dittus-Boelter equation, while the Moser et al. [22] correlation uses the Petukhov [49] correlation as the basis with a modified version of the equivalent Re analysis by Akers et al. [20]. Among these correlations, the Moser et al. correlation does a reasonably good job of predicting the present data (14% average deviation), with the Shah [19] and Cavallini and Zecchin [30] correlations resulting in some overprediction (31% and 30% average deviations, respectively.) It should be noted that the Moser et al. model is used as one of the starting points in this study for the development of a microchannel heat transfer model from the present data (as described in the following section.)

Figure 6 shows a comparison between the data from the present study and the predictions of correlations that assume homogeneous flow. Such models should be applicable to annular flow with significant liquid entrainment in the vapor core. This figure shows that the homogeneous flow correlation of Boyko and Kruzhilin [34] and the mist flow correlation of Soliman [15] are better at predicting the current data (13% and 23% average deviations, respectively) than the other correlations discussed above. Among these two, the Soliman correlation leads to some overprediction of the data.

Figure 7 shows a comparison of the data from the present study with the predictions of shear-dominated annular flow correlations using boundary layer treatments. As mentioned earlier, this type of approach started with Carpenter and Colburn [27], who related the condensation heat transfer coefficient to the wall shear stress resulting from friction, momentum, and gravity contributions. The Soliman et al. [28] correlation (18% average deviation) improves upon the momentum contribution of Carpenter and Colburn, while Chen and Kocamustafaogullari [50] (13% average deviation) extended their vertical shear-dominated correlation to horizontal flow by neglecting the gravity contribution and employing a new pressure drop model. Traviss et al. [13] and Traviss and Rohsenow [51] used boundary layer analyses for annular flow assuming the von Karman analogy between heat transfer and momentum; however, their correlation shows the largest average deviation (38%) among this category of models from the present data.

Model Development

During the condensation process, the flow changes from mist flow (where applicable) to annular film flow to intermittent, with large overlaps in the types of flow resulting in transition flow

(intermittent/annular, intermittent/annular/mist, and annular/mist.) Since in the work of Coleman and Garimella [6,7], wavy flow was not seen for $D_h=1$ mm, it is assumed that wavy flow will not exist for either test section C20 ($D_h=0.506$ mm) or C30 ($D_h=0.761$ mm), and would occur over an insignificant region of the map for test section C60 ($D_h=1.524$ mm). For all three tubes, only a small portion of the data exhibit only one kind of flow pattern, e.g., <4% of the total data are in purely intermittent flow, with the bulk of the data being in transition between annular flow and one of the other regimes mentioned above. From these observations, it was deemed that a model based on annular flow would best represent the data.

In shear-driven models of condensation, the heat transfer models are closely and inherently linked to the pressure drop models. For example, the model by Soliman et al. [28] uses the Lockhart-Martinelli [52] pressure drop correlation to compute the frictional contribution to the shear stress. Similarly, the Traviss et al. [13] model bases film thickness on data for 8 mm diameter tubes [51], with the wall shear stress determined indirectly from the Lockhart-Martinelli correlation. The equivalent Re model of Moser et al. [22], in which shear between the equivalent core and peripheral flows drives the heat transfer, is based on the calculation of the equivalent Re from the Friedel [39] two-phase multiplier and condensation data for 3.14 to 20 mm diameter tubes. However, it has been shown by Garimella et al. [11,8–10] that conventional correlations [39,52,53] are not able to predict pressure drops in microchannels accurately. Thus, the heat transfer model developed here is based on the boundary layer analyses of Traviss et al. [13] and Moser et al. [22], with the requisite shear stress being calculated from the pressure drop models of Garimella et al. [11] developed specifically for microchannels.

Most shear-driven heat transfer models in literature are based on turbulent analyses in the liquid films. Carpenter and Colburn [27] suggest that the condensate layer in annular flow might become turbulent at very low liquid Reynolds numbers (240 as compared to the typical single-phase value of 2300). For single-phase boundary-layer flows, the critical Re decreases as the turbulent intensity in the outer flow increases and as the wall roughness increases [54]. In addition, heat transfer from the boundary layer to the wall (cooling/condensation), through its effect on the liquid viscosity, could destabilize the flow due to the increase in friction drag. This is counteracted somewhat by the decrease in pressure along the direction of flow, which stabilizes the flow. Since the vapor core in annular flow is typically highly turbulent and the condensation process further destabilizes the flow, it is likely that the onset of turbulence in the liquid film occurs at much lower Reynolds numbers. For all the data points in the current study, liquid Re is less than 2300. However, a model based on turbulent parameters, with appropriate modifications to account for the conditions under study, was developed based on these considerations.

The following turbulent parameters are defined:

$$u^+ = \frac{u}{u^*} \quad (1)$$

$$y^+ = \frac{y \cdot \rho_l \cdot u^*}{\mu_l} \quad (2)$$

$$R^+ = \frac{R \cdot \rho_l \cdot u^*}{\mu_l} \quad (3)$$

where the friction velocity is given by

$$u^* = \sqrt{\frac{\tau_i}{\rho_l}} \quad (4)$$

In the above equation, the commonly used wall shear stress has been replaced by the interfacial shear stress, which better reflects the two-phase flow situation. This interfacial shear stress is ob-

tained from the pressure drop models of Garimella et al. [11]. The turbulent dimensionless temperature is defined as follows:

$$T^+ = \frac{\rho_l \cdot C_{p_l} \cdot u^*}{q''} (T_i - T_w) \quad (5)$$

The shear stress and heat flux are expressed in the usual manner

$$\tau = (\mu + \rho \cdot \varepsilon_m) \frac{du}{dy} \quad (6)$$

$$q'' = -(k + \varepsilon_h \cdot \rho \cdot C_p) \frac{dT}{dy} \quad (7)$$

Assuming that all of the heat is transferred in the liquid film and substituting T^+ from Eq. (5) yields the following expression for the condensation heat transfer coefficient. (Here it is assumed that the interface is at the saturation temperature.)

$$h = \frac{q''}{(T_{\text{sat}} - T_w)} = \frac{\rho_l \cdot C_{p_l} \cdot u^*}{T^+} \quad (8)$$

The above equation for h has two unknowns, u^* and T^+ . Using Eq. (5), for a constant wall temperature over the circumference, Eq. (7) can be represented as follows:

$$\frac{dT^+}{dy^+} = \left(\frac{1}{\text{Pr}_l} + \frac{\rho_l \cdot \varepsilon_h}{\mu_l} \right)^{-1} \quad (9)$$

Integrating the above equation requires knowledge of the turbulent film thickness, which is determined using the Baroczy [55] void fraction model

$$\alpha = \left[1 + \left(\frac{1-x}{x} \right)^{0.74} \left(\frac{\rho_v}{\rho_l} \right)^{0.65} \left(\frac{\mu_l}{\mu_v} \right)^{0.13} \right]^{-1} \quad (10)$$

Now, the film thickness is obtained as follows:

$$\delta = (1 - \sqrt{\alpha}) \frac{D}{2} \quad (11)$$

It should be noted that this is different from the manner in which Traviss et al. [13] and Traviss and Rohsenow [51] determined film thickness. Here, to maintain consistency with the corresponding pressure drop model of Garimella et al. [11], the film thickness is computed from the void fraction. The dimensionless turbulent film thickness as defined in Eq. (2) is given by

$$\delta^+ = \frac{\delta \cdot \rho_l \cdot u^*}{\mu_l} \quad (12)$$

Also, to integrate Eq. (9) we need an expression for $\rho_l \cdot \varepsilon_h / \mu_l$. Substituting $\tau = (1-y/R) \tau_w$ into Eq. (6) and expressing in terms of turbulent parameters yields the following equation:

$$\frac{\rho_l \cdot \varepsilon_m}{\mu_l} = \frac{1 - y^+/R^+}{du^+/dy^+} - 1 \quad (13)$$

In a manner analogous to the development by Traviss et al. [13], with the assumptions of small film thickness compared to the tube radius, and $\varepsilon_m \cong \varepsilon_h$, the following simplified two-region (instead of three-region) turbulent dimensionless temperature expressions are proposed based on the liquid-phase Reynolds number for $\text{Re}_l < 2100$:

$$T^+ = 5 \cdot \text{Pr}_l + 5 \cdot \ln \left[\text{Pr}_l \left(\frac{\delta^+}{5} - 1 \right) + 1 \right] \quad (14)$$

for $\text{Re}_l > 2100$:

$$T^+ = 5 \cdot \text{Pr}_l + 5 \cdot \ln(5 \cdot \text{Pr}_l + 1) + \int_{30}^{\delta^+} \frac{dy^+}{\left(\frac{1}{\text{Pr}_l} - 1 \right) + \frac{y^+}{5} \left(1 - \frac{y^+}{R^+} \right)} \quad (15)$$

Now, the only unknown quantity left is the interfacial shear stress needed for determining u^* in Eq. (8). The multiple flow regime pressure drop model by Garimella et al. [11] for condensing flows of refrigerant R134a in tubes with $0.5 < D < 4.9$ mm was used for this purpose. Although this model consists of separate submodels for the intermittent flow regime and the annular/mist/disperse flow regimes, in the current study, since the heat transfer model is developed based on an annular flow pattern, that portion of the pressure drop model is employed for the entire data set here. Thus, the interfacial friction factor is computed from the corresponding liquid-phase Re and friction factor, the Martinelli parameter, and a surface tension-related parameter

$$\frac{f_i}{f_l} = A \cdot X^a \text{Re}_l^b \psi^c \quad (16)$$

For completeness, the values of the constants and exponents A , a , b , and c that were reported in Garimella et al. [11] are reproduced here. Thus, for $\text{Re}_l < 2100$, $A = 1.308 \times 10^{-3}$, $a = 0.427$, $b = 0.930$, $c = -0.121$, and for $\text{Re}_l > 3400$, $A = 25.64$, $a = 0.532$, $b = -0.327$, and $c = 0.021$. The friction factors required for the individual-phase pressure drops in the Martinelli parameter were computed using $f = 64/\text{Re}$ for $\text{Re}_l < 2100$ and the Blasius expression $f = 0.316 \cdot \text{Re}^{-0.25}$ for $\text{Re}_l > 3400$. The Martinelli parameter X is given by

$$X = \left[\frac{(dP/dz)_l}{(dP/dz)_v} \right]^{1/2} \quad (17)$$

For this model, the liquid-phase Re is defined in terms of the annular flow area surrounding the vapor core that is occupied by the liquid phase, and the hydraulic diameter of this annular ring ($D - D_i$), which results in the following expression when related back to the tube diameter D through the void fraction α :

$$\text{Re}_l = \frac{GD(1-x)}{(1 + \sqrt{\alpha}) \mu_l} \quad (18)$$

Similarly, the gas-phase Re is calculated as follows

$$\text{Re}_v = \frac{GxD}{\mu_v \sqrt{\alpha}} \quad (19)$$

The surface tension parameter ψ in equation (16) [56] is given by

$$\psi = \frac{j_l \mu_l}{\sigma} \quad (20)$$

where $j_l = G(1-x)/\rho_l(1-\alpha)$ is the liquid velocity in the annular film.

Appropriate interpolation techniques were specified to address the regions of overlap and transition between different regimes. The interfacial friction factor thus determined is related to the pressure drop through the void fraction model [55] using the following equation:

$$\frac{\Delta P}{L} = \frac{1}{2} \cdot f_i \frac{G^2 \cdot x^2}{\rho_v \cdot \alpha^{2.5}} \cdot \frac{1}{D} \quad (21)$$

Finally, this pressure drop is used to compute the interfacial shear stress as follows:

$$\tau_i = \left(\frac{\Delta P}{L} \right) \frac{D_i}{4} \quad (22)$$

In summary, to obtain the heat transfer coefficient, the interfacial shear stress is first calculated using the pressure drop model and the above equation. The resulting shear stress is used to compute the friction velocity u^* (Eq. (4)) and the dimensionless film thickness δ^+ (Eq. (12)). The dimensionless temperature T^+ is then calculated (Eq. (15)), which yields the heat transfer coefficient (Eq. (8)).

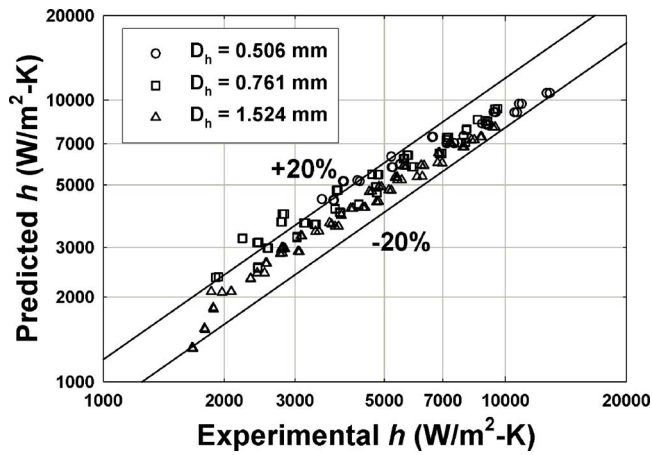


Fig. 8 Comparison of measured and predicted heat transfer coefficients from the present study

This model predicts 86% of the data within $\pm 20\%$, with an average absolute deviation $\sum_1^N \text{ABS}(\text{Measured} - \text{Predicted}) / \text{Measured} / N$ of 10% as shown in Fig. 8. This demonstrates that the utilization of the appropriate shear stress models developed specifically for microchannels is able to account for the related heat transfer phenomena accurately. The data and the predictions from the model are also plotted as a function of quality at representative mass fluxes for each tube under consideration in this study (Fig. 9). The heat transfer coefficient increases with an increase in mass flux and quality, and with a decrease in the tube diameter. The figure also demonstrates that the model is able to capture the trends in the data accurately. As the liquid film becomes thinner with increasing vapor quality, the heat transfer coefficient increases. The steep slope at the higher qualities represents an approach to a vanishingly thin film. However, it must be noted that the actual behavior in this region will be dependent on the inlet conditions of a condenser, including the inlet superheat, the coolant temperature and the consequent wall subcooling—these phenomena are not accounted for in the present model. It should also be pointed out that although the model was developed based on an annular flow mechanism, it appears to predict the heat transfer coefficients in the mist and mist-annular overlap regions in the high mass flux and high quality cases adequately. At the extreme end of the graph ($x > 80\%$), the flow may be exclusively in the mist flow region. For a given flow rate, the quality at which the mist flow regime occurs could decrease with decreasing diameter due to increased interfacial shedding. As liquid entrainment increases, the heat transfer coefficient will increase due to the thinning of the liquid film Soliman [15]. Although liquid entrainment and mist formation are not explicitly accounted for in the heat transfer part of this model, the trends in the data (the steeper slope in the data at the higher qualities, particularly for small D_h) can be interpreted on this basis.

Conclusions

An experimentally validated model for heat transfer during condensation of refrigerant R134a in horizontal microchannels with $0.506 < D < 1.524$ mm was developed. The thermal amplification technique reported earlier by the authors was used to measure heat transfer coefficients accurately as a function of quality over a wide range of mass fluxes. The data were systematically compared with correlations in the literature that assumed gravity driven or shear-driven condensation, and also those that used a homogenous flow assumption or two-phase multipliers to predict heat transfer coefficients. It was shown that these models developed for larger tubes result in significant deviations from the measured data, primarily because those models were not intended for, and could not ac-

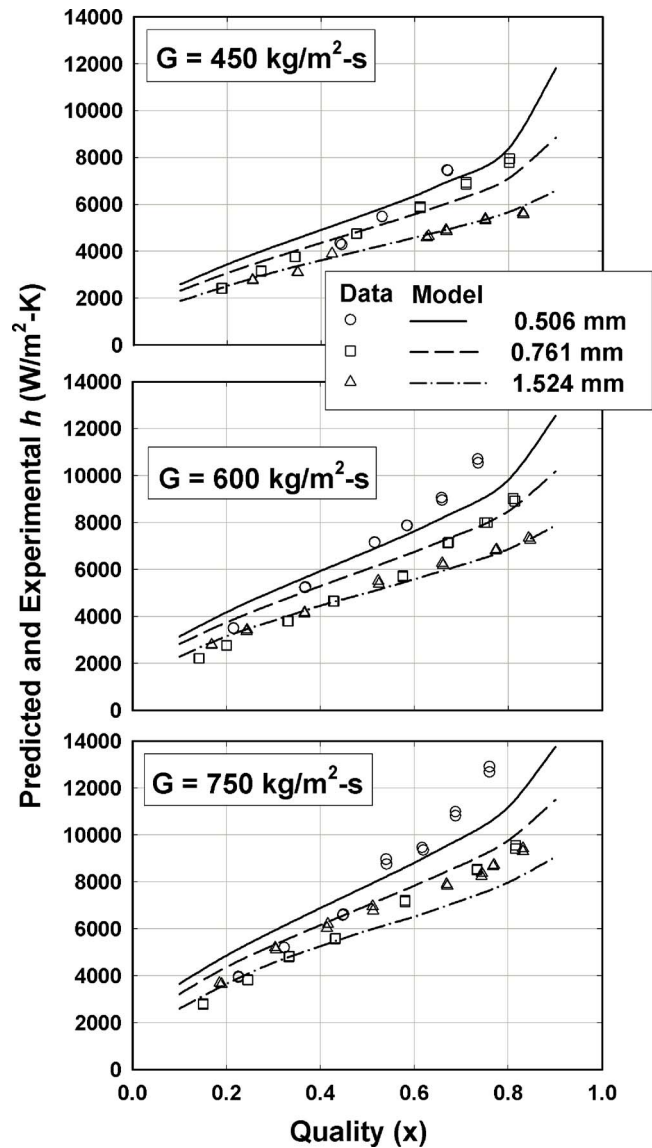


Fig. 9 Trends predicted by current model

count for, the flow phenomena and interfacial shear behavior specific to microchannels. In view of these observations, a model derived from the approaches used by Traviss et al. [13] and Moser et al. [22] was developed with the primary difference being the computation of interfacial shear based on pressure drops in these same microchannels measured and modeled by the authors in earlier work [11]. The resulting model predicts 86% of the data within $\pm 20\%$, and closely replicates the trends exhibited by the data. It was shown that the heat transfer coefficient increases with an increase in mass flux and quality, and a decrease in diameter. A more explicit accounting of the heat transfer in the liquid slugs, vapor bubbles and the film-bubble interface in intermittent flow, and of the entrainment of liquid into the vapor core in mist flow would improve the predictions further.

Nomenclature

- C_p = specific heat
- D = diameter, m or mm as noted
- ΔP = pressure drop, kPa
- f = friction factor, Darcy
- G = mass flux, $\text{kg/m}^2 \text{s}$
- h = heat transfer coefficient, $\text{W/m}^2 \text{K}$

J_L = liquid phase velocity in annular film
 L = tube length, m
 Pr = Prandtl number
 q'' = heat flux, W/m²
 R = radius, m
 Re = Reynolds number
 T = temperature, °C or K
 X = Martinelli parameter
 x = vapor quality
 α = void fraction
 μ = dynamic viscosity, kg/m s
 ρ = density, kg/m³
 σ = surface tension, N/m
 ε = eddy viscosity/diffusivity
 V, u = velocity, m/s
 u^* = friction velocity
 τ = shear stress, Pa
 y = length scale (used for film thickness)
 δ = liquid film thickness, m

Superscripts

+ = nondimensional turbulent parameter

Subscripts

avg = average
 f = friction
 h = hydraulic
 i = gas-liquid interface
 l = liquid
 m = momentum
 sat = saturation/saturated
 v = vapor
 w = wall

References

- [1] Sobhan, C. B., and Garimella, S. V., 2001, "A Comparative Analysis of Studies on Heat Transfer and Fluid Flow in Microchannels," *Microscale Thermophys. Eng.*, **5**(4), pp. 293–311.
- [2] Garimella, S. V., and Sobhan, C. B., 2003, "Transport in Microchannels—A Critical Review," *Annu. Rev. Heat Transfer*, **13**, pp. 1–50.
- [3] Garimella, S. V., and Singhal, V., 2004, "Single-Phase Flow and Heat Transport and Pumping Considerations in Microchannel Heat Sinks," *Heat Transfer Eng.*, **25**(1), pp. 15–25.
- [4] Liu, D., and Garimella, S. V., 2004, "Investigation of Liquid Flow in Microchannels," *J. Thermophys. Heat Transfer*, **18**(1), pp. 65–72.
- [5] Coleman, J. W., and Garimella, S., 1999, "Characterization of Two-Phase Flow Patterns in Small Diameter Round and Rectangular Tubes," *Int. J. Heat Mass Transfer*, **42**(15), pp. 2869–2881.
- [6] Coleman, J. W., and Garimella, S., 2000, "Two-Phase Flow Regime Transitions in Microchannel Tubes: The Effect of Hydraulic Diameter," *Am. Soc. Mech. Eng., Heat Transfer Div., HTD-366*, pp. 71–83.
- [7] Coleman, J. W., and Garimella, S., 2003, "Two-Phase Flow Regimes in Round, Square and Rectangular Tubes During Condensation of Refrigerant R134a," *Int. J. Refrig.*, **26**(1), pp. 117–128.
- [8] Garimella, S., Killion, J. D., and Coleman, J. W., 2002, "An Experimentally Validated Model for Two-Phase Pressure Drop in the Intermittent Flow Regime for Circular Microchannels," *J. Fluids Eng.*, **124**(1), pp. 205–214.
- [9] Garimella, S., Killion, J. D., and Coleman, J. W., 2003, "An Experimentally Validated Model for Two-Phase Pressure Drop in the Intermittent Flow Regime for Noncircular Microchannels," *J. Fluids Eng.*, **125**(5), pp. 887–894.
- [10] Garimella, S., Agarwal, A., and Coleman, J. W., 2003, "Two-Phase Pressure Drops in the Annular Flow Regime in Circular Microchannels," *21st IIR International Congress of Refrigeration*, August 12–22, Washington, DC, Paper No. ICR0360, International Institute of Refrigeration.
- [11] Garimella, S., Agarwal, A., and Killion, J. D., 2005, "Condensation Pressure Drop in Circular Microchannels," *Heat Transfer Eng.*, **26**(3), pp. 1–8.
- [12] Breber, G., Palen, J. W., and Taborek, J., 1980, "Prediction of Horizontal Tubeside Condensation of Pure Components Using Flow Regime Criteria," *J. Heat Transfer*, **102**(3), pp. 471–476.
- [13] Traviss, D. P., Rohsenow, W. M., and Baron, A. B., 1973, "Forced-Convection Condensation Inside Tubes: A Heat Transfer Equation for Condenser Design," *ASHRAE Trans.*, **79**(1), pp. 157–165.
- [14] Dobson, M. K., Chato, J. C., Hinde, D. K., and Wang, S. P., 1994, "Experimental Evaluation of Internal Condensation of Refrigerants R-12 and R-134a," *ASHRAE Trans.*, **100**, pp. 744–754.
- [15] Soliman, H. M., 1986, "Mist-Annular Transition During Condensation and Its Influence on the Heat Transfer Mechanism," *Int. J. Multiphase Flow*, **12**(2), pp. 277–288.
- [16] Soliman, H. M., 1982, "On the Annular-to-Wavy Flow Pattern Transition During Condensation Inside Horizontal Tubes," *Can. J. Chem. Eng.*, **60**(4), pp. 475–481.
- [17] Yang, C.-Y., and Webb, R. L., 1996, "Condensation of R-12 in small hydraulic diameter extruded aluminum tubes with and without micro-fins," *Int. J. Heat Mass Transfer*, **39**(4), pp. 791–800.
- [18] Yang, C.-Y., and Webb, R. L., 1997, "Predictive Model for Condensation in Small Hydraulic Diameter Tubes Having Axial Micro-fins," *J. Heat Transfer*, **119**(4), pp. 776–782.
- [19] Shah, M. M., 1979, "A General Correlation for Heat Transfer During Film Condensation Inside Pipes," *Int. J. Heat Mass Transfer*, **22**(4), pp. 547–556.
- [20] Akers, W. W., Deans, H. A., and Crosser, O. K., 1959, "Condensation Heat Transfer Within Horizontal Tubes," *Chem. Eng. Prog., Symp. Ser.*, **55**(29), pp. 171–176.
- [21] Dobson, M. K., and Chato, J. C., 1998, "Condensation in Smooth Horizontal Tubes," *J. Heat Transfer*, **120**(1), pp. 193–213.
- [22] Moser, K. W., Webb, R. L., and Na, B., 1998, "A New Equivalent Reynolds Number Model for Condensation in Smooth Tubes," *J. Heat Transfer*, **120**(2), pp. 410–417.
- [23] Hurlburt, E. T., and Newell, T. A., 1999, "Characteristics of Refrigerant Film Thickness, Pressure Drop, and Condensation Heat Transfer in Annular Flow," *HVAC&R Res.*, **5**(3), pp. 229–248.
- [24] Asali, J. C., Hanratty, T. J., and Andreussi, P., 1985, "Interfacial Drag and Film Height for Vertical Annular Flow," *AIChE J.*, **31**(6), pp. 895–902.
- [25] Sacks, P. S., 1975, "Measured Characteristics of Adiabatic and Condensing Single-Component Two-Phase Flow of Refrigerant in a 0.377-in. Diameter Horizontal Tube," *Proceedings of the American Society of Mechanical Engineers Winter Annual Meeting, 75-WA/HT-24*, Nov. 30–Dec. 4, ASME, New York, p. 12.
- [26] Dobson, M. K., 1994, *Heat Transfer and Flow Regimes During Condensation in Horizontal Tubes*, Ph. D., Mechanical and Industrial Engineering, University of Illinois at Urbana-Champaign, Urbana-Champaign, IL.
- [27] Carpenter, F. G., and Colburn, A. P., 1951, "The Effect of Vapor Velocity on Condensation Inside Tubes," *General Discussion of Heat Transfer*, The Institute of Mechanical Engineers and ASME, pp. 20–26.
- [28] Soliman, H. M., Schuster, J. R., and Berenson, P. J., 1968, "A General Heat Transfer Correlation for Annular Flow Condensation," *J. Heat Transfer*, **90**, pp. 267–276.
- [29] Chen, S. L., Gerner, F. M., and Tien, C. L., 1987, "General Film Condensation Correlations," *Exp. Heat Transfer*, **1**(2), pp. 93–107.
- [30] Cavallini, A., and Zecchin, R., 1974, "Dimensionless Correlation for Heat Transfer in Forced Convection Condensation," *Proceedings of the Sixth International Heat Transfer Conference*, Tokyo, Japan, Vol. 3, pp. 309–313.
- [31] Chitti, M. S., and Anand, N. K., 1995, "An Analytical Model for Local Heat Transfer Coefficients for Forced Convective Condensation Inside Smooth Horizontal Tubes," *Int. J. Heat Mass Transfer*, **38**(4), pp. 615–627.
- [32] Guo, Z., and Anand, N. K., 2000, "Analytical Model to Predict Condensation of R-410A in a Horizontal Rectangular Channel," *J. Heat Transfer*, **122**(3), pp. 613–620.
- [33] Ibrahim, O. M., 1994, "Prediction of Local Heat Transfer Coefficients During Annular Flow Condensation," *Proceedings of the 1994 ASME Fluids Engineering Division Summer Meeting. Part 2 (of 18)*, Lake Tahoe, NV, Jun. 19–23, ASME, New York, Vol. 180, pp. 77–81.
- [34] Boyko, L. D., and Kruzhilin, G. N., 1967, "Heat Transfer and Hydraulic Resistance During Condensation of Steam in a Horizontal Tube and in a Bundle of Tubes," *Int. J. Heat Mass Transfer*, **10**(3), pp. 361–373.
- [35] Chitti, M. S., and Anand, N. K., 1996, "Condensation Heat Transfer Inside Smooth Horizontal Tubes for R-22 and R-32/125 Mixture," *HVAC&R Res.*, **2**(1), pp. 79–101.
- [36] Wang, H. S., and Rose, J. W., 2004, "Film Condensation in Horizontal Triangular Section Microchannels: A Theoretical Model," *Proceedings of the Second International Conference on Microchannels and Minichannels (ICMM2004)*, Rochester, NY, Jun. 17–19, ASME, New York, pp. 661–666.
- [37] Wang, H. S., Rose, J. W., and Honda, H., 2004, "A Theoretical Model of Film Condensation in Square Section Horizontal Microchannels," *Chem. Eng. Res. Des.*, **82**(4), pp. 430–434.
- [38] Cavallini, A., Del Col, D., Doretti, L., Matkovic, M., Rossetto, L., and Zilio, C., 2005, "Condensation Heat Transfer and Pressure Gradient Inside Multiport Minichannels," *Heat Transfer Eng.*, **26**(3), pp. 45–55.
- [39] Friedel, L., 1980, "Pressure Drop During Gas/Vapor-Liquid Flow in Pipes," *Int. Chem. Eng.*, **20**(3), pp. 352–367.
- [40] Zhang, M., and Webb, R. L., 2001, "Correlation of Two-Phase Friction for Refrigerants in Small-Diameter Tubes," *Exp. Therm. Fluid Sci.*, **25**(3–4), pp. 131–139.
- [41] Mishima, K., and Hibiki, T., 1996, "Some Characteristics of Air-Water Two-Phase Flow in Small Diameter Vertical Tubes," *Int. J. Multiphase Flow*, **22**(4), pp. 703–712.
- [42] Muller-Strehagen, H., and Heck, K., 1986, "A Simple Friction Pressure Drop Correlation for Two-Phase Flow in Pipes," *Chem. Eng. Process.*, **20**(6), pp. 297–308.
- [43] Cavallini, A., Censi, G., Del Col, D., Doretti, L., Longo, G. A., and Rossetto, L., 2002, "Condensation of Halogenated Refrigerants Inside Smooth Tubes," *HVAC&R Res.*, **8**(4), pp. 429–451.
- [44] Koyama, S., Kuwahara, K., and Nakashita, K., 2003, "Condensation of Refrigerant in a Multi-Port Channel," *First International Conference on Microchannels and Minichannels*, Rochester, NY, April 24–25, AMSE, New York, pp.

193–205.

- [45] Wang, W. W.-W., Radcliff, T. D., and Christensen, R. N., 2002, “A Condensation Heat Transfer Correlation for Millimeter-Scale Tubing With Flow Regime Transition,” *Exp. Therm. Fluid Sci.*, **26**(5), pp. 473–485.
- [46] Shin, J. S., and Kim, M. H., 2005, “An Experimental Study of Flow Condensation Heat Transfer Inside Circular and Rectangular Mini-Channels,” *Heat Transfer Eng.*, **26**(3), pp. 36–44.
- [47] Garimella, S., and Bandhauer, T. M., 2001, “Measurement of Condensation Heat Transfer Coefficients in Microchannel Tubes,” *2001 ASME International Mechanical Engineering Congress and Exposition*, Nov. 11–16, ASME, New York, Vol. 369, pp. 243–249.
- [48] Kakaç, S., Shah, R. K., and Aung, W., 1987, *Handbook of Single-Phase Convective Heat Transfer*, Wiley, New York.
- [49] Petukhov, B. S., 1970, “Heat Transfer and Friction in Turbulent Pipe Flow With Variable Physical Properties,” *Adv. Heat Transfer*, **6**, pp. 503–64.
- [50] Chen, I. Y., and Kocamustafaogullari, G., 1987, “Condensation Heat Transfer Studies for Stratified, Cocurrent Two-Phase Flow in Horizontal Tubes,” *Int. J. Heat Mass Transfer*, **30**(6), pp. 1133–1148.
- [51] Traviss, D. P., and Rohsenow, W. M., 1973, “Flow Regimes in Horizontal Two-Phase Flow with Condensation,” *ASHRAE Trans.*, **79**(Part 2), pp. 31–39.
- [52] Lockhart, R. W., and Martinelli, R. C., 1949, “Proposed Correlation of Data for Isothermal Two-Phase, Two-Component Flow in Pipes,” *Chem. Eng. Prog.*, **45**(1), pp. 39–45.
- [53] Chisholm, D., 1967, “A Theoretical Basis for the Lockhart-Martinelli Correlation for Two-Phase Flow,” *Int. J. Heat Mass Transfer*, **10**(12), pp. 1767–1778.
- [54] Schlichting, H., and Gersten, K., 2000, “Laminar-Turbulent Transition,” in *Boundary Layer Theory*, Springer, New York, pp. 415–490.
- [55] Baroczy, C. J., 1965, “Correlation of Liquid Fraction in Two-Phase Flow with Applications to Liquid Metals,” *Chem. Eng. Prog., Symp. Ser.*, **61**(57), pp. 179–191.
- [56] Lee, H. J., and Lee, S. Y., 2001, “Pressure Drop Correlations for Two-Phase Flow Within Horizontal Rectangular Channels With Small Heights,” *Int. J. Multiphase Flow*, **27**(5), pp. 783–796.

The Effect of Internal Temperature Gradients on Regenerator Matrix Performance

K. L. Engelbrecht

Research Assistant
e-mail: kengelbrecht@wisc.edu

G. F. Nellis

Assistant Professor

S. A. Klein

Professor

Department of Mechanical Engineering,
University of Wisconsin,
1500 Engineering Drive,
Madison, WI 53706

Background. One-dimensional regenerator models treat the solid material as a lumped capacitance with negligible temperature gradients. Advanced regenerator geometries operating at low temperatures or active magnetic regenerators which use a liquid heat transfer fluid may have temperature gradients in the solid regenerator that significantly affect performance. It is advantageous to utilize a one-dimensional, or lumped, model of the regenerator that is coupled with a correction factor in order to account for the impact of the internal temperature gradients. Previous work relative to developing such a correction factor is shown here to be inadequate or only valid over a limited range of dimensionless conditions. **Method of Approach.** This paper describes a numerical model of a sphere subjected to a time varying fluid temperature (representing a passive process) or time varying internal heat generation induced by a magnetic field (representing an active magnetic process). The governing equations are nondimensionalized and the efficiency of the sphere is presented as a function of the Fourier number and Biot number. **Results.** An approximate correction (or degradation) factor is obtained based on these results that is valid over a wide range of dimensionless conditions and therefore useful to regenerator designers. The degradation factor correlation was developed for a sinusoidal variation in the fluid temperature, however, the same results can be applied to different functional forms of the time variation using the concept of an effective cycle time that is weighted by the magnitude of the driving temperature difference. **Conclusions.** The heat transfer degradation factor presented here can be applied to one-dimensional regenerator models in order to accurately account for the transient performance of a matrix with finite thermal conductivity. This degradation factor allows regenerator models to approximately account for internal temperature gradients without explicitly modeling them and therefore remain computationally efficient while improving the range of applicability and accuracy. [DOI: 10.1115/1.2345428]

Keywords: regenerator modeling, internal temperature gradients, Fourier number, Biot number, active magnetic regenerator

Introduction

It is often the case in a regenerator that a material with small spatial extent is subjected to a time varying boundary condition. In a passive regenerator bed, a solid sphere may be subjected to a time varying fluid temperature; the sphere temperature will therefore tend to follow the fluid temperature and consequently the material will store and release energy to the fluid during each cycle. An active magnetic regenerator is composed of a magnetocaloric material and may be subjected to both a time-varying fluid temperature as well as a volumetric heating effect that is driven by a time-varying magnetic field.

Regenerator models often neglect the temperature gradients that occur locally within the regenerator material and treat the solid as a lumped capacitance. This assumption is often justified because of the relatively large thermal conductivity and small spatial extent of most regenerators. For example, a regenerator for a Stirling cycle may consist of 500 mesh metal screens exposed to an oscillatory flow of helium. In this situation, any local temperature gradients within the screen material (i.e., temperature gradients between the center and surface of a wire at any position within the regenerator) will be much smaller than the temperature difference between the surface of the regenerator and the surrounding gas. However, this is not always the case; the magnetocaloric materials

that are required for active magnetic regenerative refrigeration (AMRR) systems [1] and other advanced regenerator materials for passive, very low temperature cryogenic systems may have relatively low conductivity [2]. Also, near room temperature AMRR systems [3] that are being developed use liquid working fluids that result in high fluid-to-particle heat transfer coefficients and therefore internal temperature gradients may be more significant in comparison. Furthermore, all of these devices become more economically competitive (i.e., smaller) as the cycle frequency increases. As a result, the thermal penetration depth may become comparable to the spatial extent of the material and therefore the performance that is predicted by a lumped capacitance model may be significantly in error in these situations.

Explicitly accounting for internal temperature gradients in the regenerator will result in a two-dimensional transient problem that will greatly increase the required computation time and the complexity of the model. The objective of this work is, therefore, the development of an approximate correction technique that may be used in the context of a one-dimensional regenerator model in order to account for internal temperature gradients without explicitly including them in the solution algorithm. The specific purpose of this analysis is to compare the amount of energy that is transferred from a sphere subjected to time varying boundary conditions (either fluid temperature or applied magnetic field) with finite conductivity to a sphere under the same conditions but with an infinite conductivity (i.e., one that may accurately be modeled as having a lumped heat capacitance).

Jefferson [4] presents a Biot number based correction that can

Contributed by the Heat Transfer Division of ASME for publication in the JOURNAL OF HEAT TRANSFER. Manuscript received May 27, 2005; final manuscript received March 20, 2006. Review conducted by N. K. Anand.

be used to correct the heat transfer coefficient in order to reflect the additional resistance associated with conduction within the regenerator matrix. However, this correction is based on a steady-state condition in which volumetric generation is used to predict the temperature gradients within the material and therefore the impact that the cycle frequency and the associated thermal penetration depth have on the participation of the regenerator medium is not considered. Hausen [5] suggests a correction factor based on an analytical model that is dependent on Biot number, cycle time, and the diffusivity of the solid material; this correction factor is derived based on a square-wave variation in the heat flux that is applied to the regenerator matrix. Hinchcliffe and Willmot [6] developed a numerical model that is used to modify the Hausen equation by calculating a time-dependent correction factor based on the Biot number and Fourier number. However, results are published only for a slab geometry with a square-wave heat flux boundary condition in graphical form, and no general solution is given. When the proposed method is applied to a packed sphere regenerator, it is only applicable when the Biot number is less than 5. Heggs and Carpenter [7] developed a numerical model that accounts for conduction in the solid material and uses a linear variation in the heat flux as opposed to a square wave. Results for infinite-conduction regenerators were compared to results for finite conduction regenerators and a method of modifying the temperature ratio in the regenerator was proposed to correct for finite conduction. Correction factors using this technique are given in Heggs et al. [8] as a function of dimensionless regenerator length, dimensionless period, and the Biot number for three specific packing geometries. These results are provided in the form of charts only; no correlations to these correction factors are provided. In a separate paper, Heggs and Carpenter [9] evaluate the limits to the conditions for which the infinite-conductivity solid (i.e., lumped) assumption is valid for a regenerator. Several researchers have applied a conduction correction factor to experimental heat transfer data for solid materials with relatively low thermal conductivity in order to develop heat transfer coefficients [10–12] that apply to specific materials, geometries and conditions without providing broadly generic and physics-based correction factors. Green et al. [13] studied the effect of finite conductivity in the regenerator on axial dispersion. San [14] applied an ε -NTU technique to a regenerator bed and reported the effectiveness of regenerators for various values of Biot number. The Biot number was found to significantly affect the performance of a passive regenerator but the results were not generalized. No work was found in the literature that investigated the effects of finite thermal conductivity on active magnetic regenerators.

Governing Equations

The governing equations for this system are derived here for both a passive and active process. The active material is assumed to have a constant partial derivative of entropy with respect to magnetic field at constant temperature $((\partial s / \partial \mu_0 H)_T)$. This property results in a time dependent volumetric generation (actually a work transfer) when the material is exposed to a time-varying magnetic field. Both the active and passive materials are assumed to have a constant specific heat capacity (c) and thermal conductivity (k) and the sphere-to-fluid heat transfer coefficient (h) is assumed to be constant throughout the cycle. The temperature distribution within the sphere is assumed to be one dimensional.

The governing equation for a sphere composed of a magnetically active material balances conduction and magnetic work transfer against the storage of energy

$$k \frac{\partial}{\partial r} \left[r^2 \frac{\partial T}{\partial r} \right] - Tr^2 \rho \left(\frac{\partial s}{\partial \mu_0 H} \right)_T \frac{d\mu_0 H}{dt} = \rho c r^2 \frac{\partial T}{\partial t} \quad (1)$$

where r is the local radius, T is the temperature of the sphere, ρ is density, and t is time. The second term in Eq. (1) provides a time-dependent but spatially uniform variation of the applied field

which results in a volumetric heating effect that is either positive or negative, depending on whether the magnetic field ($\mu_0 H$) is increasing or decreasing, respectively. The magnetic field is assumed to vary sinusoidally from 0 to a maximum value, $\mu_0 H_{\max}$:

$$\mu_0 H = \frac{\mu_0 H_{\max}}{2} \left[1 - \cos \left(\frac{2\pi t}{\tau} \right) \right] \quad (2)$$

where τ is the total duration of the cycle. The rate of change of the magnetic field is

$$\frac{d\mu_0 H}{dt} = \frac{\pi \mu_0 H_{\max}}{\tau} \sin \left(\frac{2\pi t}{\tau} \right) \quad (3)$$

Substituting Eq. (3) into Eq. (1) leads to

$$k \frac{\partial}{\partial r} \left[r^2 \frac{\partial T}{\partial r} \right] - Tr^2 \rho \left(\frac{\partial s}{\partial \mu_0 H} \right)_T \frac{\pi \mu_0 H_{\max}}{\tau} \sin \left(\frac{2\pi t}{\tau} \right) = \rho c r^2 \frac{\partial T}{\partial t} \quad (4)$$

In the limit of a near room temperature system, the absolute temperature that multiplies the second term in Eq. (4) can be assumed to be nearly constant (the fluctuation in temperature is small relative to the absolute temperature) so Eq. (4) may be rewritten approximately as

$$k \frac{\partial}{\partial r} \left[r^2 \frac{\partial T}{\partial r} \right] - \bar{T}_f r^2 \rho \left(\frac{\partial s}{\partial \mu_0 H} \right)_T \frac{\pi \mu_0 H_{\max}}{\tau} \sin \left(\frac{2\pi t}{\tau} \right) = \rho c r^2 \frac{\partial T}{\partial t} \quad (5)$$

where \bar{T}_f is the average fluid temperature. In this same limit, the amplitude of the adiabatic temperature change (ΔT_a) induced by the change in the applied field is approximately equal to

$$\Delta T_a = \left(\frac{\partial s}{\partial \mu_0 H} \right)_T \frac{\mu_0 H_{\max} \bar{T}_f}{2c} \quad (6)$$

Equation (5) can be rewritten in terms of the adiabatic temperature change, which is the characteristic temperature difference associated with an active, magnetocaloric process

$$k \frac{\partial}{\partial r} \left[r^2 \frac{\partial T}{\partial r} \right] - \Delta T_a \rho c r^2 \frac{2\pi}{\tau} \sin \left(\frac{2\pi t}{\tau} \right) = \rho c r^2 \frac{\partial T}{\partial t} \quad (7)$$

For a passive process, the magnetocaloric heating term drops out

$$k \frac{\partial}{\partial r} \left[r^2 \frac{\partial T}{\partial r} \right] = \rho c r^2 \frac{\partial T}{\partial t} \quad (8)$$

The boundary condition at the outer radius of the sphere ($r=R$) balances conduction with convection

$$-k \left. \frac{\partial T}{\partial r} \right|_{r=R,t} = h [T(r=R,t) - T_f] \quad (9)$$

where T_f is the temperature of the fluid. To simulate a passive process, the temperature of the fluid is allowed to vary sinusoidally according to

$$T_f(t) = \bar{T}_f + \Delta T_f \sin \left(\frac{2\pi t}{\tau} \right) \quad (10)$$

where ΔT_f , the amplitude of the fluid temperature oscillation, is the characteristic temperature difference associated with the passive regenerator process. For an active process, the fluid temperature is assumed to be constant

$$T_f(t) = \bar{T}_f \quad (11)$$

The temperature gradient at the center must be zero

$$\left. \frac{\partial T}{\partial r} \right|_{r=0,t} = 0 \quad (12)$$

Finally, the sphere must undergo a steady-state cycle so that

$$T(r, t = 0) = T(r, t = \tau) \quad (13)$$

These equations are made dimensionless by defining a reduced position (\tilde{r}) and reduced time (\tilde{t}):

$$\tilde{r} = \frac{r}{R} \quad (14)$$

$$\tilde{t} = \frac{t}{\tau} \quad (15)$$

The reduced temperature (θ) is defined based either on the adiabatic temperature change or the fluid temperature oscillation, depending on whether an active or passive process is being considered

$$\theta = \frac{T - \bar{T}_f}{\Delta T_a} \quad \text{or} \quad \theta = \frac{T - \bar{T}_f}{\Delta T_f} \quad (16)$$

The Fourier number (Fo) is defined according to

$$Fo = \frac{k\tau}{\rho c R^2} \quad (17)$$

The Biot number (Bi) is defined according to

$$Bi = \frac{hR}{k} \quad (18)$$

The nondimensional governing equation for the active process becomes

$$\frac{Fo}{\tilde{r}^2} \frac{\partial}{\partial \tilde{r}} \left[\tilde{r}^2 \frac{\partial \theta}{\partial \tilde{r}} \right] - 2\pi \sin(2\pi \tilde{t}) = \frac{\partial \theta}{\partial \tilde{t}} \quad (19)$$

with the outer surface boundary condition

$$-\frac{\partial \theta}{\partial \tilde{r}} \Big|_{\tilde{r}=1, \tilde{t}} = Bi \theta(\tilde{r}=1, \tilde{t}) \quad (20)$$

The nondimensional governing equation for the passive process becomes

$$\frac{Fo}{\tilde{r}^2} \frac{\partial}{\partial \tilde{r}} \left[\tilde{r}^2 \frac{\partial \theta}{\partial \tilde{r}} \right] = \frac{\partial \theta}{\partial \tilde{t}} \quad (21)$$

with the outer surface boundary condition

$$-\frac{\partial \theta}{\partial \tilde{r}} \Big|_{\tilde{r}=1, \tilde{t}} = Bi[\theta(\tilde{r}=1, \tilde{t}) - \sin(2\pi \tilde{t})] \quad (22)$$

In either case, the remaining boundary conditions are

$$\frac{\partial \theta}{\partial \tilde{r}} \Big|_{\tilde{r}=0, \tilde{t}} = 0 \quad (23)$$

and

$$\theta(\tilde{r}, \tilde{t}=0) = \theta(\tilde{r}, \tilde{t}=1) \quad (24)$$

Numerical Solution

The solution to the governing equations is obtained over a grid that extends from 0 to 1 in reduced position with m spatial steps and from 0 to 1 in reduced time with n time steps

$$\tilde{r}_i = \frac{(i-1)}{(m-1)} \quad i = 1 \dots m \quad (25)$$

$$\tilde{t}_j = \frac{(j-1)}{(n-1)} \quad j = 1 \dots n \quad (26)$$

The reduced spatial and temporal step size ($\Delta \tilde{r}$ and $\Delta \tilde{t}$, respectively) are given by

$$\Delta \tilde{r} = \frac{1}{(m-1)} \quad (27)$$

$$\Delta \tilde{t} = \frac{1}{(n-1)} \quad (28)$$

The discretized form of the dimensionless governing equation is

$$Fo \left[\frac{\theta_{i+1,j} + \theta_{i-1,j} - 2\theta_{i,j}}{\Delta \tilde{r}^2} + \frac{1}{\tilde{r}_i} \frac{(\theta_{i+1,j} - \theta_{i-1,j})}{\Delta \tilde{r}} \right] - 2\pi \sin(2\pi \tilde{t}) = \frac{\theta_{i,j} + \theta_{i,j-1}}{\Delta \tilde{t}} \quad \text{for } i = 2 \dots (m-1) \text{ and } j = 2 \dots n \quad (29)$$

and the boundary condition at the surface for the active process leads to

$$-\frac{(\theta_{m,j} - \theta_{m-1,j})}{\Delta \tilde{r}} = Bi \theta_{m,j} \quad \text{for } j = 2 \dots n \quad (30)$$

For the passive case, the discretized governing equation and external surface boundary condition are

$$Fo \left[\frac{\theta_{i+1,j} + \theta_{i-1,j} - 2\theta_{i,j}}{\Delta \tilde{r}^2} + \frac{1}{\tilde{r}_i} \frac{(\theta_{i+1,j} - \theta_{i-1,j})}{\Delta \tilde{r}} \right] = \frac{\theta_{i,j} + \theta_{i,j-1}}{\Delta \tilde{t}} \quad \text{for } i = 2 \dots (m-1) \text{ and } j = 2 \dots n \quad (31)$$

$$-\frac{(\theta_{m,j} - \theta_{m-1,j})}{\Delta \tilde{r}} = Bi \theta_{m,j} - Bi \sin(2\pi \tilde{t}_j) \quad \text{for } j = 2 \dots n \quad (32)$$

The temperature gradient at the center of the sphere is zero, which leads to

$$\theta_{1,j} - \theta_{2,j} = 0 \quad \text{for } j = 2 \dots n \quad (33)$$

Steady state is specified by

$$\theta_{i,1} = \theta_{i,n} \quad \text{for } i = 1 \dots m \quad (34)$$

Equations (29)–(34) are solved using a sparse matrix decomposition algorithm.

Verification of Model

The numerical model can be verified in the passive limit by comparison with the analytical solution presented by Carslaw and Jaeger [15] for a sphere subjected to a sinusoidal fluid temperature. Neglecting the terms in the analytical solution that disappear at long times (i.e., the noncyclic terms)

$$\theta = \frac{Bi A_1}{\tilde{r} A_2} \sin(2\pi \tilde{t} + \phi_1 - \phi_2) \quad (35)$$

where

$$A_1 \exp(i\phi_1) = \sinh \left[\sqrt{\frac{\pi}{Fo}} \tilde{r} \right] \cos \left[\sqrt{\frac{\pi}{Fo}} \tilde{r} \right] + i \cosh \left[\sqrt{\frac{\pi}{Fo}} \tilde{r} \right] \sin \left[\sqrt{\frac{\pi}{Fo}} \tilde{r} \right] \quad (36)$$

$$A_2 \exp(i\phi_2) = \sqrt{\frac{\pi}{Fo}} (1+i) \cosh \left[\sqrt{\frac{\pi}{Fo}} (1+i) \right] + (Bi-1) \sinh \left[\sqrt{\frac{\pi}{Fo}} (1+i) \right] \quad (37)$$

Figure 1 illustrates the dimensionless temperature as a function of \tilde{t} for various values of \tilde{r} at $Bi=2.5$ and $Fo=0.25$ predicted by the numerical model and by Eqs. (35) and (37).

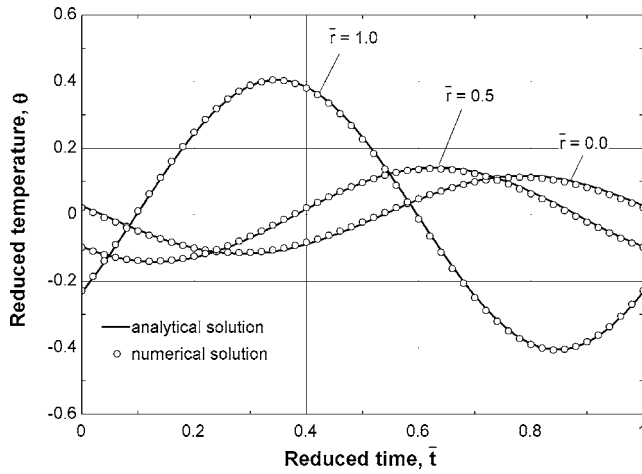


Fig. 1 Reduced temperature as a function of reduced time for various values of reduced radius with $Bi=2.5$ and $Fo=0.25$

The analytical and numerical results converge to within 0.01% for all m greater than 200 and n greater than 100 under the conditions shown in Fig. 1. The results presented in this paper use 250 spatial steps and 150 temporal steps.

Results for a Passive Regenerator

The energy stored in the sphere (U) in the passive limit is given by

$$U(t) = \rho c \int_0^R 4\pi r^2 [T(r,t) - \bar{T}_f] dr \quad (38)$$

The maximum possible energy that can be stored in the sphere during one cycle (ΔU_{\max}) occurs if the sphere temperature is spatially uniform and varies from $-\Delta T_f$ to $+\Delta T_f$. This is the limiting case for a perfect regenerator in which the conductivity and heat transfer coefficient are large ($h \rightarrow \infty$ and $k \rightarrow \infty$). This limit occurs when Fo and the $Fo Bi$ product are both large.

$$\Delta U_{\max} = \rho c \frac{8}{3} \pi R^3 \Delta T_f \quad (39)$$

The dimensionless stored energy (\tilde{U}) is the ratio of the instantaneous stored energy to the maximum possible stored energy and given by

$$\tilde{U}(\tilde{t}) = \frac{3}{2} \int_0^1 \tilde{r}^2 \theta(\tilde{r}, \tilde{t}) d\tilde{r} \quad (40)$$

The performance of the regenerator relative to this maximum possible limit is referred to as the total efficiency of the sphere (η) and is given by

$$\eta = \max[\tilde{U}(\tilde{t})] - \min[\tilde{U}(\tilde{t})] \quad \text{for } 0 \leq \tilde{t} \leq 1 \quad (41)$$

Figure 2 illustrates the total sphere efficiency as a function of the product of the Biot number and Fourier number for various values of the Fourier number. Note that the Biot Fourier number product

$$Bi Fo = \frac{\pi h}{\rho c R} \quad (42)$$

is proportional to the ratio of the cycle period to the time constant associated with the sphere if it were spatially uniform in temperature (i.e., if it were treated as a lumped capacitance). The lumped capacitance limit is consistent with the sphere having an infinite thermal conductivity and therefore, this limit represents the typical modeling assumption for a one-dimensional regenerator model (i.e., the regenerator matrix is assumed locally to be at a uniform temperature); the impact of the surface to time-varying fluid tem-

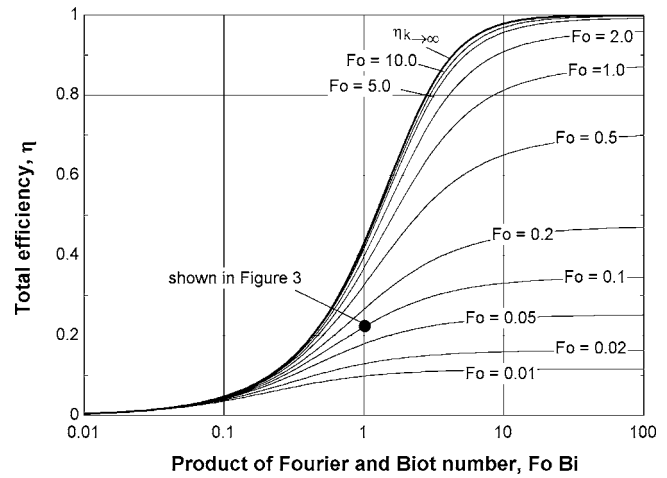


Fig. 2 Total efficiency as a function of $Fo Bi$ for various values of Fo . Also shown is the efficiency in the limit of infinite thermal conductivity.

perature difference associated with a finite heat transfer coefficient is considered, but the temperature gradients internal to the sphere (induced by the finite thermal conductivity of the sphere) are ignored in this limit. The temperature of the sphere in this infinite conductivity limit ($\theta_{k \rightarrow \infty}$) is given by

$$\theta_{k \rightarrow \infty}(\tilde{t}) = \frac{\sin(2\pi\tilde{t} - \phi)}{\sqrt{1 + \left(\frac{2\pi}{3 Bi Fo}\right)^2}} \quad (43)$$

where

$$\phi = \tan^{-1} \left[\frac{2\pi}{Bi Fo} \right] \quad (44)$$

Substituting Eq. (43) into Eq. (40) leads to

$$\tilde{U}_{k \rightarrow \infty}(\tilde{t}) = \frac{\sin(2\pi\tilde{t} - \phi)}{2\sqrt{1 + \left(\frac{2\pi}{3 Bi Fo}\right)^2}} \quad (45)$$

and therefore the total efficiency of the infinite conductivity particle ($\eta_{k \rightarrow \infty}$) is

$$\eta_{k \rightarrow \infty} = \frac{1}{\sqrt{1 + \left(\frac{2\pi}{3 Bi Fo}\right)^2}} \quad (46)$$

The total efficiency of the infinite conductivity particle is also shown in Fig. 2; note that the large Fourier number results approach this infinite conductivity limit. The Fourier number is a function of the ratio of the cycle period to the time required for a thermal wave to penetrate to the center of the sphere. When the Fourier number is large, therefore, the conductivity is sufficiently high such that the entire particle participates in the energy storage process and the efficiency is not affected by the thermal conductivity. On the other hand, when the Fourier number is small, the thermal wave does not penetrate significantly into the sphere and only the outer surface participates in the process. This behavior is shown in Fig. 3, which illustrates the reduced temperature as a function of reduced position at various values of reduced time for a small Fourier number ($Fo=0.1$) and $Fo Bi=1.0$.

One method that has been suggested and widely used to approximately correct for the finite conductivity of regenerator material is presented by Jeffreson [4]; the heat transfer coefficient is modified based on the Biot number, which represents the ratio of the resistance to conduction to the resistance to convection from

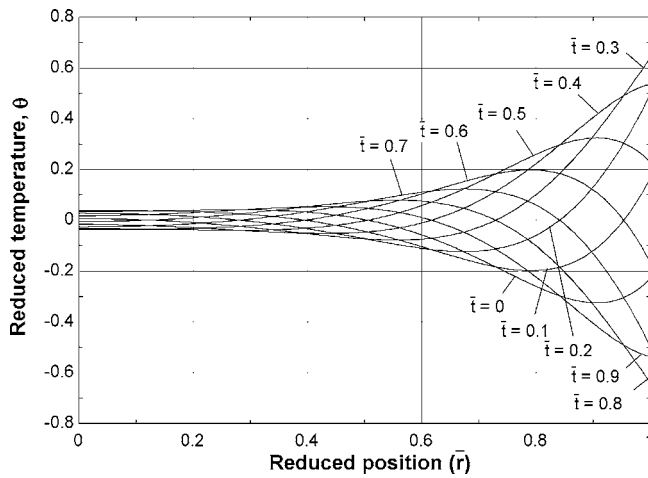


Fig. 3 Reduced temperature as a function of \bar{r} for various values of \bar{t} for $Fo=0.1$ and $FoBi=1.0$. Note that the cycle time is insufficient to allow the entire sphere to participate in the energy storage process and so only the outer edge temperature is affected by the fluid.

the surface. The Jefferson correction factor is derived by assuming a uniform and steady volumetric generation throughout the material in order to determine the temperature distribution. The temperature distribution is subsequently integrated in order to determine the elevation of the volume-weighted average temperature relative to the surface temperature. Finally, the reduction in the heat transfer coefficient that would be required to achieve the same increase in temperature in the limit of a perfectly conducting sphere is determined. The fractional reduction in the heat transfer coefficient is referred to here as a degradation factor (DF)

$$h^* = DF h \quad (47)$$

where h^* is the corrected heat transfer coefficient. The degradation factor derived by Jefferson for a spherical particle is

$$DF_J = \frac{1}{1 + \frac{Bi}{5}} \quad (48)$$

Hausen [5] presents a degradation factor for a balanced-flow regenerator that is based on Biot number and Fourier number and can be expressed as

$$DF_H = \frac{1}{1 + \frac{Bi}{5} \phi_H} \quad (49)$$

where

$$\phi_H = 1 - \frac{4}{35 Fo} \quad Fo \geq 0.4$$

$$\phi_H = \frac{5\pi}{\sqrt{27 + \frac{72}{Fo}}} \quad Fo < 0.4 \quad (50)$$

The corrected heat transfer coefficient using either the Jefferson or Hausen degradation factor is therefore less than the actual heat transfer coefficient h by an amount that grows with increasing Biot number and (for the Hausen degradation factor) decreasing Fourier number. Applying the degradation factor concept to the infinite conductivity efficiency leads to a corrected efficiency (η_c):

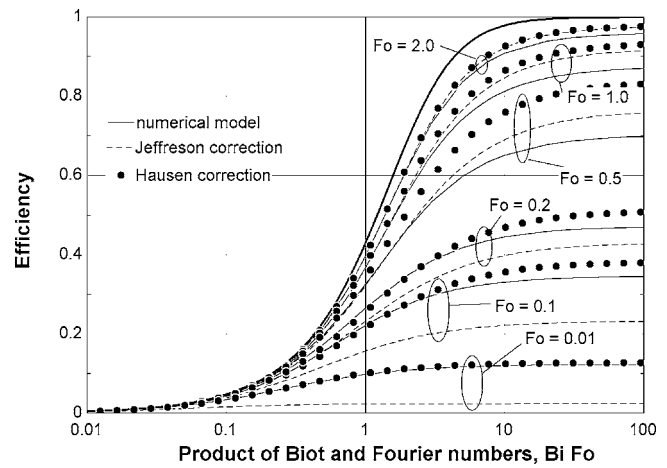


Fig. 4 Efficiency predicted by the numerical model and using lumped capacitance model corrected with the Jefferson and Hausen degradation factor. Efficiency is shown as a function of the product of the Biot and Fourier number for various values of the Fourier number.

$$\eta_c = \frac{1}{\sqrt{1 + \left[\frac{2\pi}{3 Bi Fo DF} \right]^2}} \quad (51)$$

The corrected efficiency based on the Jefferson correlation (η_J) is obtained by substituting Eq. (48) into Eq. (51):

$$\eta_J = \frac{1}{\sqrt{1 + \left[\frac{2\pi}{3 Bi Fo} \left(1 + \frac{Bi Fo}{5 Fo} \right) \right]^2}} \quad (52)$$

and the corrected efficiency based on the Hausen correction factor is

$$\eta_H = \frac{1}{\sqrt{1 + \left[\frac{2\pi}{3 Bi Fo} \left(1 + \frac{Bi Fo}{5 Fo} \phi_H \right) \right]^2}} \quad (53)$$

The corrected efficiencies based on the Jefferson and Hausen correlations and the actual efficiencies are shown in Fig. 4 as a function of $Fo Bi$ for various values of Fo . Note that both the Jefferson and Hausen corrections provide significantly improved predictions relative to the infinite conductivity limit. However, the corrected efficiency using the Jefferson correction does not match the efficiency predicted by the numerical model because it does not depend on Fo and the efficiency using the Hausen correction does not match numerical model because it is only an approximate correction based on a particular operating condition.

It is not surprising that the Jefferson correction factor, which is based on a steady state concept, does not completely represent the transient phenomena that are occurring in a regenerator. The correction factor was implicitly based on the assumption that the entire sphere participates in the energy storage process whereas Fig. 3 shows that as Fo decreases, only the outer layer participates. However, a degradation correction factor provides a technique that may be used to easily and quickly modify the heat transfer coefficient used in a one-dimensional model and therefore, this concept is very valuable; Eq. (51) may be solved for the degradation factor that forces the corrected efficiency to exactly match the actual efficiency:

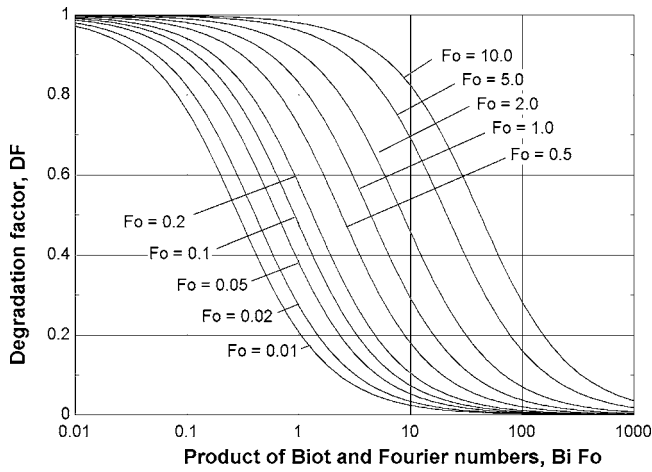


Fig. 5 Degradation factor predicted by the numerical model as a function of the product of the Biot and Fourier number for various values of the Fourier number

$$DF = \frac{\left(\frac{2\pi}{3 Bi Fo}\right)}{\sqrt{\frac{1}{\eta^2} - 1}} \quad (54)$$

Figure 5 illustrates the degradation factor as a function of the Biot Fourier number product for various values of the Fourier number. The information presented in Fig. 5 is sufficient to correct a one-dimensional passive regenerator model for internal temperature gradients; the Fourier number and Biot number that characterize the bed and operating conditions should be calculated and used to determine the degradation factor that may subsequently be applied to the heat transfer coefficient.

Using a degradation factor that has the same form suggested by Hausen leads to

$$DF = \frac{1}{1 + \frac{Bi}{5}\chi(Fo)} \quad (55)$$

where χ is a function of the Fourier number that is obtained by empirically fitting the data shown in Fig. 5:

$$\chi(Fo) = Fo \exp[0.246196 - 0.84878 \ln(Fo) - 0.05639(\ln(Fo))^2] \quad (56)$$

The efficiency based on the corrected degradation factor and the efficiency calculated by the numerical model are both shown in Fig. 6. Note the good agreement over a wide range of Fourier number and Biot number.

Results for an Active Magnetic Regenerator

The sphere in a magnetic regenerator is subjected to a volumetric process that is driven by the variation in the magnetic field. In the absence of any communication with the environment, the sphere temperature will fluctuate with an amplitude that is determined by the adiabatic magnetization temperature difference. Figure 7(a) illustrates the reduced temperature in the sphere as a function of reduced time for a situation in which the sphere experiences relatively poor thermal communication with its surroundings but high internal conductivity ($Bi=0.2$ and $Fo=5.0$). Note that the sphere is at a nearly spatially uniform dimensionless temperature which oscillates between -1.0 and 1.0 during the cycle. Figure 7(b) illustrates the situation when the communication with the environment is improved and the internal conductivity is still high ($Bi=5.0$ and $Fo=5.0$); note that the sphere remains at essen-

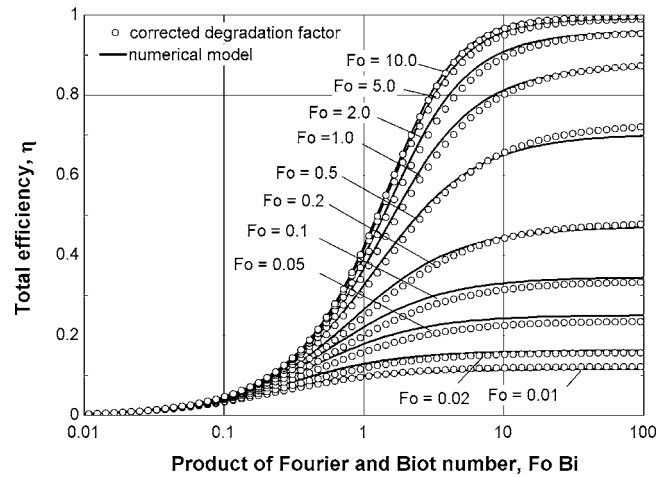


Fig. 6 Total efficiency computed using the corrected degradation factor presented in Eqs. (55) and (56) and predicted by the numerical model as a function of the product of the Biot and Fourier number for various values of the Fourier number

tially a spatially uniform temperature but the amplitude of the oscillations is reduced as the material is able to transfer more energy to and from its surroundings. Finally, Fig. 7(c) illustrates the situation when the communication with the environment is high but the internal conductivity is poor ($Bi=5.0$ and $Fo=0.2$) so that the material very near the surface remains near the surrounding fluid temperature (a reduced temperature of 0.0) whereas the temperature near the center internally fluctuates between -1.0 and 1.0 as in Fig. 7(a).

The efficiency of the sphere undergoing a magnetic process must be defined differently than in the passive case. The objective of a magnetic refrigeration process is to convert the magnetically driven volumetric heating/cooling into a heat transfer to/from the fluid; Figs. 7(a) and 7(c) show that this process is inhibited by either a low convection coefficient or poor internal conduction. The figure of merit that is most appropriate for this process is the average rate of heat transfer between the fluid and the particle during a cycle (\bar{Q}):

$$\bar{Q} = \frac{4\pi h R^2}{\tau} \int_0^\tau |T(r=R, t) - \bar{T}_f| dt \quad (57)$$

The maximum heat transfer rate occurs if the sphere is infinitely conductive and the heat transfer coefficient is infinite, in which case the temperature of the material is always at the fluid temperature. The heat transfer rate in this limit (\dot{Q}_{\max}) is

$$\dot{Q}_{\max} = \bar{T}_f \left(\frac{\partial s}{\partial \mu_0 H} \right)_T \frac{4\pi R^3}{3} \rho \frac{\pi \mu_0 H_{\max}}{\tau} \sin\left(\frac{2\pi t}{\tau}\right) \quad (58)$$

Substituting the definition of the adiabatic temperature change into Eq. (58) leads to

$$\dot{Q}_{\max} = \frac{8\pi R^3}{3} \rho c \frac{\pi}{\tau} \Delta T_a \sin\left(\frac{2\pi t}{\tau}\right) \quad (59)$$

The maximum, average rate of heat transfer is obtained by integrating Eq. (59) over a half-cycle

$$\bar{Q}_{\max} = \frac{16\pi R^3}{3\tau} \rho c \frac{\pi}{\tau} \Delta T_a \int_0^{\tau/2} \sin\left(\frac{2\pi t}{\tau}\right) dt \quad (60)$$

or

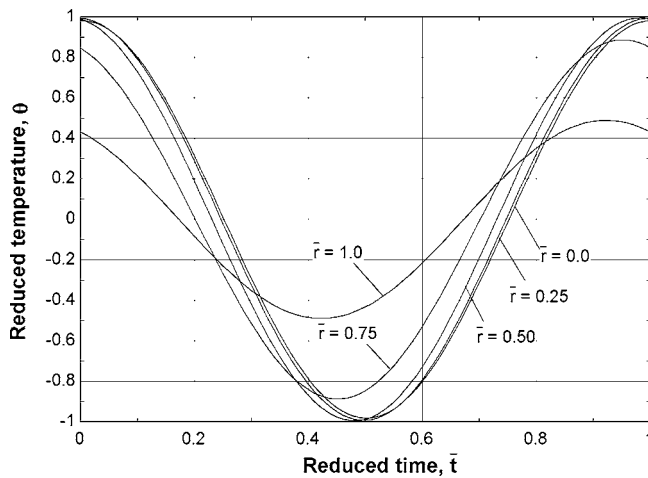
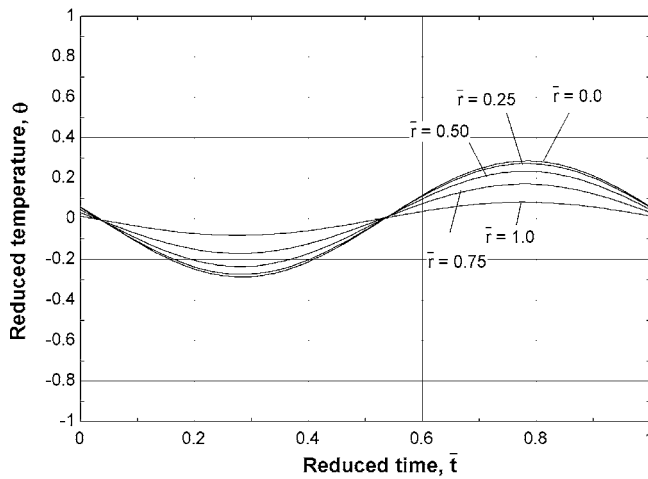
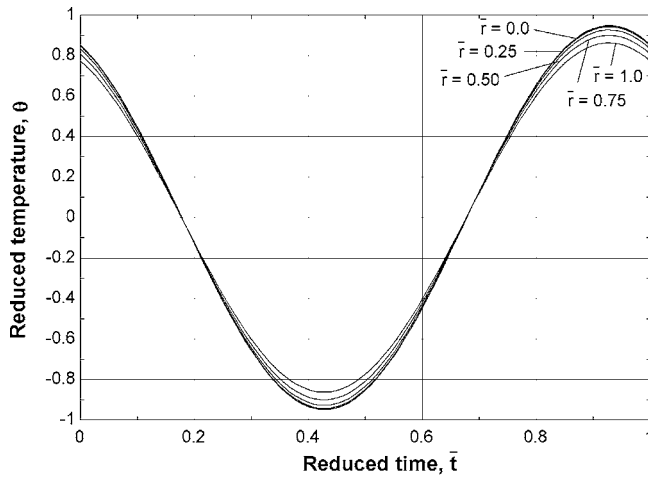


Fig. 7 Reduced temperature as a function of reduced time for various values of reduced radius for a sphere with (a) $Bi=0.2$, $Fo=5.0$, (b) $Bi=5.0$, $Fo=5.0$, and (c) $Bi=5.0$, $Fo=0.2$

$$\bar{Q}_{\max} = \frac{16\pi R^3}{3\tau} \rho c \Delta T_a \quad (61)$$

The efficiency for the active process is defined as the ratio of the actual to the maximum possible average heat transfer (η):

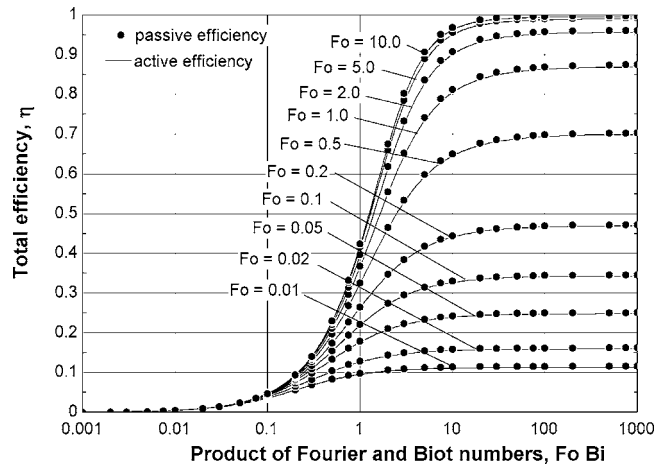


Fig. 8 Total efficiency for the active and passive processes as a function of the product of the Biot and Fourier number for various values of the Fourier number. Note that the behavior of these processes is identical when normalized in this manner.

$$\eta = \frac{\bar{Q}}{\bar{Q}_{\max}} \quad (62)$$

Substituting Eqs. (57) and (61) into Eq. (62) leads to

$$\eta = \frac{3h\tau}{4R\rho c} \int_0^1 |\theta(\bar{r}=1, \bar{\tau})| d\bar{\tau} = \frac{3}{4} Bi Fo \int_0^1 |\theta(\bar{r}=1, \bar{\tau})| d\bar{\tau} \quad (63)$$

Figure 8 illustrates the efficiency as a function of the Fourier Biot number product for various values of the Fourier number. Notice that Fig. 8 is very similar to Fig. 2 which shows efficiency of the passive process; overlaid on Fig. 8 are the efficiency curves for the passive case which shows the mathematical similarity that underlies these two processes. The degradation factor derived for the passive case and presented in Eqs. (55) and (56) can therefore be applied to the active case without modification.

Impact of Type of Time Variation

The degradation factor equations and previous results were obtained for a sinusoidal variation in temperature or applied field. In a real regenerator, the variation of fluid temperature (or magnetic field) is more complex and depends on the working fluid flow rate as well as the behavior of the rest of the bed. It is therefore interesting to evaluate the sensitivity of the regenerator sphere behavior to the functional form of the variation in its external environment. This investigation is carried out using the passive model; however, the same techniques could be applied to an active process using the appropriate reduced parameters. For the passive case, sinusoidal variation in external fluid temperature is changed to a step function by altering Eq. (32):

$$-\frac{(\theta_{m,j} - \theta_{m-1,j})}{\Delta\bar{\tau}} = Bi \theta_{m,j} - Bi \left(\text{sign} \left[\bar{\tau}_j - \frac{1}{2} \right] \right) \quad \text{for } j = 2 \dots n \quad (64)$$

where sign is the signum function which returns 1 if the argument is greater than zero and -1 otherwise. The efficiency of the process is defined by Eq. (41) as before. Figure 9 illustrates the efficiency of the passive process with a sinusoidal and stepwise temperature change as a function of the Fourier Biot number product for various values of the Fourier number. Note that the qualitative behavior is the same but, for a given Fourier number and Biot number, the stepwise change in temperature will result in a higher efficiency than the more gradual, sinusoidal variation. This behav-

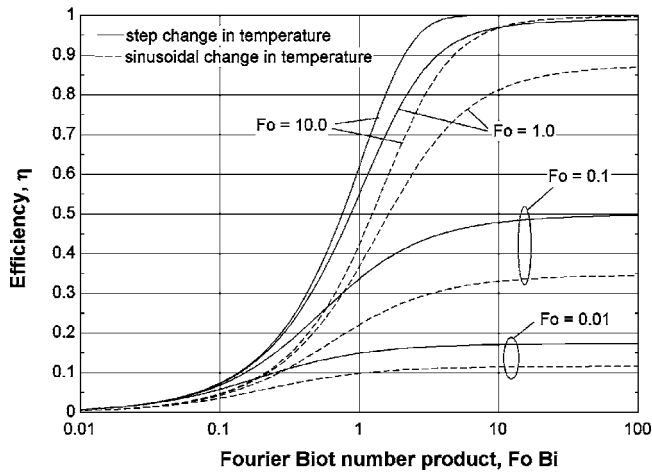


Fig. 9 Total efficiency for the passive process with a sinusoidal and step-wise variation in the fluid temperature as a function of the product of the Biot and Fourier number for various values of the Fourier number. Note that the efficiency of the step-wise variation is always higher than the sinusoidal variation due to the larger fluid-to-surface temperature difference.

ior is understandable because the sphere is exposed to a higher (or lower) temperature for a longer time and therefore has more opportunity to transfer heat.

The results shown in Fig. 9 suggest that the definition of the cycle time (τ) alone may be inadequate in terms of characterizing the effective, thermal time available for the process. Rather, an effective cycle time (τ_{eff}) that is weighted by the instantaneous fluid temperature elevation is more appropriate

$$\tau_{\text{eff}} = \frac{\pi}{2\Delta T} \int_0^{\tau} |T_f(t) - \bar{T}_f| dt \quad (65)$$

Therefore, the effective cycle time for the sinusoidal variation is the period ($\tau_{\text{eff}} = \tau$) and so the effective Fourier number remains unchanged. On the other hand, the effective cycle time for a step-wise variation is higher than the cycle period due to the higher fluid temperature elevation relative to its average value ($\tau_{\text{eff}} = \pi\tau/2$) and so the effective Fourier number should be increased by nominally 57% when computing the degradation factor in order to account for the increased exposure to a high temperature difference. Other variations can be considered as well; for example, the effective cycle time associated with a linear variation in fluid temperature is $\tau_{\text{eff}} = \pi\tau/4$ and therefore the effective Fourier number associated with a linear variation should be reduced by nominally 22% in order to account for the reduced exposure to a high temperature difference.

Figure 10 illustrates the efficiency as a function of the Fourier Biot number product for a sphere that is exposed to a sinusoidal, step-wise, and linear ramp temperature variation, all with $Fo = 0.1$. Note that, as expected, the sphere exposed to the step-wise temperature variation is characterized by the highest efficiency whereas the one exposed to the linear temperature variation has the lowest. However, the “effective Fourier number” for the step-wise process is 0.157 and for the linear process is 0.0785. Figure 10 shows that the behavior of a sinusoidal process at these values of the Fourier number more closely approaches the behavior of the step-wise and linear processes, respectively.

Empirically, it has been observed that modifying Eq. (65) so that the effective cycle time is computed using the cycle time weighted by the square of the temperature difference provides a more accurate means of correcting for nonsinusoidal time variations in the driving temperature difference

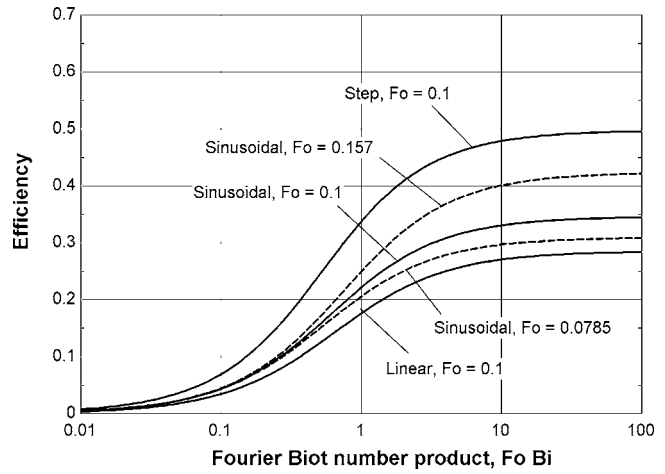


Fig. 10 Total efficiency for a sinusoidal, step-wise, and linear variation all with $Fo = 0.1$ as a function of the product of the Biot and Fourier number. Also shown are the total efficiency of sinusoidal processes with $Fo = 0.157$ and $Fo = 0.0785$ which are the appropriate effective Fourier numbers to characterize the step-wise and linear processes, respectively. Note that the sinusoidal processes with appropriately modified Fourier number more closely match the behavior of the nonsinusoidal variations.

$$\tau_{\text{eff}} = \frac{\pi^2}{4\Delta T^2} \int_0^{\tau} |T_f(t) - \bar{T}_f|^2 dt \quad (66)$$

Therefore, the effective Fourier number for a step-wise variation in the fluid temperature would be $(\pi/2)^2$ higher (nominally $2.46 \times$) that of a sinusoidal variation with the same period, and a linear variation in the fluid temperature would be $(\pi/4)^2$ higher (nominally $0.62 \times$) that of a sinusoidal variation with the same period. This correction provides good agreement over a wide range of Biot number, Fourier number, and time variations. Figure 11 illustrates the efficiency associated with a passive process in which the fluid temperature varies in a step-wise manner as a function of the Fourier Biot number product for various Fourier numbers. Also shown in Fig. 11 is the efficiency of a passive process in which the variation is sinusoidal but the Fourier number has been in-

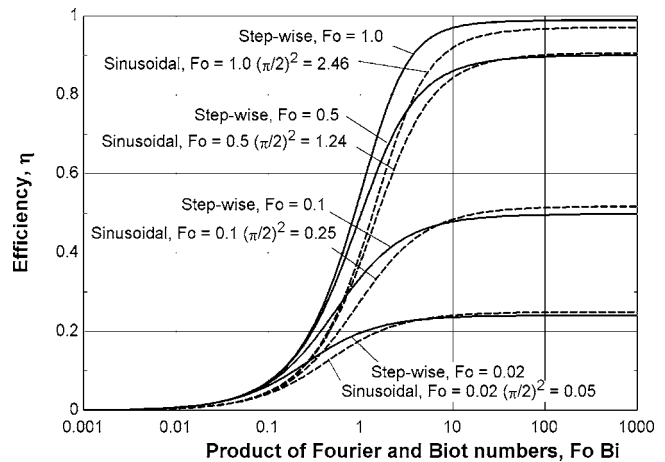


Fig. 11 Total efficiency for step-wise variation as a function of the product of the Biot and Fourier number for various values of Fo . Also shown are the total efficiency of sinusoidal processes with the Fo modified according to Eq. (66). Note that the sinusoidal processes with appropriately modified Fourier number closely match the behavior of the nonsinusoidal variations.

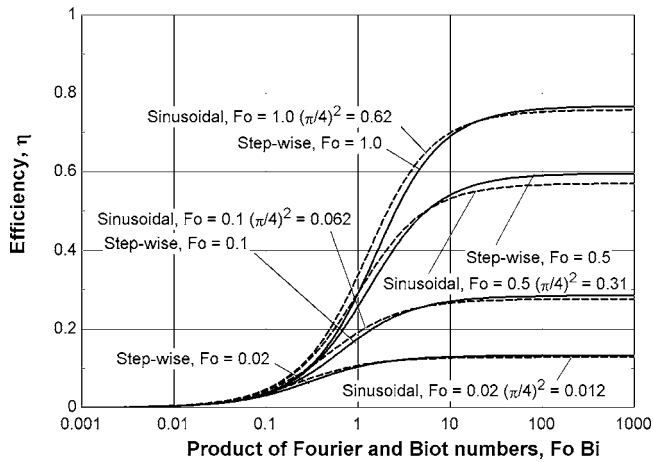


Fig. 12 Total efficiency for a linear variation as a function of the product of the Biot and Fourier number for various values of Fo . Also shown are the total efficiency of sinusoidal processes with the Fo modified according to Eq. (66). Note that the sinusoidal processes with appropriately modified Fourier number closely match the behavior of the nonsinusoidal variations.

creased by a factor of $(\pi/2)^2$, as indicated by Eq. (66). Note that, with this corrected cycle time, the sinusoidal process exhibits behavior that is consistent with the step-wise process.

The equivalent cycle time works equally well for other variations. For example, Fig. 12 illustrates the efficiency associated with a passive process in which the fluid temperature varies linearly as a function of the Fourier Biot number product for various Fourier numbers. Also shown in Fig. 12 is the efficiency of a passive process in which the variation is sinusoidal but the Fourier number has been decreased by a factor of $(\pi/4)^2$; again, note that the corrected sinusoidal process exhibits behavior that is consistent with the linear process.

Figures 11 and 12 suggest that it is possible to approximately account for nonsinusoidal variations in the driving temperature using the degradation factors derived previously for sinusoidal processes provided that the Fourier number is based on a cycle time that is weighted by the driving temperature difference squared, as computed using Eq. (66).

Conclusions

The impact of the temperature gradients that occur within a passive or active regenerator matrix may become important as the regenerator material conductivity decreases, the regenerator to fluid heat transfer coefficient increases, or the operating frequency increases. All of these limits are being pushed in various ways by advanced regenerator materials and regenerative cycles in both passive and active systems. In order to explicitly account for the internal temperature gradients, a regenerative cycle model would require a two-dimensional transient model that is, in most cases, computationally prohibitive. Therefore, a one-dimensional transient model of a single regenerator sphere undergoing an idealized passive and active regenerative process has been developed in order to evaluate the impact of the internal temperature gradients and their effect on the performance of the sphere in the context of a regenerative cycle. The model results were verified against an analytical model in an appropriate limit and subsequently used to evaluate the variation of the sphere efficiency, defined in terms of the material's participation in the cycle process, as a function of the Fourier and Biot numbers. The validity of previously published correction factors for one-dimensional models was evaluated. A Fourier number based correction factor was derived that can be applied to one-dimensional regenerative cycle results in order to account for the transient performance of the material with

finite thermal conductivity. The result is shown to be applicable over a wide range of Fourier and Biot number and applies equally well to both active and passive processes. Finally, the impact of a step-wise rather than sinusoidal variation of fluid temperature was evaluated. It was shown that nonsinusoidal variations could be approximately accounted for by modifying the Fourier number to account for the "effective" cycle time which should be defined as the cycle time weighted by the square of the average temperature difference between the fluid and the sphere.

Acknowledgment

Funding for this work by the Wisconsin Space Grant Consortium is greatly appreciated.

Nomenclature

$A_{1,2}$	= variable used in analytical solution
Bi	= Biot number, hR/k
c	= specific heat (J/kg K)
DF	= degradation factor
Fo	= Fourier number, $k\tau/\rho cR^2$
h	= heat transfer coefficient ($W/m^2 K$)
h^*	= corrected heat transfer coefficient ($W/m^2 K$)
k	= thermal conductivity ($W/m K$)
m	= number of spatial steps used in numerical solution
n	= number of time steps used in numerical solution
\dot{Q}	= heat transfer rate (W)
r	= radius (m)
\tilde{r}	= reduced position
R	= outer radius (m)
s	= entropy (J/kg K)
t	= time (s)
\tilde{t}	= reduced time
T	= temperature (K)
U	= internal energy (J/kg)

Greek Symbols

χ	= Fourier number correction factor
Δ	= change
$\Delta\tilde{r}$	= spatial step size
$\Delta\tilde{t}$	= temporal step size
ΔT_a	= adiabatic temperature changes due to magnetization (K)
$\phi_{1,2}$	= constant used for numerical solution
η	= total efficiency of sphere
$\mu_0 H$	= applied field (Tesla)
θ	= dimensionless temperature
ρ	= density (kg/m^3)
τ	= cycle duration (s)

Subscripts

c	= corrected
eff	= effective
f	= fluid
H	= Hausen
J	= Jeffreson
max	= maximum

References

- [1] Fujieda, S., Hasegawa, Y., Fujita, A., and Fukamichi, K., 2004, "Thermal Transport Properties of Magnetic Refrigerants $La(Fe_xSi_{1-x})$ and Their Hydrides, and $Gd_5Si_2Ge_2$ and $MnAs$," *J. Appl. Phys.*, **95**(5), pp. 2429–2431.
- [2] Numazawa, T., Kamiya, K., Satoh, T., Nozawa, H., and Yanagitani, T., 2005, "Status of the Development of Ceramic Regenerator Materials," *Proc. 13th Int. Cryocoolers Conf.*, pp. 373–380.
- [3] Engelbrecht, K., Nellis, G., and Klein, S., 2005, "A Numerical Model of an Active Magnetic Regenerator Refrigeration System," *Proc. 13th Int. Cryocool-*

- ers Conf.*, pp. 471–480.
- [4] Jeffreson, C. P., 1972, “Prediction of Breakthrough Curves in Packed Beds: I. Applicability of Single Parameter Models,” *AIChE J.*, **18**, pp. 409–416.
- [5] Hausen, H., 1983, *Heat Transfer in Counterflow, Parallel-Flow and Cross-Flow*, McGraw-Hill, New York.
- [6] Hinchcliffe, C., and Willmott, A. J., 1981, “Lumped Heat-Transfer Coefficients for Thermal Regenerators,” *Int. J. Heat Mass Transfer*, **24**(7), pp. 1229–1235.
- [7] Heggs, P. J., and Carpenter, K. J., 1979, “A Modification of the Thermal Regenerator Infinite Conduction Model to Predict the Effects of Intraconduction,” *Trans. Inst. Chem. Eng.*, **57**(4), pp. 228–236.
- [8] Heggs, P. J., Bansal, L. S., Bond, R. S., and Vazakas, V., 1980, “Thermal Regenerator Design Charts Including Intraconduction Effects,” *Trans. Inst. Chem. Eng.*, **58**(4), pp. 265–270.
- [9] Heggs, P. J., and Carpenter, K. J., 1978, “Prediction of a Dividing Line Between Conduction and Convection Effects in Regenerator Design,” *Trans. Inst. Chem. Eng.*, **56**(2), pp. 86–90.
- [10] Handley, D., and Heggs, P. J., 1968, “Momentum and Heat Transfer Mechanisms in Regular Shaped Packings,” *AIChE J.*, **46**(9), pp. T251–T263.
- [11] Bradshaw, A. V., Johnson, A., McLachlan, N. H., and Handley, , 1970, “Heat Transfer Between Air and Nitrogen and Packed Beds of Non-Reacting Solids,” *AIChE J.*, **48**(3), pp. T77–T84.
- [12] Heggs, P. J., and Sadrameli, M., 1992, “Prediction of the Lumped Heat Transfer Coefficient in Regenerators,” *ICHEME Symposium Series No. 129*, pp. 377–387.
- [13] Green, D. W., Perry, P. H., and Babcock, R. E., 1964, “Longitudinal Dispersion of Thermal Energy Through Porous Media with a Flowing Fluid,” *AIChE J.*, **10**(5), pp. 645–651.
- [14] San, J. Y., 1993, “Heat and Mass Transfer in a Two-Dimensional Cross-Flow Regenerator With a Solid Conduction Effect,” *Int. J. Heat Mass Transfer*, **36**(3), pp. 633–643.
- [15] Carslaw, H. S., and Jaeger, J. C., 1959, *Conduction of Heat in Solids*, 2nd Ed., Oxford University Press, New York, Chap. 9, p. 238.

Thermohydraulics of Laminar Flow Through Rectangular and Square Ducts With Transverse Ribs and Twisted Tapes

Debashis Pramanik

e-mail: debashis_pramanik@yahoo.co.in

Sujoy K. Saha¹

e-mail: sujoy_k_saha@hotmail.com

Mechanical Engineering Department,
Bengal Engineering and Science University,
Shibpur Howrah 711 103,
West Bengal, India

The heat transfer and the pressure drop characteristics of laminar flow of viscous oil through rectangular and square ducts with internal transverse rib turbulators on two opposite surfaces of the ducts and fitted with twisted tapes have been studied experimentally. The tapes have been full length, short length, and regularly spaced types. The transverse ribs in combination with full-length twisted tapes have been found to perform better than either ribs or twisted tapes acting alone. The heat transfer and the pressure drop measurements have been taken in separate test sections. Heat transfer tests were carried out in electrically heated stainless steel ducts incorporating uniform wall heat flux boundary conditions. Pressure drop tests were carried out in acrylic ducts. The flow was periodically fully developed in the regularly spaced twisted-tape elements case and decaying swirl flow in the short-length twisted tapes case. The flow characteristics are governed by twist ratio, space ratio, and length of twisted tape, Reynolds number, Prandtl number, rod-to-tube diameter ratio, duct aspect ratio, rib height, and rib spacing. Correlations developed for friction factor and Nusselt number have predicted the experimental data satisfactorily. The performance of the geometry under investigation has been evaluated. It has been found that on the basis of both constant pumping power and constant heat duty, the regularly spaced twisted-tape elements in specific cases perform marginally better than their full-length counterparts. However, the short-length twisted-tape performance is worse than the full-length twisted tapes. Therefore, full-length twisted tapes and regularly spaced twisted-tape elements in combination with transverse ribs are recommended for laminar flows. However, the short-length twisted tapes are not recommended. [DOI: 10.1115/1.2345432]

Keywords: forced convection, laminar flow, twisted tape, transverse ribs, heat transfer, augmentation, uniform wall heat flux

Introduction

Twisted tapes in their various forms are a useful heat transfer enhancement device [1–11]. The characteristic geometrical features of a twisted-tape are shown in Figs. 1(a) and 1(b).

The growth and structure of the tape-induced swirl in the laminar flow regime have been characterized by experimental flow visualization and computational simulations. The fully developed laminar swirl flows, which consist of two-asymmetrical counter-rotating helical vortices, have been shown to scale by a dimensionless swirl parameter defined on the basis of a primary force balance. The friction factor and Nusselt number correlations have been developed based on this scaling of the swirl behavior in the laminar flow regime.

Saha and Dutta [12] and Saha and Mallick [13] have shown experimentally that short-length twisted-tape performs worse than its full-length counterparts for laminar flow. Results of experimental and theoretical investigations of laminar flow heat transfer and pressure drop characteristics through a circular duct fitted with regularly spaced twisted-tape elements have been reported in [14–17]. Based on their experimental data, Saha and Mallick [13] have developed new correlations of friction factor and Nusselt number for regularly spaced twisted-tape elements in rectangular and square ducts.

Structured roughness, usually in the form of ribs, in both two-dimensional and discrete three-dimensional arrangements, has also been applied to plate type and rectangular channels [18–20]. Figure 1(c) shows transverse rib turbulators. Much of these works are directed toward compact heat exchangers and gas turbine cooling and regeneration systems. An interesting variation in the form of wedge- and delta-shaped ribs, which tend to produce longitudinal vortices in the near-wall region of the flow field, has been suggested by Han et al. [21]. Finally, as noted by Bergles [22], surface roughness is usually not considered in applications with free or natural convection. In this thermal-fluid transport regime, the buoyancy-induced fluid flow velocities are generally very low and are not easily disrupted by small-scale surface roughness so as to produce flow separation and recirculation (the primary mechanisms for roughness-induced enhancement).

As Bergles [23] has pointed out, “compound techniques offer a way to further elevate heat transfer coefficients,” and this area of enhancement technology holds much promise for future development. Many different compound schemes involving twisted-tape inserts have been considered for single-phase forced-convective and boiling applications [24–28].

It is very clear from the literature review that there are very few studies on heat transfer and pressure drop characteristics of twisted-tape-generated laminar swirl flow through square ducts and rectangular ducts of various aspect ratios; no results are available for the combined use of ribs and twisted tapes in the square and rectangular ducts.

It is because of this that the pressure drop and the heat transfer

¹Corresponding author.

Contributed by the Heat Transfer Division of ASME for publication in the JOURNAL OF HEAT TRANSFER. Manuscript received November 3, 2005; final manuscript received April 29, 2006. Review conducted by Bengt Sundén.

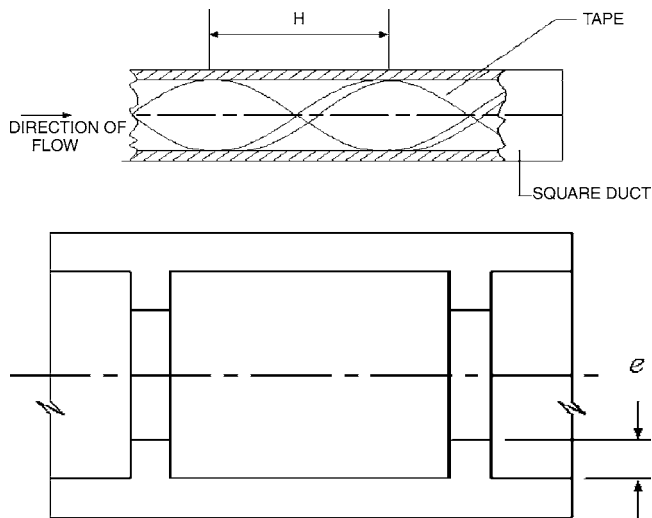


Fig. 1 (a) Full-length twisted-tape insert inside a duct, (b) regularly spaced twisted-tape elements, and (c) transverse rib turbulators

characteristics of laminar flow of single-phase viscous oil ($80 < Pr < 500$) flowing through a square duct and rectangular ducts of different aspect ratio fitted with twisted tapes and ribs have been studied experimentally. Correlations for prediction of friction factor and Nusselt number have been developed and the performance has been evaluated.

The motivation behind the present work is that the ribs influence the flow only in the near-wall region by boundary layer separation and reattachment to promote higher momentum and heat transport and the ribs do not influence the main body of the flow. On the other hand the twisted tapes are useful for laminar flow and they increase momentum and heat transport by centrifugal force created by the helical flow. It is the objective of the present work to see whether the ribs can be made useful for laminar flow when they are used in combination with twisted tapes. Most heat exchangers operate at low flow velocity for a variety of reasons. For example, the heat transfer area is usually designed conservatively to be larger than actually needed so the designed

flow velocity is low; or the flow rate of cooling medium might not be enough; or the load is not full during production and in such cases laminar flow occur. Many heat exchangers use square and rectangular ducts.

Experimental Setup, Operating Procedure and Data Reduction

A schematic diagram of the experimental setup is shown in Fig. 2. The setup consisted of (i) a storage tank in which the working fluid was stored, (ii) a working fluid circulating loop, (iii) test section, (iv) calming section, (v) an accumulator, (vi) a cooling water supply system (necessary for the heat transfer tests only), and (vii) a mixing chamber (necessary for the heat transfer tests only). The working fluid, viscous oil, was circulated through the loop by a gear pump (item no. 2 in Fig. 2) driven by a 1.5 kW electric motor. The working fluid was stored in a storage tank (item no. 1 in Fig. 2) of 0.07 m^3 capacity. The level of the fluid in the storage tank was indicated by a glass level indicator.

For the heat transfer tests, the working fluid was heated by two 2 kW heaters in the storage tank. This enabled covering a wide Prandtl number range. The heaters were connected through autotransformers so that the heating rate could be adjusted and the fluid could be heated to the desired temperature level. The working fluid passed through one of the three rotameters (item nos. 5, 6, 7 in Fig. 2), the calming section (item no. 8 in Fig. 2) to allow the velocity profile to develop fully at the entry to the test section (item no. 9 in Fig. 2) where the heat addition took place, a mixing chamber (item no. 10 in Fig. 2) for thorough mixing of the fluid, a heat exchanger coil (item no. 11 in Fig. 2) for removal of heat and a weighing platform (item no. 12 in Fig. 2) before the fluid returned to the reservoir. An accumulator (item no. 3 in Fig. 2) in the circulating loop limited the fluctuation of the pressure. A pressure gauge (item no. 4 in Fig. 2) indicated the delivery pressure of the pump.

Three heat transfer test sections were smooth 18/8 stainless steel ducts (made of sheets by soldering) having width \times depth = (1) $13 \text{ mm} \times 13 \text{ mm}$ (square duct, aspect ratio (AR)=1, $D_h = 13 \text{ mm}$), (2) $13 \text{ mm} \times 26 \text{ mm}$ (rectangular duct, AR=0.5, $D_h = 17.33 \text{ mm}$), and (3) $13 \text{ mm} \times 39 \text{ mm}$ (rectangular duct, AR = 0.333, $D_h = 19.50 \text{ mm}$). All the test sections had a length of 2 m. The test sections were heated electrically by wrapping uniformly two nichrome heater wires (20 gauge and $1.6 \Omega/\text{m}$) of identical

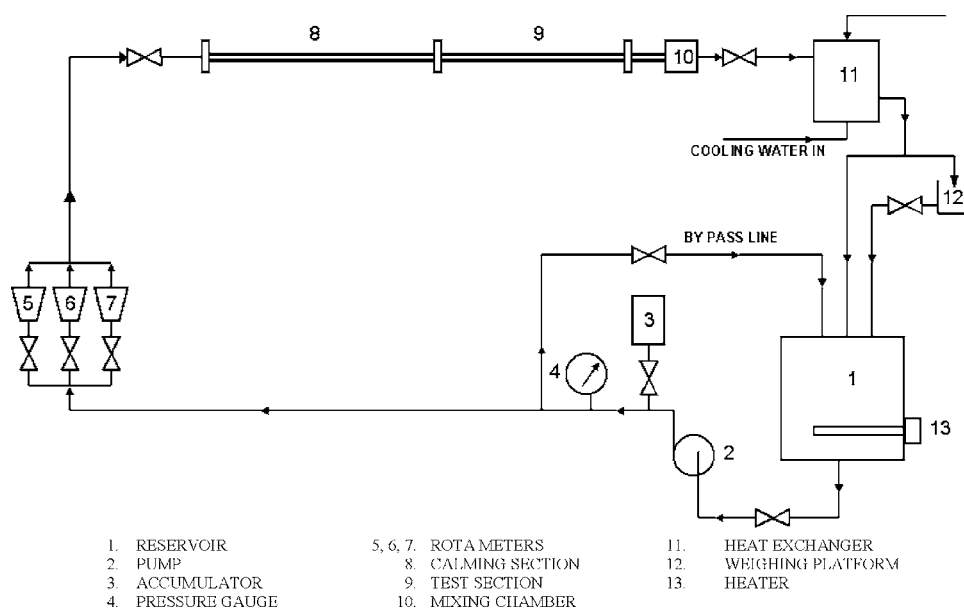


Fig. 2 Schematic diagram of experimental setup

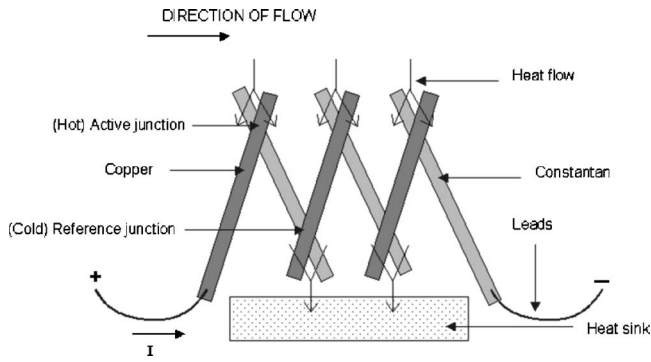


Fig. 3 Three junction thermopile

length in parallel. The resistance of each wire was 30.275Ω . The heater wires of each test section were connected through autotransformers. The power supplied to each of the test sections was measured by calibrated watt meters and this was cross checked by measurements with digital voltmeter and ammeter. The inlet and outlet bulk fluid temperatures to the test sections were measured accurately by three junction thermopiles (Fig. 3) placed in wells 5 cm upstream from the inlet and 20 cm downstream from the outlet of each test section. The fluid was assumed to have uniform temperature along the cross section at the inlet of the test channel. In order to reduce axial conduction of heat at the ends of the test sections, Teflon spacer discs of thickness 3 cm each were used on either side of the test sections. Each test section had 28 thermocouples brazed at seven axial positions on the outer surface of the duct wall to measure its temperature. The axial positions of the thermocouples from the onset of heating along the downstream direction were 0.05, 0.5, 1.00, 1.25, 1.50, 1.75, and 1.95 m, respectively. For specific cases of regularly spaced twisted-tape elements, temperatures were measured by thermocouples located at the positions shown in Fig. 4 and the flow was found to be thermally periodically fully developed. At each axial position, four thermocouples were placed at the middle of the edges. Axial grooves 6 mm long, 1.5 mm wide, and 0.6 mm deep were cut at each thermocouple location on the outer surface of the duct to facilitate brazing of the thermocouples. The working fluid circulating loop had three rotameters to cover a wide range of flow rates. These rotameters gave a measure of the flow rate and accordingly valves were adjusted to get approximately the desired flow rate. However, the actual flow rate was measured by collecting the working fluid in a container placed on the platform of a weighing machine which had a resolution of 0.001 kg. The time of collection was recorded by a stop watch (resolution 0.1 sec). The thermocouples used for measuring the temperatures were of 34 gauge copper-constantan wire. They were fabricated from a single roll and the wire was calibrated at the ice point and the steam point. The thermocouples were connected to a 36-point selector switch box, which in turn was connected to a digital multimeter and a single cold junction at 0°C .

The twisted tapes were made from a 0.5 mm thick and 9 mm wide stainless steel strip. Pieces of stainless steel rods of 1.5 mm diameter were used to make the tape-rod assembly. The ends of the rods were slotted to receive the twisted-tape elements. Twisted-tape elements were spot welded to the ends of the rods.

The pressure drop test sections were smooth acrylic ducts (made of sheets using adhesive), 3.05 m long and cross sections identical to those of heat transfer test sections. In each pressure drop channel, 12 pressure taps along the top ribbed wall were made of 30 mm long, 4.5 mm outer diameter (o.d.) pieces of acrylic tubes for static pressure drop measurement. Pressure taps were at a distance of 1.19, 1.26, 1.33, 1.40, 1.47, 1.54, 2.60, 2.67, 2.74, 2.81, 2.88, and 2.95 m from the upstream end of the pressure drop test channels. For the short-length twisted-tape tests, the

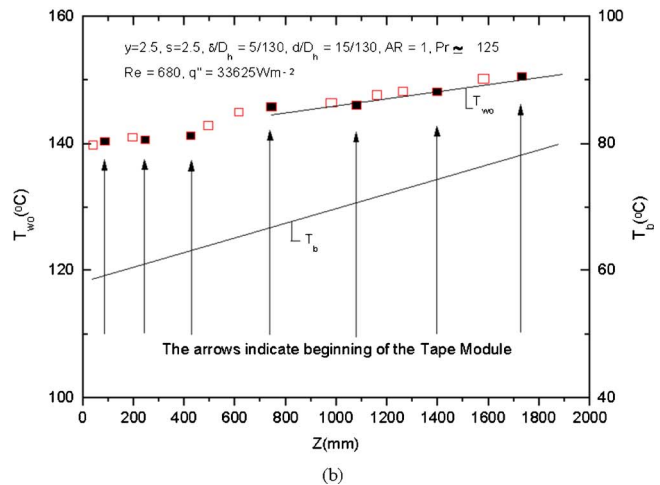
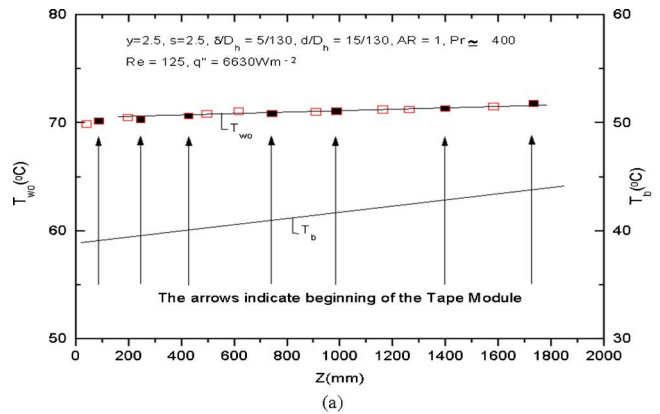


Fig. 4 Axial variation of duct outside wall temperature, AR=1

pressure drop over a length of 0.07 m along the tape length and that over a length of 0.07 m in the downstream portion of the test channel not having the twisted tape were added up to get a total pressure drop measured over a length of 0.14 m and thus the friction factor was calculated. For the regularly spaced twisted-tape elements, pressure drop over a length of 0.14 m at the downstream portion of the channel covering approximately one or more cycle(s) (one cycle comprises of one tape module and one space module) was measured for all cases. For the duct with aspect ratio $=0.333$ and $y=2.5$, $s=2.5$, $e/D_h=0.0735$, $P/e=20$, hydrodynamically periodically fully developed flow was established for $Re=105$ (Fig. 5) by measuring pressure drops with pressure taps 49 mm apart along the length of the test channel. Pressure drops in the test channel were measured by using vertical U-tube mercury manometer.

For pressure drop test channels, acrylic ribs, and for heat transfer test channels, brass ribs with a square cross section were fixed (by adhesive in pressure drop test acrylic channels and by brazing in stainless steel heat transfer test channels) periodically in line on the top and bottom walls of whole length of each channel in a required distribution. The rib geometries for each test channel are shown in Table 1 below. Figure 6 shows duct cross sections having rib and twisted tape inside the duct. The twisted tapes are centrally located leaving space in the duct corners and the wall regions of the duct where secondary flow set in. The twisted tapes were held in place inside the ducts by providing lugs.

A steady state was usually obtained after 5 to 6 h. In this state, all the thermocouple readings were noted.

The regularly spaced twisted-tape elements were adjusted lengthwise so that the distance between the taps covered the length (H) of the tape element or the length (H) of the tape element plus the space length (S). For the short-length twisted tapes,

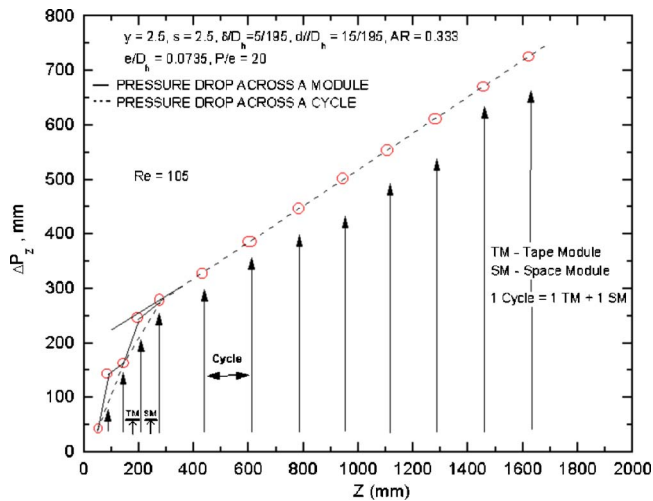


Fig. 5 Axial pressure drop results for the cases of $\gamma=2.5$ and $s=2.5$

the periodicity of the velocity and the temperature profiles in the fully developed region depended on the tape length and the length of the decay of the swirl downstream of the tape and the rib spacing thereafter.

The net heat input q_1 to the fluid was determined from the electrical energy input to the system. The enthalpy rise q_2 of the fluid was calculated from the equation

$$q_2 = \dot{m} C_p (T_{b_o} - T_{b_i}) \quad (1)$$

The set of data taken in a run were accepted only if the difference between the net heat input q_1 and the enthalpy rise q_2 was less than 3%. In such a case the actual heat input to the test section was taken as the average of q_1 and q_2 .

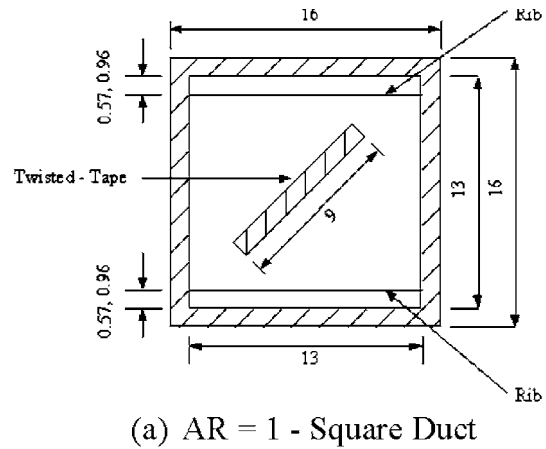
The bulk temperature of the fluid at any axial position at a distance z from the inlet was computed by assuming a linear temperature variation along the length. The duct inner wall temperatures were determined from the measured values of the outer wall temperature by applying the one dimensional heat conduction equation.

The circumferentially averaged inner wall temperature (T_{wi}) at any axial position was taken as the arithmetic mean of the inner wall temperatures at that axial position. The heat transfer coefficient (h_z) at any axial position was determined from the heat flux based on the inner surface area; the average inner wall temperature and the calculated fluid bulk mean temperature at that axial position

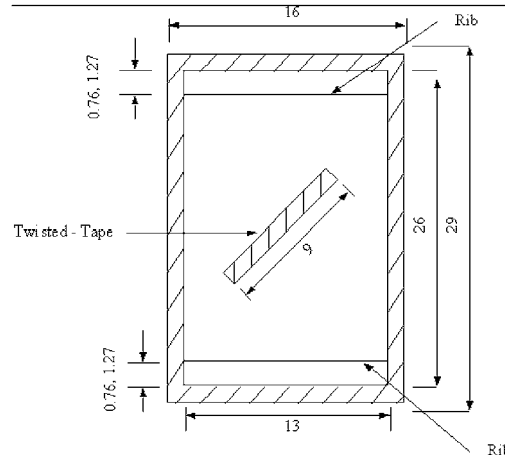
$$h_z = q'' / (T_{wi} - T_b) \quad (2)$$

The local Nusselt numbers were axially averaged by trapezoidal rule. The first two local values were averaged from the upstream end. Thereafter, this average value was used to average with the third local value. This marching procedure was followed until the extreme downstream end local value was reached.

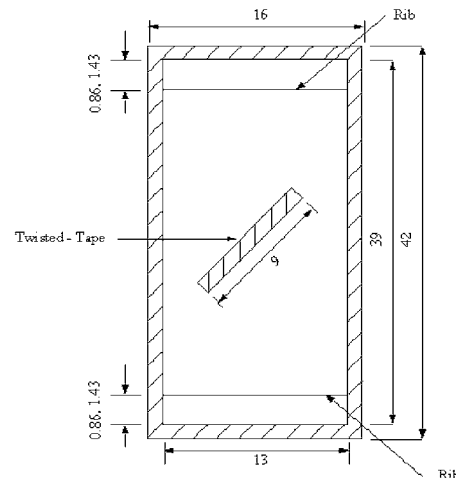
The properties of the fluid were evaluated at the mean bulk temperature. More information about the experimental setup, operating procedure, and data reduction can be obtained from [29].



(a) AR = 1 - Square Duct



(b) AR = 0.5 - Rectangular Duct I



(c) AR = 0.333 - Rectangular Duct II

Fig. 6 Duct cross sections showing rib and twisted-tape inside ducts

Table 1 Rib geometries in each test channel (mm)

Channel type	W/D, D_h	e	e/D_h	P/e	α
Square	1, 13	0.57, 0.96	0.0441, 0.0735	10, 20	90°
Rectangular I	1/2, 17.33	0.76, 1.27	0.0441, 0.0735	10, 20	90°
Rectangular II	1/3, 19.50	0.86, 1.43	0.0441, 0.0735	10, 20	90°

Table 2 The geometry information and range of parameters

Width of duct: 13 mm (for all ducts)	
Depth of duct:	Square duct—13 mm (AR=1)
	Rectangular duct—26 mm (AR=0.5), 39 mm (AR=0.333)
Length of duct:	Pressure drop tests: 3.05 m
	Heat transfer tests: 2 m
Data have been generated for the following:	
Hydraulic diameter, $D_h=13, 17.33, \text{ and } 19.5 \text{ mm}$	
Aspect ratio, AR=1, 0.5, 0.333	
Twist ratio, $\gamma=2.5$	
Space ratio, $s=2.5, 5.0$	
Twisted-tape length, $l=1, 0.9, 0.7, 0.5$	
Mass flow rate, $\dot{m}=1.264\text{--}34.784 \text{ kg/min}$	
Reynolds number, $Re=25 < Re < 1500$	
Prandtl number, $Pr=80 < Pr < 400$	
Heat flux, $q''=1250\text{--}20,000 \text{ W/m}^2$	
$\Delta T_b=T_{bo}-T_{bi}=3.185\text{--}20.532^\circ\text{C}$	
$\Delta T=T_{wi}-T_b=6.735\text{--}40.286^\circ\text{C}$	

An uncertainty analysis carried out on the lines suggested by Kline and McClintock [30] showed that uncertainties involved in the estimation of friction factors were within $\pm 4\%$ and those involved in the estimation of Nusselt number were within $\pm 7\%$.

Results and Discussion

Data have been generated for range of parameters given in Tables 1 and 2.

Validation of the Experimental Setup. The present experimental setup was validated by carrying out pressure drop experiments in plain rectangular duct with aspect ratio AR=0.333 and comparing the present friction factor data with standard value. The present experimental data was within $\pm 10\%$ of the standard data. The experimental setup was further validated by carrying out heat transfer measurements in the rectangular duct (AR=0.333) with full-length twisted-tape insert ($\gamma=2.51$) and comparing the present Nusselt number data with those predicted by the correlation given by Saha and Mallick [13]. The present experimental data was within $\pm 10\%$ of that predicted by the correlation [13]. No experimental data for laminar flow through square and rectangular ribbed ducts was readily available for comparison purpose.

Duct Wall Temperature Variation. As shown in Fig. 7, there was only 5–7% of maximum wall temperature variation in peripheral outside wall temperature measured at four locations in an axial station. Similar results have been observed for all duct configurations irrespective of Reynolds number and Prandtl number.

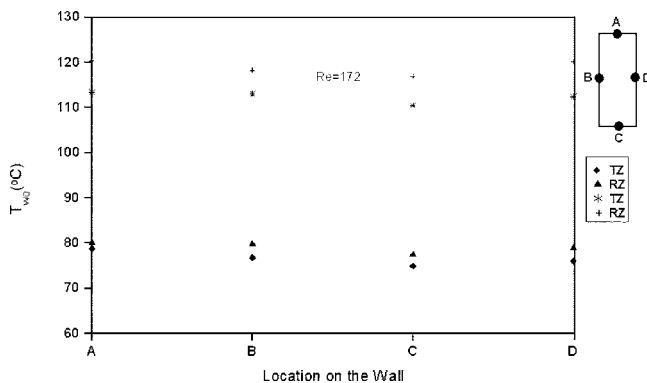


Fig. 7 Peripheral wall temperature variation—Regularly spaced twisted-tape elements, $\gamma=2.5, s=2.5$, TZ-tape zone, RZ-rod zone, AR=0.333

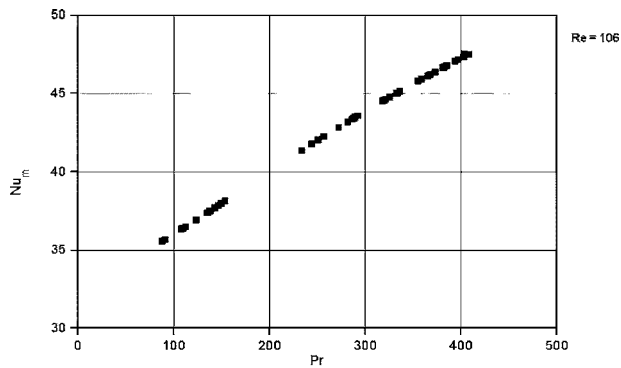
The peripheral wall temperature variation is due to buoyancy, effects of ribs, and tape-induced swirl. However, the effects are not very strong. The peripherally averaged wall temperature at an axial station was used to evaluate axially local Nusselt number.

Thermally and Hydraulically Periodic Flow. Figure 4 shows that the axial wall temperature increases linearly after certain distance from the upstream end; the slope of the outer wall temperature line is almost the same as that of the fluid bulk mean temperature. Figure 5 shows that after 2–3 tape-rod cycles from the upstream end, the cycle pressure drop varies linearly. Thus, Figs. 4 and 5 confirm thermally and hydraulically periodically fully developed flow after few cycles of tape-rod assembly in the case of regularly spaced twisted-tape elements.

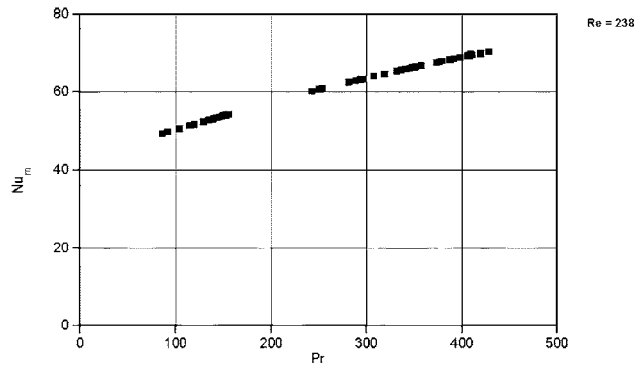
Effect of Prandtl Number on Nusselt Number. Figure 8 shows the effect of Prandtl number on Nusselt number at a given Reynolds number in the case of short-length twisted tapes and regularly spaced twisted-tape elements. In both cases Nusselt number increases with the increase in Prandtl number with a Prandtl number index of 0.3. Thus flow and thermal characteristics are strongly influenced by Prandtl number.

Comparison of Present Data With Other Data. Figures 9 and 10 show the present short-length twisted-tape and regularly spaced twisted-tape elements friction factor data, respectively, vis-à-vis data for only twisted tapes [13] and plain ducts without having twisted tapes and ribs. For lower values of Sw, the flow is distinctly laminar whereas, the transition and turbulent flowlike behavior are observed as the Sw value increases beyond a certain value. Figures 11 and 12 show corresponding Nusselt number data. Experimental data for laminar flow through square and rectangular ribbed ducts are not available. Figures 9–12 show that the present duct configurations are having maximum pressure drop and heat transfer. This shows that the twisted tapes are affecting the main body of the flow as turbulence promoter and thus the tendency of non-influence of the ribs on the main body of the flow is overcome and the ribs are also influencing the laminar flow.

Short-Length Twisted-Tape Friction Factor Results. Only isothermal friction factor data has been generated. It has been observed both experimentally and theoretically [14,16] that twisted tapes with twist ratios >5.0 do not generate sufficient swirl intensity. Again twist ratios <2.5 cause buckling of twisted tapes quite frequently while manufacturing and therefore, twist ratio $\gamma=2.5$ only has been considered. Full length twisted tapes have been considered as a bench mark and as a comparison of full length twisted tapes vis-à-vis short length twisted tapes. In the



$l = 0.5, AR = 0.333, e/D_h = 0.0441, P/e = 10$
(a)



$s = 2.5, AR = 0.333, e/D_h = 0.0441, P/e = 10$
(b)

Fig. 8 Effect of Prandtl number on Nusselt number, (a) short-length twisted tape and (b) regularly spaced twisted-tape elements

case of short-length twisted-tape-generated swirl flow, the swirl gradually developed from zero intensity at the duct entrance to its full intensity as the flow progressed in the downstream direction. Thereafter, the swirl decayed as the fluid came out of the twisted-tape zone and the straight flow tended to gradually set in.

Effect of Twisted-Tape Length. Figure 13 shows typically the effect of twisted-tape length (l) on friction factor. The figure shows that friction factor decreases as the twisted-tape length decreases since the friction surface area decreases and the swirl decays early and perhaps straight flow sets in and continues for a longer distance in the downstream direction. It has also been observed that for $AR=0.333$, the effect of the length of the twisted tape is most prominent; the less wide ducts are more influenced by the tape length. This is most evident for lower values of Sw ; as the twisted tape becomes shorter beyond a certain point, the effect of

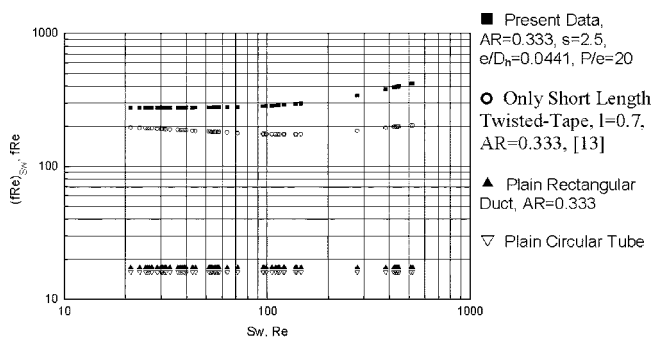


Fig. 9 Comparison of present friction factor data with other data (short-length twisted tape)

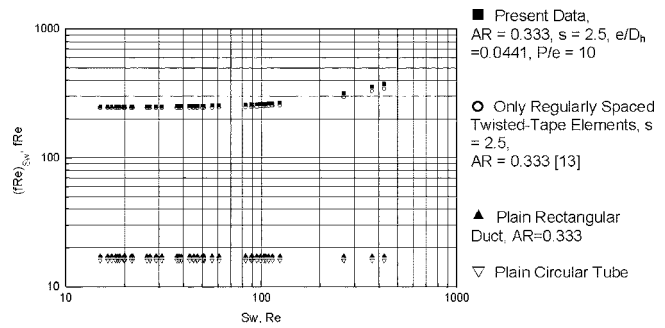


Fig. 10 Comparison of present friction factor data with other data (regularly spaced twisted-tape elements)

tape length is not very palpable since the effect of swirl developed to its full intensity is more important than the frictional surface area.

Effect of Duct Aspect Ratio. Figure 14 shows the effects of aspect ratio of duct on friction factor. It is observed that the effect of aspect ratio is by far the most prominent and it is extremely palpable. As the aspect ratio (≤ 1) decreases, the friction factor increases and this effect is evenly palpable irrespective of the values of rib height, rib spacing, and tape length. This can be appreciated since the lower the aspect ratio, the more the mixing of the more-asymmetric velocity profiles and the secondary motion and associated momentum loss.

Effect of Rib Heights. It is seen from Fig. 15 that the friction factor increases with the increase of e/D_h , i.e., with the increase of rib heights. This is particularly true for lower values of Sw . This can be explained from the fact that, as the rib height increases, the asymmetric velocity profiles in the fluid mix locally more vigorously due to stronger secondary flow and more recirculation. This effect is consistently observed for all the cases considered herein.

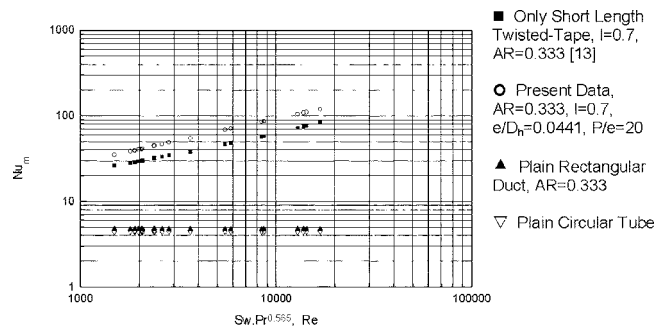


Fig. 11 Comparison of present Nusselt number data with other data (short-length twisted tape)

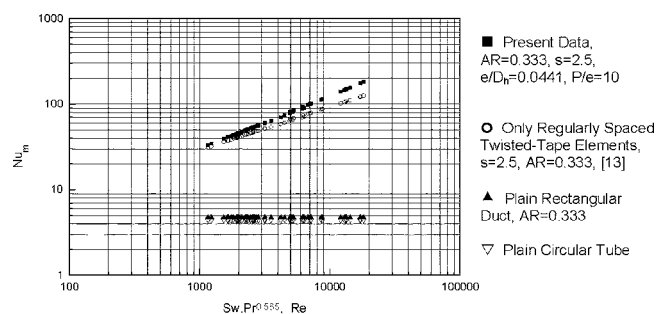


Fig. 12 Comparison of present Nusselt number data with other data (regularly spaced twisted-tape elements)

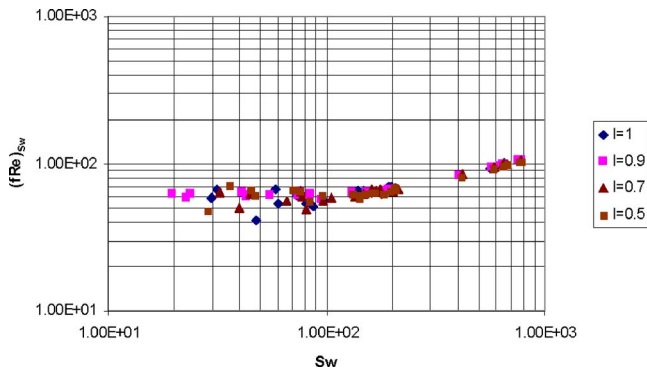


Fig. 13 $(fRe)_{Sw}$ versus Sw — $AR=1$, $e/D_h=0.0441$, $Pe=10$ (short-length twisted tape)

Effect of Rib Spacing. As it is typically observed from Fig. 16, the rib spacing has a strong effect on the friction factor for all the values of tape length, duct aspect ratio, and the rib heights. As the rib spacing increases, the friction factor decreases. This can be appreciated from the fact that with the increased rib spacing there is less number of occasions of boundary layer separation and re-attachment on the wall.

Regularly Spaced Twisted-Tape Elements Friction Factor Results. In all, 16 cases have been considered. It has been experienced [14,16] that $s > 5.0$ does not give any better results for regularly spaced twisted-tape elements and consequently $s > 5.0$ has not been considered.

Effect of Space Ratio. Figure 17 shows that the friction factor increases as s decreases since there is more frequent mixing with associated momentum loss. Also small s means an increased number of twisted-tape elements and more friction surface and atten-

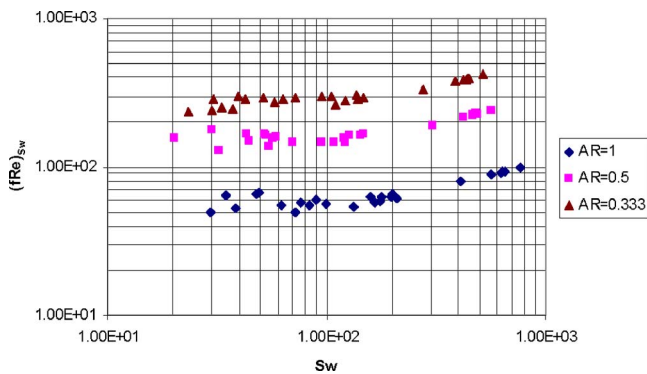


Fig. 14 $(fRe)_{Sw}$ versus Sw — $l=0.7$, $e/D_h=0.0441$, $Pe=20$

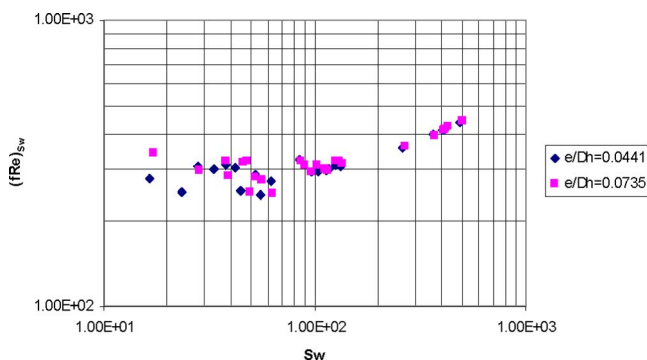


Fig. 15 $(fRe)_{Sw}$ versus Sw — $l=0.9$, $AR=0.333$, $Pe=10$

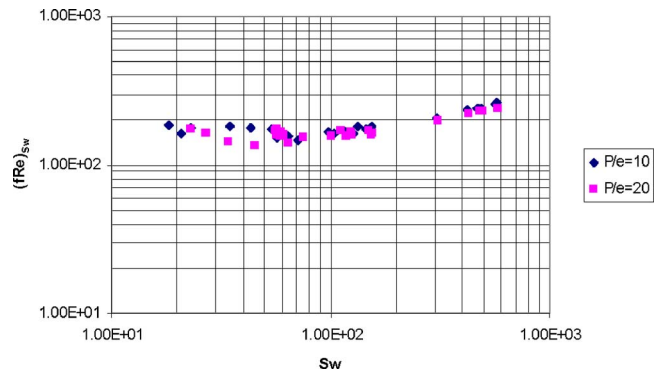


Fig. 16 $(fRe)_{Sw}$ versus Sw — $l=0.9$, $AR=0.5$, $e/D_h=0.0441$

tant pressure loss. The pressure drop measurement clearly showed the existence of decaying swirl flow in case of short-length twisted tape and periodically fully developed swirl flow in the case of regularly spaced twisted-tape elements after few cycles of tape-rod assembly.

Effect of Duct Aspect Ratio, Rib Height and Rib Spacing. The effects are similar to those observed in the case of short-length twisted tapes.

Short-Length Twisted-Tape Nusselt Number Results. The heat transfer experiments were conducted for all the cases for which pressure drop measurements were done. Figures 18–21 show the effects of twisted-tape length, duct aspect ratio, rib height, and rib spacing on Nusselt number. All observations for

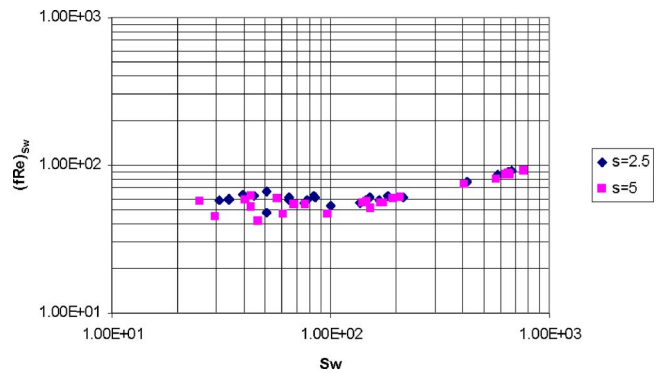


Fig. 17 $(fRe)_{Sw}$ versus Sw — $AR=1$, $e/D_h=0.0441$, $Pe=10$ (regularly spaced twisted-tape elements)

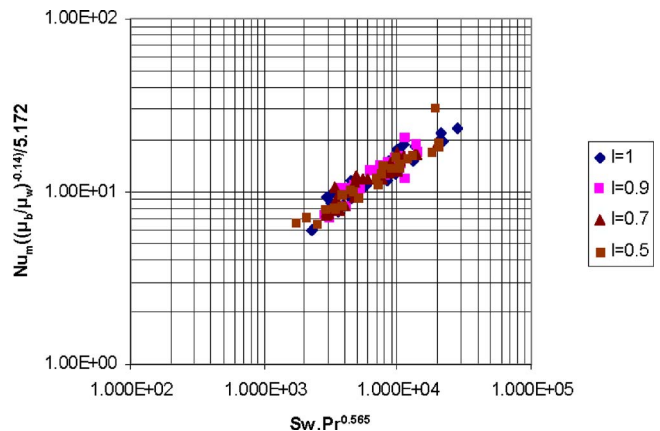


Fig. 18 $Nu_m((\mu_b/\mu_w)^{0.14})/5.172$ versus $Sw.Pr^{0.565}-AR=1$, $e/D_h=0.0441$, $Pe=10$

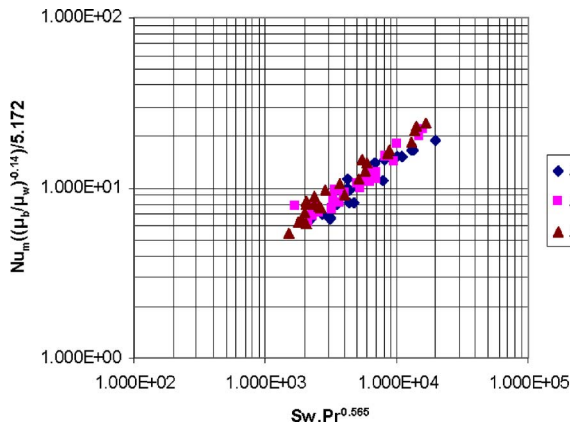


Fig. 19 $Nu_m((\mu_b/\mu_w)^{-0.14})/5.172$ versus $Sw.Pr^{0.565}-1=0.7$, $e/D_h=0.0441$, $P/e=20$

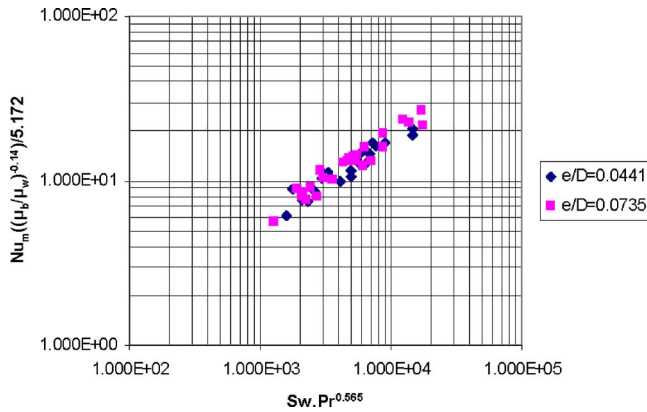


Fig. 20 $Nu_m((\mu_b/\mu_w)^{-0.14})/5.172$ versus $Sw.Pr^{0.565}-1=0.9$, $AR=0.333$, $P/e=10$

heat transfer measurements are generally the same as were those for pressure drop measurements. However, it is observed that the effect of duct aspect ratio is not as conspicuous as it was in the case of pressure drop measurements. Therefore, it can be concluded that the duct aspect ratio has a less significant effect on thermal boundary layer thickness than the hydrodynamic boundary layer thickness and the consequent convective thermal resistance.

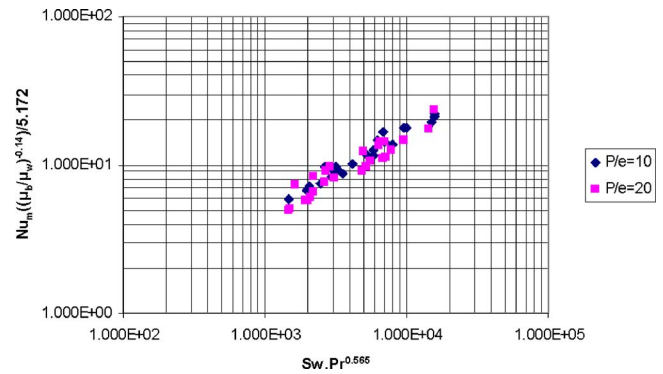


Fig. 21 $Nu_m((\mu_b/\mu_w)^{-0.14})/5.172$ versus $Sw.Pr^{0.565}-1=0.9$, $AR=0.5$, $e/D_h=0.0441$

Regularly Spaced Twisted-Tape Elements Nusselt Number Results. All observations for heat transfer measurement are similar to those for pressure drop measurements.

Correlations and Performance Evaluation

Correlations. All the correlations have been developed by log-linear regression analysis.

The correlation of friction factor for internal rib turbulators with short-length twisted tapes has been found to be

$$(fRe)_{Sw} = 17.355 \left(\frac{\pi + 2 - 2\delta/D}{\pi - 4\delta/D} \right)^2 (1 + 10^{-6} Sw^{2.67})^{1/7} (AR)^{-1.47} \times \left(1 + \frac{(e/D)^{0.0654} P^{0.215}}{(P/e)^{0.587}} \right) \quad (3)$$

The correlation of friction factor for internal rib turbulators with regularly spaced twisted-tape elements has been found to be

$$(fRe)_{Sw} = 17.355 \left(\frac{\pi + 2 - 2\delta/D}{\pi - 4\delta/D} \right)^2 (1 + 10^{-6} Sw^{2.67})^{1/7} (AR)^{-1.38} \times \left(1 + \frac{(e/D)^{0.143} d^{0.157}}{s^{1.178}} \right) \frac{1}{(P/e)^{0.161}} \quad (4)$$

The correlation of Nusselt number for internal rib turbulators with short-length twisted tapes has been found to be

$$Nu_m = 5.172 \left[\frac{((1 + 0.08932Gz^{0.9125})^{2.5} + 8.2273 \times 10^{-6} (Sw \cdot Pr^{0.565})^{2.655})^{2.0}}{1 + 1.5638 \times 10^{-15} (Re_{ax} \cdot Ra)^{2.18}} \right]^{0.1} \times \left(\frac{\mu_b}{\mu_w} \right)^{0.14} \times \left(\frac{1}{AR} + 0.1 \right)^{0.15} \left(1 + \frac{(e/D)^{0.0748} P^{0.195}}{(P/e)^{0.692}} \right), \quad AR \leq 1 \quad (5)$$

The correlation of Nusselt number for internal rib turbulators with regularly spaced twisted-tape elements has been found to be

$$Nu_m = 5.172 \left[\frac{((1 + 0.08932Gz^{0.9125})^{2.5} + 8.2273 \times 10^{-6} (Sw \cdot Pr^{0.565})^{2.655})^{2.0}}{1 + 1.5638 \times 10^{-15} (Re_{ax} \cdot Ra)^{2.18}} \right]^{0.1} \times \left(\frac{\mu_b}{\mu_w} \right)^{0.14} \times \left(\frac{1}{AR} + 0.1 \right)^{0.15} \left(1 + \frac{(e/D)^{0.1648} d^{0.135}}{s^{1.206}} \right) \frac{1}{(P/e)^{0.158}}, \quad AR \leq 1 \quad (6)$$

Table 3 $(e/D)_1=0.0441$ $(e/D)_2=0.0735$ $(P/e)_1=10$ $(P/e)_2=20$. Performance ratios R_1 and R_2 for short-length twisted tapes.

AR		$l=0.9$				$l=0.7$				$l=0.5$			
		$(e/D)_1$		$(e/D)_2$		$(e/D)_1$		$(e/D)_2$		$(e/D)_1$		$(e/D)_2$	
		$(P/e)_1$	$(P/e)_2$	$(P/e)_1$	$(P/e)_2$	$(P/e)_1$	$(P/e)_2$	$(P/e)_1$	$(P/e)_2$	$(P/e)_1$	$(P/e)_2$	$(P/e)_1$	$(P/e)_2$
1	R_1	0.997		0.997		0.991	0.993			0.983			0.987
	R_2	1.0180		1.019		1.060	1.044			1.112			1.083
0.5	R_1	0.997	0.998	0.997		0.991	0.994	0.991	0.994	0.984		0.983	0.988
	R_2	1.017	1.012	1.018		1.058	1.040	1.059	1.040	1.104		1.113	1.080
0.333	R_1	0.998	0.998	0.997	0.998			0.994	0.994	0.984	0.989	0.984	0.988
	R_2	1.016	1.013	1.017	1.012			1.040	1.043	1.110	1.070	1.112	1.081

All correlations have been found to predict the experimental data within $\pm 18\%$.

Performance Evaluation. Bergles et al. [31] have suggested several criteria for the performance evaluation of enhancement devices. The performance of the present geometry has been evaluated on the basis of the following two important criteria:

- Criterion 1—Basic geometry fixed, pumping power fixed—increase heat transfer—performance ratio R_1
- Criterion 2—Basic geometry fixed, heat duty fixed—reduce pumping power—performance ratio R_2

$$R_1 = \frac{Nu_{sltrst}}{Nu_{flt}}$$

Nu_{sltrst} at a given Re , Re_{sltrst} is obtained from the correlation for short-length twisted-tape or regularly spaced twisted-tape elements. Nu_{flt} for full-length twisted tape is taken at the Re , Re_{flt} where Re_{flt} is calculated from the constant pumping power consideration as

$$Re_{flt} = \left[\left(\frac{f_{sw,sltrst}}{f_{sw,flt}} \right) \left(\frac{A_{c,sltrst}}{A_{c,flt}} \right) Re_{sw,sltrst}^3 \right]^{1/3}$$

where $4A_{c,sltrst} = l(\pi D_h^2 - 4\delta D_h) + (1-l)\pi D_h^2$ [neglecting rib cross-sectional area]

$$4A_{c,rst} = ((\pi D_h^2 - 4\delta D_h)y + \pi(D_h^2 - d^2)s)/(y + s)$$

[Neglecting rib cross-sectional area]

$$A_{c,flt} = \left(\frac{\pi}{4} \right) D_h^2 - \delta D_h$$

$$R_2 = \frac{(f_{sw} Re_{sw}^3 A_c)_{sltrst}}{(f_{sw} Re_{sw}^3 A_c)_{flt}}$$

For a given Re , Re_{sltrst} , the Nu_{sltrst} is obtained from the correlation. Re_{flt} corresponding to Nu_{sltrst} is obtained from the correla-

tion for full-length twisted tape.

The performance ratios R_1 and R_2 for short-length twisted tapes are given in Table 3.

From the performance ratio it is clearly observed that short-length twisted tapes perform worse than their full-length counterparts and, therefore, these are not recommended. The performance ratios R_1 and R_2 for regularly spaced twisted-tape elements are given in Table 4 for $s=2.5$ and $s=5.0$.

Zhang et al. [25] have shown that both heat transfer and pressure drop are higher with the addition of ribs in the pipe fitted with full-length twisted tape. From the performance ratio in the present investigation it is clearly observed that the regularly spaced twisted-tape elements perform only marginally better than their full-length counterparts for small as well as large transverse ribs with large spacing for closely spaced twisted-tape elements ($s \leq 2.5$) in ducts with aspect ratio ≤ 1 and these are recommended.

Conclusions

The present experimental friction and heat transfer data shows that combined use of full-length twisted-tape and transverse ribs enhances the thermohydraulic performance of the square and rectangular ducts compared to the use of only twisted-tape or only transverse ribs for laminar flow. However, the performance evaluation shows that the short-length twisted tape in square and rectangular ducts with rib turbulators, through which laminar flow occurs under constant wall heat flux boundary condition performs worse than the full-length twisted tape. Regularly spaced twisted-tape elements in specific cases perform marginally better than the full-length twisted tapes. Therefore, full-length twisted tapes and regularly spaced twisted-tape elements in combination with transverse ribs are recommended for laminar flows. However, the short-length twisted tapes are not recommended.

Axially local pressure drop measurements as well as the axial variation of duct wall temperature indicated that the flow was periodically fully developed after some distance from the up-

Table 4 $(e/D)_1=0.0441$ $(e/D)_2=0.0735$ $(P/e)_1=10$ $(P/e)_2=20$. Performance ratios R_1 and R_2 for regularly spaced twisted-tape elements.

AR		$s=2.5$				$s=5.0$			
		$(e/D)_1$		$(e/D)_2$		$(e/D)_1$		$(e/D)_2$	
		$(P/e)_1$	$(P/e)_2$	$(P/e)_1$	$(P/e)_2$	$(P/e)_1$	$(P/e)_2$	$(P/e)_1$	$(P/e)_2$
1	R_1	0.962	0.997	0.964	1.007	0.919			
	R_2	1.253	1.018	1.249	0.997	1.637			
0.5	R_1	0.971	1.006	0.973	1.009	0.929		0.928	
	R_2	1.189	0.965	1.174	0.948	1.547		1.567	
0.333	R_1	0.976	1.011	0.978	1.015				0.973
	R_2	1.176	0.934	1.139	0.914				1.192

stream end in the case of regularly spaced twisted-tape elements. In the case of short-length twisted tapes the swirl decayed downstream of the twisted tape and the straight flow set in.

The buoyancy effect in the plain duct portion in the case of short-length twisted tape and in the annular space region in the case of regularly spaced twisted-tape elements has been taken care of in the Nusselt number correlations. The swirl flow inertia forces were persistent in the twisted-tape region.

The friction and thermal characteristics are governed by twist ratio, space ratio, tape-rod diameter, Re, Sw, Pr, Gz, Gr, rib height, and rib spacing and duct aspect ratio.

Predictive correlations for friction factor and Nusselt number have been developed.

Nomenclature

- A = heat transfer area, m^2
 A_c = axial flow cross-sectional area, $=(\pi D_h^2/4) - \delta D_h$, m^2
 A_o = plain duct flow cross-sectional area, $=W \cdot D$, m^2
 AR = aspect ratio $=W/D$, dimensionless.
 C_p = constant pressure specific heat, J/kgK
 D = depth of the duct cross section, m
 D_h = hydraulic diameter of the test duct, $=4A_o/P$, m
 d = nondimensional diameter of the rod connecting two successive tape elements
 d^* = actual diameter of the rod $=d \cdot D_h$, m
 e = rib height, m
 f = fully developed Fanning friction factor $=(1/2) \times [\Delta P' / (\rho V_o^2)] (D_h/z)$, dimensionless
 f_{sw} = swirl flow friction factor, $=\Delta P' D_h / (2\rho V_s^2 L_s)$
 $=f(L/L_s)(V_o/V_s)^2$, dimensionless
 $(fRe)_{sw} = (fRe)_{sw} = (fRe)((\pi - (4\delta/D_h)) / \pi)(1 + (\pi/2y)^2)^{-1}$, dimensionless
 g = gravitational acceleration, m/s^2
 G = mass flux $=\dot{m}/A_c$, $kg/m^2 s$
 Gr = Grashof number $=g\beta\rho^2 D_h^3 \Delta T_w / \mu^2$, dimensionless
 Gz = Graetz number $=\dot{m}C_p/kL$, dimensionless
 H = pitch for 180 deg rotation of twisted tape, m
 h_z = axially local heat transfer coefficient, $W/(m^2K)$.
 k = fluid thermal conductivity, $W/(mK)$.
 L = axial length, length of the duct, m
 L_s = maximum helical flow length $=L[1 + (\pi/2y)^2]^{1/2}$, m
 L_T = length of twisted tape, m
 l = nondimensional twisted-tape length $=L_T/L$, dimensionless
 \dot{m} = mass flow rate, kg/min
 Nu_m = axially averaged Nusselt number $=1/L \int_0^L h_z D_h dz / k$, dimensionless
 ΔP_z = pressure drop, mm
 $\Delta P'$ = pressure drop, N/m^2
 P = wetted perimeter in the particular cross section of the duct, rib spacing, m
 Pr = fluid Prandtl number $=\mu C_p/k$, dimensionless
 q_1 = electrical energy input to the system, W
 q_2 = defined by Eq. (1)
 $q'' = 0.5 / \pi D_h L (q_1 + q_2)$, W/m^2
 Ra = Rayleigh number $=Gr \cdot Pr$
 Re_{ax} = Reynolds number based on axial velocity $=(\rho V_a D_h) / \mu$, dimensionless
 Re_{sw} = Reynolds number based on swirl velocity $=(\rho V_s D_h) / \mu$, dimensionless
 Re = Reynolds number based on plain duct diameter $=(\rho V_o D_h) / \mu$, dimensionless
 S = space between two successive tape elements, m

- s = space ratio $=S/D_h$, dimensionless
 Sw = swirl parameter
 $= Re_{sw} / \sqrt{y} = (Re / \sqrt{y}) (\pi / (\pi - 4\delta/D_h)) \times [1 + (\pi/2y)^2]^{0.5}$, dimensionless
 T = temperature, K
 ΔT_w = wall to fluid bulk temperature difference, K
 V_a = mean axial velocity $=\dot{m} / \rho A_c$, m/s
 V_o = mean velocity based on plain duct diameter $=\dot{m} / \rho A_o$, m/s
 V_s = actual swirl velocity at duct wall $=V_a [1 + (\pi/2y)^2]^{0.5}$, m/s
 W = width of the duct cross-section, m
 y = twist ratio $=H/D_h$, dimensionless
 z = axial length, the distance between the measuring pressure taps, m

Greek Symbols

- β = coefficient of isobaric thermal expansion, K^{-1}
 δ = tape thickness, m
 μ = fluid dynamic viscosity, kg/ms
 ρ = density of the fluid, kg/m^3

Subscripts

- ax = at axial flow condition
 b = at bulk fluid temperature
 flt = full-length twisted tape
 h = hydraulic diameter
 i = inlet
 m = axially averaged
 o = outlet
 rst = regularly spaced twisted-tape elements
 slt = short-length twisted tape
 sw = at swirl flow condition
 w = at duct wall temperature
 z = local value

References

- [1] Date, A. W., 1974, "Prediction of Fully Developed Flow in a Tube Containing a Twisted-Tape," *Int. J. Heat Mass Transfer*, **17**(8), pp. 845–859.
- [2] Hong, S. W., and Bergles, A. E., 1976, "Augmentation of Laminar Flow Heat Transfer in Tubes by Means of Twisted-Tape Inserts," *J. Heat Transfer*, **98**(2), pp. 251–256.
- [3] Al-Fahed, S., Chamra, L. M., and Chakroun, W., 1998, "Pressure Drop and Heat Transfer Comparison for Both Micro Fin Tube and Twisted-Tape Inserts in Laminar Flow," *Exp. Therm. Fluid Sci.*, **18**(4), pp. 323–333.
- [4] Agarwal, S. K., and Raja, Rao., 1996, "Heat Transfer Augmentation for the Flow of a Viscous Liquid in Circular Tubes using Twisted-Tape Inserts," *Int. J. Heat Mass Transfer*, **39**(17), pp. 3547–3557.
- [5] Hochdorfer, E., and Gschwind, P., 1995, "Twisted-Tape Vortex Generators on Duct Flow: Flow Field and Heat and Mass Transfer," *Exp. Therm. Fluid Sci.*, **13**(3), pp. 262–269.
- [6] Bandyopadhyay, P. S., Gaitonde, U. N., and Sukhatme, S. P., 1991, "Influence of Free Convection on Heat Transfer During Laminar Flow in Tubes with Twisted Tapes," *Exp. Therm. Fluid Sci.*, **4**(5), pp. 577–586.
- [7] Date, A. W., 2000, "Numerical Prediction of Laminar Flow and Heat Transfer in a Tube with Twisted-Tape Insert: Effects of Property Variations and Buoyancy," *J. Enhanced Heat Transfer*, **7**(4), pp. 217–229.
- [8] Bergles, A. E., 1997, "Heat Transfer Enhancement — The Maturing of Second-Generation Heat Transfer Technology," *Heat Transfer Eng.*, **18**(1), pp. 47–55.
- [9] Marnar, W. L., and Bergles, A. E., 1989, "Augmentation of Highly Viscous Laminar Heat Transfer Inside Tubes in Constant Wall Temperature," *Exp. Therm. Fluid Sci.*, **2**(3), pp. 252–267.
- [10] du Plessis, J. P., and Kroger, D. G., 1987, "Heat Transfer Correlation for Thermally Developing Laminar Flow in a Smooth Tube with a Twisted-Tape Insert," *Int. J. Heat Mass Transfer*, **30**(3), pp. 509–515.
- [11] du Plessis, J. P., and Kroger, D. G., 1984, "Friction Factor Prediction for Fully Developed Laminar Twisted-Tape Flow," *Int. J. Heat Mass Transfer*, **27**(11), pp. 2095–2100.
- [12] Saha, S. K., and Dutta, A., 2001, "Thermohydraulic Study of Laminar Swirl Flow through a Circular Tube Fitted with Twisted Tapes," *J. Heat Transfer*, **123**(3), pp. 417–427.
- [13] Saha, S. K., and Mallick, D. N., 2005, "Heat Transfer and Pressure Drop Characteristics of Laminar Flow in Rectangular and Square Plain Ducts and

Ducts with Twisted-Tape Inserts," ASME J. Heat Transfer, **127**(9), pp. 966–977.

- [14] Saha, S. K., Gaitonde, U. N., and Date, A. W., 1989, "Heat Transfer and Pressure Drop Characteristics of Laminar Flow in a Circular Tube with Regularly Spaced Elements," *Exp. Therm. Fluid Sci.*, **2**(3), pp. 310–322.
- [15] Date, A. W., and Gaitonde, U. N., 1990, "Development of Correlations for Predicting Characteristics of Laminar Flow in a Tube Fitted with Regularly spaced Twisted-Tape Elements," *Exp. Therm. Fluid Sci.*, **3**(4), pp. 373–382.
- [16] Date, A. W., and Saha, S. K., 1990, "Numerical Prediction of Laminar Flow and Heat Transfer Characteristics in a Tube Fitted with Regularly Spaced Twisted-Tape Elements," *Int. J. Heat Mass Transfer*, **11**(4), pp. 346–354.
- [17] Saha, S. K., Dutta, A., and Dhal, S. K., 2001, "Friction and Heat Transfer Characteristics of Laminar Swirl Flow through a Circular Tube Fitted with Regularly Spaced Twisted-Tape Elements," *Int. J. Heat Mass Transfer*, **44**(22), pp. 4211–4223.
- [18] Han, J. C., 1988, "Heat Transfer and Friction Characteristics in Rectangular Channels with Rib Turbulators," ASME J. Heat Transfer, **110**, pp. 321–328.
- [19] Han, J. C., Zhang, Y. M., and Lee, C. P., 1991, "Augmented Heat Transfer in Square Channels with Parallel, Crossed, and V Shaped Angled Ribs," ASME J. Heat Transfer, **113**, pp. 590–596.
- [20] Ekkad, S. V., and Han, J. C., 1997, "Detailed Heat Transfer Distributions in Two Pass Square Channels with Rib Turbulators," *Int. J. Heat Mass Transfer*, **40**(11), pp. 2525–2537.
- [21] Han, J. C., Huang, J. J., and Lee, C. P., 1993, "Augmented Heat Transfer in Square Channels with Wedge Shaped and Delta Shaped Turbulence Promoters," *J. Enhanced Heat Transfer*, **1**(1), pp. 37–52.
- [22] Bergles, A. E., 1998, "Techniques to Enhance Heat Transfer," in *Handbook of Heat Transfer*, 3rd ed., W. M. Rohsenow, J. P. Hartnett, and Y. I. Cho, eds., McGraw-Hill, New York, Chap. II.
- [23] Bergles, A. E., 2000, "New Frontiers in Enhanced Heat Transfer," in *Advances in Enhanced Heat Transfer 2000*, R. M. Manglik, T. S., Ravigururijen, A. Muley, A. R. Papar, and J. Kim, eds., ASME, New York, pp. 13–29.
- [24] Bergles, A. E., Lee, R. A., and Mikic, B. B., 1969, "Heat Transfer in Rough Tubes with Tape-Generated Swirl Flow," *J. Heat Transfer*, **91**, pp. 443–445.
- [25] Zhang, Y. M., Azad, G. M., Han, J. C., and Lee, C. P., 2000, "Turbulent Heat Transfer Enhancement and Surface Heating Effect in Square Channels with Wavy, and Twisted Tape Inserts with Interrupted Ribs," *J. Enhanced Heat Transfer*, **7**(1), pp. 35–49.
- [26] Zimparov, V., 2001, "Enhancement of Heat Transfer by a Combination of Three-Start Spirally Corrugated Tubes with a Twisted Tape," *Int. J. Heat Mass Transfer*, **44**(3), pp. 551–574.
- [27] Van Rooyen, R. S., and Kroger, D. G., 1978, "Laminar Flow Heat Transfer in Internally Finned Tubes with Twisted-Tape Inserts," in *Heat Transfer 1978*, Vol. 2, Hemisphere Publishing, Washington, DC, pp. 577–581.
- [28] Usui, H., Sano, Y., and Iwashita, K., 1984, "Heat Transfer Enhancement Effects by Combined Use of Internally Grooved Rough Surfaces and Twisted Tapes," *Heat Transfer-Jpn. Res.*, **13**(4), pp. 19–32.
- [29] Pramanik, D., 2005, "Thermohydraulic Studies of Laminar Flow through Non-Circular Ducts," Ph.D. thesis, Besus, India.
- [30] Kline, S. J., and McClintock, F. A., 1953, "Describing Uncertainties in Single Sample Experiments," *Mech. Eng. (Am. Soc. Mech. Eng.)*, **75**(1), pp. 3–8.
- [31] Bergles, A. E., Blumenkrantz, A. R., and Taborek, J., 1974, "Performance Evaluation Criteria for Enhanced Heat Transfer Surfaces," Paper FC 6.3, in *Heat Transfer 1974, Proceedings 5th International Heat Transfer Conference*, Vol. 2, Tokyo, pp. 239–243.

Design Optimization of Size and Geometry of Vortex Promoter in a Two-Dimensional Channel

Tunc Icoz

Thermal Scientist
GE Global Research,
Thermal Systems Laboratory,
Niskayuna NY 12309

Yogesh Jaluria

Board of Governors Professor
Rutgers University,
Department of Mechanical & Aerospace
Engineering,
New Brunswick NJ 08901

Thermal management of electronic equipment is one of the major technical problems in the development of electronic systems that would meet increasing future demands for speed and reliability. It is necessary to design cooling systems for removing the heat dissipated by the electronic components efficiently and with minimal cost. Vortex promoters have important implications in cooling systems for electronic devices, since these are used to enhance heat transfer from the heating elements. In this paper, an application of dynamic data driven optimization methodology, which employs concurrent use of simulation and experiment, is presented for the design of the vortex promoter to maximize the heat removal rate from multiple protruding heat sources located in a channel, while keeping the pressure drop within reasonable limits. Concurrent use of computer simulation and experiment in real time is shown to be an effective tool for efficient engineering design and optimization. Numerical simulation can effectively be used for low flow rates and low heat inputs. However, with transition to oscillatory and turbulent flows at large values of these quantities, the problem becomes more involved and computational cost increases dramatically. Under these circumstances, experimental systems are used to determine the component temperatures for varying heat input and flow conditions. The design variables are taken as the Reynolds number and the shape and size of the vortex promoter. The problem is a multiobjective design optimization problem, where the objectives are maximizing the total heat transfer rate Q and minimizing the pressure drop ΔP . This multiobjective problem is converted to a single-objective problem by combining the two objective functions in the form of weighted sums. [DOI: 10.1115/1.2345433]

Introduction

Advancements in microelectronics technology and increasing demand for faster and more reliable electronic systems have resulted in higher-power densities and smaller electronic packages. Proper thermal management, however, remains one of the strongest obstacles to the future development of such systems. In order to satisfy the increasing demands for high-speed data transfer and communication, which lead to higher-power dissipation levels, inexpensive and compact thermal management solutions have to be found. These alternative solutions include modifications in the geometry and structure of the fluid flow by inserting solid bodies into the flow field. Using a vortex generator is known to be one of the passive enhancement techniques, which increases the heat removal rates from the components. The vortex shedding from a cylinder has been investigated by a number of researchers [1–4]. Davis and Moore [1] numerically studied the generation and development of vortex downstream of a rectangular cylinder. An experimental study by Okajima [2] of vortex shedding in a wind tunnel revealed the frequencies of generated vortices. The confined wakes behind a square cylinder in a channel were numerically investigated and the Strouhal number was found to increase with the blockage ratio [3]. The damping effect of the sidewalls on the oscillations was also observed to be significant. An experimental study on the transition to turbulence in a rectangular channel with eddy promoters was carried out and critical Reynolds numbers were determined [4].

Enhanced heat transfer rates were obtained by inserting vortex-promoting cylinders upstream of the heat sources [5]. Up to 82%

increase in the heat removal rate was experimentally found in [6] with the increase in the diameter of the promoter. Vortex generators are also widely used in the heat exchanger applications. Enhancement in the heat transfer rate and the effect on pressure drop are presented in [7,8]. A maximum improvement of 18.5% in the average heat transfer coefficient was obtained using wave type vortex generators in fin-tube heat exchangers [7]. The effects of inclined baffles and ribs were studied in [9] on the heat transfer rate in advanced combustion turbine blades and vanes. Combining ribs and inclined baffles was shown to increase the average Nusselt number, at the expense of increased pressure drop. The heat transfer and fluid flow in a channel, under fully developed flow conditions, were investigated in [10] using staggered ribs. They reported significant heat transfer augmentation for moderately high Prandtl number fluids such as water.

Protruding heating elements located in enclosures is one of the most widely used configurations in electronic systems. The flow structure and heat transfer in a channel with periodically mounted transverse vortex promoters were investigated in [11]. The improved mixing between the core fluid and fluid near the heated walls was observed to be due to self-sustained oscillations, leading to increased heat transfer rate. The enhancement in the heat transfer rates, from discrete protruding heat sources located in a channel, by means of vortex shedding were studied in [12–14]. Garimella and Eibeck [12] studied the enhancement in heat transfer from an array of heat sources by installing a row of half-delta shaped vortex generators upstream of the array. The maximum increase in the heat transfer rate was found at the second row of elements and was up to 40% in the laminar flow regime. In the turbulent regime, this increase dropped to 5%. This decrease in enhancement was attributed to the existence of a good mixing between the cold air and heated air, even without a promoter at high turbulence levels. Kim et al. [13] numerically studied the thermal interaction between isolated heat sources in pulsating channel flow. Their results indicated that the recirculating flows,

Contributed by the Heat Transfer Division of ASME for publication in the JOURNAL OF HEAT TRANSFER. Manuscript received January 10, 2006; final manuscript received July 8, 2006. Review conducted by Yogendra Joshi. Paper presented at the 2005 ASME Heat Transfer Summer Conference (HT2005), July 15–22, 2005, San Francisco, CA.

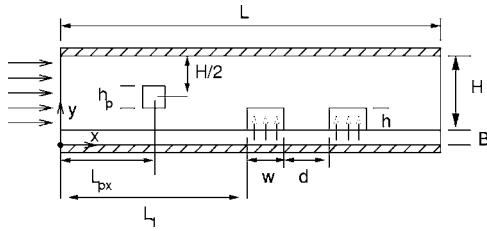


Fig. 1 Schematic representation of the problem

behind the second block and in the interblock region, were significantly affected by the oscillations, which influence the thermal transport from the discrete sources. Wang and Jaluria et al. [14] investigated the resonance of the oscillatory flow in a channel and the resulting effect on thermal transport from protruding heat sources in a channel.

In this study, the transport and heat transfer characteristics with a vortex generator installed in the flow field is investigated over a wide range of Re , promoter size, and shape. The optimization of the size and geometry of a vortex promoter and of the flow conditions for maximizing the heat transfer rate, from the isolated heat sources located on the bottom wall of a channel, and minimizing the pressure drop is presented. The problem considered is schematically represented in Fig. 1. It is an application of dynamic data driven optimization methodology (DDDOM), which employs concurrent use of experimental and numerical simulation, and the methodology is explained briefly in this paper and in detail in [15]. The problem is a multicriteria design optimization since the problem involves more than one objective function. Various combinations of these individual objective functions are studied and optimal values of the design variables are determined.

Experimental System

Figure 2 depicts a schematic of the experimental apparatus. The airflow is provided by means of a compressor. The flow rate of air entering the channel is controlled with a proportional valve, which is operated using an analog signal. A DC power supply with a built in signal amplifier is employed to drive this proportional valve. The channel is rectangular in cross section, with a width to height ratio, i.e., W/H , of 6, to keep the three-dimensional (3D) effect due to sidewalls minimal. The incoming air is passed through a stagnation chamber, a converging inlet section, and a series of screens and honeycomb filters to ensure that flow is uniform at the inlet to the test section.

Two 25×200 mm strip heaters, operating with AC voltage, are used to heat the copper blocks, which simulate electronic components. The heat input to the sources is controlled by means of AC transformers. Heat flux sensors, with less than 0.2 mm thickness,

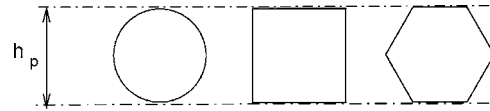


Fig. 3 Geometries and orientations of the vortex promoters used in experiments

are installed between the strip heaters and copper sinks to measure the heat input of each heat source. The operating range of these sensors is $0-9500 \text{ W/m}^2$. The temperatures of the heat sources are measured at three locations to monitor the uniformity of the temperatures. The difference between the thermocouple readings is observed to be less than 0.2°C . Steady state conditions are assumed when the change in average temperatures is less than 0.4°C over 15 mins. The heating elements are located at distances of $4.5H$ and $6H$ downstream of the channel inlet. The height of the heat sources is kept at $h=0.25H$ and the separation distance between the heat sources is set at $d=0.5H$.

Various vortex generator geometries and sizes are used to investigate their effect on the fluid flow and the heat transfer rate. Circular, hexagonal, and square cylinders are used as vortex promoters. All three types of promoters are placed in the cavity such that the resulting blockage ratios h_p/H , the ratio of the projected area of the promoter in the flow direction to the cross sectional area of the channel, would be the same for the same sizes of different geometries, as shown in Fig. 3. A hotwire probe for measuring air velocity is placed at a distance of H from the vortex promoter center. The centers of the promoters are located at $L_{px} = 3H$ from the inlet of the channel in the streamwise direction and are at the midpoints of the channel in vertical direction. The inline pressure drop is measured using two pressure probes located at H and $12H$ downstream of the channel inlet. The uncertainties associated with the heat transfer and pressure drop measurements are found to be $\pm 4.2 \text{ W/m}$ and $\pm 0.13 \text{ Pa}$, respectively.

Numerical Method

The numerical simulation is an efficient tool for laminar two- and three-dimensional flows, which arise at relatively low Re and Gr . In the present study, the numerical approach is used only for square vortex promoter when $Re < 1500$. Only the square vortex promoter is studied numerically, since implementation for non-rectangular geometries is cumbersome and increases the computational cost. The governing nondimensional differential equations for laminar mixed convection flow, with constant thermophysical properties and Boussinesq approximations, can be written as given below:

The mass, momentum, and energy equations within the flow

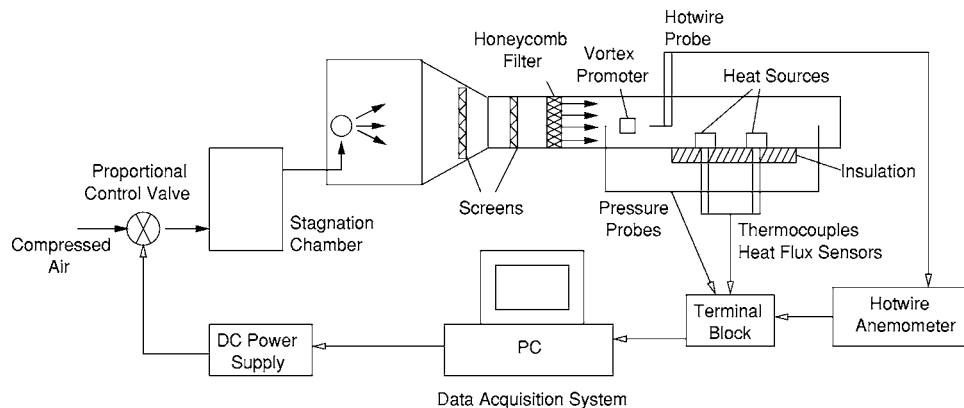


Fig. 2 Experimental setup

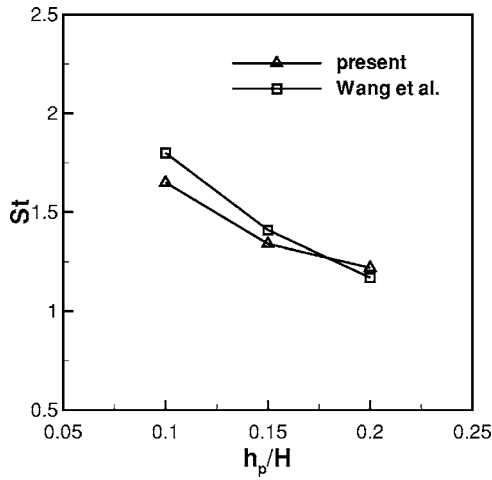


Fig. 4 Comparison of computed and published Strouhal numbers in channel, downstream of the vortex promoter, without any heat sources

field are

$$\nabla \cdot \vec{V} = 0 \quad (1)$$

$$\frac{\partial \vec{V}}{\partial \tau} + \vec{V} \cdot \nabla \vec{V} = -\nabla P + \frac{1}{\text{Re}} \nabla^2 \vec{V} - \frac{\text{Gr}}{\text{Re}^2} \theta \cdot \vec{g} \quad (2)$$

$$\frac{\partial \theta}{\partial \tau} + \vec{V} \cdot \nabla \theta = \frac{1}{\text{Re Pr}} \nabla^2 \theta \quad (3)$$

Conduction heat transfer is taken into account for the bottom plate, i.e., $Y < B/H$

$$\frac{\partial \theta}{\partial \tau} = \frac{1}{\text{Re Pr}} \nabla^2 \theta \quad (4)$$

The inflow velocity profile is assumed to be uniform $U=1$ at the inlet $X=0$. The temperature of the air entering the duct is set at ambient temperature, i.e., $\theta=0$. At the exit of the duct, fully developed flow conditions are assumed to be satisfied, i.e.,

$$\frac{\partial U}{\partial X} = 0; \quad V=0 \quad \text{and} \quad \frac{\partial \theta}{\partial X} = 0 \quad \text{at} \quad X=L/H \quad (5)$$

The no-slip conditions and adiabatic surface assumption at the top and the bottom walls are implemented as follows:

$$U=0; \quad V=0 \quad \text{and} \quad \frac{\partial \theta}{\partial X} = 0 \quad \text{at} \quad Y=0 \quad \text{and} \quad (B+H)/H \quad (6)$$

The local convective heat transfer from the heat sources is described by the local Nusselt number Nu defined as

$$\text{Nu} = \frac{h_c \cdot h}{k} \quad (7)$$

The average convective heat transfer coefficient, is found by integrating over the surface of the heat source

Table 1 Grid independence test

Grid size	151 × 58	251 × 68	351 × 78
$\text{Nu}_{\text{av}1}$	18.92	18.73	18.80
$\text{Nu}_{\text{av}2}$	13.82	14.46	14.50
ΔP_{av} (Pa)	0.163	0.132	0.130

Table 2 Typical time requirements for computations and experiments

	Experiment (h)	Computation (h)
Initial run (time to reach first steady state)	6	6
Change in flow conditions (no hardware change)	2	6
Change in hardware (no fabrication needed)	7	6
Change in hardware (fabrication needed)	24–48	6

$$h_{\text{av}} = \int_{C_{\text{hs}}} h_c(n) dn \quad (8)$$

Then, the average Nusselt number for a heat source Nu_{av} becomes

$$\text{Nu}_{\text{av}} = \frac{h_{\text{av}} h}{k} \quad (9)$$

The preceding governing equations are solved using the finite volume method for primitive variables on a nonuniform staggered grid. Pressure calculations are done using a scheme similar to the SIMPLER algorithm as explained in [16] in detail. The alternating direction implicit (ADI) method is used to solve the governing differential equations.

Validation of the Computations and Grid Independence

Study. For validation purposes, the Strouhal number St , based on the channel height is calculated when only a square promoter is located at the center of the channel. The width of the promoter is changed from $0.1H$ to $0.3H$ and Re is kept at 600. The results are compared to the results from [14] and they are found to be in very good agreement, as shown in Fig. 4.

The grid independence study is also performed for $\text{Re}=900$ and $h_p=0.235H$ and results are tabulated in Table 1. The most appropriate grid system, when the accuracy of the results and the computational effort are considered, is found to be 251×68 . Other numerical parameters, such as time step and convergence criterion, are also verified to obtain results that are independent of the values chosen.

Design Methodology

The advantage of using concurrent simulation and experiment is that these approaches can be carried out for different design spaces in a concurrent manner and the results can be used to provide quantitative inputs for increased efficiency in design. This methodology represents a dynamic data driven application system since experiment and simulation are performed concurrently in

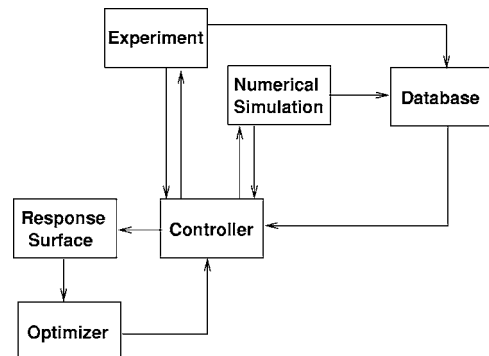


Fig. 5 Schematic representation of DDDOM methodology

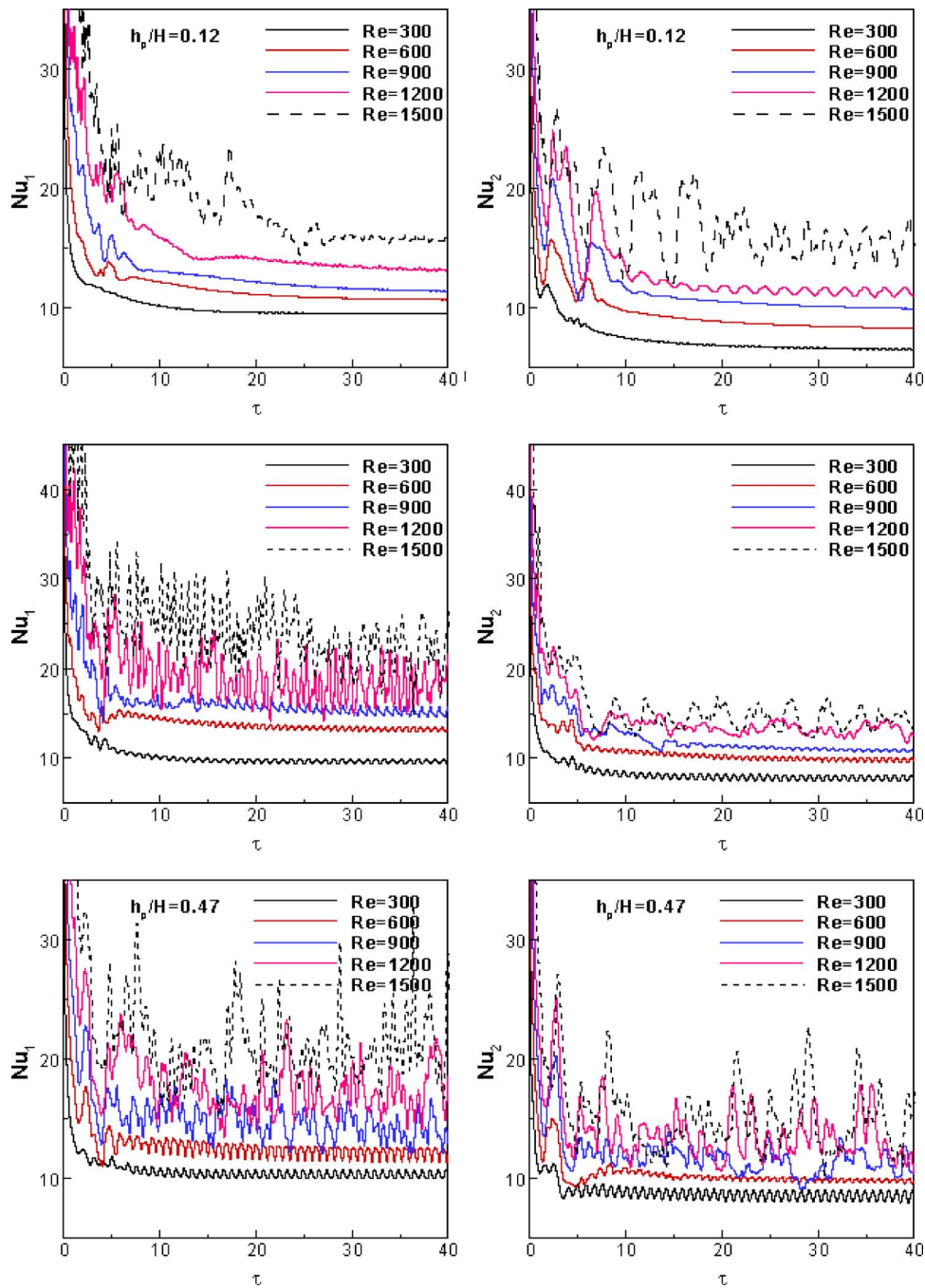


Fig. 6 Transient Nu for (a) $h_p/H=0.12$ first heat source, (b) $h_p/H=0.12$ second heat source, (c) $h_p/H=0.235$ first heat source, (d) $h_p/H=0.235$ second heat source, (e) $h_p/H=0.47$ first heat source, and (f) $h_p/H=0.47$ second heat source

real time [15,17]. This is a significant departure from the conventional approach, wherein experiment and simulation are performed sequentially. Typical time requirements to obtain a result, for the current system of interest, using both methods are tabulated in Table 2.

The proposed design strategy, as shown in Fig. 5, consists of a controller, an optimizer, a surrogate model, experiment, and simulation. Only the features of the components are given in this paper, detailed descriptions of these components are given in [15]. The controller provides direction and control of the design and optimization process. That is, it is responsible for choosing the right tool (experimentation or computation) for the next data point. The choice is made according to the operating point. In this study, only

the Reynolds number and promoter geometry have been used as the choice criteria. The critical Re values, at which the computations resulted in chaotic and high unstable flows, are obtained using numerical simulation. For lower Re values simulation is used and for higher Re values experimentation is employed. The purpose of the database is to store all the earlier results that may be fed into the surrogate model to avoid duplicate or unnecessary runs or testing. The results obtained in an earlier study [18] on heat transfer and pressure drop from protruding heat sources without any vortex generator are considered as a baseline and used in the development of the response surfaces. The enhancement factors are also calculated with respect to the results presented in this early study. The surrogate model (response surface) is developed

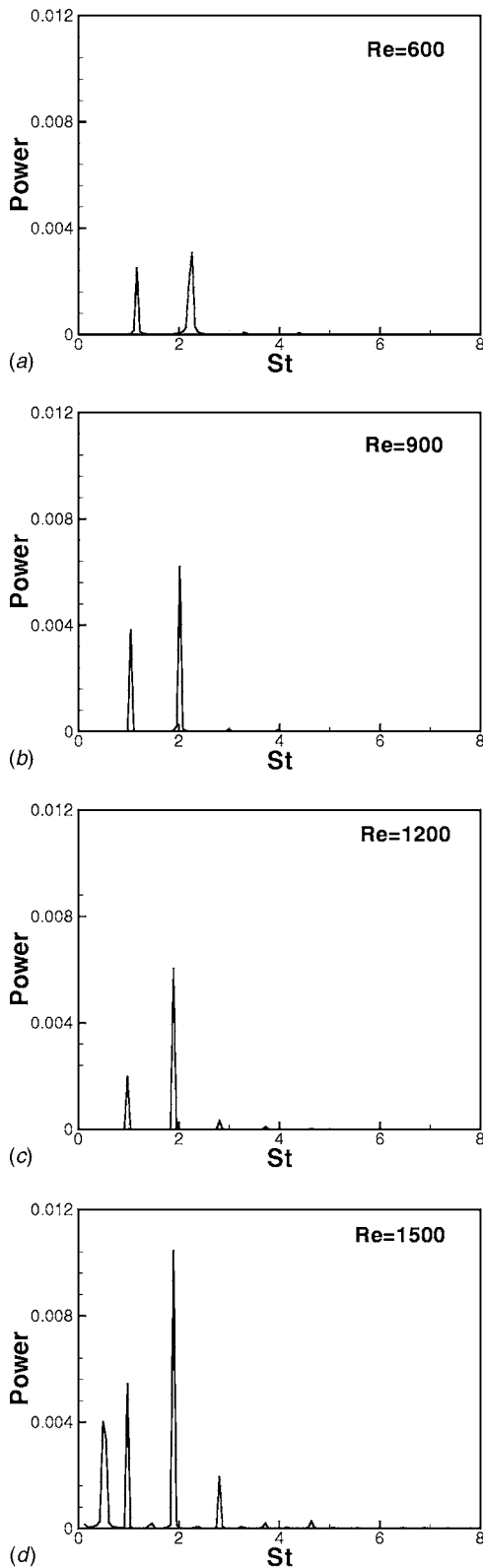


Fig. 7 Power spectrum of axial velocity component downstream of the vortex promoter at (a) $Re=600$, (b) $Re=900$, (c) $Re=1200$, and (d) $Re=1500$

using the experimental and numerical results obtained. The response surface generated is then used by the optimizer to find the optimal design variables. Although not used in the present study, this process can be repeated by reducing the size of the search domain in an iterative manner to improve the optimal points.

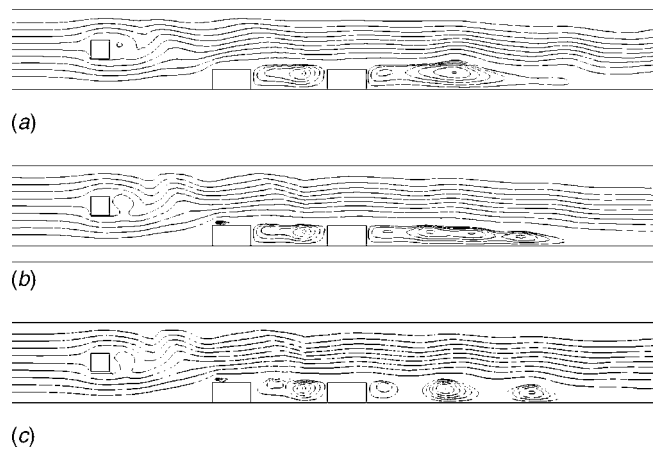


Fig. 8 Streamlines for $h_p/H=0.235$ at (a) $Re=300$, (b) $Re=900$ and (c) $Re=1200$

Results and Discussions

The temperature and velocity distributions, the heat transfer rates, and the pressure drop are calculated using the described simulation code for laminar and oscillatory flows. For higher Re values, at which chaotic flow behavior is observed computationally, experiments are employed. The switch between simulation and experiment is determined based on the critical Reynolds number Re_{cr} at which transition to chaotic flow conditions takes place.

Computed time dependent Nu values, as shown in Fig. 6, revealed the onset of chaotic flow. These critical Re values are found to be 1500 for $h_p/H=0.12$, 1200 for $h_p/H=0.235$, and 900 for $h_p/H=0.47$. Moreover, the power spectrums of the axial velocities downstream of the vortex promoter of size $h_p/H=0.235$, without any heat sources located in the channel, as displayed in Fig. 7, reveal the existence of two dominant frequencies, which are represented by the Strouhal number St for all Re values up to 1200. Above $Re=1200$ the initial transition to chaotic flow is observed, where the number of oscillation frequencies increases rapidly after this flow condition, indicating a more complex flow structure.

Based on the observations of the critical values of Re , the application ranges of numerical simulation and experiment for the design variables are determined for the controller. The criteria are selected such that numerical simulation is used for $Re < Re_{cr}$ and for rectangular geometries (only square used in this study) and

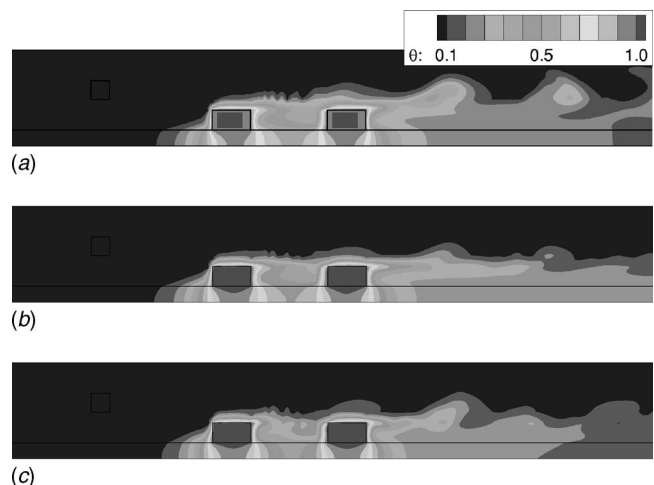


Fig. 9 Temperatures for $h_p/H=0.235$ at (a) $Re=300$, (b) $Re=900$, and (c) $Re=1200$

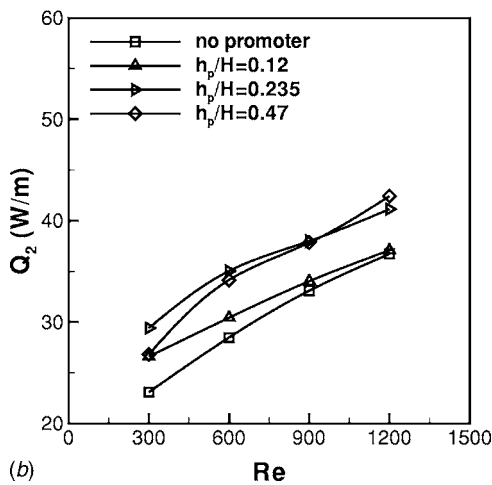
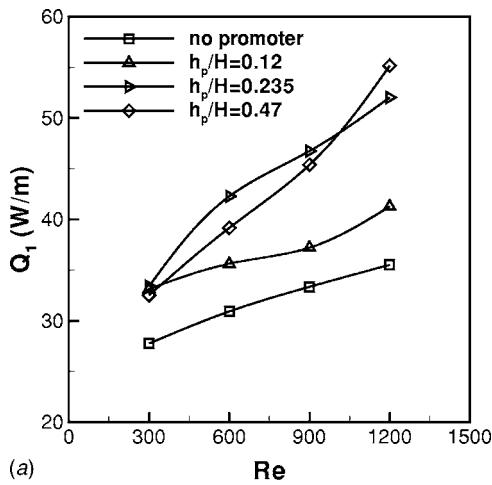


Fig. 10 Computed heat transfer rate as a function of Re and h_p/H (a) first heat source and (b) second heat source

various promoter sizes. Experiment however, is employed for $Re > Re_{cr}$, for square, hexagonal, and circular geometries of different sizes ranging from $0.12H$ to $0.47H$.

For all computations, the temperatures of the heat sources are set at 60°C , i.e., $(T_s - T_\infty) = 60^\circ\text{C}$, which is assumed to be the allowable temperature limit for the electronic components, in order to compute the maximum heat transfer rate from the heat sources. Similarly, during the experiments, the heat transfer rates are measured when steady state component temperatures reach this allowable temperature limit. The locations of the vortex promoter and the first heat source are set at $L_{px} = 3H$ and $L_1 = 4.5H$, respectively, for all computations and experiments. The separation distance between the heat sources is set at $d = H$.

The computed streamlines and temperature contours are displayed in Figs. 8 and 9 for $h_p/H = 0.235$. The streamlines at different Re values show that the vortices generated by the promoter cause an unsteady flow over the thermal sources. The vortex promoter splits and accelerates the airflow through the first heat source. As Re increases the circulating cells located between the heat sources get closer to the second heat source. In addition to the two major circulation zones, a relatively small secondary flow generated at top of the first heat source is observed. The temperature contours reveal that the air temperature between the sources is about the same for $Re = 300$ and $Re = 900$, but decreases as it is raised to 1200.

The heat transfer rates as functions of Re and promoter size are displayed in Figs. 10–13. The vortex promoter causes flow separation,

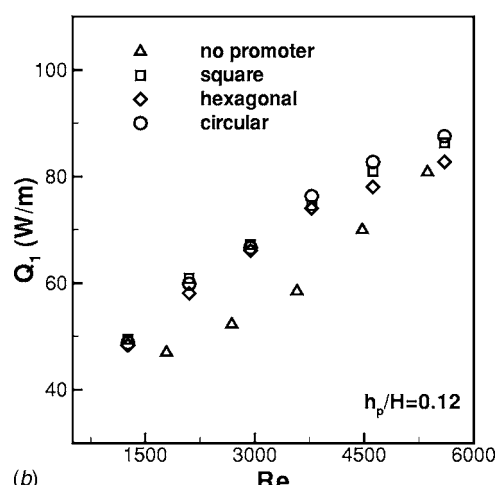
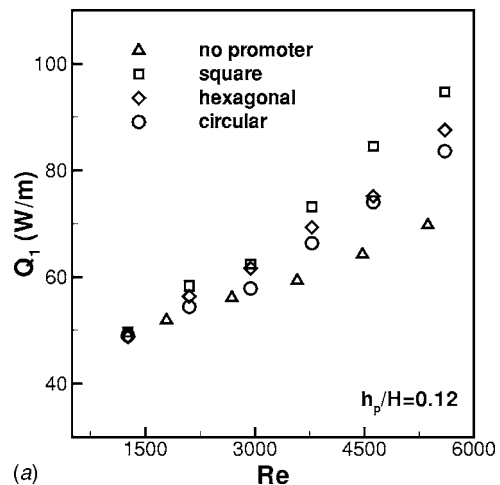


Fig. 11 Measured heat transfer rates for vortex promoter of size $h_p/H = 0.12$ (a) first heat source and (b) second heat source

and through the bottom of the promoter, air is pushed to the first heat source at a higher velocity. This causes the convection heat transfer coefficient to increase locally at the upstream face of the first heat source and enhances the heat transfer rate. The heat transfer from the second heat source however, suffers from thicker thermal boundary layer due to the flow separation, which takes place at the top left corner of the first heat source. The results show that the heat removal rate from the first heat source is about 18% to 35% more than that from second heat source. The raise in Q as Re is increased from 300 to 1200 is found to be about 25% to 80% for the first and 40% to 60% for the second source. The enhancement due to the vortex generator is more profound for the first source causing 20% to 56% increase in Q_1 and about 15% in Q_2 when compared to results obtained without a vortex promoter. In the chaotic flow regime and for all promoter sizes, the square and the hexagonal vortex generators are found to enhance heat transfer about 6–14% more than the circular promoter. The increase in the heat removal rate due to the placement of a vortex promoter depends on the promoter height and is found to be directly proportional for the first heat source. That is, a larger vortex promoter results in more heat transfer from the first heat source. The maximum enhancements in Q_1 is obtained using a square promoter and measured to be around 27% for $h_p/H = 0.12$, around 38% for $h_p/H = 0.235$, and around 50% for $h_p/H = 0.47$. The maximum increase in Q_1 is observed at the maximum Re value, i.e., $Re = 5600$. The enhancement in Q_2 due to the vortex generator however, is almost constant for all promoter sizes, and measured

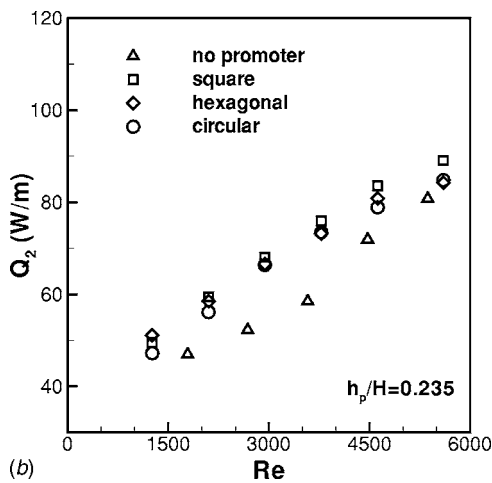
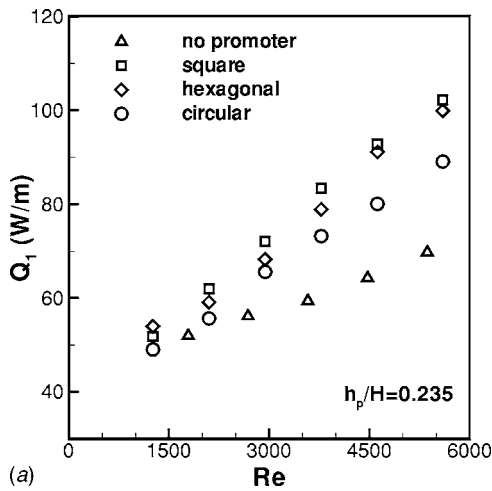


Fig. 12 Measured heat transfer rates for vortex promotor of size $h_p/H=0.235$ (a) first heat source and (b) second heat source

to be between 10% and 25%. The maximum increase in Q_2 is obtained in the Re range of from 2000 to 4000. At higher Re values, the existence of the vortex promotor is found to have no effect on Q_2 .

One of the main goals in the design of cooling systems is to minimize pressure drop, which affects the required fan power and cost. The addition of the vortex generator, which is found to be effective in increasing the heat transfer capabilities, however, introduces additional pressure drop into the system. It promotes turbulence in the channel and thus increases the mixing in the flow field which leads to rise in the loss of pressure. Thus, in the design and optimization of the size and geometry of the vortex generator, including this pressure drop for practical applications is required. The effects of promotor size and shape on the pressure drop are studied over a wide range of Re. The results from numerical simulation and experiments are shown in Figs. 14 and 15. In the sub Re_{cr} flow regime, the promotor of size $h_p/H=0.12$ causes almost no additional pressure drop in the system, however, the raise in pressure drop gets significant as the promotor size is increased. A promotor of size $h_p/H=0.47$ is found to produce about 350% to 460% increased pressure drop as Re is increased from 300 to 1200. The pressure loss drastically increases with Re in the high Re_{cr} flow regime. The smallest size promotor causes up to 48% more ΔP in the channel than the system without any promotor. This increase in ΔP becomes even more severe at larger sizes, resulting in 92% when h_p/H is set at 0.235 and 300% when

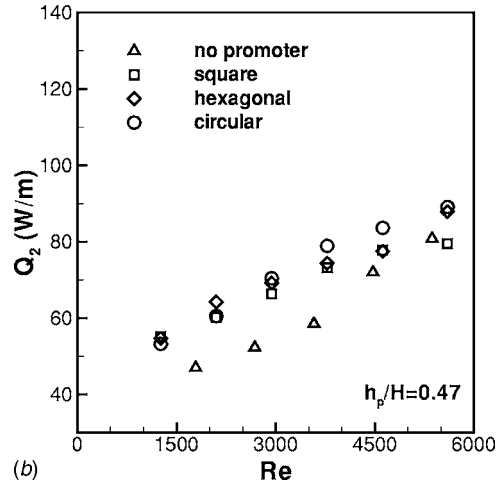
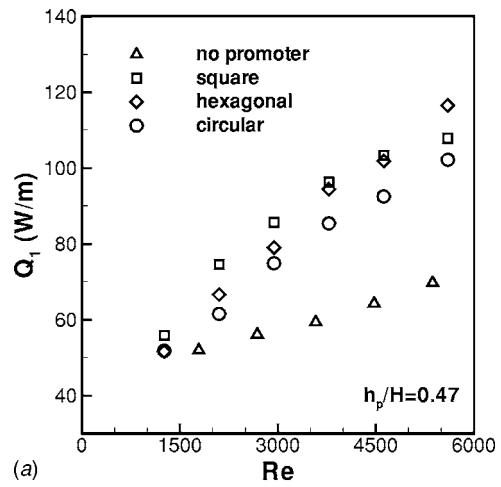


Fig. 13 Measured heat transfer rates for vortex promotor of size $h_p/H=0.47$ (a) first heat source and (b) second heat source

h_p/H is set at 0.47. The results obtained with different promotor geometries with the same blockage ratios reveal that the shape of the promotor has no significant effect on the pressure drop for $h_p/H=0.12$ and 0.235. However, for $h_p/H=0.47$, the circular promotor is found to cause 26% less ΔP than the other two shapes.

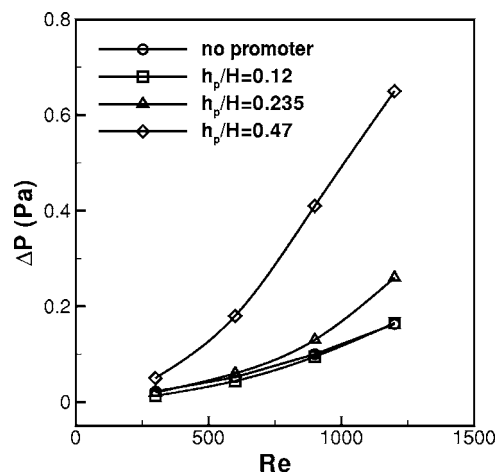


Fig. 14 The effect of vortex promotor size on the pressure drop

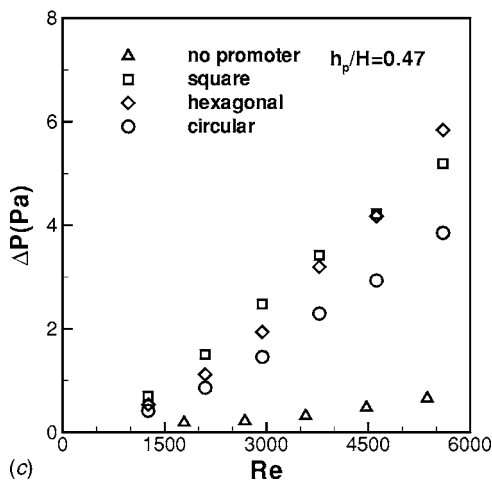
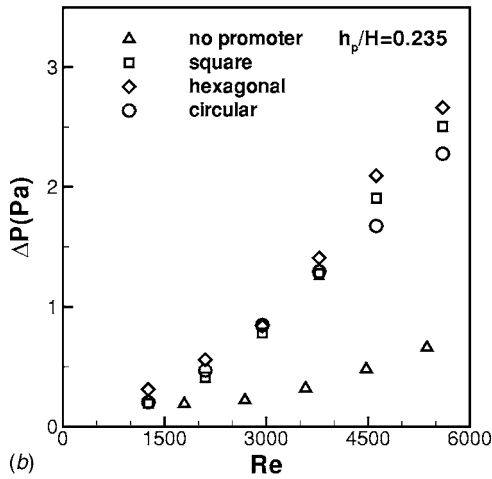
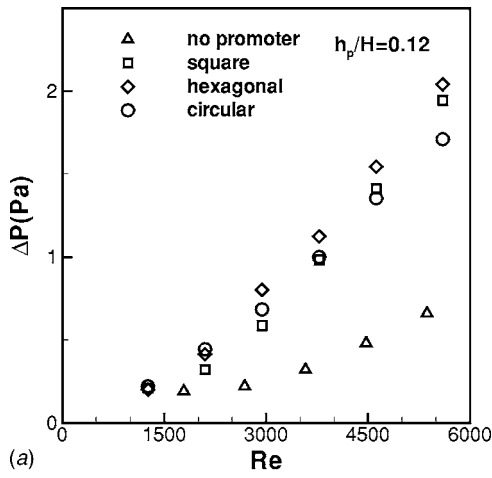


Fig. 15 Measure pressure drop as a function of Re for (a) $h_p/H=0.12$, (b) $h_p/H=0.235$, and (c) $h_p/H=0.47$

Combining Computational and Experimental Results. The implemented design methodology is founded on combining computational and experimental inputs for design optimization. This leads to extended search domains and more accurate results in a time efficient way compared to traditional approaches. The results, obtained using numerical simulation and experiment as displayed in Figs. 16 and 17, show very good agreement. The numerical model is used efficiently for low Re values at which

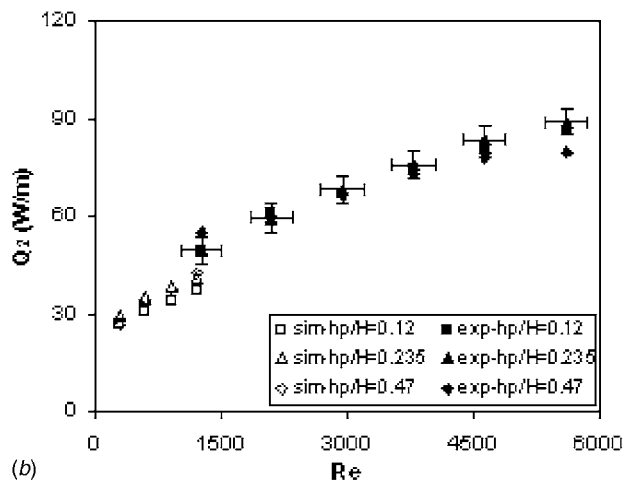
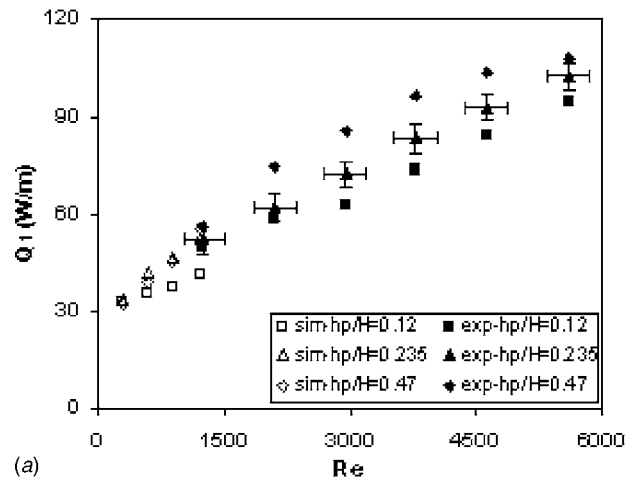


Fig. 16 Combined computational and experimental results for (a) Q_1 and (b) Q_2

experimental approach is costly and requires expensive equipment. However, due to the lack of accuracy of current turbulent models used in cooling problems at high Re values, experiment provides more reliable inputs for design.

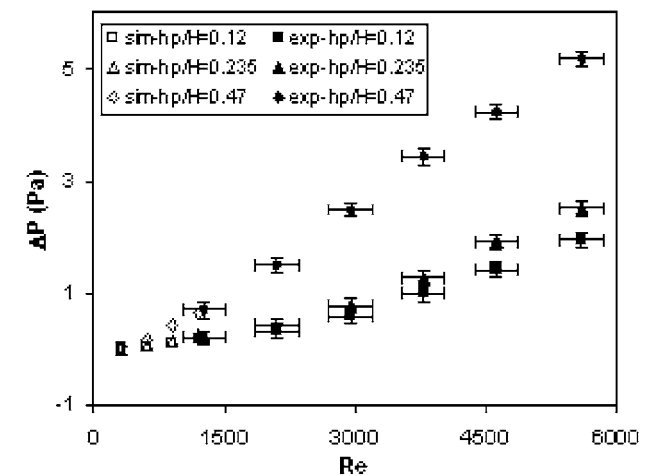


Fig. 17 Combined computational and experimental results for ΔP

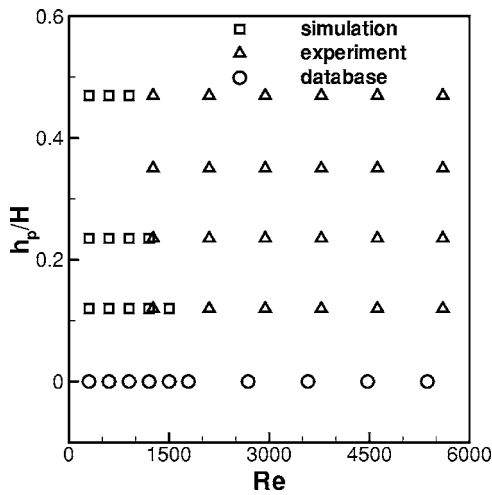
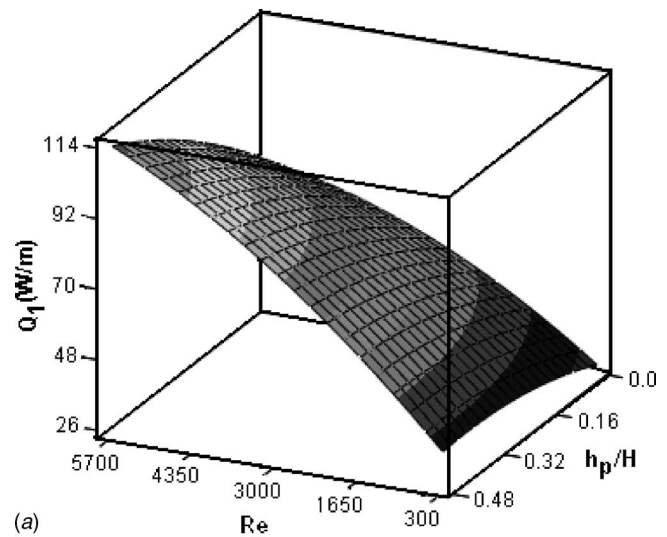


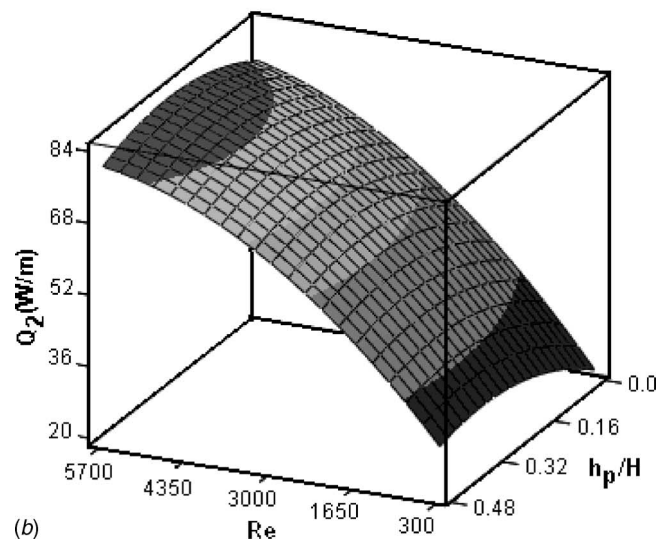
Fig. 18 Distribution of data points used to generate the responses

Design Optimization of the System. The database, which is used in the present design methodology, is created using the results obtained from an early study [18] on mixed convection problem in a channel. The inputs from the database are used to estimate the heat transfer rates and the pressure loss when $h_p/H=0$. This reduces the total number of new data points to be added to generate the response surfaces. The data points used in the response surface are depicted in Fig. 18. Although the efficiency of design methodology, in terms of the number of required data points, is not considered for the present study, the inputs from the database helps improve the performance of the methodology by eliminating the possibility of replicating an existing data point. The response surfaces for Q_1 , Q_2 , and ΔP , as functions of Re and h_p/H for a square promoter are shown in Figs. 19 and 20. The calculated correlation coefficients, R^2 and R_{adj}^2 , are found to be more than 0.80, as given in Table 3, and the difference between them is observed to be less than 0.02.

The results show that the heat removal rates from both of the heat sources, and the pressure drop increase with Re, regardless of the size of the vortex promoter. Therefore, the optimal values of the vortex promoter size are presented for a given Re. The objective function chosen for finding the optimal promoter sizes play an important role, as the optimal values change depending on the design objectives. The variation of the optimal size of a square vortex generator as a function of Re is shown in Fig. 21, for various objective functions. The results for the heat removal rate from the first heat source reveal that an optimal promoter size, which maximizes Q_1 , is found to be $h_p/H=0.47$ for $Re>1300$. The response of Q_2 however, shows that the optimal size is inversely proportional to Re for this thermal source. As Re increases, smaller promoter is observed to be desirable for the maximization of Q_2 . When the total heat transfer from the system is considered as the main objective the first heat source is found to be the dominant source, because the effect of promoter size is observed to be more profound on Q_1 than Q_2 , and thus, the optimal values of promoter size are found to monotonically increase as Re raises. The larger size promoters allow more air passes over the first heat source and increases the heat removal rate. However, the thermal wakes originated at the top left corner of the first source mixes with the cold air penetrating into the groove between the two heat sources and increases the air temperature in this region. This, in turn, results in reduced heat transfer rate from the second heat source and its effect becomes more significant as the size of the promoter increases. However, the increase in Q_1 is found to be more than the amount of decrease in Q_2 , leading the total Q to increase.



(a)



(b)

Fig. 19 Response surfaces of the heat transfer rates from (a) first heat source and (b) second heat source, for the square promoter

The response surface of the pressure loss shows that ΔP increases both with Re and h_p . Therefore, considering ΔP as the sole objective function results in the trivial solution that gives the minimum values of the design variables as the optimal values. Hence, the heat transfer rates and the pressure drop, in their normalized forms, are combined to form a single objective function F , which can be written as

$$F = W_1 \bar{Q}_1 + W_2 \bar{Q}_2 - W_3 \bar{\Delta P} \quad (10)$$

where W 's are the weights of the objective functions. The determination of the weights strongly depends on the design priorities. The responses of two different multiobjective design optimization problems are presented in Fig. 22 and Table 4 shows the optimal values of the design variables for different weight combinations.

The geometry of the vortex promoter is another important design variable for the present problem. Performances of three different geometries, namely, square, hexagonal, and circular, are studied experimentally and various objective functions are used to find the optimal one, in terms of maximizing the heat transfer rate and minimizing the pressure drop. Figures 23 and 24 show the responses of the heat transfer rates and the pressure drop obtained using different vortex generator geometries. The maximum heat

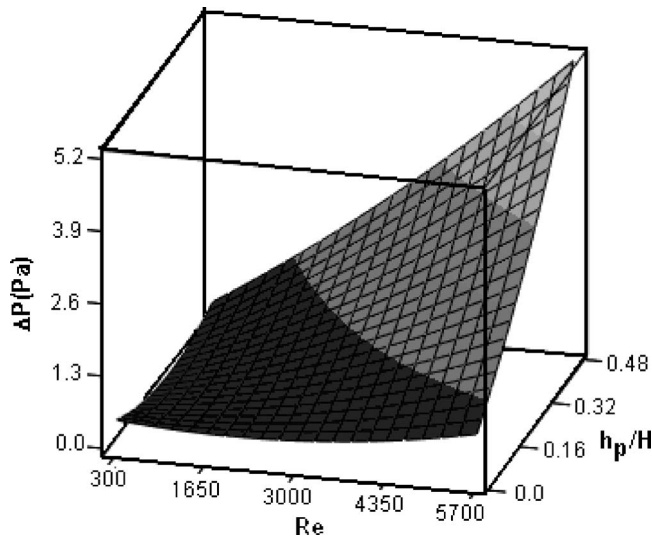
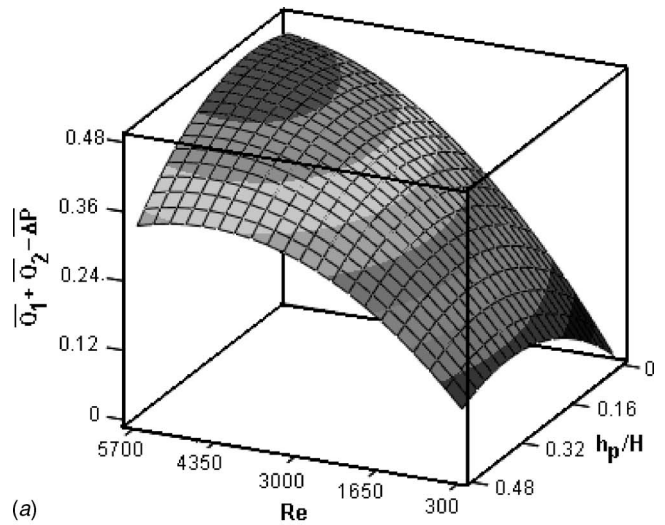
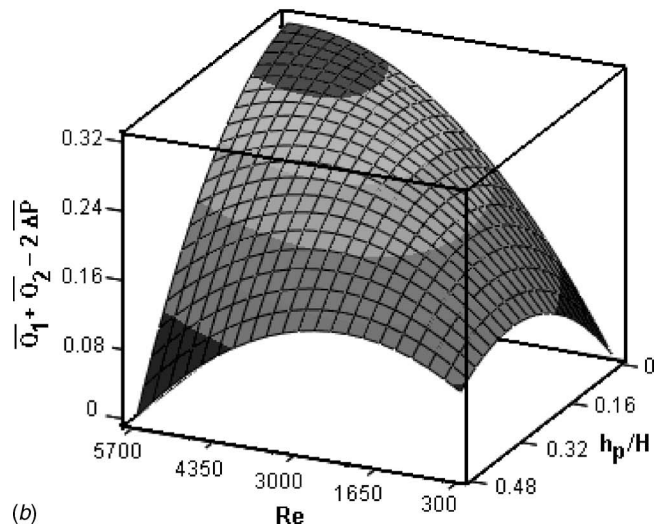


Fig. 20 Response surface of the pressure drop for the square promoter

transfer rate from the first heat source is obtained using a hexagonal promoter at $Re=5600$ and $h_p/H=0.47$. The square promoter resulted in close Q_1 values compared to the hexagonal, however, the circular promoter is found to be the less effective in terms of enhancing Q_1 . On the other hand, the heat transfer rate from the second heat source is greatest with a circular promoter, then with the hexagonal promoter and the least effective one is found to be the square promoter. The enhancement in the heat transfer rates is obtained at the expense of increased pressure drop, as shown in Fig. 24. The responses of all the promoters reveal that ΔP is maximum at $Re=5600$ and $h_p/H=0.47$. The hexagonal and square promoters cause the same amount of pressure drop and the maximum ΔP values are about 5.5 Pa, whereas the circular vortex generator increases ΔP the least, resulting in a maximum ΔP of



(a)



(b)

Table 3 Correlation coefficients for response surfaces

	Q_1	Q_2	ΔP
R^2	0.94	0.92	0.82
R^2_{adj}	0.93	0.91	0.80

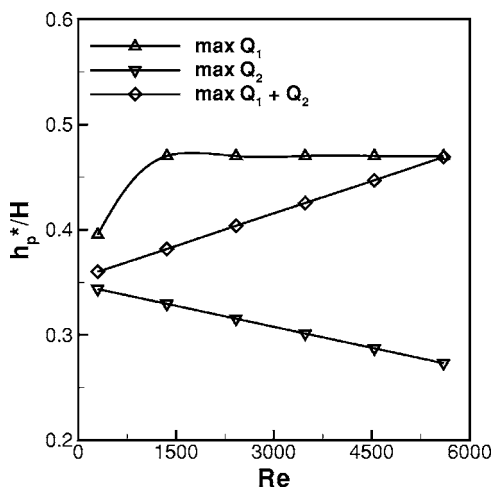


Fig. 21 Optimal size of the square promoter with Re for various objective functions

Fig. 22 Response surfaces for the objective function $F = W_1 Q_1 + W_2 Q_2 - W_3 \Delta P$ (a) $W_1 = W_2 = W_3$ and (b) $W_1 = W_2 = W_3/2$

about 4 Pa.

Table 5 gives the optimal shape and optimal values of the design variables for different objective functions. The results show that when ΔP is the major design concern, the use of the vortex promoter is not desired, and placement of a promoter makes the design worse. However, when the heat transfer rates are considered as sole design objectives and when both objectives have equal importance, vortex generators are found to improve the system performance. When only Q_1 is to be maximized, hexagonal promoter is found to be the best choice, when only Q_2 is to be maximized, circular is found to be the best choice, and when total

Table 4 Optimal points for different weight combinations for the objective function $F = W_1 Q_1 + W_2 Q_2 - W_3 \Delta P$

	Re^*	h_p^*/H	Objective value
$W_1 = W_2 = W_3$	5600	0.12	0.482
$W_1 = W_2 = 2 \times W_3$	5600	0.26	0.654
$W_1 = W_2 = 3 \times W_3$	5600	0.32	0.742
$W_1 = W_2 = W_3/2$	5460	0	0.328
$W_1 = W_2 = W_3/3$	5000	0	0.251

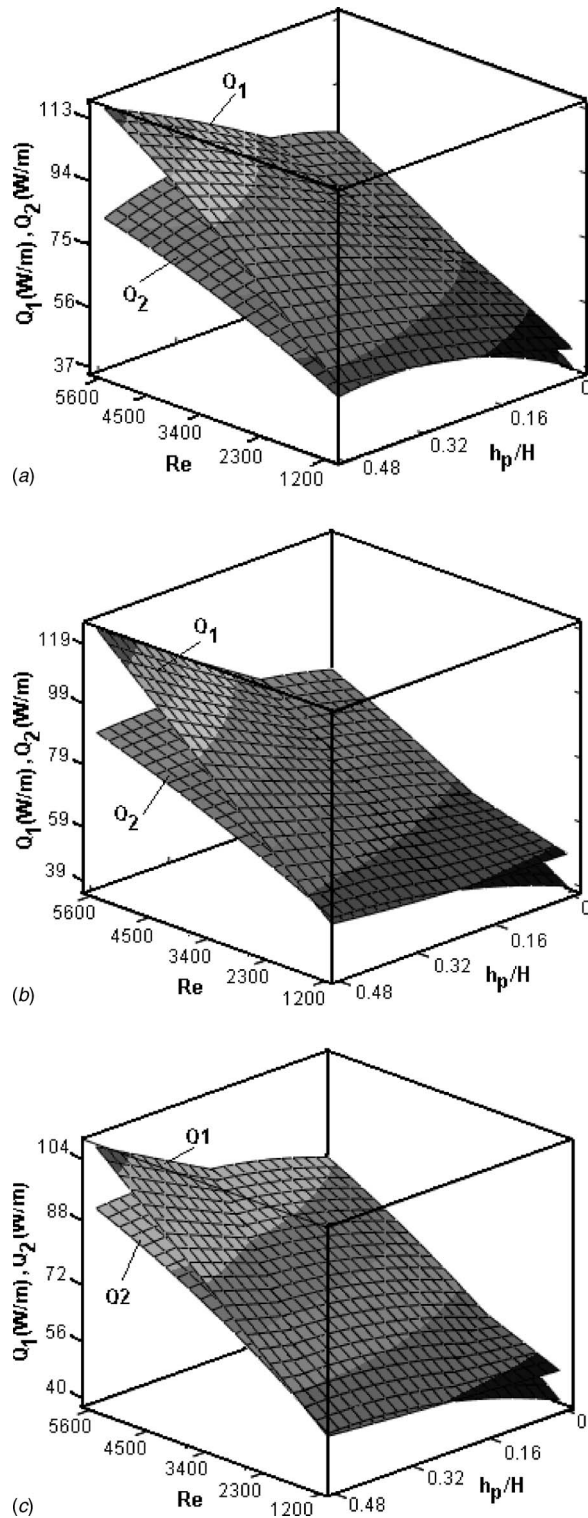


Fig. 23 Responses of Q_1 and Q_2 for (a) square, (b) hexagonal, and (c) circular vortex promoter

Q is to be maximized, square promoter is found to be the best choice. For the case, when maximizing the heat transfer rates and minimizing the pressure drop have equal importance, the square promoter of size $h_p/H=0.16$ is obtained to provide the optimal performance.

Conclusions

In the present study, optimization of the size and geometry of a vortex promoter located in a channel is carried out. Concurrent

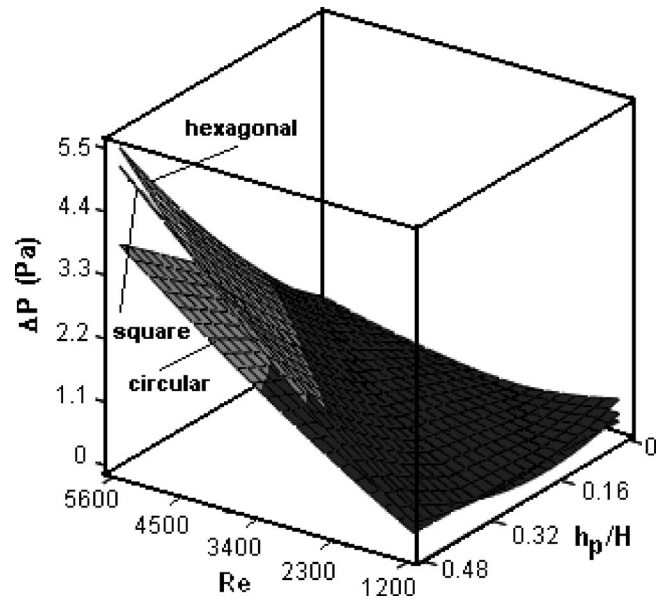


Fig. 24 Response of ΔP for three promoter geometries

use of numerical simulation and experiment is used to generate response surfaces for the optimization of the size of a square promoter, and the flow condition. The results obtained from the earlier studies, which have been stored in the database, are used effectively to find more accurate and reliable responses. It is shown that combining computational and experimental approaches lead to faster, accurate, and more reliable design optimizations.

Three different types of vortex generator geometries are studied experimentally, and their performances are evaluated as a multi-objective design problem. Square and hexagonal promoters are observed to have similar performances, in terms of the heat removal rates and the pressure drop, but hexagonal promoter is noticed to cause little more ΔP than the square promoter does. The enhancement in heat transfer rates because of the vortex generator is measured to be around 27–50%. Hexagonal and square geometries are found to enhance Q_1 about 10% more than the circular promoter. The maximum enhancement in Q_1 is observed when a hexagonal promoter of size $h_p/H=0.47$ is used, whereas the circular geometry, independent of the promoter size, is obtained to be the most desirable for maximizing Q_2 . The heat transfer rate from the first heat source shows a monotonic increase with Re , making the largest Re value the most favorable. For Q_2 however, the greatest enhancement is observed to occur in the range of

Table 5 Optimal geometry and design variables for different weight combinations of the objective function $F=W_1Q_1+W_2Q_2-W_3\Delta P$

	Geometry	Re^*	h_p^*/H	Objective value
$W_1=1, W_2=W_3=0$	Hexagonal	5600	0.47	1.000
$W_2=1, W_1=W_3=0$	Circular	5600	0.36	1.012
$W_3=1, W_1=W_2=0$	No vortex promoter			
$W_1=W_2, W_3=0$	Hexagonal	5600	0.47	0.975
$W_1=W_2=W_3$	Square	5600	0.16	0.423
$W_1=W_2=2 \times W_3$	Circular	5600	0.47	0.590
$W_1=W_2=3 \times W_3$	Hexagonal	5600	0.47	0.693
$W_1=W_2=W_3/2$	No vortex promoter			
$W_1=W_2=W_3/3$	No vortex promoter			

Re=2000 to 4000, and as Re > 4500 the use of vortex promoter is found not to increase the heat transfer performance of the second component.

When the pressure drop characteristics of different geometries are compared, the greatest ΔP is obtained using the largest size hexagonal promoter, resulting in 26% more ΔP than that of a circular promoter of the same size. All geometries are observed to cause about 48–92% of raise in ΔP for blockage ratios less than 0.235. The sacrifice in the pressure drop is observed to be more severe as the promoter size is further increased, being as much as 300% when a hexagonal promoter of size $h_p/H=0.47$ is placed into the flow field at Re=5600.

The individual objective functions are combined to form a single objective function, which reflects the dual effects of the vortex promoters. The circular promoter is found to be the best choice when the pressure is the main design concern. As the importance of the pressure drop is reduced relative to the heat transfer rates, hexagonal and square geometries are obtained to have better performances.

Nomenclature

B	= thickness of the bottom plate
d	= separation distance between heat sources
f	= oscillation frequency, Hz
g	= gravitational acceleration
Gr	= Grashof number, $Gr = g\beta H^3(T_s - T_\infty) / \nu^2$
H	= channel height
h	= height of protruding heat sources
h_p	= height of the vortex promoter
k	= thermal conductivity
L	= length of the channel
L_{px}	= axial location of the center of the vortex promoter
L_1	= location of the first heat source
Nu	= local Nusselt number
\overline{Nu}_{tot}	= normalized total average Nusselt number
Nu_{av}	= surfaced averaged Nusselt number
P	= dimensionless pressure
Pr	= Prandtl number, $Pr = \nu / \alpha$
R^2	= coefficient of multiple determinations
R^2_{adj}	= adjusted R^2 value
Re	= Reynolds number based on channel height
St	= Strouhal number, $St = fH / U_\infty$
T	= temperature
T_s	= heat source temperature
t	= time
U, V	= dimensionless velocity components in x - and y -axis
W_i	= weight coefficients of individual objective functions
w	= heat source width
X, Y	= coordinate axes

Greek Symbols

α	= thermal diffusivity
β	= coefficient of thermal expansion
ν	= kinematic viscosity

ρ	= density of fluid
ΔP	= pressure drop (Pa)
$\overline{\Delta P}$	= normalized pressure drop
τ	= dimensionless time, $\tau = tU_\infty / H$
θ	= dimensionless temperature, $\theta = (T - T_\infty) / (T_s - T_\infty)$
θ_s	= dimensionless heat source temperature

Subscripts

1	= first heat source
2	= second heat source
∞	= uniform or ambient

Superscripts

*	= optimal value
---	-----------------

References

- [1] Davis, R. W., and Moore, E. F., 1982, "A Numerical Study of Vortex Shedding From Rectangles," *J. Fluid Mech.*, **116**, pp. 475–506.
- [2] Okajima, A., 1982, "Strouhal Number of Rectangle Cylinders," *J. Fluid Mech.*, **123**, pp. 379–398.
- [3] Mukhopadhyay, A., Biswas, G., and Sundararajan, T., 1992, "Numerical Investigation of Confined Wakes Behind a Square Cylinder in a Channel," *Int. J. Numer. Methods Fluids*, **14**, pp. 1473–1484.
- [4] Kapat, J. S., Ratnathicam, J., and Mikic, B. B., 1994, "Experimental Determination of Transition to Turbulence in a Rectangular Channel with Eddy Promoters," *ASME J. Fluids Eng.*, **116**, pp. 484–487.
- [5] Karniadakis, G. E., Mikic, B. B., and Patera, A. T., 1988, "Heat Transfer Enhancement by Flow Destabilization: Application to the Cooling of Chips," *Cooling Technology for Electronic Equipment*, Hemisphere, Washington D.C.
- [6] Ratts, E., Amon, C. H., Mikic, B. B., and Patera, A. T., 1988, "Cooling Enhancement of Forced Convection Air Cooled Chip Array Through Flow Modulation Induced by Vortex Shedding Cylinders in Cross Flow," *Cooling Technology for Electronic Equipment*, Hemisphere, Washington D.C.
- [7] Lin, C. N., and Jang, J. Y., 2002, "Conjugate Heat Transfer and Fluid Flow Analysis in Fin-Tube Heat Exchangers with Wave-Type Vortex Generators," *J. Enhanced Heat Transfer*, **9**, pp. 123–136.
- [8] Wang, L. B., Zhang, Y. H., Su, Y. X., and Gao, S. D., 2002, "Local and Average Heat/Mass Transfer over Flat-Tube Bank Fin Mounted In-Line Vortex Generators with Small Longitudinal Spacing," *J. Enhanced Heat Transfer*, **9**, pp. 77–87.
- [9] Khan, J. A., Hinton, J., and Baxter, S. C., 2002, "Enhancement of Heat Transfer with Inclined Baffles and Ribs Combined," *J. Enhanced Heat Transfer*, **9**, pp. 137–151.
- [10] Webb, B. W., and Ramadhyani, S., 1985, "Conjugate Heat Transfer in a Channel with Staggered Ribs," *Int. J. Heat Mass Transfer*, **28**(9), pp. 1679–1687.
- [11] Valencia, A., 1999, "Heat Transfer Enhancement Due to Self-Sustained Oscillating Transverse Vortices in Channels with Periodically Mounted Rectangular Bars," *Int. J. Heat Mass Transfer*, **42**, pp. 2053–2062.
- [12] Garimella, S. V., and Eibeck, P. A., 1991, "Enhancement of Single Phase Convective Heat Transfer from Protruding Elements using Vortex Generators," *Int. J. Heat Mass Transfer*, **34**, pp. 2431–2433.
- [13] Kim, S. Y., Kang, B. H., and Jaluria, Y., 1998, "Thermal Interaction Between Isolated Heated Electronic Components in Pulsating Channel Flow," *Numer. Heat Transfer, Part A*, **34**, pp. 1–21.
- [14] Wang, Q., and Jaluria, Y., 2002, "Unsteady Mixed Convection in a Horizontal Channel with Protruding Heated Blocks and a Rectangular Vortex Promoter," *Phys. Fluids*, **14**(7), pp. 2113–2127.
- [15] Zhao, H., Icoz, T., Jaluria, Y., and Knight, D. D., 2007, "Application of Data Driven Design Optimization Methodology to a Multi-objective Design Optimization Problem," *J. Eng. Design*, in press.
- [16] Patankar, S. V., 1980, *Numerical Heat Transfer and Fluid Flow*, Hemisphere, New York.
- [17] Knight, D., Elliott, G., Jaluria, Y., Langrana, N., and Rasheed, K., 2002, "Automated Optimal Design Using Concurrent Integrated Experiment and Simulation," *AIAA Paper No. 2002-5636*, AIAA/ISSMO Symposium on Multidisciplinary Analysis and Optimization, Atlanta, GA.
- [18] Icoz, T., and Jaluria, Y., 2006, "Design of Air and Liquid Cooling Systems For Electronic Components Using Concurrent Simulation and Experiment," *ASME J. Electron. Packag.*, in press.

A Discussion of Transpiration Cooling Problems through an Analytical Solution of Local Thermal Nonequilibrium Model

J. H. Wang¹

H. N. Wang

Department of Thermal Science and Energy Engineering,
University of Science and Technology of China,
Jinzhai Road No. 96 Hefei 230027 Anhui,
P. R. China

To study transpiration cooling problems, an analytical solution of the local thermal nonequilibrium (LTNE) model with the second or third boundary conditions is presented. This solution is obtained through neglecting the thermal conduction of the fluid coolant in porous media. By the analytical solution, two problems are investigated. At first, the parameters which influence transpiration cooling effects are analyzed, and the analysis indicates that the cooling effects are dominated by coolant mass flow rate, the Biot number at the hot surface of porous plate, and the Biot number in the pores. Second, the error caused by the assumption of the local thermal equilibrium (LTE) model is quantitatively discussed, and the variation trend of the LTE error is analyzed. Based on the analytical solution and the error analysis, a quantitative criterion to choose the LTNE or LTE model is suggested, and the corresponding expression is also given in this paper.

[DOI: 10.1115/1.2345434]

Keywords: analytical solution, local thermal non-equilibrium, transpiration cooling

Introduction

Transpiration cooling has been proven an efficient way of thermal protections by many investigations [1–6], and is widely used in various regions, such as hypersonic vehicles, gas turbine blades, rocket combustors. A physical sketch of the transpiration cooling is depicted in Fig. 1. Fluid coolant is injected into a porous plate in the direction opposite to heat flux, to protect the hot surface of the porous plate from the heat flux.

¹Corresponding author; e-mail: jhwang@ustc.edu.cn

Contributed by the Heat Transfer Division of ASME for publication in the JOURNAL OF HEAT TRANSFER. Manuscript received November 27, 2005; final manuscript received April 12, 2006. Review conducted by Ranga Pitchumani.

In some studies associated with heat and fluid flow in porous media [7,8] the assumption that the fluid coolant and the solid matrix in porous media have the same temperature is used. The model based on this assumption is called the local thermal equilibrium (LTE) model. It is a second-order differential equation. To solve this equation, only two boundary conditions (BCs) are necessary. In the studies [9,10], a common conclusion has been obtained that the LTE tends to be valid when the effective conductivity ratio of solid to fluid is extremely low. But in actual fact, the solid conductivity is usually larger than that of gaseous coolant. Investigations [11–14] also indicated that the temperatures of the two phases are not always the same, especially in the cooling or heating process with a high Reynolds number, a low Biot number, or a high Darcy number, thus the local thermal nonequilibrium (LTNE) model is suggested. This model consists of two second-order differential equations. One is the energy equation for the fluid coolant and the other for the solid matrix. But up to now, the limit of the LTE model, how high are these numbers, is still uncertain in the investigation of transpiration cooling problems.

Although the LTNE model is more reasonable, in general, to solve the two second-order differential equations, four BCs are required. However, only three formulas are widely seen to be reasonable BCs in the investigation of transpiration cooling problems, and several empirical formulas as the fourth BC are discussed in the investigations [12,15–18]. Therefore, the fourth BC of the LTNE model is still an uncertain problem.

The present work focuses on the first uncertain problem. To avoid the second problem, the thermal diffusion of the fluid coolant in porous media is neglected. Based on this simplification, the LTNE model can be analytically solved with the three BCs. Through the analytical solution, the relative difference between the temperatures of the fluid coolant and the solid matrix can be obtained, and a quantitative criterion to choose the model is suggested. By the variation trend of the analytical solution, the parameters which influence transpiration cooling effects are discussed. The objective of this work is to provide the investigators of transpiration cooling problems with a method and a quantitative criterion to choose the model and a reference to control the cooling effect.

Formulation

Governing Equations and Boundary Conditions. As shown in Fig. 1, fluid coolant with a temperature of T_c and a constant mass flow rate of m approaches the porous plate. This is a steady and one-dimensional problem. According to Amiri and Vafai [19], this problem can be described by the LTNE model

$$\text{Fluid: } (\rho c)_f v_f \frac{dT_f}{dy} = \frac{d}{dy} \left(k_{fe} \frac{dT_f}{dy} \right) + h_{sf} a_{sf} (T_s - T_f) \quad (1)$$

$$\text{Solid: } \frac{d}{dy} \left(k_{se} \frac{dT_s}{dy} \right) = h_{sf} a_{sf} (T_s - T_f) \quad (2)$$

Here $k_{se} = (1 - \epsilon)k_s$ is effective thermal conductivity of the solid matrix, $k_{fe} = \epsilon k_f + k_{dis}$ is effective thermal conductivity of the fluid

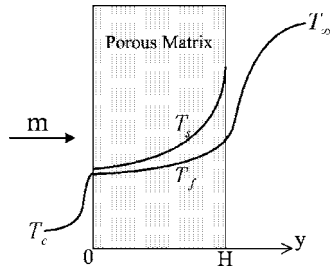


Fig. 1 Heat exchange between fluid coolant and solid matrix

coolant. k_{dis} is dispersion conductivity in the porous plate. Calmidi and Mahajan [20] indicated that it is difficult to describe the dispersion effect with an accurate quantity. However, Wakao et al. [21] and Alazmi and Vafai [19] used the following empirical formula to estimate the dispersion conductivity in packed beds:

$$k_{dis} = 0.5k_f \left(\frac{\rho_f v d_p}{\mu_f} \right) Pr.$$

In transpiration cooling problems, the conductivities of porous matrix are much larger than that of gaseous coolant, the porosity and characteristic length are small values, and the effective conductivity ratio of solid to coolant is much larger than 1. Thus the first term of the right-hand side in Eq. (1) can therefore be neglected [15–17]. For the porous media with high porosity such as metal foam, this simplification is also reasonable. An explanation of this simplification is shown in Appendix A. After elimination of the first term, Eq. (1) can be written as

$$h_{sf} a_{sf} (T_s - T_f) = mc_{pf} \frac{dT_f}{dy} \quad (3)$$

Here $m = (\rho v)_f = \text{const.}$ To solve Eqs. (2) and (3), only three BCs are required. According to Burch et al. [16] and Polezhaev and Seliverstov [17], the three BCs are

$$y = 0, \quad h(T_s - T_c) = k_{se} \frac{dT_s}{dy} \quad (4)$$

$$h(T_s - T_c) = mc_{pf}(T_f - T_c) \quad (5)$$

$$y = H, \quad k_{se} \frac{dT_s}{dy} = q \quad \text{the second BC} \quad (6a)$$

$$h(T_\infty - T_s) = k_{se} \frac{dT_s}{dy} \quad \text{the third BC} \quad (6b)$$

By introducing the following dimensionless parameters:

$$Y = y/H,$$

$$\theta = (T - T_c)/(qH/k_{se}) \quad \text{the second BC,}$$

$$\theta = (T - T_c)/(T_\infty - T_c) \quad \text{the third BC,}$$

Eqs. (2)–(5), (6a), and (6b) can be transformed into

$$\frac{d^2 \theta_s}{dY^2} - Bi(\theta_s - \theta_f) = 0 \quad (7)$$

$$Bi(\theta_s - \theta_f) = M \frac{d\theta_f}{dY} \quad (8)$$

$$Y = 0, \quad \frac{d\theta_s}{dY} = MSt\theta_s \quad (9)$$

$$\theta_f = St\theta_s \quad (10)$$

$$Y = 1, \quad \frac{d\theta_s}{dY} = 1 \quad \text{the second BC} \quad (11a)$$

$$Bi_h(1 - \theta_s) = \frac{d\theta_s}{dY} \quad \text{the third BC} \quad (11b)$$

Here, $M = mc_{pf}H/k_{se}$ is dimensionless coolant mass flow rate, $Bi = h_{sf}a_{sf}H^2/k_{se}$ is the Biot number in the pores of the porous plate, $St = h/mc_{pf}$ is the Stanton number at the cold surface. From Eq. (10), $St \in [0, 1]$. $Bi_h = hH/k_{se}$ is the Biot number at the hot surface for the third BC.

Analytical Solution. The analytical solution of differential Eqs. (7) and (8) associated with BCs (9)–(11) can be written out by the following

$$\theta_f = C_1 e^{k_1 Y} + C_2 e^{k_2 Y} + C_3$$

$$\theta_s = K_1 C_1 e^{k_1 Y} + K_2 C_2 e^{k_2 Y} + C_3 \quad (12)$$

Here

$$K_{1,2} = 1 + \frac{M}{Bi} k_{1,2}$$

$$k_{1,2} = \frac{-\frac{Bi}{M} \pm \sqrt{\left(\frac{Bi}{M}\right)^2 + 4Bi}}{2}$$

$$C_i = \frac{\Delta_i}{\Delta} \quad i = 1, 2, 3$$

Δ_i and Δ can be calculated by the Cramer's rule [22] and the following coefficient matrix:

$$\begin{pmatrix} K_1 St - 1 & K_2 St - 1 & St - 1 & 0 \\ M - k_1 K_1 & M - k_2 K_2 & M & 0 \\ K_1 k_1 e^{k_1} & K_2 k_2 e^{k_2} & 0 & 1 \end{pmatrix} \quad \text{the second BC}$$

$$\begin{pmatrix} K_1 St - 1 & K_2 St - 1 & St - 1 & 0 \\ M - k_1 K_1 & M - k_2 K_2 & M & 0 \\ (Bi_h + k_1)K_1 e^{k_1} & (Bi_h + k_2)K_2 e^{k_2} & Bi_h & Bi_h \end{pmatrix} \quad \text{the third BC}$$

A detailed description is shown in Appendix B.

Results and Discussions

From the above-obtained analytical solution and the description in Appendix B, it can be found that the temperatures of the solid matrix and the fluid coolant are dominated by four dimensionless parameters, Bi, M, Bi_h, St , at the third BC and by three parameters, Bi, M, St , at the second BC.

Effects of the Parameters on Hot Surface Temperature. Through the analytical solution, it can be verified that the influence of the Stanton number on the temperature of the solid surface is always less than 0.1% within the entire range of the Stanton number. Therefore the Stanton number is taken at 1 in the following discussions. Therefore, the temperatures of the solid matrix and the fluid coolant are dominated by three dimensionless parameters, Bi, M, Bi_h , at the third BC and by two parameters, Bi, M , at the second BC.

Figure 2 illustrates the influence of the coolant mass flow rate and the Biot number in the pores on the hot surface temperature of the solid matrix at the second BC. It can be found that at a large coolant mass flow rate M , the temperature falls rapidly when the Biot number in the pores increases. The reason is that a large Biot number Bi means an enhancement of the heat exchange between the coolant and the solid matrix, thus the cooling effect rises, the solid temperature falls. At a small M , the temperature variance with the Biot number is very small. The reason is that if the

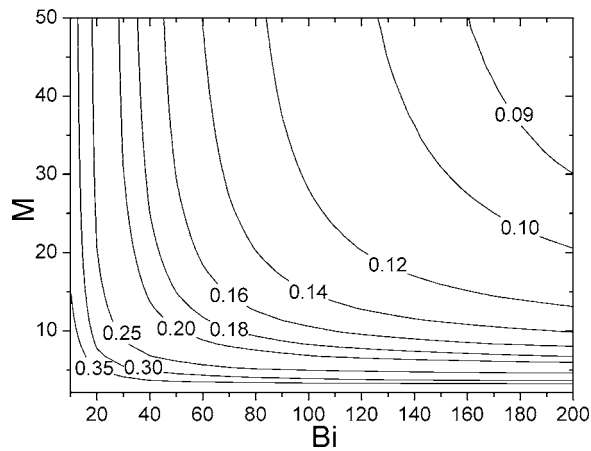


Fig. 2 Solid temperature $\theta_s|_{Y=1}$ at hot surface with coolant mass flow rate and the Biot number in the pores at the second BC

coolant mass flow rate is too small, although the heat exchange is enhanced, the total heat energy absorbed from the solid matrix is limited by the coolant mass flow rate.

Figure 3 illustrates the influence of coolant mass flow rate and the Biot number in the pores on the hot surface temperature of the solid matrix at the third BC, the Biot number at the hot surface Bi_h is 20 in Fig. 3(a) and 200 in Fig. 3(b), respectively. Through comparison of Figs. 3(a) and 3(b), it is observed that at the same

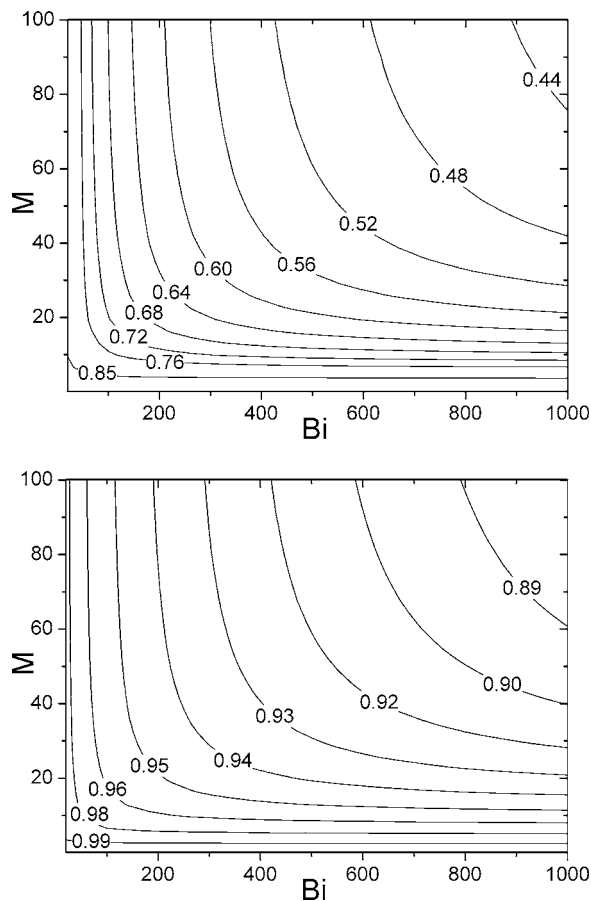


Fig. 3 Solid temperature $\theta_s|_{Y=1}$ variation with the coolant mass flow rate and the Biot numbers under the third BC. (a) $Bi_h=20$ (b) $Bi_h=200$.

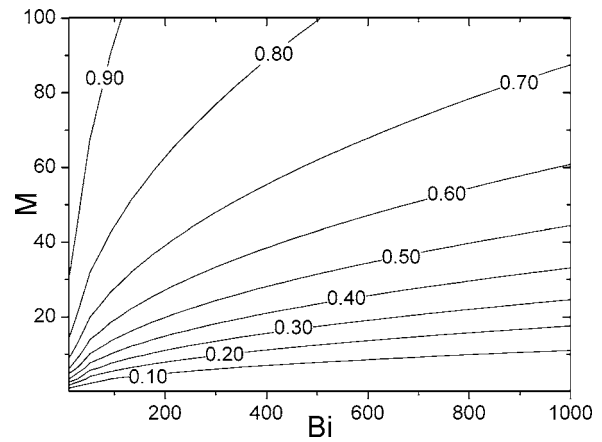


Fig. 4 The LTE error variation with the coolant mass flow rate and the Biot number in the pores

M and Bi , a large hot surface Biot number Bi_h can result in a significant increase of the hot surface temperature of the solid matrix. The reason is clear that the large hot surface Biot number corresponds to an intense convective heat exchange at the hot surface. From Figs. 2 and 3, it is also observed that the temperature variations at the second and the third BCs have a similar trend.

Effects of the BC on the LTE Assumption. In order to investigate the model problem of the LTE or the LTNE, a relative temperature difference between the solid matrix and the fluid coolant at the hot surface of the porous plate is defined as

$$Y = 1 \quad \delta = \frac{\theta_s - \theta_f}{\theta_s}$$

This relative difference is called “the LTE error” in the present paper, because in the local thermal equilibrium assumption, the two temperatures are seen to be the same. According to the above-obtained analytical solution, the LTE error can be written as

$$Y = 1 \quad \delta = \frac{(K_1 - 1)C_1 e^{k_1} + (K_2 - 1)C_2 e^{k_2}}{K_1 C_1 e^{k_1} + K_2 C_2 e^{k_2} + C_3} \quad (13)$$

The hot surface Biot number does not exist in the expression of the analytical solution at the second BC, but it exists at the third BC and can significantly influence the hot surface temperature, as shown in Fig. 3. However, the hot surface Biot number does not influence the LTE error, since it can be eliminated from Eq. (13), a detailed validation is shown in Appendix B. Thus, the hot surface Biot number does not influence the LTE assumption. It can also be verified that the influence of the Stanton number on the LTE error is less than 0.1% within the entire range.

Effect of the Coolant Mass Flow Rate and the Biot Number in the Pores on the LTE Error. Although the coefficient matrices of the analytical solution for the two kinds of BCs are different, the final expression of the LTE error is the same, a detailed validation is also presented in Appendix B. This interesting phenomenon leads to a unified expression of the LTE error for the two BCs. In this expression, the LTE error is only dependent on the coolant mass flow rate and the Biot number in the pores.

Figure 4 shows the distribution of the LTE error with the coolant mass flow rate and the Biot number in the pores. It is clear that the error decreases with the coolant mass flow rate and increases when the Biot number in the pores decreases. This conclusion is in accordance with the former studies [14,17,23,24]. This phenomenon can be explained by the fact that when the coolant mass flow rate decreases, the fluid velocity is slow, and the opportunity of the heat exchange between the fluid coolant and the solid matrix increases, the coolant temperature approximates to the solid

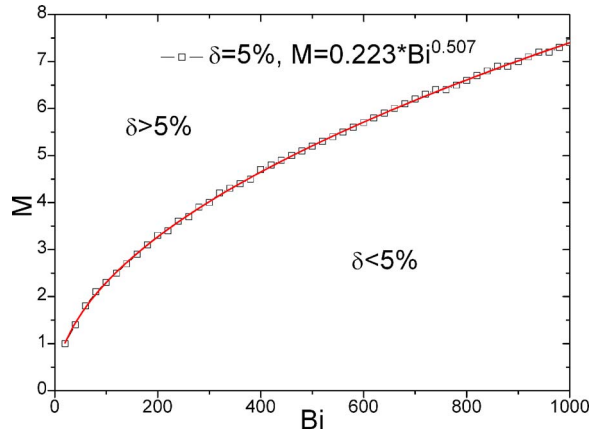


Fig. 5 The LTE and LTNE regions divided by the curve fitted using the analytical solution

temperature and the LTE assumption tends to be reasonable; whereas when the Biot number in the pores decreases, the heat exchange between the two phases also decreases, the temperature difference of the two phases increases, and the LTE model is invalid.

Through Eq. (13), a curve at which the LTE error is equal to 5% can be fitted, as shown in Fig. 5. The curve equation is

$$M = 0.223Bi^{0.507} \quad (14)$$

If the error is less than 5% and can be defined as the limit criterion of the LTE assumption, in the region below the curve, the criterion $\delta < 5\%$ is satisfied; whereas in the region above the curve, where $\delta > 5\%$, the LTE assumption is not reasonable. Consequently, the following expression is recommended as the quantitative criterion of the LTE model by this paper

$$M < 0.223 Bi^{0.507} \quad (15)$$

This quantitative expression, Eq. (15), is also in accordance with the qualitative formula [24]. And it should be emphasized again that in the investigation of the transpiration cooling problems, this criterion is valid for the second and the third BCs at the hot surface. However, the analytical solution is conditional, only when the fluid thermal diffusion in the porous plate can be neglected, is it exact.

Conclusions

In this work, an analytical solution of one-dimensional, steady and local thermal nonequilibrium model of transpiration cooling problems is obtained by neglecting the thermal diffusion of the fluid coolant in the porous plate. Through the analytical solution, the parameters which control the transpiration cooling effect and the LTE error are analyzed and discussed. Through this work, the following conclusions can be drawn:

- (1) The hot surface temperature of the porous plate is not sensitive to the Stanton number at the second and the third BCs. The key parameters to control the cooling effect are the coolant mass flow rate, the Biot number in the pores, and the hot surface Biot number (at the third BC), respectively.
- (2) The Stanton number and the Biot number at the hot surface (at the third BC) are worthless in the choice of the LTE model or LTNE model. The coolant mass flow rate and the Biot number in the pores are the important parameters which influence the choice of the two models.
- (3) If the LTE error is less than 5%, the LTE model is valid, the following expression can be used as a quantitative criterion:

$$M < 0.223 Bi^{0.507}$$

- (4) This criterion expression is conservative, because the thermal diffusion of the fluid coolant in the porous plate is neglected. If this term is considered, the actual fluid temperature should be higher than the value obtained by the analytical solution, and closer to the solid temperature.

Acknowledgment

Financial support of NSFC (No. 90305006), AHMFC (No. 2004kj365zd), and SRF for ROCS SEM are gratefully appreciated.

Nomenclature

a_{sf}	= specific surface, m^{-1}
Bi	= Biot number in pores, $h_{sf}a_{sf}H^2/k_{se}$
Bi_h	= Biot number at hot surface, hH/k_{se}
c_p	= specific heat, $J/kg \cdot K$
d_p	= characteristic size of the solid matrix, m
h	= interfacial transfer coefficient, $W/m^2 \cdot K$
h_{sf}	= heat transfer coefficient in the pores, $W/m^2 \cdot K$
H	= thickness of the porous plate, m
k	= heat conductivity, $W/m \cdot K$
$k_{1,2}, K_{1,2}, C_{1,2,3}, \Delta, \Delta_{1,2,3}$	= coefficients of analytical solution
m	= coolant mass flow rate, kg/m^2s
M	= dimensionless coolant mass flow rate, $mc_{pf}H/k_{se}$
Pr	= Prandtl number
St	= Stanton number, h_c/mc_{pf}
T	= temperature, K
v_f	= velocity, m/s
y	= coordinate, m
Y	= dimensionless coordinate

Greek Letters

ϵ	= porosity
θ	= dimensionless temperature
δ	= LTE error
ρ	= density, kg/m^3
μ	= viscosity, kg/ms

Subscripts

c	= coolant
e	= effective
f	= fluid
s	= solid
∞	= infinite

Appendix A

Through Eqs. (1) and (2), we obtain

$$(\rho c)_f v_f \frac{dT_f}{dy} = \frac{d}{dy} \left(k_{fe} \frac{dT_f}{dy} \right) + \frac{d}{dy} \left(k_{se} \frac{dT_s}{dy} \right)$$

through nondimensionlization

$$\frac{(\rho c)_f v_f H}{k_{fe}} \frac{d\theta_f}{dY} = \frac{d^2 \theta_f}{dY^2} + \frac{k_{se}}{k_{fe}} \frac{d^2 \theta_s}{dY^2}$$

If only $k_{se}/k_{fe} \gg 1$, the diffusion term of fluid can be neglected.

Appendix B

For the second BC

$$\Delta_1 = \begin{vmatrix} 0 & K_2 St - 1 & St - 1 \\ 0 & M - k_2 K_2 & M \\ 1 & K_2 k_2 e^{k_2} & 0 \end{vmatrix} = \begin{vmatrix} K_2 St - 1 & St - 1 \\ M - k_2 K_2 & M \end{vmatrix}$$

$$\Delta_2 = \begin{vmatrix} K_1 St - 1 & 0 & St - 1 \\ M - k_1 K_1 & 0 & M \\ K_1 k_1 e^{k_1} & 1 & 0 \end{vmatrix} = - \begin{vmatrix} K_1 St - 1 & St - 1 \\ M - k_1 K_1 & M \end{vmatrix}$$

$$\Delta_3 = \begin{vmatrix} K_1 St - 1 & K_2 St - 1 & 0 \\ M - k_1 K_1 & M - k_2 K_2 & 0 \\ K_1 k_1 e^{k_1} & K_2 k_2 e^{k_2} & 1 \end{vmatrix} = \begin{vmatrix} K_1 St - 1 & K_2 St - 1 \\ M - k_1 K_1 & M - k_2 K_2 \end{vmatrix}$$

$$\Delta = \begin{vmatrix} K_1 St - 1 & K_2 St - 1 & St - 1 \\ M - k_1 K_1 & M - k_2 K_2 & M \\ K_1 k_1 e^{k_1} & K_2 k_2 e^{k_2} & 0 \end{vmatrix}$$

For the third BC

$$\Delta_1 = \begin{vmatrix} 0 & K_2 St - 1 & St - 1 \\ 0 & M - k_2 K_2 & M \\ Bi_h & (Bi_h + k_2) K_2 e^{k_2} & Bi_h \end{vmatrix} = Bi_h \begin{vmatrix} K_2 St - 1 & St - 1 \\ M - k_2 K_2 & M \end{vmatrix}$$

$$\Delta_2 = \begin{vmatrix} K_1 St - 1 & 0 & St - 1 \\ M - k_1 K_1 & 0 & M \\ (Bi_h + k_1) K_1 e^{k_1} & Bi_h & Bi_h \end{vmatrix} = -Bi_h \begin{vmatrix} K_1 St - 1 & St - 1 \\ M - k_1 K_1 & M \end{vmatrix}$$

$$\Delta_3 = \begin{vmatrix} K_1 St - 1 & K_2 St - 1 & 0 \\ M - k_1 K_1 & M - k_2 K_2 & 0 \\ (Bi_h + k_1) K_1 e^{k_1} & (Bi_h + k_2) K_2 e^{k_2} & Bi_h \end{vmatrix}$$

$$= Bi_h \begin{vmatrix} K_1 St - 1 & K_2 St - 1 \\ M - k_1 K_1 & M - k_2 K_2 \end{vmatrix}$$

$$\Delta = \begin{vmatrix} K_1 St - 1 & K_2 St - 1 & St - 1 \\ M - k_1 K_1 & M - k_2 K_2 & M \\ (Bi_h + k_1) K_1 e^{k_1} & (Bi_h + k_2) K_2 e^{k_2} & Bi_h \end{vmatrix}$$

The LTE error at the second and the third BCs has the same expression

$$Y = 1 \quad \delta = \frac{(K_1 - 1)\Delta_1 e^{k_1} + (K_2 - 1)\Delta_2 e^{k_2}}{K_1 \Delta_1 e^{k_1} + K_2 \Delta_2 e^{k_2} + \Delta_3}$$

$$= \frac{(K_1 - 1)e^{k_1} \begin{vmatrix} K_2 St - 1 & St - 1 \\ M - k_2 K_2 & M \end{vmatrix} - (K_2 - 1)e^{k_2} \begin{vmatrix} K_1 St - 1 & St - 1 \\ M - k_1 K_1 & M \end{vmatrix}}{K_1 e^{k_1} \begin{vmatrix} K_2 St - 1 & St - 1 \\ M - k_2 K_2 & M \end{vmatrix} - K_2 e^{k_2} \begin{vmatrix} K_1 St - 1 & St - 1 \\ M - k_1 K_1 & M \end{vmatrix} + \begin{vmatrix} K_1 St - 1 & K_2 St - 1 \\ M - k_1 K_1 & M - k_2 K_2 \end{vmatrix}}$$

This expression contains three dimensionless numbers, M , Bi , and St . The Biot number at the hot surface Bi_h can be eliminated at the third BC, therefore the LTE error is independent of the hot surface Biot number. If the Stanton number is substituted by 1, the LTE error is only dependent on M , Bi .

$$\delta = \frac{(K_1 - 1)e^{k_1} \begin{vmatrix} K_2 - 1 & 0 \\ M - k_2 K_2 & M \end{vmatrix} - (K_2 - 1)e^{k_2} \begin{vmatrix} K_1 - 1 & 0 \\ M - k_1 K_1 & M \end{vmatrix}}{K_1 e^{k_1} \begin{vmatrix} K_2 - 1 & 0 \\ M - k_2 K_2 & M \end{vmatrix} - K_2 e^{k_2} \begin{vmatrix} K_1 - 1 & 0 \\ M - k_1 K_1 & M \end{vmatrix} + \begin{vmatrix} K_1 - 1 & K_2 - 1 \\ M - k_1 K_1 & M - k_2 K_2 \end{vmatrix}}$$

References

- [1] Hartnett, J. P., and Eckert, E. R. G., 1957, "Mass Transfer Cooling in a Laminar Boundary Layer with Constant Fluid Properties," *Trans. ASME*, **79**, pp. 247–254.
- [2] Rohsenow, W. M., Hartnett, J. P., and Ganic, E. N., 1985, *Handbook of Heat Transfer Applications*, McGraw-Hill, New York.
- [3] Eckert, E. R. G., and Cho, H. H., 1994, "Transition from Transpiration to Film Cooling," *Int. J. Heat Mass Transfer*, **37**, pp. 3–8.
- [4] Landis, J. A., and Bowman, W. J., 1996, "Numerical Study of a Transpiration Cooled Rocket Nozzle," AIAA Pap. **96-2580**.
- [5] Trevino, C., and Medina, A., 1999, "Analysis of the Transpiration Cooling of a Thin Porous Plaque in a Hot Laminar Convective Flow," *Eur. J. Mech. B/Fluids*, **18**, pp. 245–260.
- [6] Glass, D. E., Dille, A. D., and Kelly, H. N., 2001, "Numerical Analysis of Convection/Transpiration Cooling," *J. Spacecr. Rockets*, **38**, pp. 15–20.
- [7] Vafai, K., and Kim, S. J., 1989, "Forced Convection in a Channel Filled with a Porous Medium: An Exact Solution," *ASME J. Heat Transfer*, **111**, pp. 1103–1106.
- [8] Quintard, M., and Whitaker, S., 1995, "Local Thermal Equilibrium for Transient Heat Conduction: Theory and Comparison with Numerical Experiments," *Int. J. Heat Mass Transfer*, **38**, pp. 2779–2796.
- [9] Lee, D. Y., and Vafai, K., 1999, "Analytical Characterization and Conceptual Assessment of Solid and Fluid Temperature Differentials in Porous Media," *Int. J. Heat Mass Transfer*, **42**, pp. 423–435.
- [10] Marafie, A., and Vafai, K., 2001, "Analysis of Non-Darcian Effects on Temperature Differentials in Porous Media," *Int. J. Heat Mass Transfer*, **44**, pp. 4401–4411.
- [11] Vafai, K., and Sozen, M., 1990, "Analysis of Energy and Momentum Transport for Fluid Flow Through a Porous Bed," *ASME J. Heat Transfer*, **96**, pp. 690–699.
- [12] Amiri, A., Vafai, K., and Kuzay, T. M., 1995, "Effects of Boundary Conditions on Non-Darcian Heat Transfer Through Porous Media and Experimental Comparisons," *Numer. Heat Transfer, Part A*, **27**, pp. 651–664.
- [13] Nield, D. A., 1998, "Effects of Local Thermal Non-equilibrium in Steady Convective Processes in a Saturated Porous Medium: Forced Convection in a Channel," *J. Porous Media*, **1**, pp. 181–186.
- [14] Phanikumar, M. S., and Mahajan, R. L., 2002, "Non-Darcy Natural Convection in High Porosity Metal Foams," *Int. J. Heat Mass Transfer*, **45**, pp. 3781–3793.
- [15] Green, Leon J., 1952, "Gas Cooling of a Porous Heat Source," *J. Appl. Mech.*, **19**, pp. 173–178.
- [16] Burch, D. M., Allen, R. W., and Peavy, B. A., 1976, "Transient Temperature Distributions within Porous Slabs Subjected to Sudden Transpiration Heating," *ASME J. Heat Transfer*, **98**, pp. 221–225.
- [17] Polezhaev, Y. V., and Seliverstov, E. M., 2002, "A Universal Model of Heat

- Transfer in Systems with Penetration Cooling," *High Temp.*, **40**, pp. 856–864.
- [18] Alazmi, B., and Vafai, K., 2002, "Constant Wall Heat Flux Boundary Conditions in Porous Media under Local Thermal Non-equilibrium Conditions," *Int. J. Heat Mass Transfer*, **45**, pp. 3071–3087.
- [19] Alazmi, B., and Vafai, K., 2000, "Analysis of Variants within the Porous Media Transport Models," *ASME J. Heat Transfer*, **122**, pp. 303–326.
- [20] Calmidi, V. V., and Mahajan, R. L., 2000, "Forced Convection in High Porosity Metal Foams," *ASME J. Heat Transfer*, **122**, pp. 557–565.
- [21] Wakao, N., Kaguei, S., and Funazkri, T., 1979, "Effect of Fluid Dispersion Coefficients on Particle-To-Fluid Heat Transfer Coefficients in Packed Beds," *Chem. Eng. Sci.*, **34**, pp. 325–336.
- [22] Pixley, A. F., c1980, *Applied Linear Algebra*, University Press of America, Lanham, MD.
- [23] Nield, D. A., and Kuznetsov, A. V., 1999, "Local Thermal Non-equilibrium Effects in Forced Convection in a Porous Media Channel: A Conjugate Problem," *Int. J. Heat Mass Transfer*, **42**, pp. 3245–3252.
- [24] Nield, D. A., Kuznetsov, A. V., and Xiong, M., 2002, "Effect of Local Thermal Non-equilibrium on Thermally Developing Forced Convection in a Porous Medium," *Int. J. Heat Mass Transfer*, **45**, pp. 4949–4955.

Similarity Solution of Laminar Axisymmetric Jets With Effect of Viscous Dissipation

A. M. Kalteh

A. Abbassi

e-mail: abbassi@aut.ac.ir

Department of Mechanical Engineering,
Amirkabir University of Technology,
Hafez Ave., P.O. Box 15875-4413,
Tehran, Iran

In this work the similarity solution of the thermal boundary layer for a laminar axisymmetric jet with viscous dissipation is derived and solved numerically, using a fourth-order Runge-Kutta method. The results are compared with the existing solutions, in which viscous dissipation is neglected. After that the effects of Reynolds and Prandtl numbers of the incoming hot jet on the temperature profile of the jet is investigated. It is seen that inclusion of viscous dissipation term results in a more rapid heat exchange between the incoming jet and quiescent fluid than the case where the viscous dissipation term is neglected. Also, it is observed that by increasing the Reynolds and Prandtl numbers of the jet, the heat penetrates better in locations near the symmetry line, whereas in locations farther from the symmetry axis the penetration is less. [DOI: 10.1115/1.2345435]

Keywords: laminar axisymmetric jet, similarity solution, thermal boundary layer, numerical solution

1 Introduction

The first work on axisymmetric jets was completed by Schlichting [1–3]. He solved the momentum boundary layer equation for laminar axisymmetric jets by introducing a new similarity variable. In the industrial application of jets such as annealing of metal and plastic sheets, drying of textiles, cooling of microelectronic equipments, and so forth, the temperature of the incoming jet should be different from that of the quiescent fluid. Therefore, the solution of the thermal boundary equation is required. The thermal boundary layer solution of a narrow axisymmetric plane jet was given by Schlichting and Gersten [1]. However, heat transfer for axisymmetric laminar jets has been studied by few other researchers. In the book written by Pai [4], which is specified for jets, the thermal boundary layer has not been included. The thermal boundary layer for a point heat source was presented by Fujii [5]. Fang [3] and Zhang and his co-workers [6] worked on the thermal boundary layer of an axisymmetric laminar jet. They solved the problem using the similarity variable defined by Schlichting. But, none of them considered the viscous dissipation in the energy equation. They solved the thermal boundary layer equation by neglecting the viscous dissipation term.

In this study the similarity equation of the thermal boundary layer for a laminar axisymmetric jet with viscous dissipation is derived and solved numerically using a fourth-order Runge-Kutta method. Results are then compared with Fang's solution [3], taking into account the effect of viscous dissipation on the value of

heat penetration. Finally, the effects of the Reynolds and Prandtl numbers of the incoming jet on the heat transfer from a laminar axisymmetric jet are investigated.

2 Mathematical Formulation

The geometry of the jet is shown in Fig. 1. The momentum boundary layer equations governing the axisymmetric laminar jets are as below [2]

$$\frac{\partial u}{\partial x} + \frac{1}{r} \frac{\partial}{\partial r}(rv) = 0 \quad (1)$$

$$u \frac{\partial u}{\partial x} + v \frac{\partial u}{\partial r} = \frac{\nu}{r} \frac{\partial}{\partial r} \left(r \frac{\partial u}{\partial r} \right) \quad (2)$$

Subject to the boundary conditions [3]

$$v(x,0) = 0, \quad \frac{\partial u}{\partial r}(x,0) = 0 \quad \text{and} \quad u(x, \infty) = 0 \quad (3)$$

Considering the viscous dissipation, the boundary layer energy equation for constant pressure flows (with $\partial^2 u / \partial x^2 \ll \partial^2 u / \partial r^2$) shall be as follows [1]:

$$\rho c_p \left(u \frac{\partial T}{\partial x} + v \frac{\partial T}{\partial r} \right) = \frac{1}{r} \frac{\partial}{\partial r} \left(kr \frac{\partial T}{\partial r} \right) + \mu \left(\frac{\partial u}{\partial r} \right)^2 \quad (4)$$

This can be rewritten

$$u \frac{\partial T}{\partial x} + v \frac{\partial T}{\partial r} = \frac{\nu}{Pr} \cdot \frac{1}{r} \frac{\partial}{\partial r} \left(r \frac{\partial T}{\partial r} \right) + \frac{\nu}{c_p} \left(\frac{\partial u}{\partial r} \right)^2 \quad (5)$$

In which the term $(\nu/c_p)(\partial u/\partial r)^2$ indicates the viscous dissipation with boundary conditions [1]

$$\frac{\partial T}{\partial r}(x,0) = 0 \quad \text{and} \quad T(x, \infty) = T_o \quad (6)$$

Schlichting concluded that the jet thickness grew linearly, so that the proper similarity variable was r/x . He defined a stream function as below [2]

$$\psi(r,x) = \nu x F(\eta) \quad \eta = \frac{r}{x} \quad (7)$$

From which the axisymmetric velocity components can be written as [2]

$$u = \frac{1}{r} \frac{\partial \psi}{\partial r} = \frac{\nu F'}{r}$$

$$v = -\frac{1}{r} \frac{\partial \psi}{\partial x} = \frac{\nu}{r} (\eta F' - F) \quad (8)$$

The similarity equation of the momentum boundary layer can be written as [2]

$$\frac{d}{d\eta} \left(F'' - \frac{F'}{\eta} \right) = \frac{1}{\eta^2} (FF' - \eta F'^2 - \eta F F'') \quad (9)$$

Whereas the analytical solution is as follows [2]:

$$F(\eta) = \frac{(c\eta)^2}{1 + (c\eta/2)^2} \quad (10)$$

Where $c = (3J/16\pi\rho\nu^2)^{1/2}$ and J is the given momentum flux.

Since the momentum boundary layer has been solved before, in this study, only the thermal boundary layer has been considered.

Using the same similarity variable as Schlichting, Fang [3] defined $T(x,r) - T_o = \nu\theta(\eta)/r$ and found the boundary layer energy equation as

Contributed by the Heat Transfer Division of ASME for publication in the JOURNAL OF HEAT TRANSFER. Manuscript received December 26, 2005; final manuscript received July 9, 2006. Review conducted by Louis C. Burmeister.

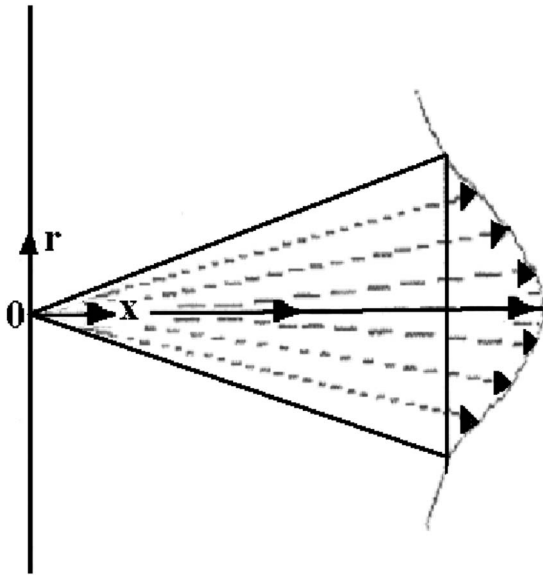


Fig. 1 Schematic representation of a laminar axisymmetric jet

$$\frac{-F'\theta}{\eta} - \frac{F\theta'}{\eta} + \frac{F\theta}{\eta^2} = \frac{1}{\text{Pr}} \left(\theta'' - \frac{\theta'}{\eta} + \frac{\theta}{\eta^2} \right) \quad (11)$$

Subject to the boundary conditions

$$\theta(0) = 0 \quad \text{and} \quad \theta(\infty) = 0 \quad (12)$$

Considering Eq. (11) with boundary conditions Eq. (12), Fang [3] found the solution as

$$\theta(\eta) = \frac{A\eta}{[1 + (c\eta/2)^2]^{2\text{Pr}}} \quad (13)$$

In which constant A can be determined by defining the enthalpy flux in the cross section for any x , as follows [3]:

$$H = \int \rho c_p [T(x, r) - T_o] \cdot u(x, r) 2\pi \cdot r \cdot dr \quad (14)$$

In the present study, Eq. (11) was solved, using the fourth-order Runge-Kutta method with the boundary conditions shown as Eq. (12). The results were then compared with those obtained by Fang [3]. Results found from a computer code for fourth-order Runge-Kutta showed a very good agreement with Fang's analytical solution.

Having been assured of the mathematical model results being accurate, the model was extended by inclusion of the viscous dissipation term and the investigation was continued.

To solve Eq. (5), the temperature profile was defined

$$T(x, r) - T_o = \frac{q\theta(x, r)}{r^m} \quad (15)$$

In which T_o is the temperature of the quiescent fluid, m is a parameter which should be determined by similarity solution, and q is a constant parameter.

If the same similarity variable defined by Schlichting is used and Eqs. (10) and (15) are substituted into Eq. (5), the similarity energy equation will be independent of x and r so that a similarity solution exists only when m is equal to 2.

Thus the governing similarity equation for a thermal boundary layer of laminar axisymmetric jet with viscous dissipation can be found as

$$\theta'' = \left(\frac{-2\text{Pr} \cdot F'}{\eta} + \frac{2\text{Pr} \cdot F - 4}{\eta^2} \right) \cdot \theta + \left(\frac{3 - \text{Pr} \cdot F}{\eta} \right) \theta' - \frac{v^2 \cdot \text{Pr}}{c_p \cdot q} \left(F'' - \frac{F'}{\eta} \right)^2 \quad (16)$$

And subject to boundary conditions

$$\theta(0) = 0 \quad \text{and} \quad \theta(\infty) = 0 \quad (17)$$

Substituting Eq. (15) into Eq. (14) and using Eq. (8)

$$H = \int_0^\infty 2\pi\rho c_p v F' \frac{q\theta}{x\eta^2} d\eta \quad (18)$$

It is seen from Eq. (18) that the enthalpy flux decreases as x (distance from nozzle exit port) increases. Therefore, this is not similar to the case for a laminar axisymmetric jet in which by neglecting viscous dissipation, the enthalpy flux at any x would be conserved.

From Eq. (14) the incoming enthalpy flux can be calculated as

$$H = \rho c_p \frac{\pi d^2}{4} (T_i - T_o) u_i \quad (19)$$

Where d is the jet diameter, T_i is temperature of the incoming jet, T_o is the temperature of quiescent fluid, and u_i is the incoming jet velocity.

To calculate the enthalpy flux of the incoming jet from Eq. (18), using the concept of virtual origin defined by Schlichting and Gersten [1] and the results given by Rankin and Sridhar [7], it follows that:

$$x_v = \frac{630}{307} \times 3.1 \times 10^{-2} \times \text{Re}_d \quad (20)$$

In which x_v is position of virtual origin.

So, comparing enthalpy flux calculated from numerical integration of Eq. (18) at $x=x_v$ and Eq. (19), the magnitude of constant q can be determined.

3 Results and Discussion

As mentioned before, the problem was initially solved without inclusion of the viscous dissipation term for a specified case (specified Re , Pr , d) and compared with solutions found by Fang [3]. Results indicated that the numerical solution was in very good agreement with the given analytical solution by Fang [3].

Having tested the numerical method and making sure about its adequacy, the viscous dissipation term was added to the model and results were compared with the case without inclusion of the viscous dissipation term. The corresponding results are shown in Fig. 2. It can be seen from Fig. 2 that viscous dissipation decreases the penetration of heat to the quiescent fluid. In fact, the viscous dissipation inclusion results in a more rapid exchange of heat between the incoming jet and the quiescent fluid than the case in which it was neglected.

Finally, the problem was considered further under two different conditions to investigate the effect of the Reynolds and Prandtl numbers of the incoming jet on the heat transfer rate to the quiescent fluid.

3.1 Effect of Reynolds Number. In this study the effect of different jet Reynolds numbers on the temperature profile has been investigated. For Reynolds numbers of 500, 1000, and 1500 the temperature profile at $x=0.2$ m (distance from exit port) has been plotted while other parameters such as the Prandtl number, jet diameter, and the incoming temperature difference are kept constant. Results have been shown in Fig. 3. It is seen that increasing the Reynolds number causes heat to penetrate more at locations near the symmetry axis and less at locations far from the symmetry axis. At high Reynolds numbers because of high kinetic energy of fluid particles, the penetration of heat at locations far-

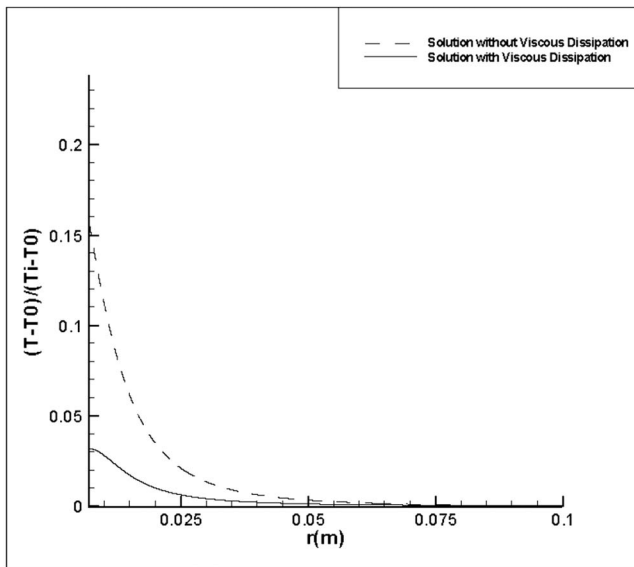


Fig. 2 Comparison between the temperature profile of a laminar axisymmetric jet with and without viscous dissipation ($x=0.05$ m, $Re_d=50$, $Pr=0.7$, $d=0.004$ m)

ther from symmetry axis is less, which is expected. But at locations near the symmetry axis because of approximations in virtual origin correlation results indicate a different behavior.

3.2 Effect of Prandtl Number. The effects of different jet Prandtl numbers on temperature profiles are investigated. The problem is solved for Prandtl numbers 0.7, 0.9, and 1.06 which are equivalent Prandtl numbers for the air, ammonia, and steam, respectively. The temperature profile at $x=0.05$ m (distance from nozzle exit) has been shown while other parameters such as Reynolds number, jet diameter, and the incoming temperature differ-

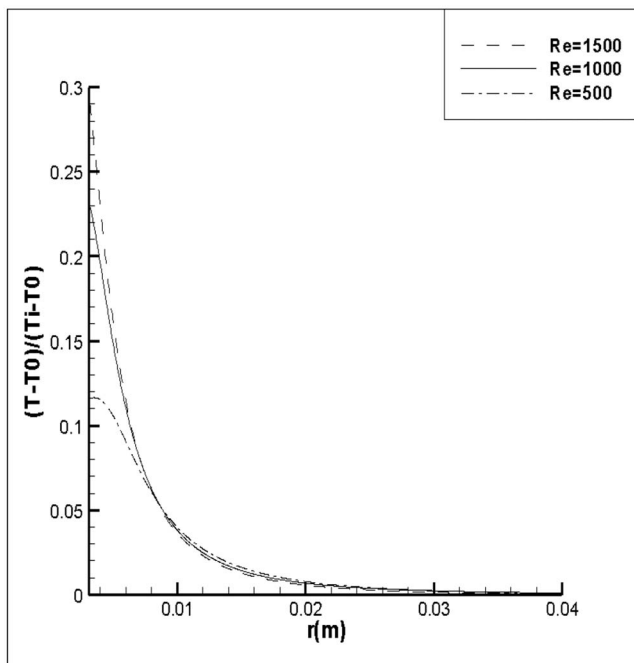


Fig. 3 Effect of the Reynolds number on the temperature profile of a laminar axisymmetric jet ($x=0.2$ m, $Pr=0.7$, $d=0.004$ m)

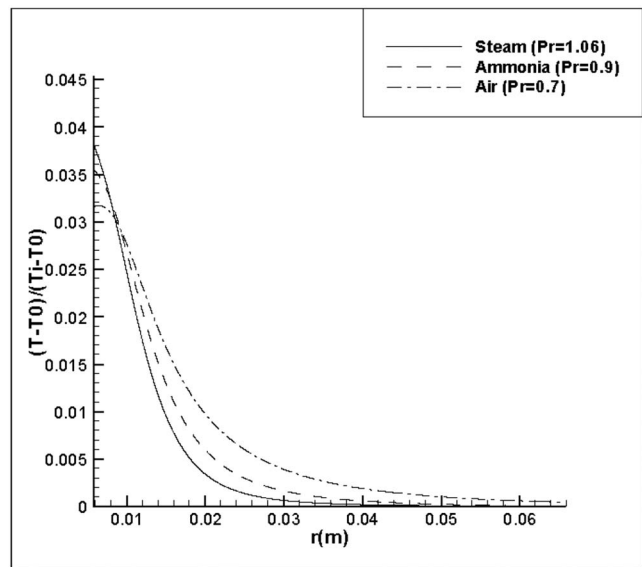


Fig. 4 Effect of the Prandtl number on the temperature profile of a laminar axisymmetric jet ($x=0.05$ m, $Re_d=50$, $d=0.004$ m)

ence are kept constant.

The corresponding results are shown in Fig. 4. It can be seen that the effect of increasing the Prandtl number is similar to increasing the Reynolds number. It follows from the definition of the Pr number (which is the fraction of momentum to thermal diffusivities), an increase in Pr Number, result in a decrease of heat penetration, as expected. But at locations near the symmetry results indicate a somewhat different behavior, which is due to approximations in virtual origin correlation.

4 Conclusions

In the present study the thermal boundary layer of a laminar axisymmetric jet with viscous dissipation was solved using similarity solution. The governing similarity equations were solved numerically using a fourth-order Runge-Kutta method. The results were compared with the case in which viscous dissipation was neglected. It was seen that inclusion of the viscous dissipation term would result in a more rapid heat exchange between the incoming jet and the quiescent fluid. Also, inclusion of viscous dissipation results in a decrease in the enthalpy flux along the jet axis. Finally effects of the Reynolds and Prandtl numbers on the heat transfer to quiescent fluid were investigated. It was seen that they both have similar effects. Increasing the Reynolds and Prandtl numbers, would result in a better heat penetration at locations near the symmetry axis and less heat penetration at locations farther from the symmetry axis.

Nomenclature

- A = integration constant
- C = integration constant
- F = dimensionless free stream function
- F' = first derivative of F
- F'' = second derivative of F
- H = enthalpy flux (kJ/s)
- J = total momentum flux ($\text{kg}\cdot\text{m}^2/\text{s}$)
- k = thermal conductivity (W/m.K)
- Pr = Prandtl number ($=\nu/\alpha$)
- Re_d = incoming flow Reynolds ($=\rho u_i d/\mu$)
- T = fluid temperature (K)
- T_o = quiescent fluid temperature (K)
- T_i = incoming jet fluid temperature (K)
- c_p = specific heat (kJ/kg.K)

d = incoming flow jet diameter (m)
 m = constant parameter
 q = integration constant
 r = radial coordinate (m)
 u = axial fluid velocity (m/s)
 u_i = incoming flow jet velocity (m/s)
 v = radial velocity (m/s)
 x = axial coordinate (m)
 x_v = position of virtual origin (m)

Greek

η = similarity variable
 ν = kinematic viscosity (m²/s)
 ρ = fluid density (kg/m³)
 θ = similarity temperature function
 θ' = first derivative of θ
 θ'' = second derivative of θ
 ψ = stream function

μ = dynamic viscosity (N.s/m²)
 π = Pi number

References

- [1] Schlichting, H., and Gersten, K., 2000, *Boundary Layer Theory*, 8th revised and enlarged edition (English), Springer, New York, pp. 222 and 331–334.
- [2] White, F. M., 1991, *Viscous Fluid Flow*, 2nd ed., McGraw-Hill, New York, pp. 301–302.
- [3] Fang, T., 2002, “Similarity Solution of Thermal Boundary Layers for Laminar Narrow Axisymmetric Jets,” *Int. J. Heat Fluid Flow*, **23**, pp. 840–843.
- [4] Pai, S. I., 1954, *Fluid Dynamics of Jets*, D. Van Nostrand Company, pp. 78–79.
- [5] Fujii, T., 1963, “Theory of the Steady Laminar Natural Convection Above a Horizontal Line Heat Source and a Point Heat Source,” *Int. J. Heat Mass Transfer*, **6**, pp. 597–606.
- [6] Zhang, X., and Zheng, L., 2004, “Similarity Solution of Momentum and Energy Equations for an Axi-symmetric Laminar Jet,” *J. Therm. Sci.*, **13**(4), pp. 334–337.
- [7] Rankin, G. W., and Sridhar, K., 1978, “Developing Region of Laminar Jets With Uniform Exit Velocity Profiles,” *J. Fluids Eng.*, **100**, pp. 55–59.

Heat Transfer Correlations for Turbulent Mixed Convection in the Entrance Region of a Uniformly Heated Horizontal Tube

Walter Grassi

e-mail: w.grassi@ing.unipi.it

Daniele Testi

e-mail: d.testi@ing.unipi.it

LOTHAR (Low gravity and Thermal Advanced Research laboratory)

Department of Energetics "L. Poggi,"

University of Pisa,

via Diotisalvi 2,

56126 Pisa, Italy

Flow of perfluorohexane in the entry region of a uniformly heated horizontal cylindrical duct was studied in a regime of weakly turbulent mixed convection. Heat transfer coefficients were measured at five cross sections along the heated length and various values of flow rate and heat flux were imposed. A different thermo-fluid-dynamic behavior was observed between the upper and lower sides of the pipe. Correlations of the Nusselt number for developed and developing flow were proposed, showing agreement with the experimental data within the 10% deviation band. [DOI: 10.1115/1.2345436]

Keywords: mixed convection, developing flow, buoyancy, entrance region, heat transfer correlations

Introduction

In the heat transfer process between a solid boundary and a moving fluid, buoyancy forces can be of the same order of magnitude as the external forces responsible for the forced circulation. This especially happens in the domain between laminar and weakly turbulent flow. The combination of free and forced convection is known as mixed convection and the dimensionless parameter representing the ratio of buoyancy and inertial forces is the Richardson number, defined as

$$Ri = \frac{Gr}{Re^2} \quad (1)$$

Mixed convection almost always occurs when heating or cooling channel walls at small fluid velocities, while pure forced laminar convection can only be obtained in capillaries [1].

In mixed convection, the hydrodynamic and the thermal fields are interdependent. The buoyant forces, which are due to the change in fluid density with temperature, modify the velocity and temperature profiles of the pure forced convection case and may also cause transition to turbulence of a duct flow at a Reynolds number value much less than 2300 [2]. The maps recommended in [3] illustrate the transition region between the laminar and the turbulent regimes, together with the boundaries between mixed convection and pure forced or free convection.

Buoyancy has a different influence on the internal convection heat transfer, depending on whether the flow is laminar or turbulent, cooled or heated, and on duct geometry and orientation (horizontal or inclined, upflow, or downflow).

For a horizontal duct, the forces of free and forced convection act orthogonally to each other. Temperature variations in the fluid may lead not only to velocity profiles modifications, but also to a secondary flow motion, with counter-rotating vortices, superimposed on the streamwise main flow. When heat is supplied through the wall, the fluid particles ascend along the sides, arrive at the top, and descend in the center of the channel. If the pipe is cooled, the direction of the secondary flow is reversed. Thus, the circulation that is imposed on the main flow results in the formation of two spiraling flows. This secondary flow can significantly increase the heat transfer rates, with respect to the case of pure forced convection [4].

Although a comprehensive account of effects of this sort on convective heat transfer in duct flows can be found in [5], fundamental understanding of the heat transfer behavior of combined free and forced convection in the thermal entrance region of horizontal ducts is very limited. In fact, valuable works concerning mixed convection in horizontal ducts mainly treat the fully developed situation [6–17]. However, in practical applications we rarely deal with a fully developed flow.

On the other hand, both experimental and numerical research on the effect of the entry zone is generally conducted at quite low Reynolds [18–35] or Rayleigh numbers [36–40], respectively, $Re < 2500$ and $Ra < 10^7$. Very few studies deal with developing, weakly turbulent mixed convection at moderate and high Rayleigh numbers. In particular, Wang et al. [41] and Osborne and Incropera [42] have performed experiments between horizontal, parallel plates.

The influence of buoyancy is less pronounced under transitional and turbulent regimes rather than in laminar flow. However, the effects are still significant and much remains to be learned. Hence, the experimental campaign reported in this paper intends to provide a preliminary characterization of the developing, weakly turbulent regime of mixed convection in a uniformly heated horizontal cylindrical duct. To our knowledge, the range of Reynolds, Prandtl, and Rayleigh numbers investigated herein is still unexplored for this geometry, though of practical interest for applications like liquid-cooled heat sinks for electronic components and circuitry.

Experimental Apparatus

The dielectric fluid chosen for the experiments is perfluorohexane, a Fluorinert™ Electronic Liquid manufactured by 3M (St. Paul, MN), commercially named FC-72. The main physical properties of the liquid are reported in Table 1.

FC-72 is thermally and chemically stable, compatible with sensitive materials, non-flammable, nontoxic, colorless, and has no ozone depletion potential. This combination of properties, together with its particularly low viscosity, makes FC-72 appropriate for applications like heat sinks for electronic components.

A test loop was built as shown in the schematic of Fig. 1.

The fluid, moved by a gear pump, circulated through the test specimen at volumetric flow rates in the range 1.00–2.00 l min⁻¹. A flowmeter measured the flow rate with an accuracy of ± 0.0086 l min⁻¹. The fluid, uniformly heated in its flow along the horizontal test section, was cooled to the desired inlet temperature by means of a shell-tube heat exchanger, with countercurrent chilled water flowing in the shell. An expansion vessel was used to compensate the volume increase in the loop due to temperature variations and to set the pressure of the position it was mounted on. An absolute pressure transducer was placed right upstream of the gear pump, in order to check that the lowest pressure of the loop was above the room pressure, thus avoiding air from being sucked in by the pump. All the tests were performed at an absolute pressure of about 2 bars.

Contributed by the Heat Transfer Division of ASME for publication in the JOURNAL OF HEAT TRANSFER. Manuscript received January 13, 2006; final manuscript received March 6, 2006. Review conducted by N. K. Anand.

Table 1 FC-72 physical properties at 25°C and 1 bar (by courtesy of 3 M)

Freezing point	-90°C
Boiling point	56°C
Density	$1.68 \cdot 10^3 \text{ kg m}^{-3}$
Kinematic viscosity	$3.8 \cdot 10^{-7} \text{ m}^2\text{s}^{-1}$
Specific heat	$1.1 \cdot 10^3 \text{ J kg}^{-1}\text{K}^{-1}$
Thermal conductivity	$5.7 \cdot 10^{-2} \text{ W m}^{-1}\text{K}^{-1}$
Coefficient of expansion	$1.56 \cdot 10^{-3} \text{ K}^{-1}$

Table 2 Position of the monitored cross sections along the heated length

Section A	$x=25 \text{ mm}$
Section B	$x=105 \text{ mm}$
Section C	$x=185 \text{ mm}$
Section D	$x=265 \text{ mm}$
Section E	$x=345 \text{ mm}$

A detailed schematic of the test section is shown in Fig. 2.

The pipe was made of stainless steel and had an inner diameter $D=17.3 \text{ mm}$ and a wall thickness $s=2 \text{ mm}$. The fluid was warmed up by an electrical resistance heater applied to the outer wall for a length $L=500 \text{ mm}$. The applied heat flow ranged from 30 W to 80 W. Temperature measurements were made by type-T thermocouples, placed on the outer wall, under the heater, at five

cross sections along the heated length, as shown in Table 2. Each cross section had eight measurement points, one every 45 deg, starting from the top.

Two more thermocouples were placed at the inlet and at the outlet of the test section. These two measurements were performed inside ducts with a much larger cross section than the heated duct, as shown in Fig. 2. This larger regions function as mixing chambers, favoring the elimination of pre-existing temperature gradients.

To minimize heat losses, the entire specimen was covered with a 34 mm thick thermal insulator ($\lambda_i=0.038 \text{ W m}^{-1} \text{ K}^{-1}$). In this way, the heat flow was almost entirely directed toward the liquid, due to the considerably higher thermal resistance of the outer path (insulation plus air on the outside) with respect to the inner path (pipe thickness plus liquid in the duct). Thus, for analysis purposes, we assumed that the heat flow entering the duct was always equal to the one supplied by the heater. As a further check, we evaluated the following expression of the energy balance:

$$\dot{Q} = \dot{m}c_p(T_{\text{out}} - T_{\text{in}}) \quad (2)$$

valid in steady state, with negligible heat generation by viscous dissipation within the fluid.

All the thermocouples used a zero-point reference joint, whose temperature was controlled by a reference resistance thermometer. The overall accuracy of each thermocouple after calibration in the 15°C–60°C range was $\pm 0.2 \text{ K}$.

The available differential pressure transducer had a sensitivity of 30 Pa and was not able to measure appreciable pressure drops through the test section. Further details on the experimental apparatus can be found in [43].

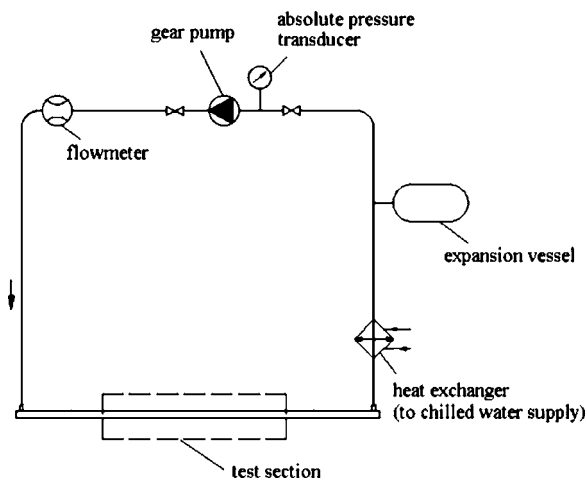


Fig. 1 Schematic of the test loop

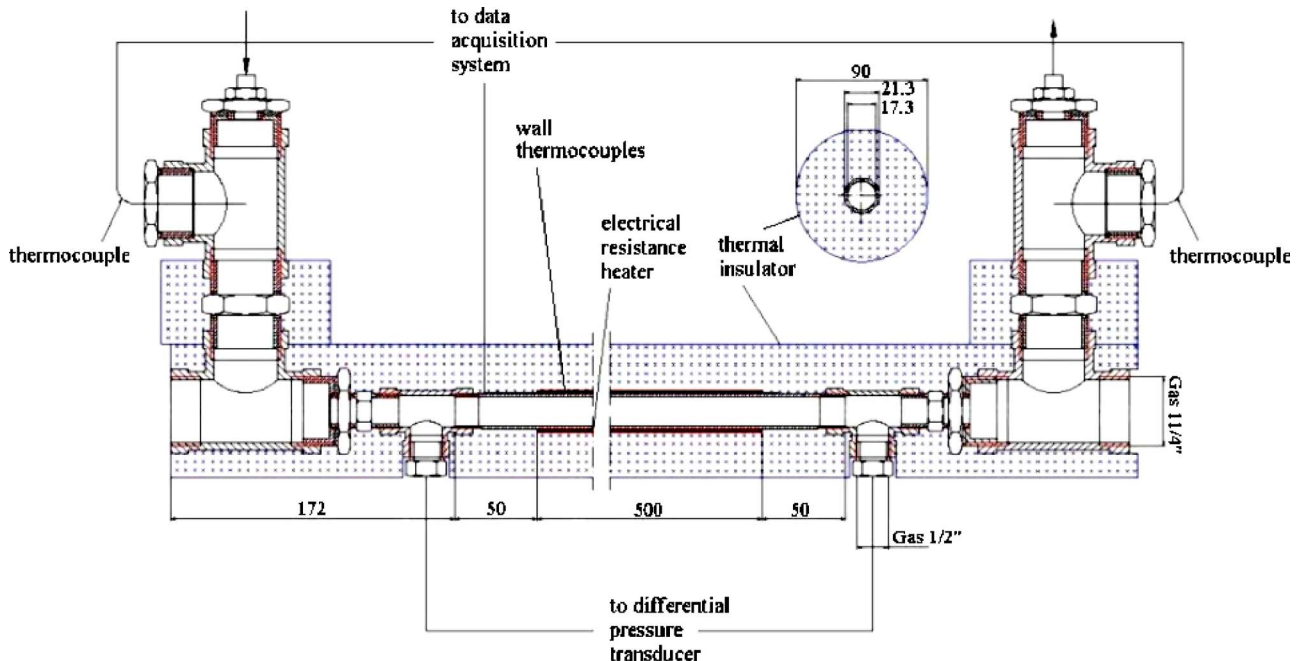


Fig. 2 Detail of the test section

Table 3 Value of the free parameters and accuracy of the proposed correlations (Eqs. (6) and (7))

Examined cross sections	Number of data points	Points within 5% deviation	Points within 10% deviation	γ	m	n	p	Utilized equation
A,B,C,D,E (upper side)	90	58 (64%)	84 (93%)	0.169	0.458	0.071	-0.159	Developing flow (Eq. (6))
A,B,C (lower side)	54	46 (85%)	54 (100%)	0.175	0.353	0.120	-0.136	Developing flow (Eq. (6))
C,D,E (lower side)	54	48 (85%)	54 (100%)	0.160	0.288	0.137	n/a	Developed flow (Eq. (7))

Test Procedure and Data Analysis

Every test was run under constant volumetric flow rate and heat flow and a steady state condition was awaited. The thermocouples' signals were acquired every 6 s by a scanner mounted on a digital multimeter; then the data were sent to a computer in order to be recorded and processed.

As a direct consequence of the energy balance in steady state, with uniform heat flux, and with negligible viscous dissipation, the bulk temperature of the fluid, defined as the temperature of adiabatic mixing for the examined cross section, linearly grows through the heated length, starting from the inlet temperature.

The temperatures of the inner side of the wall were obtained from the ones measured on the outer face, properly accounting for one-dimensional heat conduction within the duct thickness

$$T_{w,in} = T_{w,out} - \frac{\Theta}{2\pi\lambda_w L} \ln\left(\frac{D+2s}{D}\right) \quad (3)$$

The one-dimensional (1D) analysis is justified by the fact that the axial heat flux is negligible with respect to the radial one. In fact, temperature gradients are definitely smaller in the axial direction. This assumption was confirmed by a computational analysis, which we performed by using the finite element method.

The dimensionless numbers describing mixed convection in uniform heat flux conditions (i.e., Nu, Re, Gr_q, and Pr) were calculated as

$$\left\{ \begin{aligned} \text{Nu} &= \frac{\alpha D}{\lambda_f} = \frac{qD}{\lambda_f(T_{w,in} - T_b)} = \frac{1}{\pi} \frac{\Theta}{\lambda_f(T_{w,in} - T_b)L} \\ \text{Re} &= \frac{u\rho_f D}{\eta_f} = \frac{4}{\pi} \frac{\dot{V}}{Dv_f} \\ \text{Gr}_q &= \text{GrNu} = \frac{\beta_f g q D^4}{\lambda_f \nu_f^2} = \frac{1}{\pi} \frac{\beta_f g \Theta D^3}{\lambda_f \nu_f^2 L} \\ \text{Pr} &= \frac{\eta_f c_p}{\lambda_f} \end{aligned} \right. \quad (4)$$

having defined the film temperature as

$$T_f = \frac{T_b + T_{w,in}}{2} \quad (5)$$

Even at the highest heat flow, the fluid temperatures in correspondence of the inner side of the heated wall were fairly below the boiling point, never exceeding 50°C.

The maximum experimental error on the Nusselt number, corresponding to the lowest temperature difference between T_{w,in} and T_b, was 2.7%, while the maximum relative error on the Reynolds number, obtained at the lowest flow rate, was 0.9%.

Discussion of Heat Transfer Results

In every test, the data were obtained averaging 50 measurements recorded consecutively once a steady state condition was

reached. The Grashof number based on the wall heat flux ranged from 1.26 · 10⁸ to 4.97 · 10⁸, while the Reynolds number from 3050 to 6800. Having used a single working fluid, the Prandtl number varied only from 10.9 to 12.6. According to the maps reported in [3], our tests were run under a regime of weakly turbulent mixed convection.

The Nusselt number results are presented as an azimuthal average, made, respectively, on the measurement points belonging to the upper half (Nu_{up}) and to the lower half of the duct (Nu_{down}). The two midheight measurement points were included in both averages.

In the lower region, at a fixed flow rate and heat flow, the Nusselt number decreased passing from section A to section C, then remaining almost the same, as in a developed region, passing from section C to section E. On the other hand, on the upper side, the heat transfer coefficient kept decreasing from section A to section E, as in a developing flow. Thus, it seems that when buoyancy helps in removing hot fluid from the heated surface, rather than doing the opposite, the flow tends to develop earlier. Also, Nu_{up} is more sensitive to Re and less sensitive to Gr_q than Nu_{down}, a trend already observed for turbulent mixed convection between horizontal, parallel plates [42].

In order to lump all the above-mentioned effects into a simple expression, the experimental data were fitted by a least square procedure as

$$\text{Nu} = \gamma \text{Re}^m \text{Gr}_q^n \text{Pr}^{0.196} \left(\frac{x}{D}\right)^p \quad (6)$$

for developing flow, and

$$\text{Nu} = \gamma \text{Re}^m \text{Gr}_q^n \text{Pr}^{0.196} \quad (7)$$

for developed flow. Due to the narrow range in which the Prandtl number varied, we opted for fixing its exponent. The value of 0.196 was chosen in accordance with [2].

The results of the statistical analysis are summarized in Table 3. A search on the available literature concerning developing mixed convection in cylindrical horizontal pipes shows that the proposed correlations cover an unexplored range of Reynolds, Prandtl, and Rayleigh numbers.

Being in mixed convection, heat transfer coefficients on the top of the pipe were always lower than on the bottom. However, we could make the ratio between Nu_{up} and Nu_{down} tend to the unity (i.e., tend to a regime of pure forced convection) in three ways: decreasing the heat flow, increasing the flow rate, or getting closer to the beginning of the heated length. A single dimensionless number capable of taking into account all three of these variables was derived

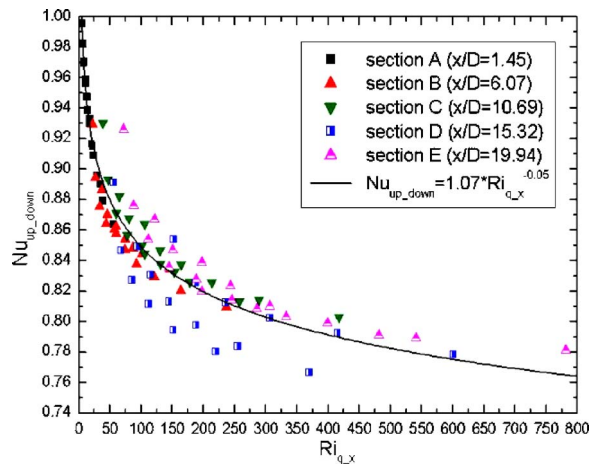


Fig. 3 $Nu_{up,down}$ versus $Ri_{q,x}$

$$Ri_{q,x} = \frac{Gr_{q,x}}{Re_x^2} = \frac{Gr_x Nu}{Re_x^2} = \frac{\beta_f g (T_{w,in} - T_b) x^3 \alpha D}{\left(\frac{ux}{v_f}\right)^2 \lambda_f} = \frac{\pi \beta_f g x \Theta D^4}{16 \dot{V}^2 L \lambda_f} \quad (8)$$

The following direct correlation between $Nu_{up,down}$ and $Ri_{q,x}$ was then proposed:

$$Nu_{up,down} = \chi Ri_{q,x}^r \quad (9)$$

with $Ri_{q,x}$ ranging from 5.2 to 780 and having chosen $\chi=1.07$ and $r=-0.05$ for best fitting the experimental data (see Fig. 3).

The deviation from the prediction of Eq. (9) is shown in Fig. 4, with 89 out of 90 points (99%) lying within the 5% band. The accuracy of Eq. (9) seems to indicate that the dimensionless group $Ri_{q,x}$ is of fundamental importance in the characterization of developing turbulent mixed convection under a condition of uniform heat flux.

Conclusions

In this work we examined the flow of perfluorohexane in the entry region of a uniformly heated horizontal cylindrical pipe in a regime of weakly turbulent mixed convection. Differences between the upper and lower sides of the duct were highlighted,

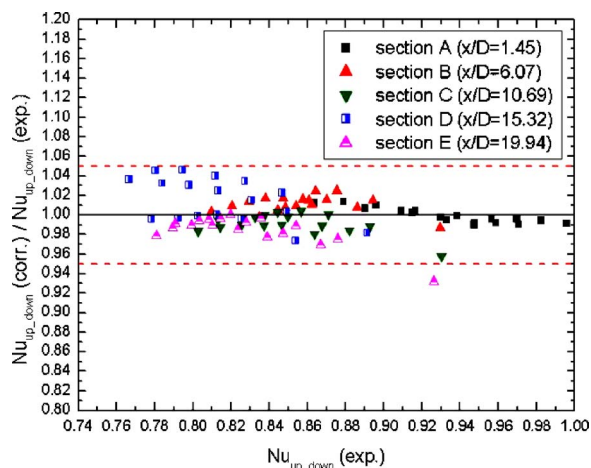


Fig. 4 Deviation between the experimental data and the values predicted by Eq. (9)

namely, a shorter thermal entry length on the lower region and a different sensitivity of the heat transfer coefficients to flow rate and heat flow. Correlations for the Nusselt number on both the upper and lower regions were proposed, closely approximating the experimental data.

In spite of the differences, the Nusselt numbers on the lower and upper sides of the tube were put in relation to each other with high accuracy by means of a single dimensionless group never employed in scientific literature, the Richardson number based on the wall heat flux and on the characteristic length x , suggesting to us that this parameter has to be greatly representative in describing developing mixed convection under uniform heat flux.

Acknowledgment

The authors are particularly indebted to Roberto Manetti for his skillful technical assistance and would also like to thank the graduate and undergraduate students who contributed with great commitment to running the experimental apparatus: Mario Saputelli, Davide Della Vista, Libera La Face, and Andrea Meo.

Nomenclature

- c_p = Fluid specific heat ($J kg^{-1} K^{-1}$)
- D = inner diameter of the heated wall (m)
- g = acceleration due to gravity ($m s^{-2}$)
- Gr = $\beta_f g (T_{w,in} - T_b) D^3 / \nu_f^2$, Grashof number
- Gr_q = Grashof number based on the wall heat flux
- $Gr_{q,x}$ = Grashof number based on the wall heat flux and on the characteristic length x
- Gr_x = Grashof number based on the characteristic length x
- L = heated length (m)
- m = correlation exponent (Eqs. (6) and (7))
- \dot{m} = $\rho \dot{V}$, mass flow rate ($kg s^{-1}$)
- n = correlation exponent (Eqs. (6) and (7))
- Nu = Nusselt number
- $Nu_{up,down}$ = ratio between Nu_{up} and Nu_{down}
- p = correlation exponent (Eq. (6))
- Pr = Prandtl number
- q = heat flux ($W m^{-2}$)
- r = correlation exponent (Eq. (9))
- Ra = $GrPr$, Rayleigh number
- Re = Reynolds number
- Re_x = Reynolds number based on the characteristic length x
- Ri = Richardson number
- $Ri_{q,x}$ = Richardson number based on the wall heat flux and on the characteristic length x
- s = heated wall thickness (m)
- T = temperature (K)
- u = fluid velocity ($m s^{-1}$)
- \dot{V} = volumetric flow rate ($m^3 s^{-1}$)
- x = distance from the beginning of the heated length (m)

Greek letters

- α = convective heat transfer coefficient ($W m^{-2} K^{-1}$)
- β = coefficient of cubic expansion (K^{-1})
- χ = correlation constant (Eq. (9))
- γ = correlation constant (Eqs. (6) and (7))
- η = dynamic viscosity (Pa s)
- λ = thermal conductivity ($W m^{-1} K^{-1}$)
- ν = η / ρ , kinematic viscosity ($m^2 s^{-1}$)
- Θ = heat flow (W)
- ρ = mass density ($kg m^{-3}$)

Subscripts

b	=	bulk
down	=	lower side of the duct
f	=	film
i	=	insulator
in	=	inlet
out	=	outlet
up	=	upper side of the duct
w	=	wall
w_{in}	=	inner side of the heated wall
w_{out}	=	outer side of the heated wall

References

- [1] Polyakov, A. F., 1997, "Mixed (Combined) Convection," *International Encyclopedia of Heat and Mass Transfer*, G. F. Hewitt, G. L. Shires, and Y. V. Polezhaev, eds., CRC Press LLC, Boca Raton, FL, pp. 725–727.
- [2] Metais, B., 1963, "Criteria for Mixed Convection," Technical Report No. 51, Heat Transfer Laboratory, University of Minnesota, Minneapolis, MN.
- [3] Metais, B., and Eckert, E. R. G., 1964, "Forced, Mixed, and Free Convection Regimes," *J. Heat Transfer*, **86**, pp. 295–296.
- [4] Kakaç, S., Shah, R. K., and Aung, W., 1987, *Handbook of Single-Phase Convective Heat Transfer*, Wiley, New York, Chap. 15.
- [5] Petukhov, B. S., and Polyakov, A. F., 1988, *Heat Transfer in Turbulent Mixed Convection*, Hemisphere Publishing Corporation, New York, Chap. 3, 5.
- [6] Mori, Y., Futagami, K., Tokuda, S., and Nakamura, M., 1966, "Forced Convective Heat Transfer in Uniformly Heated Horizontal Tubes, 1st Report—Experimental Study on the Effect of Buoyancy," *Int. J. Heat Mass Transfer*, **9**, pp. 453–463.
- [7] Mori, Y., and Futagami, K., 1967, "Forced Convective Heat Transfer in Uniformly Heated Horizontal Tubes (2nd Report, Theoretical Study)," *Int. J. Heat Mass Transfer*, **10**, pp. 1801–1813.
- [8] Faris, G. N., and Viskanta, R., 1969, "An Analysis of Laminar Combined Forced and Free Convection Heat Transfer in a Horizontal Tube," *Int. J. Heat Mass Transfer*, **12**, pp. 1295–1309.
- [9] Hwang, G. J., and Cheng, K. C., 1970, "Boundary Vorticity Method for Convective Heat Transfer with Secondary Flow—Application to the Combined Free and Forced Laminar Convection in Horizontal Tubes," *Proc. Fourth International Heat Transfer Conf.*, Paris-Versailles, France, Vol. 4, Paper NC3.5, pp. 1–12.
- [10] Petukhov, B. S., and Polyakov, A. F., 1970, "Flow and Heat Transfer in Horizontal Tubes under Combined Effect of Forced and Free Convection," *Proc. Fourth International Heat Transfer Conf.*, Paris-Versailles, France, Vol. 4, Paper NC3.7, pp. 1–11.
- [11] Morcos, S. M., and Bergles, A. E., 1975, "Experimental Investigation of Combined Forced and Free Laminar Convection in Horizontal Tubes," *J. Heat Transfer*, **97**, pp. 212–219.
- [12] Hattori, N., and Kotake, S., 1978, "Combined Free and Forced-Convection Heat-Transfer for Fully-Developed Laminar Flow in Horizontal Tubes—Experiments," *Bull. JSME*, **21**, pp. 861–868.
- [13] Patankar, S. V., Ramadhyani, S., and Sparrow, E. M., 1978, "Effect of Circumferentially Nonuniform Heating on Laminar Combined Convection in a Horizontal Tube," *J. Heat Transfer*, **100**, pp. 63–70.
- [14] Hattori, N., 1979, "Combined Free and Forced Convection Heat Transfer for Fully Developed Laminar Flow in Concentric Annuli (Numerical Analysis)," *JSME Trans.*, **45**, pp. 227–239.
- [15] Kotake, S., and Hattori, N., 1985, "Combined Free and Forced Convection Heat Transfer for Fully Developed Laminar Flow in Concentric Annuli," *Int. J. Heat Mass Transfer*, **28**, pp. 2115–2120.
- [16] Ciampi, M., Faggiani, S., Grassi, W., Incropera, F. P., and Tuoni, G., 1986, "Experimental Study of Mixed Convection in Horizontal Annuli for Low Reynolds Number," *Proc. Eighth International Heat Transfer Conf.*, San Francisco, CA, Vol. 3, pp. 1413–1418.
- [17] Ciampi, M., Faggiani, S., Grassi, W., Tuoni, G., and Incropera, F. P., 1987, "Mixed Convection Heat-Transfer in Horizontal, Concentric Annuli for Transitional Flow Conditions," *Int. J. Heat Mass Transfer*, **30**, pp. 833–841.
- [18] McComas, S. T., and Eckert, E. R. G., 1966, "Combined Free and Forced Convection in a Horizontal Circular Tube," *J. Heat Transfer*, **88**, pp. 147–153.
- [19] Shannon, R. L., and Depew, C. A., 1968, "Combined Free and Forced Laminar Convection in a Horizontal Tube with Uniform Heat Flux," *J. Heat Transfer*, **90**, pp. 353–357.
- [20] Shannon, R. L., and Depew, C. A., 1969, "Forced Laminar Flow Convection in a Horizontal Tube with Variable Viscosity and Free-Convection Effects," *J. Heat Transfer*, **91**, pp. 251–258.
- [21] Depew, C. A., and August, S. E., 1971, "Heat Transfer due to Combined Free and Forced Convection in a Horizontal and Isothermal Tube," *J. Heat Transfer*, **93**, pp. 380–384.
- [22] Kamotani, Y., and Ostrach, S., 1976, "Effect of Thermal Instability on Thermally Developing Laminar Channel Flow," *J. Heat Transfer*, **98**, pp. 62–66.
- [23] Kamotani, Y., Ostrach, S., and Miao, H., 1979, "Convective Heat Transfer Augmentation in Thermal Entrance Regions by means of Thermal Instability," *J. Heat Transfer*, **101**, pp. 222–226.
- [24] Yousef, W. W., and Tarasuk, J. D., 1982, "Free Convection Effects on Laminar Forced Convective Heat Transfer in a Horizontal Isothermal Tube," *J. Heat Transfer*, **104**, pp. 145–152.
- [25] Barozzi, G. S., Zanchini, E., and Mariotti, M., 1985, "Experimental Investigation of Combined Forced and Free Convection in Horizontal and Inclined Tubes," *Meccanica*, **20**, pp. 18–27.
- [26] Osborne, D. G., and Incropera, F. P., 1985, "Laminar, Mixed Convection Heat Transfer for Flow between Horizontal Parallel Plates with Asymmetric Heating," *Int. J. Heat Mass Transfer*, **28**, pp. 207–217.
- [27] Incropera, F. P., Knox, A. L., and Maughan, J. R., 1987, "Mixed-Convection Flow and Heat-Transfer in the Entry Region of a Horizontal Rectangular Duct," *J. Heat Transfer*, **109**, pp. 434–439.
- [28] Maughan, J. R., and Incropera, F. P., 1987, "Experiments on Mixed Convection Heat Transfer for Airflow in a Horizontal and Inclined Channel," *Int. J. Heat Mass Transfer*, **30**, pp. 1307–1318.
- [29] Maughan, J. R., and Incropera, F. P., 1990, "Regions of Heat Transfer Enhancement for Laminar Mixed Convection in a Parallel Plate Channel," *Int. J. Heat Mass Transfer*, **33**, pp. 555–570.
- [30] Lei, Q. M., and Trupp, A. C., 1991, "Experimental Study of Laminar Mixed Convection in the Entrance Region of a Horizontal Semicircular Duct," *Int. J. Heat Mass Transfer*, **34**, pp. 2361–2372.
- [31] Zhang, C., and Bell, K. J., 1992, "Mixed Convection inside Horizontal Tubes with Nominally Uniform Heat Flux," *AIChE Symp. Ser.*, **88**, pp. 212–219.
- [32] Choi, D. K., and Choi, D. H., 1994, "Developing Mixed Convection Flow in a Horizontal Tube under Circumferentially Non-Uniform Heating," *Int. J. Heat Mass Transfer*, **37**, pp. 1899–1913.
- [33] Wang, M., Tsuji, T., and Nagano, Y., 1994, "Mixed Convection with Flow Reversal in the Thermal Entrance Region of Horizontal and Vertical Pipes," *Int. J. Heat Mass Transfer*, **37**, pp. 2305–2319.
- [34] Shome, B., and Jensen, M. K., 1995, "Mixed Convection Laminar Flow and Heat Transfer of Liquids in Isothermal Horizontal Circular Ducts," *Int. J. Heat Mass Transfer*, **38**, pp. 1945–1956.
- [35] Islam, N., Gaitonde, U. N., and Sharma, G. K., 2001, "Mixed Convection Heat Transfer in the Entrance Region of Horizontal Annuli," *Int. J. Heat Mass Transfer*, **44**, pp. 2107–2120.
- [36] Hussain, N. A., and McComas, S. T., 1970, "Experimental Investigation of Combined Convection in a Horizontal Circular Tube with Uniform Heat Flux," *Proc. Fourth International Heat Transfer Conf.*, Paris-Versailles, France, Vol. 4, Paper NC3.4, pp. 1–11.
- [37] Ghajar, A. J., and Tam, L.-M., 1994, "Heat Transfer Measurements and Correlations in the Transition Region for a Circular Tube with Three Different Inlet Configurations," *Exp. Therm. Fluid Sci.*, **8**, pp. 79–90.
- [38] Ghajar, A. J., and Tam, L.-M., 1995, "Flow Regime Map for a Horizontal Pipe with Uniform Wall Heat Flux and Three Inlet Configurations," *Exp. Therm. Fluid Sci.*, **10**, pp. 287–297.
- [39] Tam, L.-M., and Ghajar, A. J., 1998, "The Unusual Behavior of Local Heat Transfer Coefficient in a Circular Tube with a Bell-Mouth Inlet," *Exp. Therm. Fluid Sci.*, **16**, pp. 187–194.
- [40] Ghajar, A. J., Tam, L.-M., and Tam, S. C., 2004, "Improved Heat Transfer Correlation in the Transition Region for a Circular Tube with Three Inlet Configurations Using Artificial Neural Networks," *Heat Transfer Eng.*, **25**, pp. 30–40.
- [41] Wang, G. S., Incropera, F. P., and Viskanta, R., 1983, "Mixed Convection Heat Transfer in a Horizontal Open-Channel Flow with Uniform Bottom Heat Flux," *J. Heat Transfer*, **105**, pp. 817–822.
- [42] Osborne, D. G., and Incropera, F. P., 1985, "Experimental Study of Mixed Convection Heat Transfer for Transitional and Turbulent Flow between Horizontal, Parallel Plates," *Int. J. Heat Mass Transfer*, **28**, pp. 1337–1344.
- [43] Grassi, W., and Testi, D., 2006, "Heat Transfer Augmentation by Ion Injection in an Annular Duct," *J. Heat Transfer*, **128**, pp. 283–289.